Detectors developments for the UA9 experiment at the CERN SPS

Andrii Natochii

université PARIS-SACLAY

UNIVERSITÉ PARIS SUD
Comprendre le monde, construire l'avenir

NNT : 2019SACLS254

Thèse de doctorat

Detectors developments for the UA9 experiment at the CERN SPS

Thèse de doctorat
de l'Université Nationale Taras Shevchenko de Kyiv
et de l'Université Paris-Saclay
préparée à l'Université Paris-Sud

Ecole doctorale n°576 Particules, Hadrons, Énergie et Noyaux: Instrumentation, Images, Cosmos et Simulation (PHENIICS)
Spécialité de doctorat: Instrumentation Spatiale

Thèse présentée et soutenue à Orsay, le 13 septembre 2019, par

ANDRII NATOCHII

Composition du Jury :

M. Fabien Cavalier Professeur, Université Paris-Sud	Président
M. Mykola Shulha Professeur, V.N.Karazin KhNU	Rapporteur
M. Giovanni Calderini Directeur de Recherche, LPNHE	Rapporteur
M. Walter Scandale Directeur de Recherche, CERN	Examinateur
M. Achille Stocchi Professeur, Université Paris-Sud	Directeur de thèse
M. Oleg Bezshyyko Professeur Agrégé, T.Shevchenko KNU	Co-directeur de thèse
M. Patrick Robbe Chargé de Recherche, LAL	Invité
M. Igor Kadenko Professeur, T.Shevchenko KNU	Invité

Statement of Originality

I declare herewith, that the work presented is my own original work, and the work of others is referred. During the period of my PhD I was responsible for the following:

- Development of the beam-finder setup, based on motorized linear stages and SiPM detectors.
- Cherenkov detector (CpFM) operation and calibration with bent crystals during the dedicated UA9 SPS machine development (MD) runs and H8 test-beams (DAQ and data analysis).
- Data analysis of the bent crystals measurements at the H8 SPS extraction beamline with a particle tracker telescope (channeling efficiency, crystal deflection angle measurements, inelastic nuclear interaction (INI) probability estimation).
- GEANT4 Monte-Carlo simulation of the experimental setup at the H8 with high-energy proton/pion and ion beams.
- Development of the pulse counter for the alignment of the INI plastic scintillators with respect to the beam axis.
- H8 and SPS beam characterisation with a Timepix detector (DAQ and data analysis).
- Preparation of the Timepix detectors for the UA9 setup upgrade at the SPS for a double-crystal measurements.
- Development of the particle tracker telescope based on Timepix detectors for further bent crystal characterisations (particle tracking).
- Development of the motorized translation stages for the UA9 experiment (hardware, firmware and software development with a graphic user interface for remote controlling).

- Beam monitoring and characterisation at the SPS for double-crystal (with and without target) setup with Timepix, CpFM and beam loss monitor (BLM) detectors (measurements of the single-pass and multiturn particle deflection efficiency of the crystal).
- Characterisation of the fused silica bar surface quality with a β-source (experimental setup, data acquisition and analysis, GEANT4 Monte-Carlo simulation).
- Development of the new geometry for the CpFM detector (GEANT4 Monte-Carlo simulation) in order to improve Cherenkov light collection at the SPS.
- Simulation of the double-crystal setup for short-lived baryon magnetic dipole moment measurements at the SPS.

The work was done in the frame of the UA9 Collaboration with a strong support of the Linear Accelerator Laboratory team, Medipix collaboration, Imperial College London tracker team, PNPI institute group and Nuclear Department of the Taras Shevchenko National University of Kyiv. All their respective publications are referred in the manuscript.

Andrii Natochii

October 8, 2019

Contents

List of Figures

List of Tables

Synthèse en français

Cette thèse a été faite dans le cadre de la Collaboration UA9 au CERN. L'objectif de cette collaboration est d'étudier de manière approfondie les caractéristiques des cristaux courbés pour la collimation et l'extraction de faisceaux de particules de haute énergie, à la fois au Supersynchrotron à protons (SPS) et au Grand collisionneur de hadrons (LHC) du CERN.

Au **Chapitre 2** nous décrivons la physique des interactions des particules de haute énergie avec un réseau monocristallin. Une particule chargée sous l'influence d'un champ électrostatique peut être canalisée entre une paire de plans atomiques voisins formant un puits de potentiel (Fig. 1). Un tel processus est appelé canalisation si l'angle entre la direction de la particule incidente et l'orientation des plans cristallins est petit ($\sim$1–10 μrad). Sur la base de ce principe, si le cristal est courbé dans la direction de la particule, celle-ci suivra la courbure tout au long du cristal ($\sim$1–10 mm). Une telle propriété des cristaux trouve une application en physique des accélérateurs, principalement pour dévier les faisceaux de particules de haute énergie avec des angles de l'ordre d'environ 100–1000 μrad. Le champ électrostatique interplanaire dans le référentiel au repos des particules devient un champ magnétique effectif puissant ($\sim$10–1000 T). Par conséquent, un cristal courbé peut être utilisé au lieu des aimants conventionnels.

Dans le cadre de l'expérience UA9, j'ai participé à de nombreuses mesures sur la ligne d'extraction des faisceaux et aussi au SPS. Au **Chapitre 3** nous donnons une description des mécanismes de base et des principes de fonctionnement des accélérateurs, avec une attention particulière à l'accélérateur SPS, où la Collaboration UA9 dispose d'une section expérimentale (plus de 100 m de long) permettant de réaliser diverses mesures de l'efficacité de la collimation des faisceaux de particules à l'aide de cristaux courbés. Dans **Chapitre 4**, les informations principales sur l'expérience UA9 et ses équipements de recherche sont présentées. Il convient de noter que pour les mesures du flux de particules déviées par les cristaux courbés, les détecteurs utilisés dans les collisionneurs se trouvent dans le vide primaire et dans un environnement à forte dose de rayonnement et donc ils sont soumis à des exigences

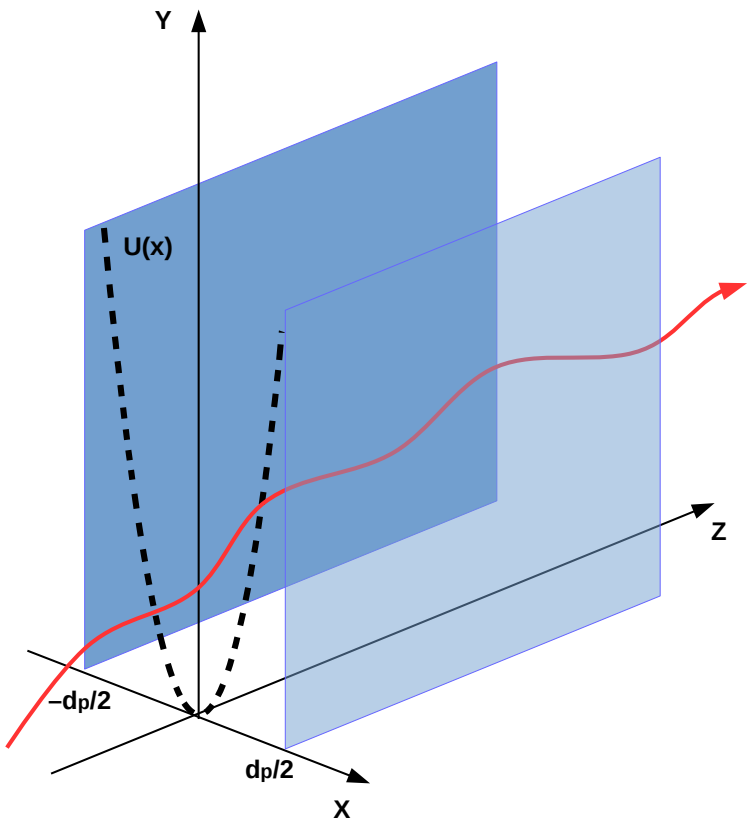

Figure 1: Illustration graphique du mouvement des particules sous l'effet de la canalisation et du système de coordonnées, où $U(x)$ (trait pointillé noir) est la somme des plans cristallins voisins, séparés par l'espace interplanaire de d_p, une courbe en trait plein rouge représente la particule incidente chargée positivement.

assez strictes. Le **Chapitre 5** décrit le principe de fonctionnement des détecteurs Cherenkov (CpFM) et détecteurs de pixels (Timepix) sélectionnés comme moniteurs de faisceau pour le SPS et ayant le potentiel de être installés au LHC (Fig. 2). **Chapitre 6** présente brièvement les résultats des mesures effectuées dans le cadre de l'expérience UA9. Les résultats des caractéristiques des détecteurs sont également présentés. Une partie importante de ce chapitre est consacré au développement et à l'étalonnage des nouveaux détecteurs Cherenkov et des détecteurs à pixels.

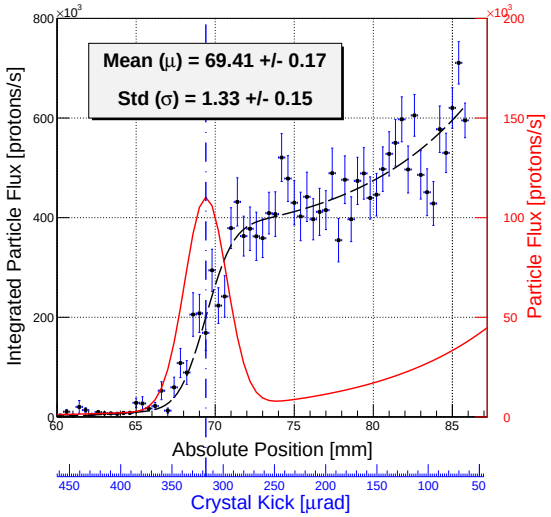

(a) Comptage intégré des particules CpFM le long du balayage linéaire. Une corbeille est égale à 0.4 mm. L'ajustement a été effectué au moyen de la fonction d'erreur + fonction exponentielle (ligne pointillée noire). Les valeurs sigma et moyennes correspondent à l'écart type du faisceau canalisé et à sa position dans le repère de détecteur CpFM. Un dérivé (trait plein rouge) de l'ajustement représente un profil du faisceau, c'est-à-dire un flux de particules.

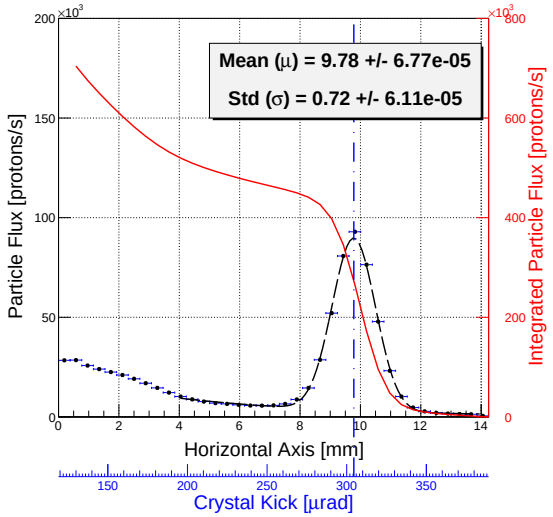

(b) Projection d'axe horizontal de Timepix. Une corbeille est égale à 0,385 mm. L'ajustement a été effectué au moyen de la fonction de Gauss (canalisation) + de la fonction exponentielle (décanalisation) (ligne pointillée noire). Les valeurs sigma et moyennes correspondent à l'écart type du faisceau canalisé et à sa position dans le repère de référence du détecteur Timepix. Une intégrale de la distribution (trait continu rouge) représente un profil de faisceau intégré le long de l'axe horizontal du détecteur, c'est-à-dire un flux de particules intégré.

Figure 2: Mesures du faisceau dévié à l'aide de détecteurs CpFM et Timepix. Les marqueurs noirs avec des barres d'erreur bleues représentent des données expérimentales. L'axe bleu inférieur correspond au coup de pied en cristal équivalent à la position du détecteur.

Dans cette thèse, je présente également une idée de mesure du moment dipolaire magnétique (MDM) des baryons charmés (particules composites composées d'au moins un c-quark) à l'aide des cristaux courbés. Le MDM est une caractéristique

fondamentale, qui décrit l'interaction de la particule avec un champ magnétique externe et permet également d'examiner la structure de la particule en déterminant le facteur gyromagnétique (g). En effet un fermion avec un facteur non nul (g-2) indique qu'il ne s'agit pas d'une particule élémentaire. Jusqu'ici, ce paramètre a été mesuré pour un large spectre de particules constituées de quarks légers (u, d, s). Les résultats expérimentaux sont tous obtenus en utilisant les méthodes classiques, à savoir la mesure de l'angle de précession du vecteur de polarisation lorsque la particule se déplace dans un champ magnétique intense en analysant la distribution angulaire des produits de désintégration. Cependant, il n'a jamais été mesuré pour des baryons plus lourds contenant un quark charmé ou bas. La raison principale de la non disponibilité des informations expérimentales sur les moments magnétiques des baryons charmés/beaux tient au fait que leur durée de vie est trop courte ($\sim 10^{-13}$ s) pour permettre de mesurer le moment magnétique par des techniques standard (champs magnétique trop faible et sur une courte distance). Notre proposition pour pouvoir mesurer les moments magnétiques de ces baryons consiste à utiliser le puissant champ magnétique effectif contenu dans les canaux d'un cristal courbé au lieu du champ magnétique conventionnel qui permet une rotation mesurable du vecteur de polarisation sur une courte distance (Fig 3).

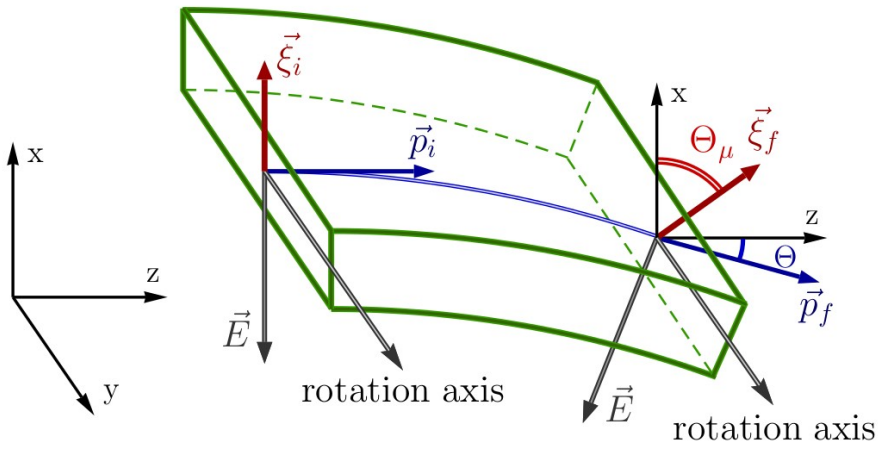

Figure 3: Schéma de l'expérience. Le champ électrique effectif $\overrightarrow{E}$ est orthogonal à la quantité de mouvement $\overrightarrow{p}$. La figure montre le cas de $g > 2$. De [1].

Le travail pour cette thèse se concentre sur une proposition d'expérience pour mesurer le MDM du baryon Λ_c^+ (udc) au SPS et LHC. Les baryons Λ_c^+ polarisés sont produits par interaction forte suite à la collision d'un faisceau de protons extrait (utilisant un premier cristal courbé) contre une cible ; après la cible un deuxième

cristal courbé à grand angle (de plusieurs mrad) est utilisé pour canaliser les baryons Λ_c^+ et induire une rotation mesurable de leur polarisation. Ce système s'appelle une configuration à double cristal (Fig. 4). L'avantage de cette approche est la possibilité de travailler en mode parasite auprès des expériences principales du collisionneur (ATLAS, CMS, ALICE, LHCb).

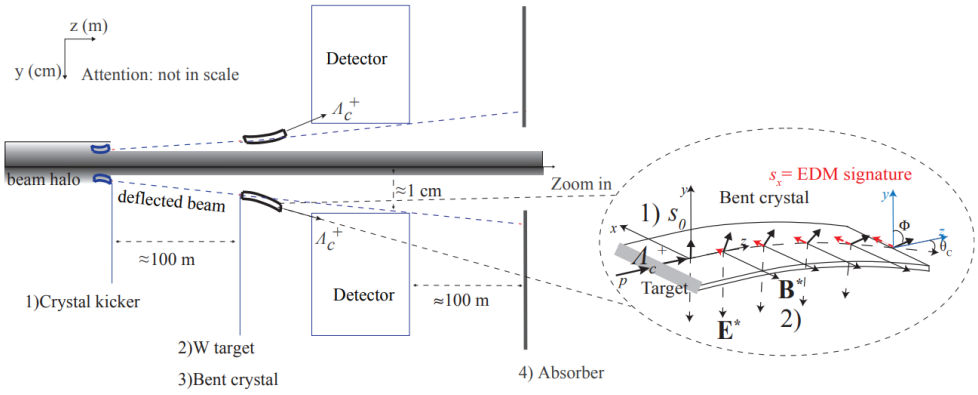

Figure 4: Présentation conceptuelle de la configuration à cible fixe. De [2].

Dans cette thèse, je décrirai la configuration du LHC ainsi que la possibilité d'obtenir les premières mesures au SPS.

Pendent la thèse j'ai développé et testé la configuration à double cristal au SPS (Fig. 5). Ainsi, à **Chapitre 7**, il y a une description de cette configuration qui a été installée à l'intérieur du tube de faisceau sans causer des perturbations sur le faisceau principal. Dans ce chapitre je montre également les principaux résultats obtenus par l'expérience UA9 au SPS.

Les précisions attendus pour de la mesure MDM au LHC et au SPS sont présentées au **Chapitre 8**. Deux réalisations expérimentales possibles basées sur la configuration à double cristal pour effectuer la mesure (MDM, marquage de particules, etc.) au SPS sont également considérées et décrites (Fig. 6).

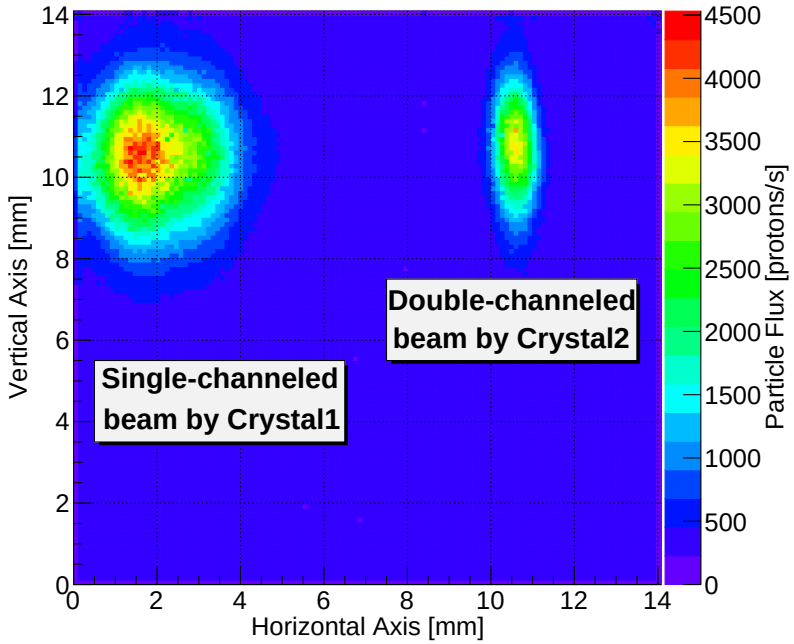

Figure 5: Image Timepix du faisceau dévié par un cristal courbé au niveau du SPS.

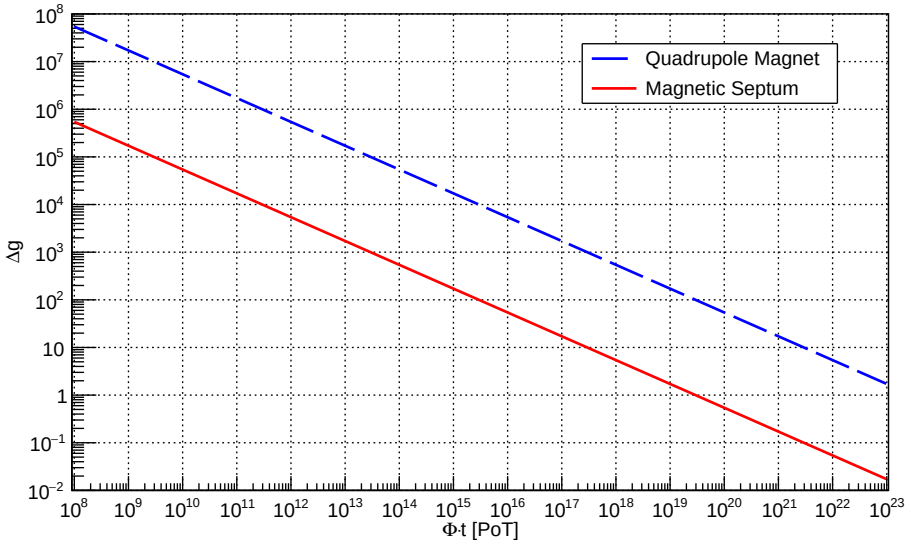

Figure 6: Valeur estimée de l'erreur absolue du facteur g en fonction des particules sur une cible (PoT) au SPS.

Chapter 1

Introduction

I did the works of my thesis in a framework of the UA9 Collaboration at CERN. The aim of the collaboration is to intensively study the characteristics of the bent crystal for high-energy particle beam collimation and extraction purposes, both at the Super Proton Synchrotron (SPS) and Large Hadron Collider (LHC) at CERN.

According to physics of the high-energy particle interaction with a monocrystalline lattice introduced in **Chapter 2**, a pair of neighbour atomic planes form a potential well in which a charged particle under the influence of an electrostatic field follows along this channel. Such a process is called channeling if the angle between the incident particle direction and the orientation of the crystalline planes is keeping small ($\sim$1–10 μrad). Based on this principle, if the crystal is bent in the direction of the particle, then under the influence of the interplanar field, it will follow the curvature of the bending along the crystal length ($\sim$1–10 mm). Such a property of the crystals found an application in accelerator physics, mainly for the deflection of the high-energy particle beam by about 100–1000 μrad. And in this way, according to the Lorentz transformations, the interplanar electrostatic field in the particle rest frame becomes a strong effective magnetic field ($\sim$10–1000 T). Therefore, a curved crystal can be used instead of conventional magnets.

Within the UA9 experiment, I have been involved in many different measurements at the extraction beamline and circular accelerator. Therefore, **Chapter 3** will serve as a good collection of the basic mechanisms and principles of operation of the machine that will be necessary for further consideration of the material of this thesis. The main focus is on the SPS accelerator, where the UA9 Collaboration has an experimental section (more than 100 m long) for conducting various measurements of the efficiency of particle beam collimation using bent crystals. Thus, in **Chapter 4**, the main information about the UA9 experiment and its research equipment is brought. It should be noted that for the measurements of the flux of

particles deflected by the bent crystal, there are quite strict requirements for the detectors used at the circular accelerator inside the primary vacuum with a high radiation dose environment. Therefore, **Chapter 5** describes the operational principle of the Cherenkov (CpFM) and pixel (Timepix) detectors that were selected as beam monitors for the SPS with the possibility of installation at the LHC. In **Chapter 6**, the results of measurements carried out as a part of the UA9 experiment are briefly introduced. The results of the characteristics of the detectors are shown as well. A significant part of this chapter is devoted to the development and calibration of the new Cherenkov and pixel detectors.

In this thesis, I also present an idea of measuring the magnetic dipole moment (MDM) of the charmed baryons (composite particles made of at least one c-quark) using a bent crystal. MDM is the fundamental characteristic, which describes the interaction of the particle with an external magnetic field. But it also makes it possible to investigate the structure of the particle by determining the gyromagnetic (g) factor. According to the Standard Model (SM), a fermion with non-zero (g-2)-factor indicates a composite structure and that it is not an elementary particle. So far, this parameter was measured for a wide spectrum of particles consisting of light quarks (u, d, s). The experimental results are all obtained by using the conventional methods, namely the measurement of the precession angle of the polarisation vector when the particle is traveling through an intense magnetic field by analyzing the angular distribution of the decay products. However, it has never been measured for heavier baryons containing a charm or bottom quark. A reason of the non-availability of experimental information on the magnetic moments of baryons with heavy flavoured quarks is because their lifetimes are too short ($\sim 10^{-13}$ s) to measure the magnetic moment by standard techniques. Our proposal to meet the challenge of measuring the magnetic moments of baryons with heavy flavoured quarks is to use the strong effective magnetic field inside the channels of a bent crystal instead of the conventional magnetic field to process the polarization vector and measure the magnetic moment.

This work concentrates on a proposed experiment to measure the MDM of the $\Lambda_c^+(udc)$ baryon at the SPS and LHC. Polarised Λ_c^+ baryons are produced by a strong interaction of extracted proton beam (using a first bent crystal) impinging onto a a target followed by the second large angle bent crystal (of several mrad) to channel the Λ_c^+ baryons and to rotate their polarization vector. This configuration is called a double-crystal setup. The advantage of this approach is a possibility to work in a parasitic mode to the main experiments at the collider (ATLAS, CMS, ALICE, LHCb).

In this thesis, I will describe the LHC setup and the possibility of obtaining the first measurements at the SPS.

During my thesis I developed and tested the double-crystal setup at the SPS. Thus, in **Chapter 7**, there is a description of this configuration, that provides measurements inside the beam pipe without perturbation of the main beam. In this chapter, the main results of the UA9 experiment at the SPS with and without a target-converter are discussed as well.

The precision expected for the MDM measurement at the LHC and SPS are given in **Chapter 8**. Two possible experimental configurations based on the double-crystal setup for conducting the measurement (MDM, particle tagging, etc.) at the SPS are also considered and described.

Chapter 2

Crystal Channeling Physics

Scientists are interested in the passage of charged particles through the crystal structure from the beginning of the last century. Many experimental and theoretical works have been carried out to explain the nature of those effects that occur when a charged particle passes near crystallographic planes or atomic strings. The first hypothesis about the non-anisotropy of directions in the crystal for charged particles was put forward by Stark in 1912 [3]. From that moment on, the attention of the scientific world was focused on the study of this question and its experimental confirmation.

Over the past century, many theoretical models have been created describing the passage of high-energy particles through the crystal structure. Many experimentally observed effects have confirmed our understanding of the nature of what is happening, and also gave a reason to think about the application of these results in various fields of science.

In this chapter we will consider only the main aspects of the interaction of charged particles in the crystals, i.e. planar channeling. A more detailed description of the channeling physics can be found in [4].

2.1 Introduction

Further in the text we will examine the main principles of the channeling with theoretical explanations. Our attention will be focused mainly on positively charged particle beams, such as protons, pions, and ions with energies greater than 70 GeV per nucleon. The main processes that will interest us and arise when a charged high-energy particle passes through a straight or curved crystal are the Planar (PCH) and Axial Channeling (ACH), which are accompanied by the Dechanneling (DCH) process. In the bent crystal some effects may arise, which are related to the asymmetry

of the interplanar potential, such as Volume Reflection (VR) and Volume Capture (VC). A non-secondary aspect of the use of oriented crystals in accelerators is the measurement of the Inelastic Nuclear Interaction (INI) probability of high-energy particles with atoms of a crystal lattice, which will be discussed in Chapter 6.

We will be focused mainly on silicon and, more rarely, germanium crystals, due to the level of perfections of the crystal structure (crystal lattice) and well-developed technology of growing large semiconductor crystals. Silicon and germanium are crystallized with the structure of diamond, which is face-centered cubic (fcc) lattice (Fig. 2.1a). To describe the lattice Miller indices can be used [4], using (hkl) or $< hkl >$ for the plane and axis notation, where h, k and l are the Miller indices (Fig. 2.1b).

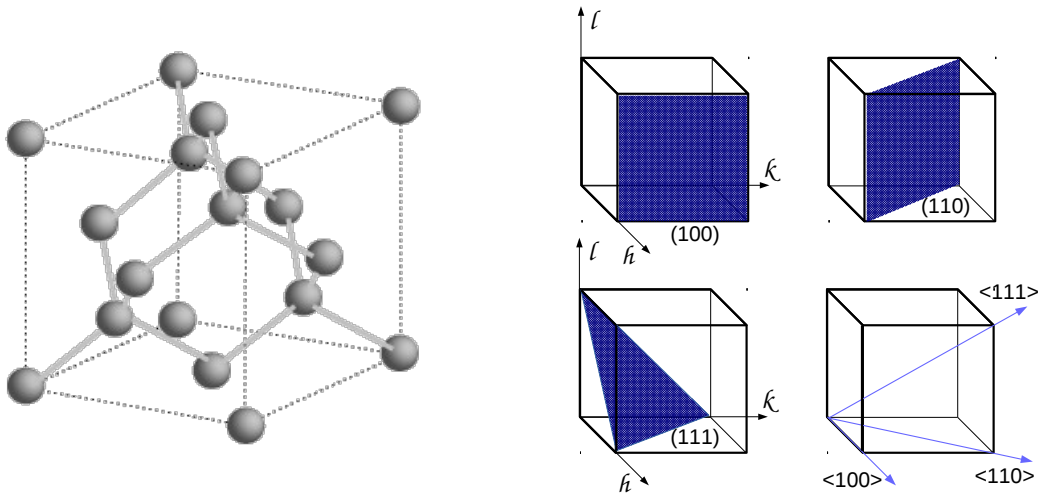

(a) Face-centered cubic crystalline lattice.

(b) The main planes and axes of the simple cubic lattice. Since for Miller indices the minimal possible numbers are used, the planes and axes are represented with h=0,1, k=0,1, and l=0,1.

Figure 2.1: Illustration of the crystal structure.

2.2 Charged particle channeling

Within the framework of the classical mechanics, Lindhard [5] developed a theory of the orientational effects of the fast charged particles in crystals, which successfully explained the experimental results which had been obtained by that time. In evaluating the adequacy of the particle motion classical description, it is necessary to take into account the following considerations [6]:

1. In channeling, particles execute finite motion in the transverse direction, and their transverse energies are quantized. The distance between levels for positively charged particles in the field of a planar channel, assuming that it is harmonic, is $\hbar\omega$, where ω is the oscillation frequency. For the number of levels in a channel potential well (for positively charged particles, the potential well is generated by the repulsion given by the atomic plane, having the same charge of the particles) of depth U_0 we have:

$$n = \frac{d_p}{\hbar\sqrt{8}}\sqrt{U_0 m\gamma} \tag{2.1}$$

where d_p is the distance between crystalline plane and $m\gamma$ is the relativistic mass of the particle.

2. When the transverse de Broglie wavelength of the particle ($\lambda = h/p$, where p is particle momentum) is much smaller than the channel width, the quantized tunneling of particles to the sub-barrier region (inside a well) can be neglected.

Therefore, the classical approach developed by Lindhard for heavy relativistic particles and electrons (positrons) with energy above 100 MeV is completely applicable for channeling effect description.

2.2.1 Equation of motion

It was shown by Lindhard [5] that with a small angle between incident charged particle and crystal plane (axis) the consecutive collisions of the particles with atoms of the lattice are correlated between each other and it is necessary to consider an interaction of the charged particle with atomic plane (atomic string). Thus it was decided to replace the the potentials of each separate atom by the averaged continuous potential.

Considering a particle moving not in any major string direction, but still nearly parallel to a plane in a lattice (Fig. 2.2), the continuous potential is the following:

$$U_{pl}(x) = Nd_p \int\int_{-\infty}^{+\infty} V(x,y,z)dydz \tag{2.2}$$

where $V(x,y,z)$ is a potential of the particle interaction with an atom, N is a number of atoms per unit volume, d_p is a distance between neighbor planes. Under Molière approximation an interaction potential between crystalline plane and particle with a charge of $Z_i e$ can be written as the follow:

$$U_{pl}(x) = 2\pi N d_p Z_i Z e^2 a_{TF} \sum_{i=1}^{3} \frac{\alpha_i}{\beta_i} exp\left(-\frac{\beta_i x}{a_{TF}}\right) \tag{2.3}$$

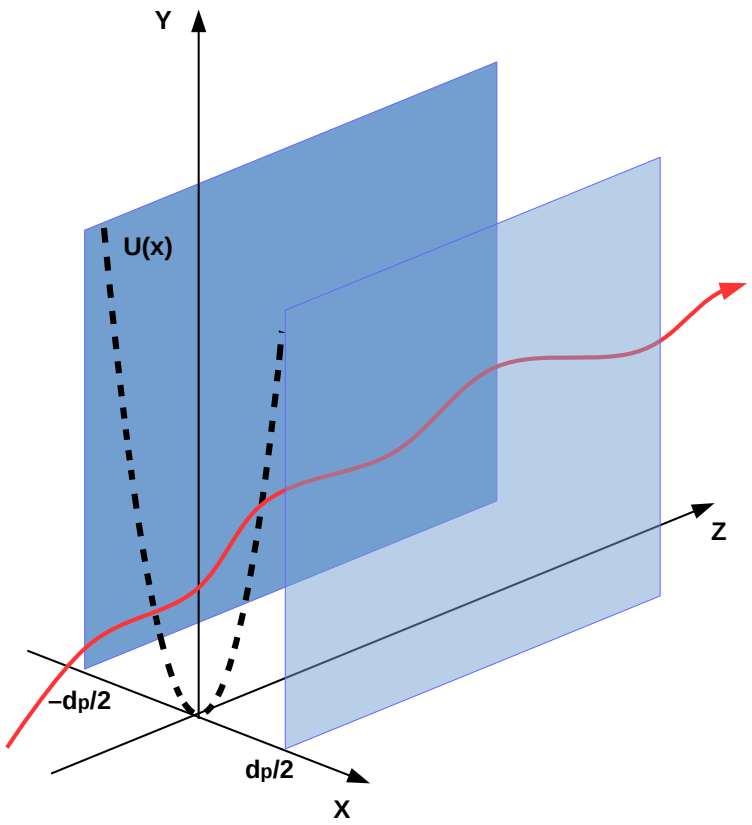

Figure 2.2: Graphic illustration of the particle motion under channeling effect and coordinate system, where $U(x)$ (black dashed line) is a sum of the neighbor crystalline planes, separated by the interplanar space of d_p, a red solid curve represents the incident positively charged particle.

where $\alpha = (0.1; 0.55; 0.35)$, $\beta = (6.0; 1.2; 0.3)$, Thomas-Fermi screening parameter $a_{TF} = 0.8853 a_B Z^{-1/3}$, $a_B = 0.529$Å. Thermal vibrations of the atoms change the potential Eq. 2.2 near the plane at distances of the order of the thermal vibrations amplitude u_T. More details about the modified potential can be found in [7].

A particle, which is moving inside the crystal, is present in the potential, which is a sum of potentials of the separate planes:

$$U(x) \approx U_{pl}(d_p/2 - x) + U_{pl}(d_p/2 + x) - 2U_{pl}(d_p/2) \tag{2.4}$$

(contributions of two nearest atomic planes dominate), where x is defined with respect to the midplane between the atomic layers and $U(0) = 0$. The distance between crystalline planes for silicon crystal with (110) orientation is $d_p = 1.92$Å; for (111) orientation the large distance is $d_p^L = 2.35$Å and a small one is $d_p^S = \frac{1}{3} d_p^L$ [4]. Figure 2.3 shows the potential for (110) and (111) planes of silicon crystal.

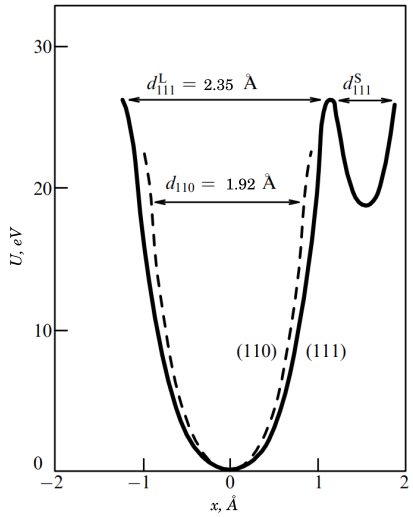

Figure 2.3: Calculated continuous potentials of the planes (110) (dashed line) and (111) (solid line) for silicon.

The potential-well depth U_0 in silicon is of the order of 20 eV (Fig. 2.4a). The value of the maximum interplanar electric field $U'(x)$ for silicon is around 6×10^9 V/cm (Fig. 2.4b), for tungsten is up to 10^{11} V/cm. Some channels parameters for different crystals are shown in the Table 2.1.

The transverse motion of the particle, which is moving at small angle (the scale of these angles will be discussed later) to the crystalline plane or axis, is defined by the continuous potential of the crystalline lattice. Early it was written that the fields crystal planes or axes produce potential wells, in which the particle motion can be stable. In this case we can speak about particle channeling (CH): planar channeling

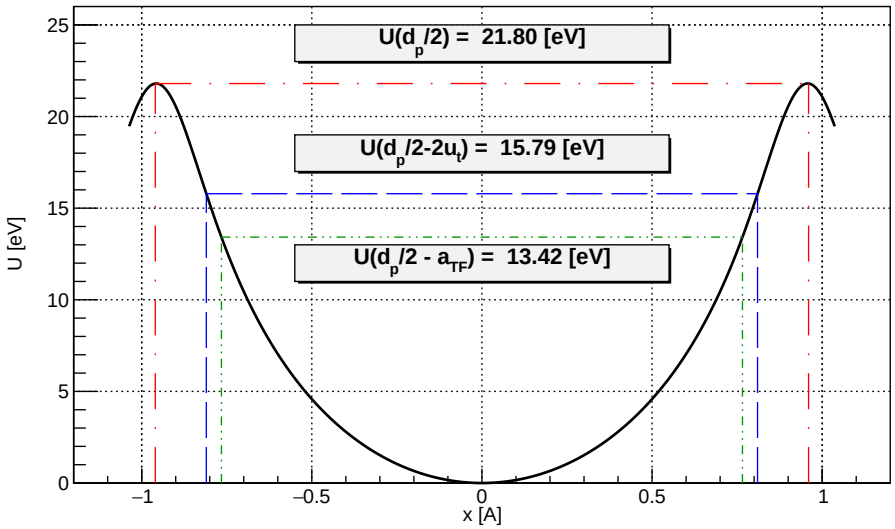

(a) The interplanar Moliere potential.

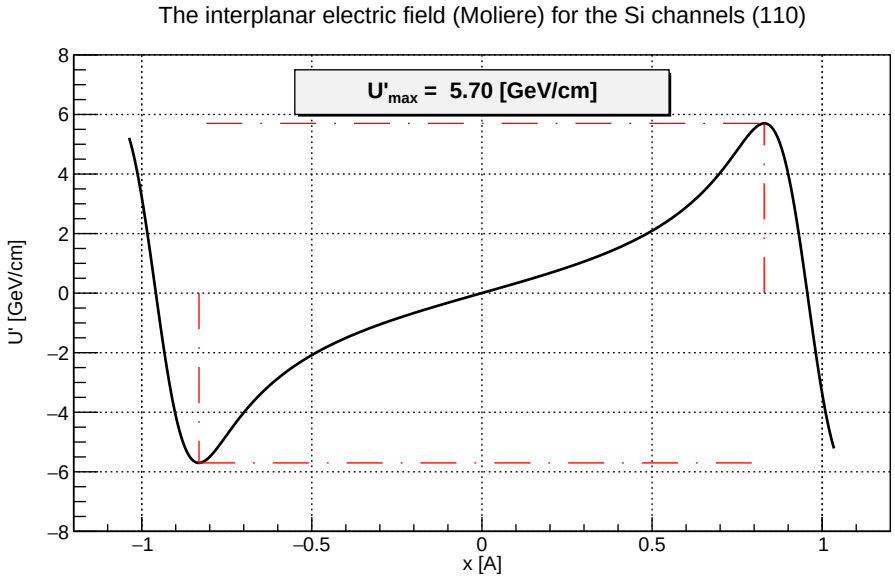

(b) The interplanar electric field (Moliere).

Figure 2.4: Characteristics of the Si channels (110).

Channel	d_p [Å]	a_{TF} [Å]	u_T Å	$U(x_c)$ [eV]	$U'(x_c)$ [GeV/cm]
Si		0.194	0.075		
(110)	1.92			16	5.7
(111)L	2.35			19	5.6
(111)S	0.78			4.2	3.5
Ge		0.148	0.085		
(110)	2.00			27	10
(111)L	2.45			30	9.4
(111)S	0.81			7.2	6.4
W		0.112	0.050		
(100)	1.58			63	30
(110)	2.24			105	43

Table 2.1: Parameters of some planar channels of the crystals of silicon, germanium, and tungsten, at room temperature. The potentials are given at $x_c = d_p/2 - 2u_T$ in the Molière approximation [4].

(PCH) if the particle is connected to the plane and axial channeling (ACH) if the motion goes along axis.

For the negatively charged particles the continuous potential is simply the negative of that governing the motion of positively charged particles [7]. Figure 2.5 shows the differences between the potentials $U^+(x)$ and $U^-(x)$ for the PCH of positrons (β^+) and electrons (β^-), respectively. The minimum of the potential well for electrons lies in the strings or planes of crystal atoms while for positrons (as for protons) it lies between them. We will concentrate our attention on the positive charged particles as the most used type of the high-energy particle beam at CERN accelerator facilities, while the detailed information about channeling of high-energy negatively charged particles can be found in [7].

Lets take a look on equation of high-energy particle $(p^2c^2 + m^2c^4)^{1/2}$ motion in the transverse to the motion potential $U(x)$. If the transverse component p_x of the particle momentum p is much smaller than longitudinal component p_z (i.e. $\theta = p_x/p_z \ll 1$), we can write the equation of the total energy conservation $E = (p_x^2c^2 + p_z^2c^2 + m^2c^4)^{1/2} + U(x) = const$ like

$$\frac{p_x^2c^2}{2E_z} + U(x) + E_z = const, \tag{2.5}$$

where $E_z = (p_z^2c^2 + m^2c^4)$ and the sum of the first two components in Eq. 2.5 is the transverse energy $E_x(x, p_x)$. During the movement in the potential $U(x)$ the

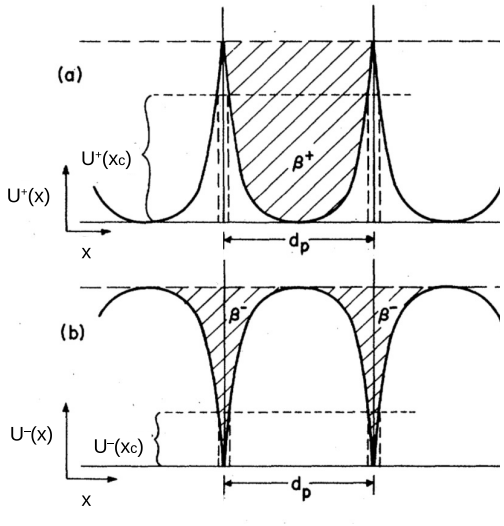

Figure 2.5: Schematic illustration of the planar continuous potential for (a) positrons and (b) electrons. The shaded areas correspond to the potential wells in which channeled particles can move. $U^+(x)$ and $U^-(x)$ are the potentials evaluated at the critical distance $x_c = d_p/2 - 2u_T$ from a plane. Note that $U^-(x)$ represents a lower limit for the transverse energy at which stable electron channeling is possible, while $U^+(x)$ is the corresponding upper limit for positrons [7].

longitudinal component conserves, which means the conservation of E_x:

$$E_x = \frac{p_x^2 c^2}{2E_z} + U(x) = \frac{p_z^2 c^2}{2E_z}\theta^2 + U(x) = const. \tag{2.6}$$

Assuming $E_z \cong E,\ p_z \cong p$ and using $pc^2 = vE$, where v is particle velocity, we can rewrite Eq. 2.6 as the follow:

$$E_x = \frac{pv}{2}\theta^2 + U(x) = const. \tag{2.7}$$

Differentiating Eq. 2.6 in z and taking into account the same substitution, we get an equation

$$pv\frac{d^2x}{dz^2} + U'(x) = 0 \tag{2.8}$$

for one-dimension transverse movement in the $U(x)$ potential. It describes oscillations of the particle in the potential well of the planar channel. In the harmonic potential $U_0(2x/d_p)^2$ the oscillation period λ is $\pi d_p\sqrt{pv/2U_0}$ (~ 30 μm for 100 GeV proton and up to 0.5 mm for 20 TeV proton inside silicon crystal).The solution of the Eq. 2.8 is an equation of particle motion (a sinusoidal oscillation) under channeling condition:

$$x = \frac{d_p}{2}\sqrt{\frac{E_z}{U_0}}sin\left(\frac{2\pi z}{\lambda} + \phi\right), \tag{2.9}$$

$$\theta = \sqrt{\frac{2E_z}{pv}} cos\left(\frac{2\pi z}{\lambda} + \phi\right), \tag{2.10}$$

the particle trajectory may be obtained by integration of

$$dz = \frac{dx}{\sqrt{\frac{2}{pv}[E_z - U(x)]}}. \tag{2.11}$$

The condition for particle trapping into the channeling mode is

$$\frac{pv}{2}\theta^2 + U(x) < U_0. \tag{2.12}$$

Assuming that $x = 0$, we get a limiting angle introduced by Lindhard:

$$\theta_L = \sqrt{\frac{2U_0}{pv}}. \tag{2.13}$$

According to [8], due to the scattering by nuclei particle can escape the channel (dechanneling) and the distance, at which particle capture becomes to be destroyed, is of order of a_{TF}. Therefore the critical coordinate in transverse direction for channeling motion can be determined as

$$x_c \approx (d_p/2) - a_{TF} \tag{2.14}$$

and the critical channeling angle is:

$$\theta_c = \sqrt{\frac{2E_c}{pv}}, \tag{2.15}$$

where $E_c = U(x_c)$ is the critical transverse energy. The thermal vibration contribution was experimentally investigated at FNAL [9].

Some values of critical angles, for protons and silicon crystal, are given in the Table 2.2 for some energies of the particle beam (will be discussed later in the text).

Beam Energy, GeV	θ_c, μrad	λ, μm
180	15.6	38.8
270	12.7	47.5
400	10.4	57.8
450	9.8	61.3
7000	2.5	241.7

Table 2.2: Critical angle for channeling (θ_c), oscillation period (λ) for a straight Si(110) crystal, where $E_c = U_{max}$.

2.2.2 Bent crystal

The suggestion to use a bent crystal for charged particle beam steering was pointed out by Tsyganov in 1976 [10, 11]. The first realization of the proposition was experimentally held at JINR in 1979 [12].

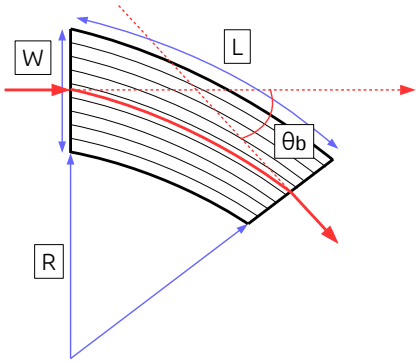

Figure 2.6: Schematic drawing of the crystal with θ_b of bending angle. Red solid lines represent particle trajectory along the crystal with L length and width of W. To avoid the crystal lattice structure destroying under the bending pressure, the curvature radius R has to be larger than the crystal width W.

Lets consider the motion of the particle in the crystal under channeling condition. In contradiction to the straight crystal case, this time the crystal is curved with the bending radius of R, which defines the bending angle θ_b of the crystal together with its length L (Fig. 2.6) as $\theta_b = L/R$. Now we can rewrite the equation 2.8 of particle motion taking into account the centrifugal force pv/R:

$$pv\frac{d^2x}{dz^2} + U'(x) + \frac{pv}{R} = 0. \tag{2.16}$$

Therefore the particle moves as if it were in the effective interplanar potential:

$$U_{eff}(x) = U(x) + \frac{pv}{R}x. \tag{2.17}$$

An example of the different effective potentials for straight and bent crystals is shown in Figure 2.7.

Due to the acting of the centrifugal force the minimum of the potential well is shifted and the potential well depth is decreased between two neighbor atomic planes. The critical radius is then defined by combining the centrifugal force and

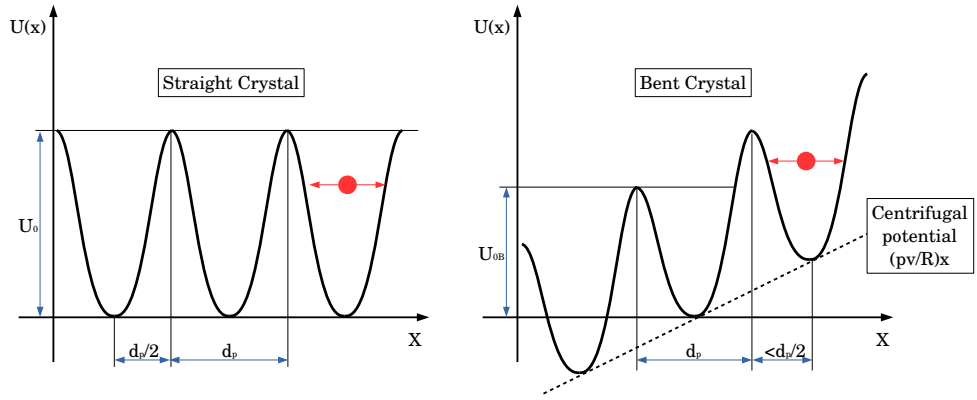

Figure 2.7: Effective potential for straight (left) and bent (right) crystals. Illustration of the channeling process.

maximum electric force for a straight crystal $U'_{max} = \left(\frac{dU(x)}{dx}\right)_{max}$. Thus it can be written in the following way:

$$R_c = \frac{pv}{U'_{max}(x)}. \tag{2.18}$$

This variable defines the minimal bending radius for which the channeling regime for charge particle is still possible. Taking into account the harmonic potential approximation the potential depth for bent crystal is:

$$U_{0B}\left(\frac{R_c}{R}\right) = U_0\left(1 - \frac{R_c}{R}\right)^2, \tag{2.19}$$

where U_0 is the potential well depth for a straight crystal. The critical angle for a particle to be captured in to the channeling regime is:

$$\theta_c\left(\frac{R_c}{R}\right) = \theta_{c0}\left(1 - \frac{R_c}{R}\right), \tag{2.20}$$

where θ_{c0} is the critical angle for a straight crystal (Eq. 2.15).

Taking into account above, the equation of motion for the bent crystal case can be written as the follow:

$$x = -x_{min} + x_c\sqrt{\frac{E_z}{U_{0B}}}sin\left(\frac{2\pi z}{\lambda} + \phi\right), \tag{2.21}$$

where the new equilibrium point will be:

$$x_{min} = -\frac{pv(d_p/2)^2}{2RU_0} \tag{2.22}$$

2.3 Volume Reflection and Volume Capture

Together with channeling effect in the bent crystal there is another effect, which conserves the total transverse energy and it's called volume reflection (VR). It is the single reflection of the particle from the crystal plane in opposite direction to the channeling (CH). When the particle enters the crystal with an angle bigger then the critical angle for the channeling in a straight crystal, the effect of VR takes place. It was discovered by Taratin and Vorobiev in the computer analysis of particle trajectories at a bent crystal [13]. An analytical theory of this phenomenon as a process of fast particles scattering in central field of specific configuration was proposed in the work [14].

Using a simple geometrical approach to understand the main concept of the VR effect (Fig. 2.8), we can say that along the passage of the crystal an incident particle angle decreases and if at some plane (e.g. $i^{th} plane$) this angle (θ_i) will become smaller than θ_{0c} the particle will be reflected increasing impact angle with respect to the following planes.

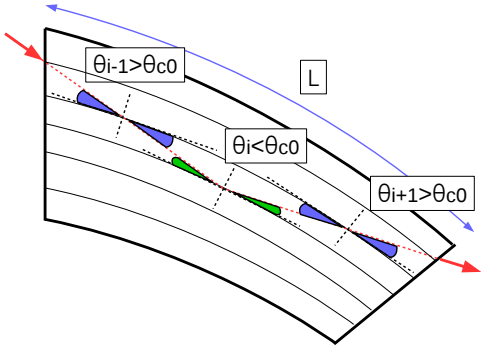

Figure 2.8: Simple scheme of the VR effect interpretation.

The VR effect has been investigated for high-energy protons in [15–18]. It was measured that the VR deflection angle is increasing with the critical angle for CH as $1.4\theta_c$ [18]. The value of the its deflection efficiency is very close to 100% and it is limited by the another concurrent process of volume capture (VC) or feed-in process. The latter is a trapping of particles into the channeling regime, when the particle is close to an atomic plane (the density of electrons is higher) loses some transverse energy (Fig. 2.9). The probability of VC process increases with the bend

radius because the tangency VC area length where the particle momentum direction is close to be tangent to the bent planes is increased $\sim R\theta_c$ [19].

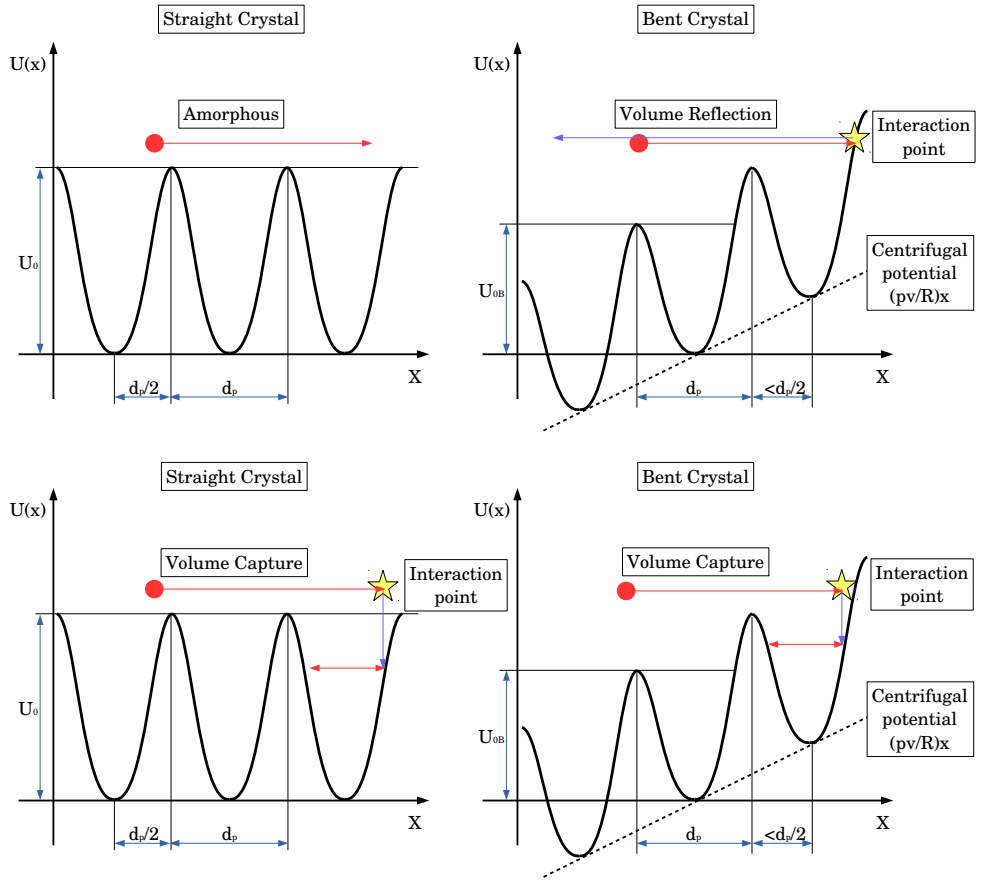

Figure 2.9: Effective potential for straight (left) and bent (right) crystals. Illustration of the VR (top) and VC (bottom) processes. When the particle goes through the crystal with a transverse energy much higher than its interplanar potential well it sees the crystal as an amorphous material (top left). For above-barrier particles with a lower energy there is a probability to interact with one of the crystalline planes and to be reflected (top right). In the same time this particle can be captured in a channeling regime after interactions with atomic nuclei or electrons (bottom).

2.4 Dechanneling

The dechanneling (DCH) or feed-out process is the opposite to the VC effect (Fig. 2.10). It takes place when the particle passing the crystal in the CH regime increasing its transverse energy in collisions with electrons (with nucleus for neg-

atively charged particle) closer to the atomic plane, where the electron (nucleus) density is higher. Therefore, when the transverse energy exceeds some acceptance level, the particle leaves the channeling regime. It was shown [20] that for the given well settled manufacturing process, the influence of the crystal imperfections can be neglected.

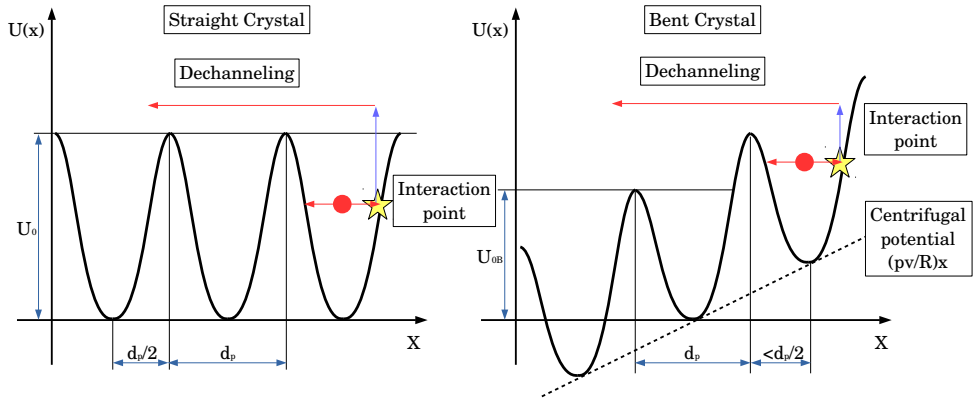

Figure 2.10: Effective potential for straight (left) and bent (right) crystals. Illustration of the dechanneling process. Channeling particle interactions with atomic nuclei and electrons can results in an increase of the its transverse energy. As a result the particle escapes the channeling regime.

According to [4, 6] the DCH process can be described as:

$$N = N_0 e^{-z/L_D}, \tag{2.23}$$

where N and N_0 are the numbers of the channeled and incoming to the crystal particles respectively, z is a position along the crystal and L_D is a dechanneling length. For a bent crystal with bending radius of R, L_D can be written as:

$$L_D(pv, R) = L_{D,0}(pv)\left(1 - \frac{R_c(pv)}{R}\right)^2, \tag{2.24}$$

where $L_{D,0}$ is the dechanneling length for a straight crystal and R_c is a critical radius (Eq. 2.18). For a fixed radius the dechanneling length for a bent crystal can be rewritten in the following way:

$$L_D(pv, R) = spv\left(1 - \frac{pv}{(pv)_c}\right)^2, \tag{2.25}$$

where s is a normalization parameter (around 0.54 mm/GeV for 60 – 200 GeV/c protons in Si crystal at room temperature) [4]. In case of a long crystal, the maximum value of L_D (at $pv = (1/3)(pv)_c$) can be used to minimize the dechanneling losses.

2.5 Axial channeling

When the charged particle is moving along one of the crystalline axis with a small angle the axial channelling (ACH) process takes place [5]. In this case the particle moves in the average potential formed by the atomic strings with angular acceptance of $\pm\theta_c^{ax}$, where θ_c^{ax} is a critical angle for ACH.

There are two types of particle states under the ACH regime: hyperchanneling [21] and doughnut scattering [22]. The hyperchanneling is the confinement of the particle bounded up with a single axial channel. Due to the low potential well between neighbor crystalline strings the maximum potential energy is very small compare to the PCH case. That is why, even for a perfectly aligned crystal, only a small fraction of particle beam can be trapped into this regime. The usual potential well value for Si crystal in $< 110 >$ orientation is about 6 eV and for the $< 111 >$ is only 1 eV. However, particles which have transverse energy higher than potential well, mentioned above, still can be in the axial channeling regime due to the doughnut scattering. This effect of unbounded state is a process of scattering by atomic strings that does not smear the transverse momentum of particles and they can continue to follow the axis curvature. Some experimental results of ACH deflection efficiency for $< 111 >$ and $< 110 >$ orientations can be found in [23] and [24] respectively.

2.6 Channeling efficiency definition

In the next chapters we will see how bent crystals are used for different applications in high energy physics (HEP). We focus on the high-energy accelerator environment with extraction lines and circulating beams. For these cases we have to determine the deflection efficiency of the bent crystal. In general, statistically speaking, the efficiency of some process can be defined like the ratio between a number of interesting or good events (in our case it is a number of channeled particles N_{ch}) and a number of all events (total number of incident to the crystal particles N_{tot}). Indeed, this calculation has to be done taking into account special condition, which are favorable for the interesting effect (geometrical and angular acceptance of the crystal for a given particle beam). Thereby, we can write the efficiency of specific process (channeling) like:

$$\eta = \frac{N_{ch}}{N_{tot}} \tag{2.26}$$

However, depending on the experimental setup (detection methods, beam line, circulation beam, etc.), different restrictions has to be applied. Here we are trying to

outline the main concept for its calculation.

When the particle crosses the crystal only once along its path, it means that a single-pass process takes place. For this case it is necessary to take into account, for efficiency estimation, only the fraction of the incident beam which is within the geometrical (impinging the crystal) and angular (almost parallel to the crystalline planes) cuts. In this way we can find optimal orientation of the crystal which has a maximum deflection single-pass efficiency. Most of the time such technique is applicable for the extraction beam line like H8 SPS in the North Area (see Chapter 4).

For a circular machine like CERN LHC or SPS we will speak mostly about multi-turn efficiency. For this type of machine the bent crystals used for collimation and extraction and they are inserted in the beam halo to deviate particles. Each particle in the halo can pass the crystal several time along its circular movement. In this condition the calculation of the N_{tot} can be done using the total rate of lost particles using a beam loss monitor (BLM) located close to the movable obstacle (e.g. beam collimator jaw) intercepting the deflected beam by the crystal. This method was proposed in [25].

2.7 Bending method

To qualitatively deflect a beam of charged particles using a curved crystal, it is necessary to achieve a high channeling efficiency. This value is affected by a number of different parameters, but the most significant of them is the size of the potential well of the crystal. The higher the potential barrier (U_{x_c}), the greater the angular acceptance of the crystal (θ_c), and it is more likely for the particle to remain in channeling mode ($L_D \to \infty$). It is also necessary to note, that the number of imperfections of the crystal (e.g. the density of dislocations) influences the efficiency of the charged particle channeling. Table 2.1 shows the potential barriers for some crystals of different materials (more studied materials for beam deflection). It is easy to see that for a large Z crystal (tungsten) the value of the potential well is higher than for a low Z material (silicon). It would seem logical to use crystals with a large Z, but the problem lies in the difficulty of producing very pure single crystals with a large Z. Since nowadays the production technology of the ultra-pure silicon monocrystalline samples (dislocation density $< 1/\text{cm}^2$) has reached high quality, silicon crystals become more popular for crystals producing for the particle deflection.

Silicon has Face-centered cubic (FCC) lattice and for producing even a small bending angle crystal it is necessary to apply quite big torque. As it is shown in [26],

we can use mechanical properties of silicon for obtaining the secondary curvature. Applying the force to different orientations we can achieve the following bending effects: anti-clastic [27, 28] and quasi-mosaic [29]. The anti-clastic method (AC) usually used for (110) crystal orientation (Fig. 2.11a and 2.11b), while the quasi-mosaic (QM) for (111) (Fig. 2.11c and 2.11d). The difference between potential wells is illustrated in Figure 2.3. Figure 2.11 shows the crystals and their bending devices made from titanium.

(a) Anti-clastic crystal photo.

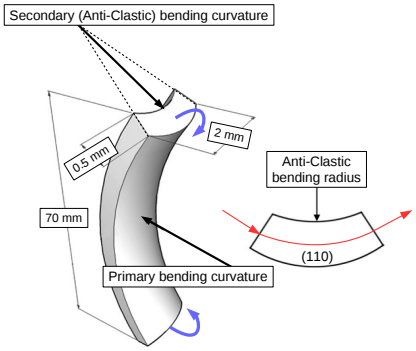

(b) Induced anti-clastic curvature scheme. Red line represents an incident particle; blue lines show the applied force direction.

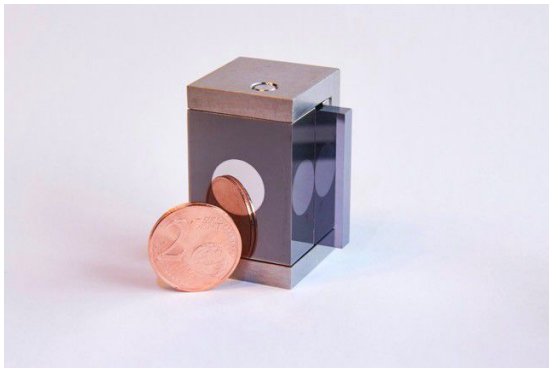

(c) Quasi-mosaic crystal photo.

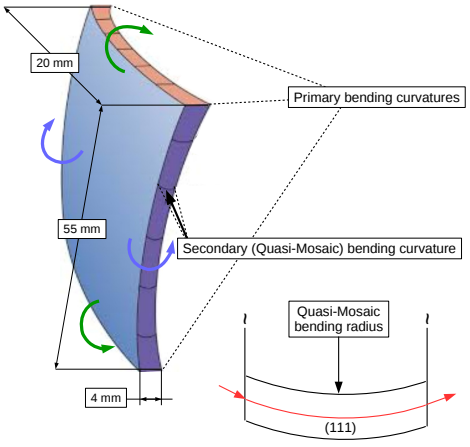

(d) Induced quasi-mosaic curvature scheme. Red line represents an incident particle; blue and green lines show the applied forces directions.

Figure 2.11: Bent silicon crystals in the titanium holders. Typical crystal sizes are indicated.

Chapter 3

Accelerator physics

In this chapter, we will discuss the basic principles of the synchrotron accelerators operation and, at a basic level, consider the equations of motion for high-energy charged particles in this machine. We will stop only on the most important aspects of this question, writing down the equations necessary for further consideration of the material in this thesis. More detailed information about accelerator physics can be found in [30].

3.1 Transverse beam dynamics

3.1.1 Equation of motion

The basic idea to use accelerator for increasing the particle energy leads to the solution of the following issues: (1) how to keep a particle inside a beam pipe? (2) how to increase its energy? (3) how to store the beam for a long time? For all this questions there is an optimal solution, which is strong focusing synchrotron machine, composed only of dipole magnets, quadrupole magnets and accelerating resonant cavities. The magnetic field of the dipole magnet deflects particle trajectory in order to keep it on a circular orbit. The ideal orbit of the particle is called reference or design orbit, and all other particles coordinates in the beam are taken with respect to the reference particle (Fig. 3.1). Quadrupole magnetic field is used to control the beam size and its divergence. A single quadrupole magnet focuses particle beam in one plane (e.g. XS) and defocuses in the orthogonal plane (e.g. YS). To keep the beam of high-energy particles for along time (distance) without increasing its cross-section size a set of focusing and defocusing magnets is needed, and they will form a FODO cell structure [30], which is the most fundamental accelerator lattice. Resonant cavities are needed to accelerate particles and to compensate the energy

losses due to the synchrotron radiation in the machine.

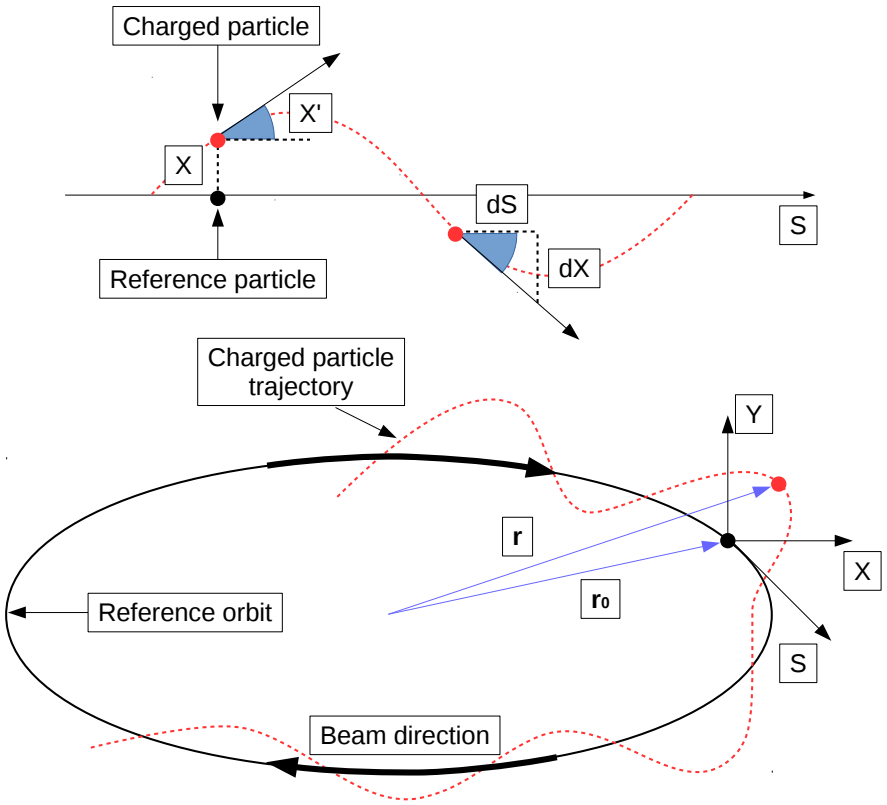

Figure 3.1: Illustration of the particle coordinate system in the circular machine.

Lets write down an equation of particle motion in the accelerator magnetic lattice using Maxwell's equations. The reference system can be chosen as it is illustrated in Figure 3.1. The state of a particle is represented with 6-dimensional phase-space vector: $(x, x', y, y', s, \delta)$, where x and y are transverse particle coordinates with respect to the reference particle, s is a longitudinal position of the particle along the reference orbit, $x' = dx/ds$ and $y' = dy/ds$ are the transverse angles, $\delta = (p - p_0)/p = \Delta p/p_0$ is a relative momentum offset taking into account a total momentum p of the particle and reference momentum $p_0 = m_0 v_0 \gamma$. To fix the reference particle trajectory one can start from the Lorentz force, which is acting on the charge e with velocity $\mathbf{v}$:

$$\mathbf{F} = e(\mathbf{E} + \mathbf{v} \times \mathbf{B}) = \dot{\mathbf{p}}. \tag{3.1}$$

For the relativistic case the electric field $\mathbf{E}$ and magnetic field $\mathbf{B}$ have the same effect if $\mathbf{E} = c\mathbf{B}$. Nowadays, the magnetic field is used for the beam steering in

the modern accelerators due to the easy production of 1 T magnetic field compared to the corresponds electric field of 3×10^8 V/m. Neglecting **E**, we can rewrite the Eq. 3.1 in the reference frame shown in Fig. 3.1 as:

$$\ddot{\mathbf{r}} = \frac{e}{m}(\dot{\mathbf{r}} \times \mathbf{B}). \tag{3.2}$$

One of the most important particle accelerator parameters is beam rigidity:

$$R = B \cdot \rho = \frac{p}{q}, \tag{3.3}$$

where ρ is a bending radius of the orbit due to a given dipole magnetic field B, p and q are particle momentum and charge, respectively. It can be rewritten for a single charge in a more convenient form for calculation:

$$R = B[T] \cdot \rho[m] \simeq \frac{p[GeV/c]}{0.3}. \tag{3.4}$$

This equation shows the relation between the magnetic field of the machine and the maximum achieved particle momentum. For example, in the LHC ($\rho \simeq 2800$ m) for 7000 GeV/c particle momentum a 8.3 T magnetic field is needed.

A general solution of the Eq. 3.2 can be found in [30], however for a linear machine (i.e. only dipole and quadrupole magnets are present) we can write it down for a particle in transverse planes as:

$$x''(s) + \left(\frac{1}{R^2(s)} - k(s)\right) x(s) = \frac{1}{R(s)} \frac{\Delta p}{p}, \tag{3.5}$$

$$y''(s) + k(s)y(s) = 0, \tag{3.6}$$

describing magnetic fields using the energy invariant dipole strength $1/R(s)$ and quadrupole strength $k(s)$. For the reference particle ($\Delta p/p = 0$) a component $(1/R(s))(\Delta p/p)$ in Eq. 3.5 vanishes and such equations called Hill's differential equations of motion. The trajectory functions $x(s)$ and $y(x)$ describes a transverse oscillation about the orbit, known as a betatron oscillation [30].

3.1.2 Twiss parameters

The general solution of the reference ($\Delta p/p = 0$) particle trajectory is:

$$x(s) = A\sqrt{\beta_x(s)}cos(\phi_x(s) + \phi_0), \tag{3.7}$$

which is valid for both x and y planes, where $\beta(s)$ is an amplitude function of the betatron oscillation, $\phi(s)$ is a phase advance, defined as:

$$\phi(s) = \int_0^s \frac{d\sigma}{\beta_x(\sigma)}. \tag{3.8}$$

Also we can introduce other parameters:

$$\alpha_x(s) = -\frac{\beta'(s)}{2}, \tag{3.9}$$

$$\gamma_x(s) = \frac{1+\alpha_x^2(s)}{\beta_x(s)}, \tag{3.10}$$

which are, together with $\beta(s)$, define Twiss parameters or Courant-Snyder parameters. The amplitude factor A in Eq. 3.7 can be replace by $\sqrt{\varepsilon}$, called emittance. Taking into account the obtained Twiss parameters we can write the equations of motion in the following way:

$$x(s) = \sqrt{\varepsilon}\sqrt{\beta(s)}cos(\phi_x(s)+\phi_0), \tag{3.11}$$

$$x'(s) = -\frac{\sqrt{\varepsilon}}{\sqrt{\beta(s)}}[\alpha(s)cos(\phi_x(s)+\phi_0) + sin(\phi_x(s)+\phi_0)]. \tag{3.12}$$

If we eliminate the terms with the phase ϕ_x in order to be able to describe the particle motion in the $x-x'$ phase space (Fig. 3.2), we will have a general equation of an ellipse in the $x-x'$ plane:

$$\gamma(s)x^2(s) + 2\alpha(s)x(s)x'(s) + \beta(s)x'^2(s) = \varepsilon, \tag{3.13}$$

where ε is now has a well-defined meaning of the Courant-Snyder invariant of Action. It is a parametric representation of an ellipse in the $x-x'$ space, where the shape and orientation of the ellipse are given by the Twiss parameters (α, β and γ). The area of the ellipse, $\pi \cdot \varepsilon$, is an intrinsic beam parameter and cannot be changed by the focal properties.

To calculate the beam envelope size we can consider an emittance of the entire beam ε_b (statistically), which has a Gaussian distribution in the transverse planes:

$$\sigma_x(s) = \sqrt{\varepsilon_b\beta_x(s)}, \tag{3.14}$$

$$\sigma_{x'}(s) = \sqrt{\varepsilon_b\gamma_x(s)}, \tag{3.15}$$

where $\sigma_x(s)$ and $\sigma_{x'}(s)$ are the standard deviation (RMS or STD) betatron width and divergence of the beam, respectively.

3.1.3 Accelerator tune

In the circular accelerator the particle beam each turn pass through the same magnet lattice. Taking into account the fact, that any imperfection in the machine

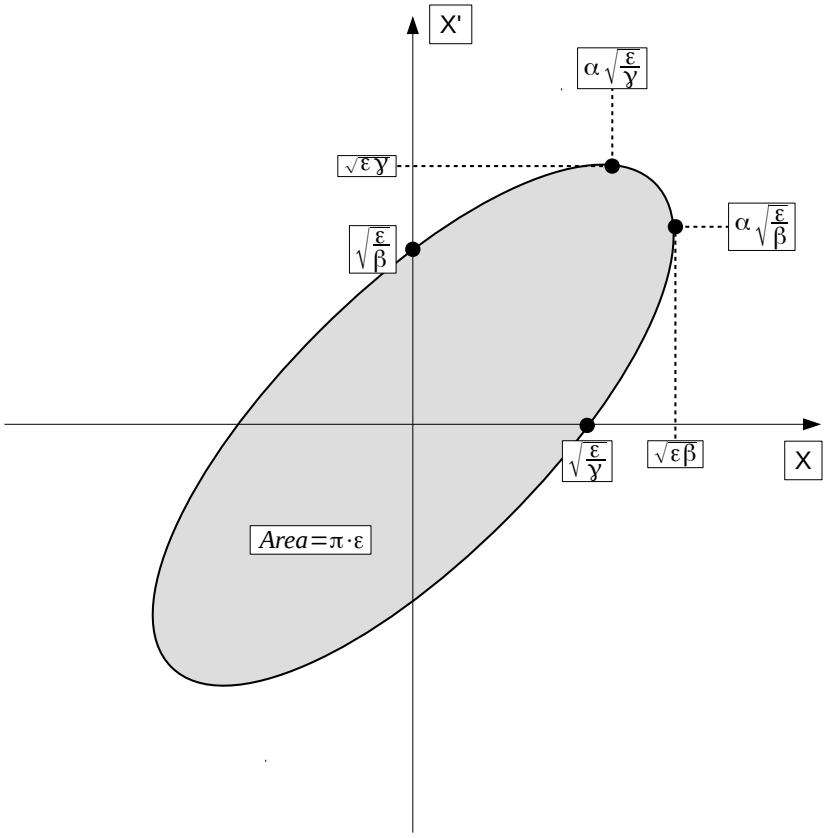

Figure 3.2: The phase space ellipse of particle motion in the $x - x'$ plane [30].

can cause particle stability, for instance, any quadrupole can increase the particle oscillation amplitude, which leads to the increasing of the transverse beam size every turn and at the end to the lost of the beam. This phenomenon is called an optical resonance. It strongly depends on the betatron phase over one complete particle revolution: $\Delta\phi = \phi(s + L) - \phi(s)$, where L is an accelerator circumference. Thus we can define the tune Q of the accelerator in the following way:

$$Q = \frac{\Delta\phi}{2\pi} = \frac{1}{2\pi}\int_0^L \frac{ds}{\beta(s)} = \frac{1}{2\pi}\oint \frac{ds}{\beta(s)}. \tag{3.16}$$

The tune means the number of betatron oscillations the particle does per one turn. One can mention, that for an integer (dipole field error) and a low level rational number (i.e. 1/2 (quadrupole error), 1/3 (sextupole error), etc.), it can lead to the beam instability due to a resonant oscillator condition.

"The finite mechanical tolerance and the limited pole width of the magnets mean that in principle all possible multipole fields are present in an accelerator. As a result there are always resonances when $mQ = p$, where m and p are integers. We must bear in mind that every accelerator has two tune values, namely Q_x in horizontal and Q_y in the vertical plane. In general these are different, and so there are resonance conditions in both planes. For higher multipole fields the strength in one plane depends on the beam position in other, which leads to coupling between the betatron oscillations in the two planes and hence to coupled resonances. The condition for optical resonance in both planes may thus be expressed as:

$$mQ_x + nQ_y = p, (m, n, p = integers). \tag{3.17}$$

The sum $|m| + |n|$ is called the order of the resonance. For stable operation a pair of values for Q_x and Q_y must be chosen which avoid optical resonances. This pair of values is termed the working point. The strength of the resonance decreases rapidly with the order, and so when choosing a working point we are generally only concerned about resonances up to 5th order." [30]

3.1.4 Transfer matrix formalism

To describe a particle motion in the circular machine we can use an approximated matrix formalism based on Twiss parameters, which were mentioned before.

With a transfer matrix $M(s_1|s_2)$ we can compute a transverse particle position at any point along the orbit s_2, starting from any other location of the machine s_1:

$$\begin{pmatrix} x(s_2) \\ x'(s_2) \end{pmatrix} = M(s_1|s_2) \begin{pmatrix} x(s_1) \\ x'(s_1) \end{pmatrix}. \tag{3.18}$$

To derive the matrix $M(s_1|s_2)$ we can start from the general trajectory solution (Eq. 3.7) written in the following form:

$$x(s) = a\sqrt{\beta_x(s)}sin(\phi_x(s)) + b\sqrt{\beta_x(s)}cos(\phi_x(s)) \tag{3.19}$$

If we will assume that the particle coordinates at s_1 are known, we can write:

$$a = x(s_1)\left[\frac{sin(\phi_x(s_1)) + \alpha_x(s_1)cos(\phi_x(s_1))}{\sqrt{\beta_x(s_1)}}\right] + x'(s_1)\sqrt{\beta_x(s_1)}cos(\phi_x(s_1)), \tag{3.20}$$

$$b = x(s_1)\left[\frac{cos(\phi_x(s_1)) - \alpha_x(s_1)sin(\phi_x(s_1))}{\sqrt{\beta_x(s_1)}}\right] - x'(s_1)\sqrt{\beta_x(s_1)}sin(\phi_x(s_1)). \tag{3.21}$$

Substituting above equations into Eq. 3.18, we can obtain the transform matrix for evaluation the particle coordinates at s_2 position:

$$M(s_1|s_2) = \begin{pmatrix} \sqrt{\frac{\beta_2}{\beta_1}}(cos(\phi_{21}) + \alpha_1 sin(\phi_{21})) & \sqrt{\beta_2\beta_1}sin(\phi_{21}) \\ -\frac{1+\alpha_1\alpha_2}{\sqrt{\beta_2\beta_1}}sin(\phi_{21}) + \frac{\alpha_1-\alpha_2}{\sqrt{\beta_2\beta_1}}cos(\phi_{21}) & \sqrt{\frac{\beta_1}{\beta_2}}(cos(\phi_{21}) - \alpha_2 sin(\phi_{21})) \end{pmatrix}, \tag{3.22}$$

where $\phi_{21} = \phi_2 - \phi_1$ is a phase advance between position s_2 and s_1, $\beta_i = \beta_x(s_i)$, $\alpha_i = \alpha_x(s_i)$ and $\phi_i = \phi_x(s_i)$ for $i = 1, 2$. Using the obtained transfer matrix it is possible to calculate particle coordinates at any position along the machine, if the Twiss parameters are known:

$$M(s_k|s_m) = \prod_{i=0}^{k-m-1} M(s_{k-i}|s_{k-i-1}) \tag{3.23}$$

To calculate the trajectory of the particle deflected by a crystal at position s_1, we can evaluate the kick θ given to the particle as:

$$\begin{pmatrix} x(s_1) \\ x'(s_1) \end{pmatrix} = \begin{pmatrix} x(s_1) \\ x'(s_1) + \theta \end{pmatrix}. \tag{3.24}$$

Therefore the transverse coordinate of the particle at any position s_2 after the crystal kick can be defined as:

$$x(s_2) = \sqrt{\frac{\beta_2}{\beta_1}}(cos(\phi_{21}) + \alpha_1 sin(\phi_{21}))x(s_1) + \sqrt{\beta_2\beta_1}sin(\phi_{21})(x'(s_1) + \theta). \tag{3.25}$$

Using the obtained equation above it is possible to calculate the kick at position s_1 of the deflected beam for a given coordinate $x(s_2)$ along the machine:

$$\theta = \frac{1}{\sqrt{\beta_2\beta_1}sin(\phi_{21})}\left(x_2 - \sqrt{\frac{\beta_2}{\beta_1}}(cos(\phi_{21}) + \alpha_1 sin(\phi_{21}))x_1 - \sqrt{\beta_2\beta_1}sin(\phi_{21})x'_1\right). \tag{3.26}$$

3.2 Longitudinal beam dynamics

As it was mentioned before the resonant cavities (RF) are used to compensate the energy losses due to the synchrotron radiation and to accelerate the particles (energy ramp) in the machine. The potential of the RF cavities if sinusoidal with frequency proportional to the revolution frequency of the accelerator. The action of the potential creates stable region in the beam called bucket. Inside each bucked particles form bunches. The energy gain by particle after each passage of the RF is:

$$\Delta E = qV_{RF}sin(\varphi(t)), \tag{3.27}$$

where $\varphi(t)$ is a relative phase between the particle with charge q and RF, V_{RF} is the maximum value of the RF potential. For the particle with nominal energy (i.e. $\varphi(t) = \pi n, n = 0, 1, 2...$) there is no action of the RF field, while for particles, which are off-momentum (i.e. $\varphi(t) \neq \pi n$), the energy increases and decreases each turn. This particles motion called synchrotron motion. The illustration of this effect is presented in Figure 3.3.

Thus for particles acceleration they have to arrive in the RF with $0 < \varphi < \pi/2$. However, taking into account the relativistic effect:

$$\Delta p = \frac{\Delta E}{c}, \tag{3.28}$$

the orbit variation due to the momentum offset is:

$$\frac{\Delta L}{L} = \alpha_c \frac{\Delta p}{p}, \tag{3.29}$$

where α_c is the momentum compaction factor. According to the fact, that the revolution time (1) will decrease due to the shrinking of the particle trajectory under increasing of the dipole field, and at the same time, (2) will increase due to the slowdown of the particle under increasing of the relativistic mass, we have a correlation between orbit length and revolution frequency (phase focusing):

$$\frac{\Delta T}{T} = \left(\alpha_c - \frac{1}{\gamma^2}\right)\frac{\Delta p}{p}, \tag{3.30}$$

where T is a revolution period and γ is a relativistic factor. It is easy to see that now two regimes are defined by a given gamma transition (γ_{tr}) factor:

$$\gamma_{tr} = \sqrt{\frac{1}{\alpha_c}}, \tag{3.31}$$

for which $\Delta T/T = 0$ for any $\Delta p/p$. This condition must be avoided. Therefore, for $\gamma < \gamma_{tr}$ (i.e. $(\alpha_c - (1/\gamma^2)) < 0$) we have a regime when the particle has to arrive in

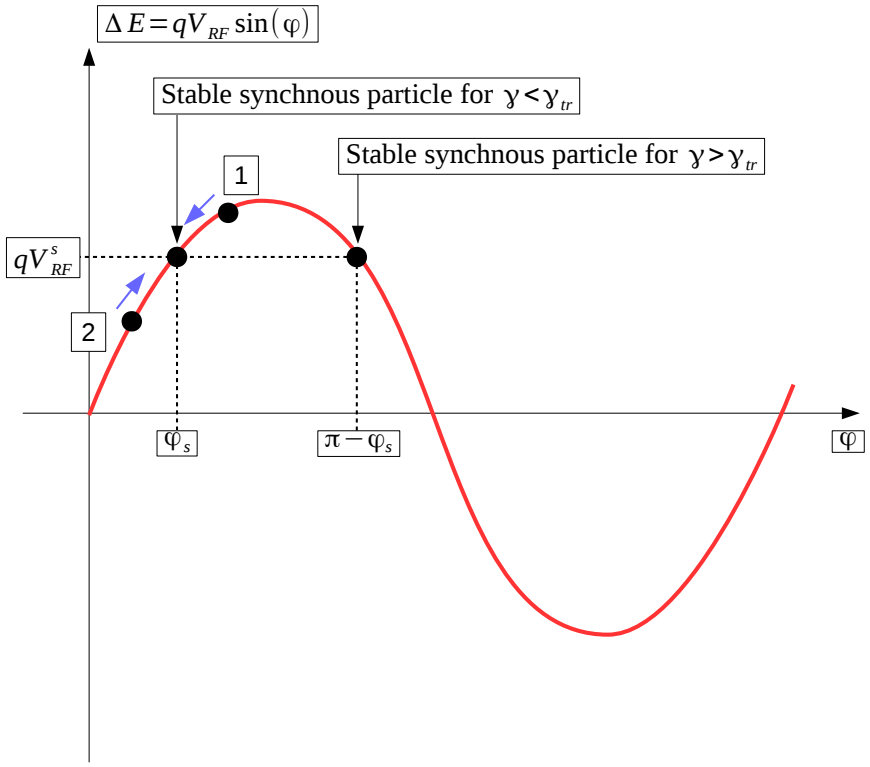

Figure 3.3: Illustration of the phase stability principle. Particle 1: the particle is accelerated with higher ΔE; bellow transition, an increase in energy means an increase in revolution frequency; the particle arrives earlier - tends toward φ_s. Particle 2: the particle is accelerated with lower ΔE; decrease in energy - decrease in revolution frequency; the particle arrives later - tends towards φ_s.

the RF with $0 < \varphi < \pi/2$, and for $\gamma > \gamma_{tr}$ (i.e. $(\alpha_c - (1/\gamma^2)) > 0$) another regime when the same particle has to arrive with $\pi/2 < \varphi < \pi$ (Fig. 3.3).

Lets consider the energy oscillation motion in the $E - \varphi$ phase space:

$$\ddot{\varphi} + \frac{\Omega_s^2}{cos(\varphi_s)}(sin(\varphi) - sin(\varphi_s)), \tag{3.32}$$

where Ω_s is a synchrotron angular frequency. Multiplying the obtained equation by $\dot{\varphi}$ and integrating we get the invariant of the motion [31]:

$$\frac{\dot{\varphi}^2}{2} - \frac{\Omega_s^2}{cos(\varphi_s)}(cos(\varphi) + \varphi sin(\varphi_s)) = const. \tag{3.33}$$

Thus we have harmonic energy oscillations around the nominal value for a particle with a small $\Delta p/p$. Figure 3.4 shows graphically the stable and unstable region in the $E - \varphi$ phase space. The stable region, called separatrix, defines the energy acceptance of the machine, which is the given by the FWHM of the RF bucket:

$$\Delta E_b = k\sqrt{1 - \left(\frac{\pi}{2} - \varphi_s\right) tg(\varphi_s)}, \tag{3.34}$$

where k is a constant. Outside the separatrix the particle motion is unstable.

More details about the longitudinal beam dynamics can be found in [31].

3.3 Dispersion

In this section we will give a short overview of the dispersion function and its influence on the particle trajectory in the circular machine.

So far, for transverse beam dynamics we have been focused on a monochromatic particle beam ($\Delta p = p - p_0 = 0$, momentum offset), which does not suitable for the real case. There is a small momentum spread among all particles ($\Delta p \neq 0$). Taking into account Eq. 3.3, Figure 3.5 shows an effect of the dipole field for three particles with different momentum with respect to the reference one (p_0). The correlation between particle momentum and transverse position is well known as dispersion, which is an intrinsic property of the dipole magnets.

3.3.1 Solution of the inhomogeneous Hill's equation

Let consider the magnetic rigidity (Eq. 3.3), taking into account particle momentum offset (define $\delta = \frac{\Delta p}{p_0}$):

$$B\rho = \frac{p}{q} = \frac{p_0(1+\delta)}{q} = B\rho_0(1+\delta) \Rightarrow \rho = \rho_0(1+\delta). \tag{3.35}$$

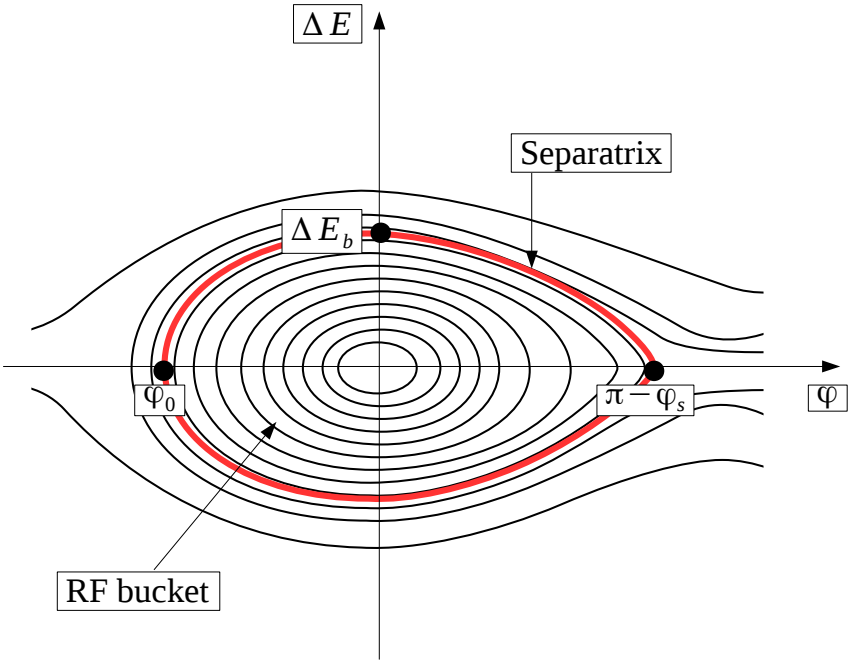

Figure 3.4: Stable phase space particles longitudinal trajectories. Red line indicates the stable motion separatix.

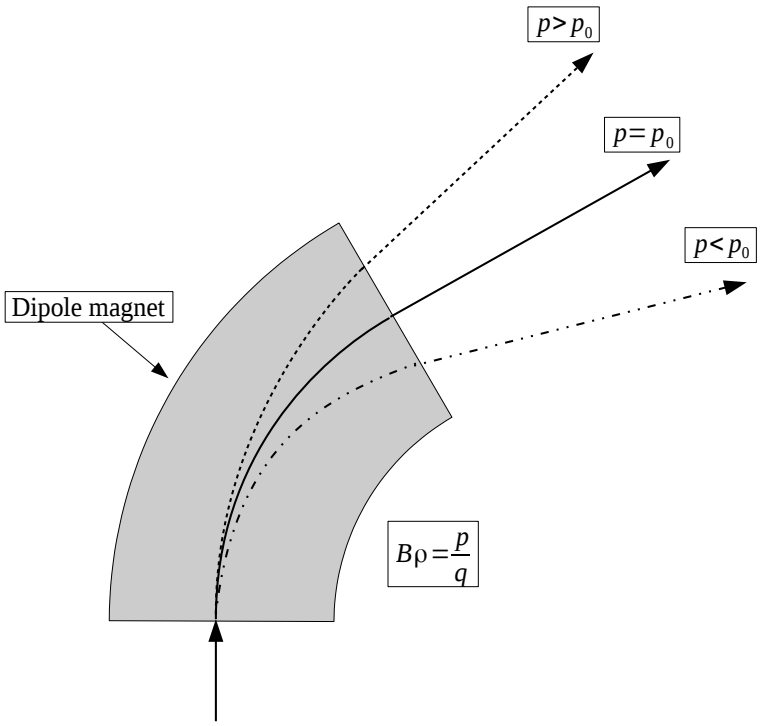

Figure 3.5: Dispersion effect of the dipole magnet.

Remembering Equation 3.5 (with $\rho = R(s)$), which is the inhomogeneous Hills' equation, we can write its solution in the following form:

$$x(s) = x_\beta(s) + x_D(s), \tag{3.36}$$

where $x_D(s) = D(s)\frac{\Delta p}{p_0}$. $x_\beta(s)$ is a betatron amplitude for on-momentum particles with $\Delta p/p_0 = 0$, $D(s)$ (dispersion function) is a special orbit, which particle will have for $\Delta p/p_0 = 1$, $x_D(s)$ describes the deviation of the new closed orbit for an off-momentum particle with a certain ΔP. To evaluate the $D(s)$ function it is necessary to substitute Eq.3.36 in Eq. 3.5. The total amplitude (Eq. 3.11,3.12) of the betatron motion is:

$$x(s) = \sqrt{\varepsilon}\sqrt{\beta(s)}cos(\phi_x(s) + \phi_0) + D(s)\frac{\Delta p}{p_0}, \tag{3.37}$$

$$x'(s) = -\frac{\sqrt{\varepsilon}}{\sqrt{\beta(s)}}[\alpha(s)cos(\phi_x(s) + \phi_0) + sin(\phi_x(s) + \phi_0)] + D'(s)\frac{\Delta p}{p_0}. \tag{3.38}$$

Chapter 4

UA9 experiment at CERN SPS

The usage of the bent crystals (see Chapter 2) has found a wide range in the HEP applications, in particular for accelerator physics. The first results for crystal extraction of the high-energetic beams were obtained at CERN [32–34], IHEP-Protvino [35], RHIC [36] and FNAL [37]. In the beginning of the XXI century, it was proposed to use curved crystals for a particle beam (such as LHC [38]) collimation.

The standard collimation system is based on two stages [39]: a primary collimator, which absorbs particles from the primary halo and infuses a small scattering angle in random directions to the not trapped particles, creating a secondary halo; and a secondary absorber, which catches the particles scattered by the primary collimator. However, the LHC has a three-stages collimation system [40]. Using of the crystal as a primary collimator give a possibility to steer the particles from the primary halo to the specific direction and more efficient absorb them by the downstream located absorber. In such cases, the crystal called a smart collimator.

In 2008 UA9 experiment[1] was approved by CERN for the investigation of the crystal-based collimation technique for high-energy proton and ion beams like the LHC. The main goal of the experiment is to show, how much a crystal collimation system is more efficient with respect to the traditional one. Also in 2010 it was decided to create the High Luminosity LHC (HL-LHC) Project at CERN. In a frame of this project it was planned to increase the LHC instantaneous luminosity (rate of collisions) by a factor of five beyond the original design value and the integrated luminosity (total collisions created) by a factor ten [41]. Such increasing of the intensity makes a new challenge for the crystal collimation system. More detailed information about these investigations can be found in [42] and [43].

In this Chapter we are going to discuss an experimental setup of the UA9 experiment at CERN accelerator facilities. We will focus on the parts, which are more

[1] `https://home.cern/science/experiments/ua9`

important for the present work. More details can be found in [44] and [45].

4.1 UA9 layout

Since 2009 the UA9 experiment uses CERN Super Proton Synchrotron (SPS) accelerator for further investigation of the channeling effect in a bent crystal and development of the crystal-based collimation technique for LHC. Multiturn channeling (see Section 2.6) measurements are carried out in the SPS Long Straight Section 5 (LSS5), and for a single-pass channeling efficiency investigation it was placed at H8 extraction beam line of the SPS North Area (NA) (Fig. 4.1).

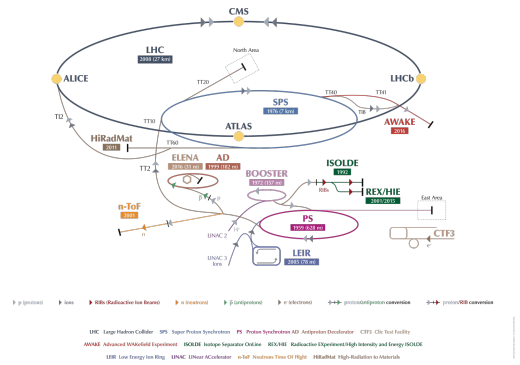

(a) CERN accelerator facilities.

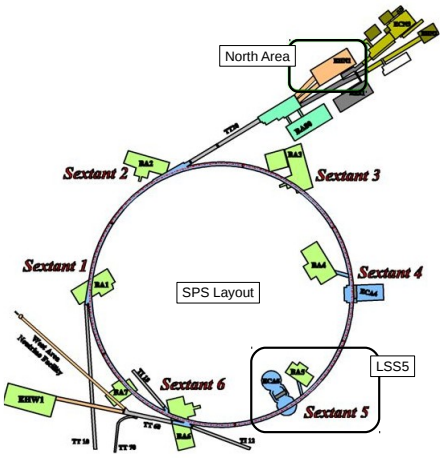

(b) CERN SPS with marked NA and LSS5 zones.

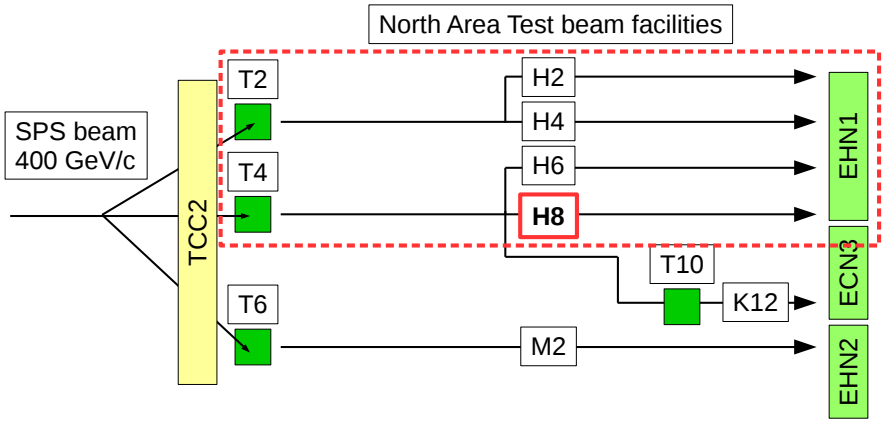

(c) NA beam lines.

Figure 4.1: UA9 experiment locations at CERN SPS.

4.1.1 H8 beam line experimental setup

As it was mention before, the single pass crystal characteristics, such as channeling efficiency, inelastic nuclear interaction (INI) probability, deflection angle, etc., were measured at H8 SPS extraction beam line. The UA9 section of the H8 SPS extraction line is composed by a dedicated tracker [46] to reconstruct particle tracks before and after the crystal (Fig.4.2).

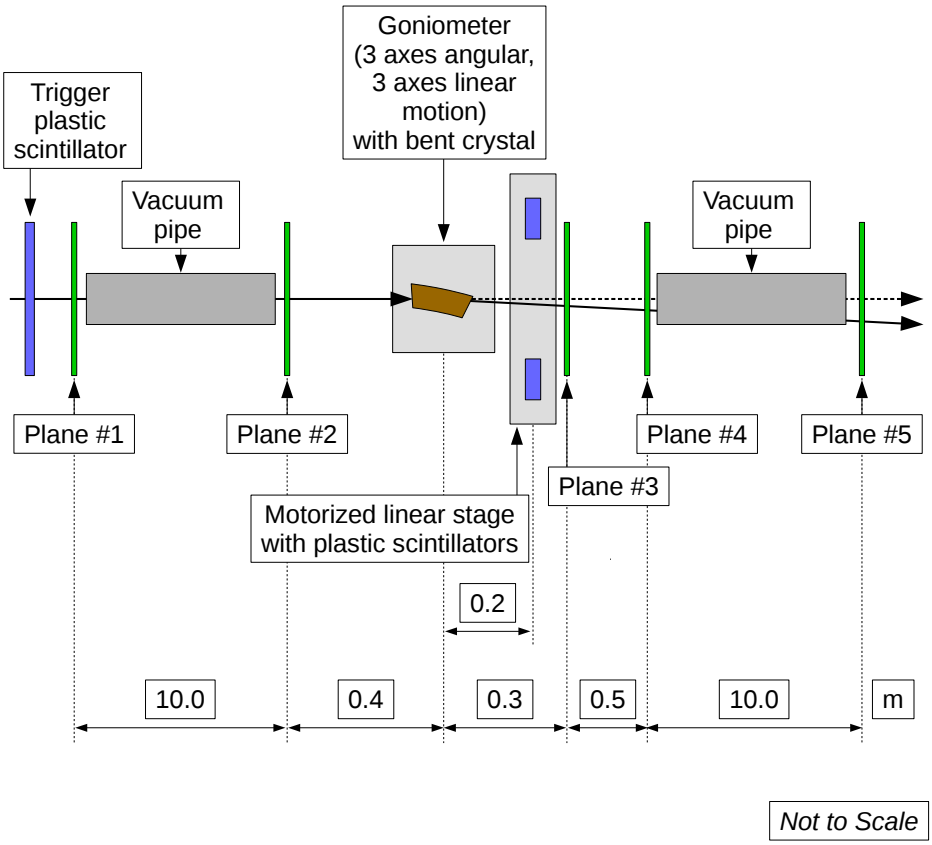

Figure 4.2: H8 apparatus of the UA9 experiment. The rough distances are given in meters.

The tracker consists of five position sensitive microstrip planes. The angular resolution of each arm (upstream arm: Plane 1 and Plane 2; downstream arm: Plane 3, Plane 4 and Plane 5) of the tracker is 2.8 μrad for 400 GeV/c proton beam. Due to the multiple Coulomb scattering [47] a cumulative angular resolution is 5.2 μrad.

"The sensors are instrumented by a system based on the CMS Tracker electronic readout chain, including analogue signal readout for optimal spatial resolution. The

system profits from modified CMS software and hardware to provide a data acquisition capable of peak trigger rates of at least 7 kHz." [46].

A high-precision 6D axes (3 angular and 3 linear axes) goniometer is used to orient the crystal planes with respect to the incident particle beam in order to have the optimal channeling orientation. Two plastic scintillators [48, 49] were placed on the linear motorized stages [50] to perform the remote alignment of the detectors for the INI measurements [51, 52].

An integrated data acquisition (DAQ) system collects all information from the tracker telescope, plastic scintillators and a crystal goniometer in order to perform a track reconstruction data analysis. As a result, we have an output file with a ROOT CERN [53] format data structure, containing all necessary information (e.g. angular and spatial coordinates of the tracks) for the further crystal characterisation analysis.

4.1.1.1 Motorized linear stages

Until 2017 UA9 collaboration used a pair of the plastic scintillator detectors for the INI investigation [51, 52], manually aligning them with respect to the particle beam axis. This procedure required a lot of experimental time and frequent beam interruptions. Therefore, it was decided to develop a motorized linear stage for the remote detector alignment [50]. Figure 4.3 shows a 3D drawing of the stage done using SolidWorks 3D CAD[2]. A friendly graphic user interface (GUI) based on MATLAB[3] was developed in order to control the stage. A user PC communicates through the Ethernet connection via TCP/IP protocol with a controller box of the system, which contains motor drivers and Arduino[4] microcontroller board. All source codes and 3D models can be found on the CERN UA9 Collaboration DFS storage[5].

During 2017 and 2018 the stage has been regular used for the INI detectors alignment. Figure 4.4 shows the experimental configuration of the scintillators and results of the alignment procedure. A good performances of the stage satisfy all expectations for our measurements at the extraction beamline. More details about all linear motorized stages developed for the UA9 experiment at H8 can be found in [50].

Another translational stage developed at the Linear Accelerator Laboratory

[2] `https://www.solidworks.com`

[3] `https://www.mathworks.com/products/matlab.html`

[4] `https://www.arduino.cc`

[5] `https://dfsweb.web.cern.ch/dfsweb/Services/DFS/DFSBrowser.aspx/Experiments/UA9/Documentation/Equipment%20UA9/TranslationStageUA9/`

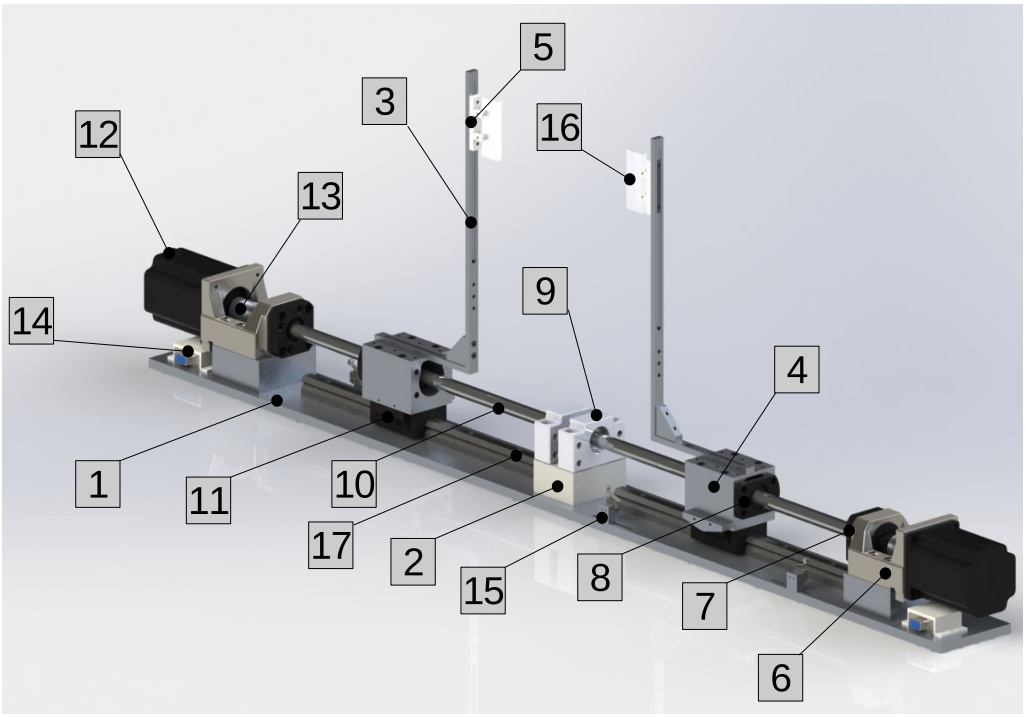

Figure 4.3: A 3D drawing of the double linear stage with mounted plastic scintillators. 1 – base plate, 2 – block for support, 3 – holder for the scintillator, 4 – ballnut bracket, 5 – plastic holder for the scintillator, 6 – motor mounts (MBA 10-C), 7 – ballscrew support (FK10-C7, with mounting method B), 8 – ballnut (R1204T3-FSKD), 9 – ballscrew support (BF10-C7), 10 – ball-screw (R1204-C7, length 400 mm), 11 – bearing block (BGX-H-15-FN-ZF), 12 – stepper motor (SY57STH76-4004A NEMA23), 13 – flexible coupling (BF-D25L34), 14 – DB9 connector, 15 – microswitch (HONEYWELL 1SX1-T), 16 – plastic scintillator, 17 – normal grade profile rail (BGR-15-LN, length 294 mm).

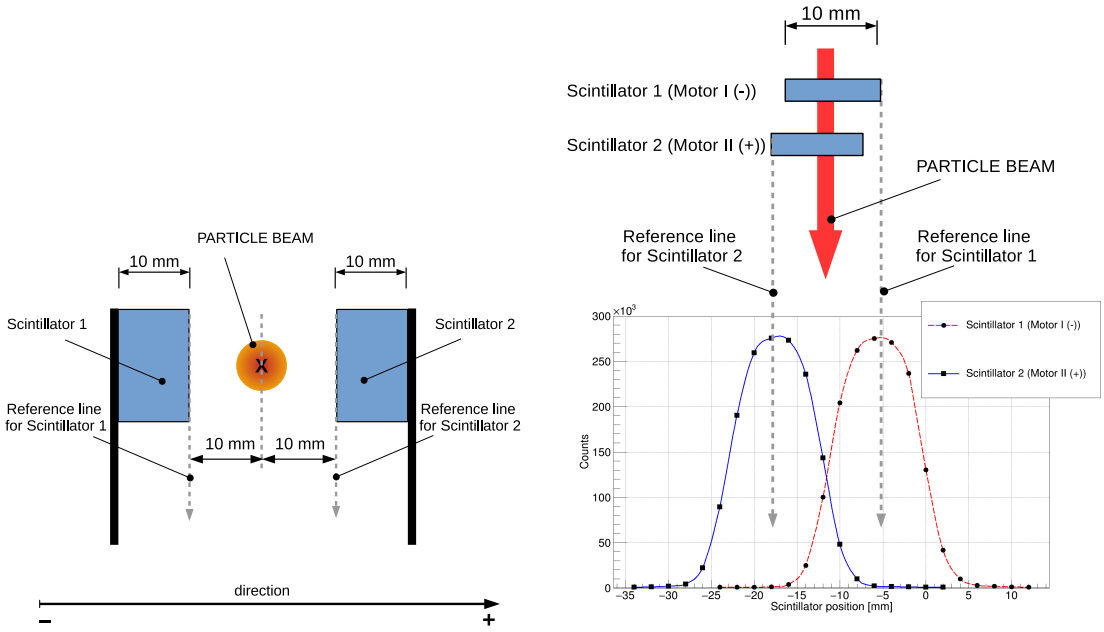

(a) Geometrical configuration for the plastic scintillators with respect to the particle beam axis.

(b) Beam profile measured by the two plastic scintillators.

Figure 4.4: Plastic scintillators alignment done by the linear stage.

(LAL) is used 50 m downstream the crystal position for different detectors setup alignment. The stage consists of two parts (Fig. 4.5), which are able to move in (1) 3D and (2) 2D directions. The hardware and software are similar to the double linear stage for INI measurements, as mentioned above.

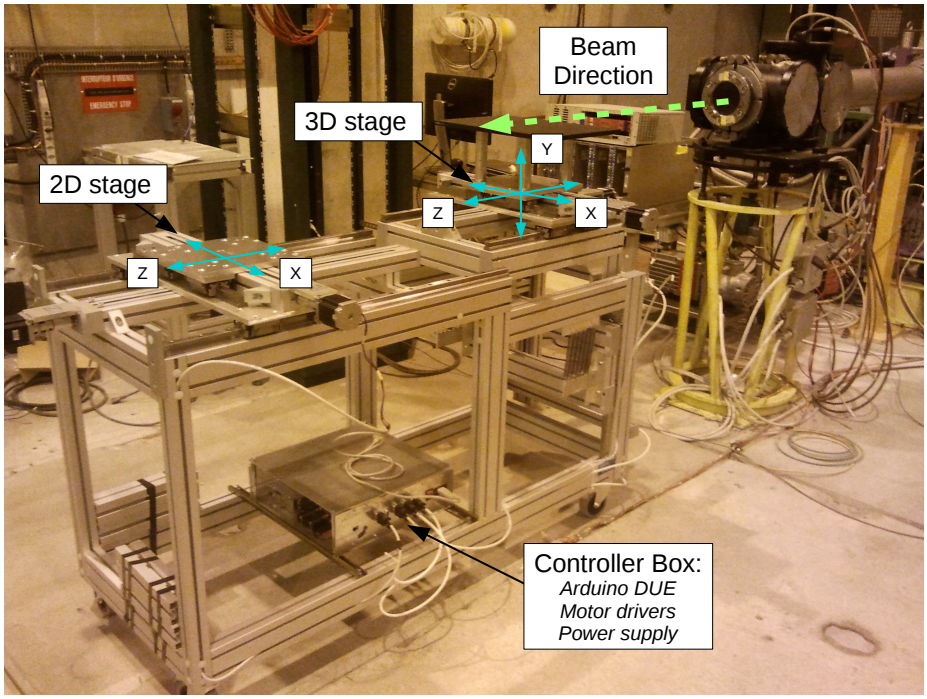

Figure 4.5: A photo of the motorized system with 2D and 3D linear stages.

4.1.2 SPS experimental setup

Since 2016 the experimental setup of the UA9 collaboration at the SPS has been changed three times (July 2017, Winter 2017-2018, June 2018). Before 2017 the full layout is schematically shown in Fig. 4.6, a modified part of the layout in 2017 is shown in Fig. 4.7a and the final setup for 2018 is illustrated in Fig. 4.7b. In the presented drawings each box describes a UA9 device or some components of the machine. The name of the box is made of the official SPS acronym, such as TCSM.51934, where the first 3 or 4 letters indicates the specific functionality of the device and the last 5 numbers are its location.

A detailed information about the SPS UA9 components alignment procedure is well described in [54].In 2016 the layout of the UA9 experiment (Fig. 4.6) consists of two IHEP goniometers (with a couple of bent silicon crystals per goniometer). Each goniometer provides crystals horizontal linear movements and rotation with

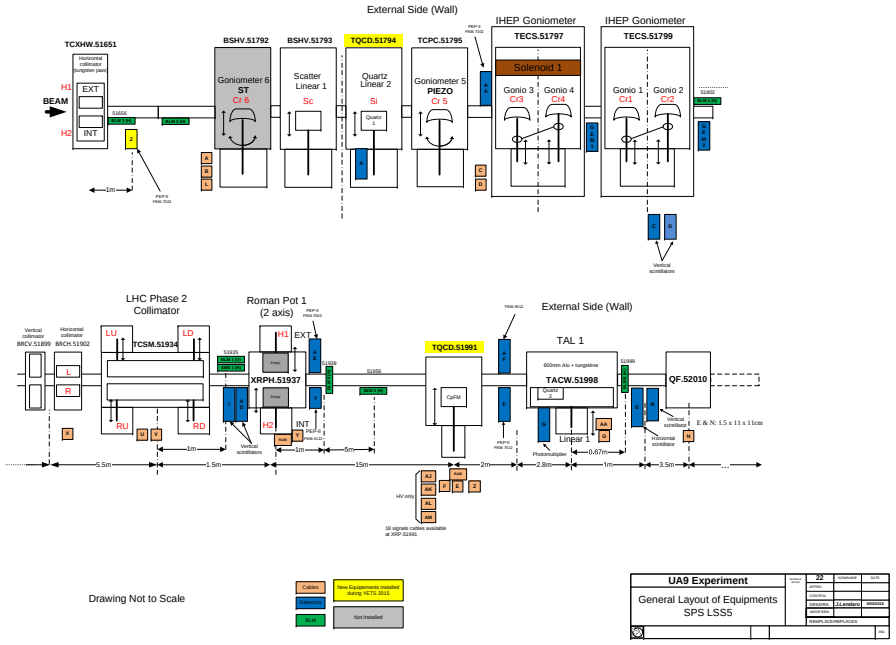

(a) Schematic drawings.

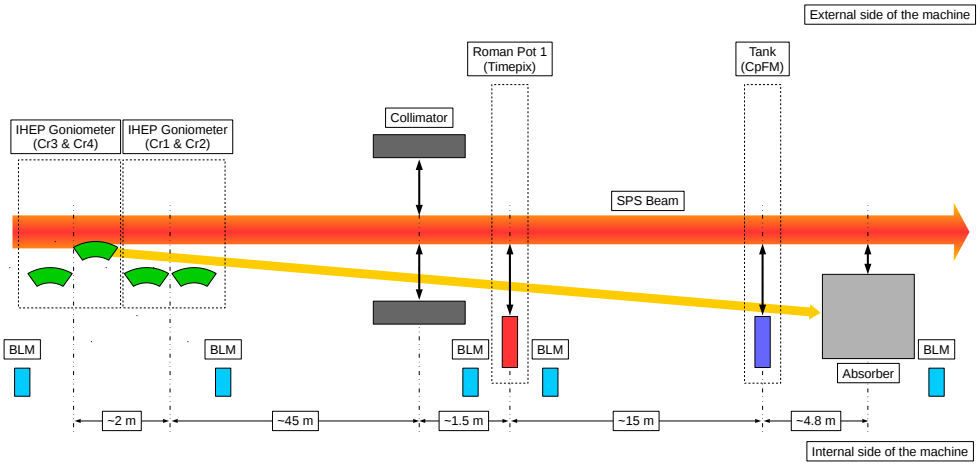

(b) Conceptual layout.

Figure 4.6: Setup of the UA9 experiment at CERN SPS LSS5 zone in 2016.

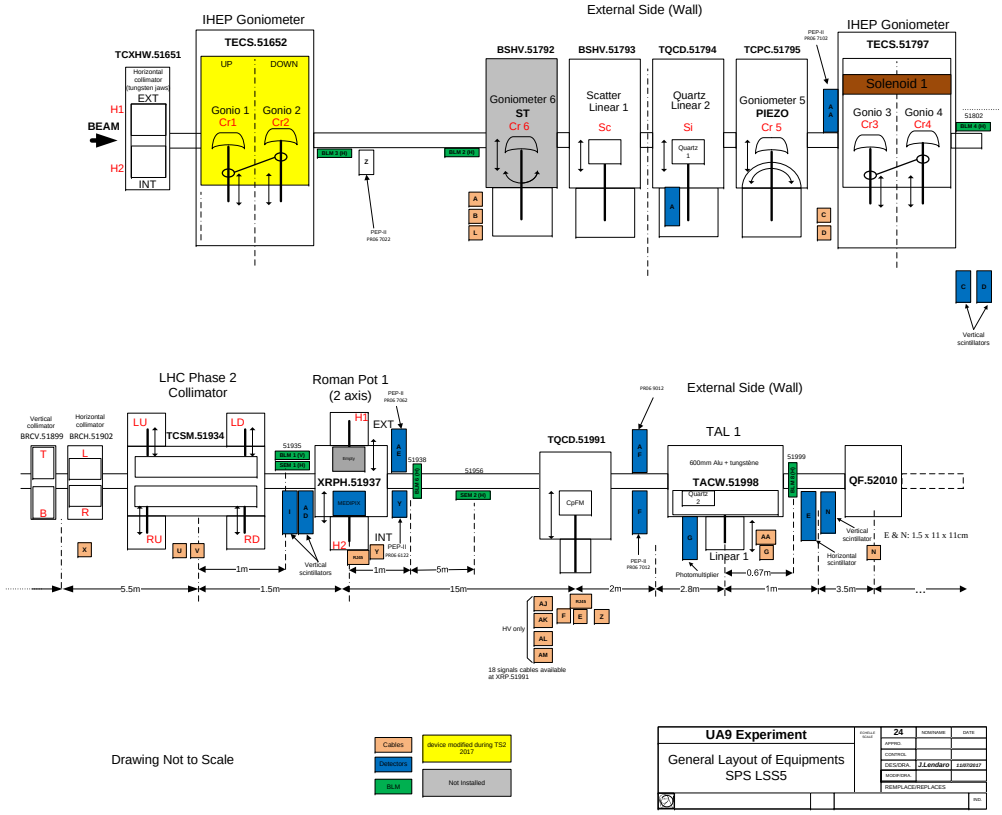

(a) After the July 2017 upgrade.

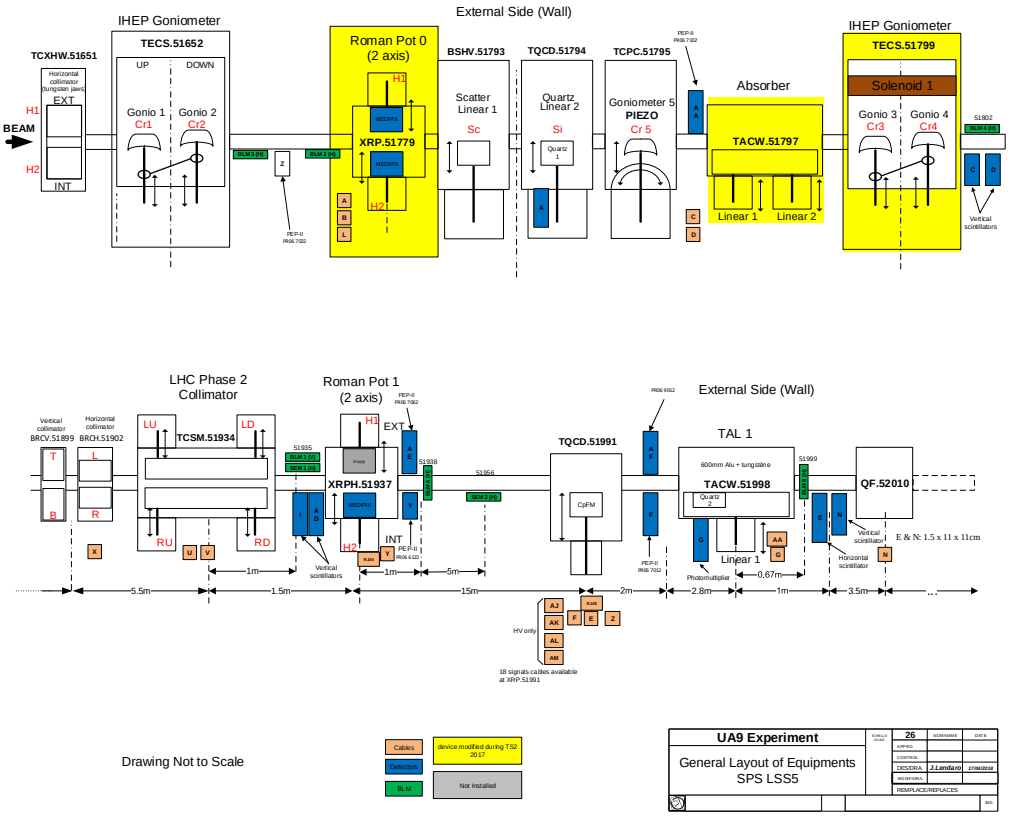

(b) After the winter 2017-2018 upgrade.

Figure 4.7: Schematic drawings of the UA9 experiment at CERN SPS LSS5 zone.

a designed angular resolution of 1 μrad and an accuracy (repeatability) close to 10 μrad. The deflected beam is intersected by a movable tungsten absorber (TAL). It has a cross-section of 70×60 mm^2 and length of 60 cm, and placed around 60 m downstream the crystals with a phase advance of about 60°, in order to maximize the separation between channeled and primary beams (Eq. 3.25). In the region between crystals and TAL an LHC-type collimator with two horizontal graphite (1 m of length) jaws are located. About 1.5 m downstream the collimator there is a Roman Pot 1 (RP1) tank with a Timepix detector installed inside secondary vacuum. A horizontal motorized linear axis is used for the detector alignment. The pot has 0.2 mm thin aluminium walls and is 3.4 cm wide along the beam direction. There are different types of detectors installed close to each device, outside the beam pipe, such as polystirene scintillators and LHC-type BLMs [45, 54], which are composed of a 50 cm long cylinder of 9 cm diameter, filled with N_2 at 100 mbar overpressure and using an integration time of 1.2 s.

A Beam Wire Scanners (BWS) [55] is an instrument, which is used for the main beam profile measurements. During the experiment the results of the BWS measurements (Fig. 4.8a) are used for the beam emittance estimation. While the intensity of the beam in the machine is measured by means of a Beam Current Transformer (BCT) (Fig. 4.8b) [56].

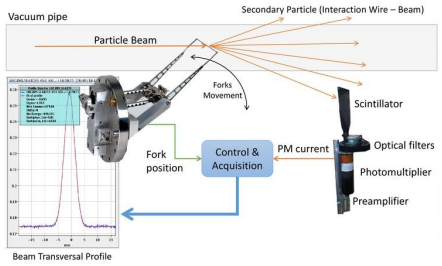

(a) Beam Wire Scanners. From [55].

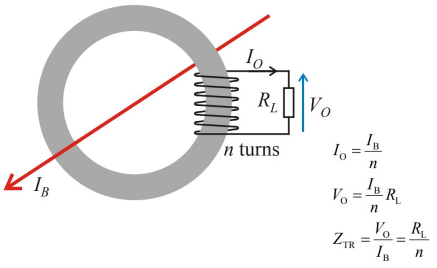

(b) Beam Current Transformer. From [56].

Figure 4.8: Working principle of the beam instrumentation devices.

In July 2017 one of the IHEP goniometer with Cr1 and Cr2 was moved around 50 m upstream from the second goniometer, which contains Cr3 and Cr4. During the 2017–2018 Winter Technical Stop new optimized crystals were installed together with a new absorber and another Roman Pot 0 (RP0) just in front of Cr3 and Cr4. The last upgrade includes a new crystal in the second IHEP goniometer with a short tungsten target in front of it.

Chapter 5

Detectors theory

In the UA9 we have developed a diversified setup for detecting the particles deflected by the bent crystal. In the present work I described the development of Cherenkov and pixel detectors for the particles flux measurement. In this chapter we will discussed the main characteristics of the detectors and their operational principles.

5.1 Cherenkov detector

Charged particles at high energies can pass through different materials (gas, liquid or solid) with a speed exceeding the speed of light in these materials. As a result of such process, appears a glow, which is called Cherenkov radiation with photons spectrum from the ultraviolet into the visible portion of the electromagnetic radiation spectrum [57]. If the particle exceeds a certain threshold energy it causes coherent polarization of the molecules in the matter which leads to photons emission. There are several applications for Cherenkov radiation, but we will stop at the high-energy particle counting and detectors which use Cherenkov effect for a particle registration.

5.1.1 Cherenkov radiation theory

Vavilov-Cherenkov or Cherenkov effect was discovered by Pavel Cherenkov [58] in 1934 while he was working on his PhD thesis under Sergei Vavilov supervision. They investigated the luminescence of solutions of uranyl salts under the action of gamma radiation of radium. Using visual photometry method Cherenkov discovered a glow, which cannot be explained by simple mechanism of fluorescence. The main conclusions of their measurements are the following:

- the glow is not a fluorescence;
- the radiation is caused by fast electrons;
- the intensity does not depend on the environment charge Z;
- it is directed radiation with respect to the charged particle movement;
- a spectrum of the radiation is continuous.

The theoretical description of the nature of this phenomenon was done by Tamm and Frank in 1937 [59]. They explained the Cherenkov effect as caused by a charged particle travelling in a medium at a speed (v) higher than the phase speed of light in this medium (c/n):

$$v > \frac{c}{n}, \tag{5.1}$$

where c is a speed of light ($c \simeq 3 \cdot 10^8$ m/s). The Cherenkov effect can be described in two ways:

1. Classical approach.

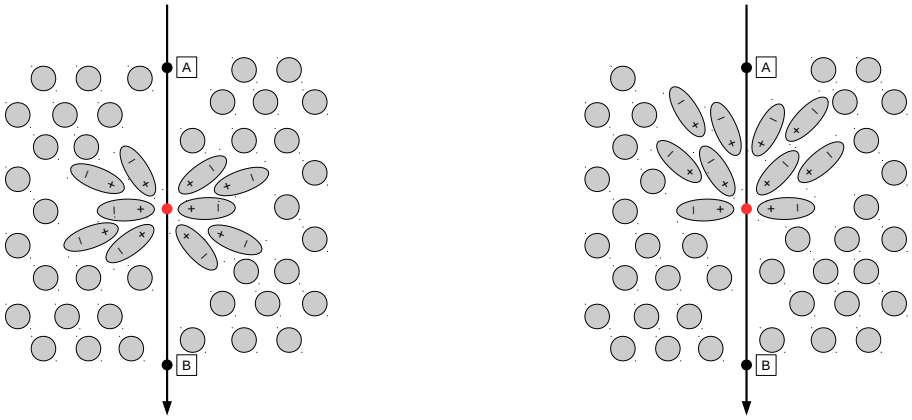

(a) $v < c/n$ (b) $v > c/n$

Figure 5.1: Medium polarization during the passage of a charged particle.

A charged particle, moving in the medium with a refractive index of n induces a polarization of the medium atoms along its path. These atoms create dipoles for a very short period of time. The oscillation of the dipoles, accompanying the relaxation of polarized atoms to the initial state, leads to the appearance of the electromagnetic radiation. If the particle moves with a speed v, which is smaller than the speed of light in the medium, the polarization appears

before and after the particle. (Fig. 5.1a). This polarization has a spherical symmetry and the total radiation of the dipoles is compensated. If the particle has $v > c/n$, polarization appears only before the particle (Fig. 5.1b). As a result, all dipoles are oriented in the particle movement direction. In this case must exist orientation with coherent radiation of the dipoles, due to the fact that radiated waves in different points along the path can be in the same phase. Thus, the radiation will be observed only at a certain angle θ (Fig. 5.2) relative to the particle trajectory (AB), at which the waves are coherent and form a plane wave front (CB). To find the direction of the light propagation one can write the path, which particle will travel during time t with velocity v, as $AB = t \cdot v$, and for the same time a wave, radiated by a dipole in a point A, will pass $AC = t \cdot (c/n)$. Taking into account that $AC = AB \cdot cos(\theta)$, it is easy to show that $(c/n) \cdot t = v \cdot t \cdot cos(\theta)$, which leads to:

$$cos(\theta) = \frac{1}{n\beta}, \tag{5.2}$$

where $\beta = \frac{v}{c}$. Naturally, the wave can be radiated only in case of $cos(\theta) \leq 1$, i.e. $v \geq \frac{c}{n}$ – the speed of the charged particle has to exceed phase velocity of light in the medium with $n > 1$ (due to $\beta \leq 1$ and $n\beta > 1$). For instance, if $n = 1.33$ (water) the energy of the electron must be not smaller than 260 kV.

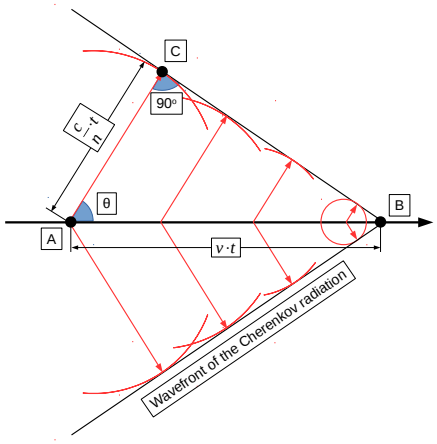

Figure 5.2: Huygens scheme of the Cherenkov radiation illustration. According to the principle of Huygens, every point in space, into which radiation has come, is itself a source of electromagnetic waves.

2. Quantum approach.

It is known that the light radiation is quantized. The energy of a photon (a quantum of the light) is $E_\gamma = h\nu$, momentum $p_\gamma = \frac{E_\gamma}{v_\gamma}$ and velocity $v_\gamma = \frac{c}{n}$. For the particle with non-zero rest mass m the energy, momentum and velocity are the following: $E = \frac{mc^2}{\sqrt{1-\beta^2}}$, $p = \frac{\beta E}{c}$ and $\beta = \frac{v}{c}$. Lets the charged particle moves along Z-axis with velocity v and at some point emits a photon with energy E_γ at angle θ. At the same time the particle deflects at angle ϕ with energy E'. The equations of energy and momentum conservation are:

- energy conservation:
$$E = E_\gamma + E' \tag{5.3}$$
- Z-axis projection momentum conservation:
$$p = p_\gamma \cdot cos(\theta) + p' \cdot cos(\phi) \tag{5.4}$$
- orthogonal to Z-axis projection momentum conservation:
$$0 = p_\gamma \cdot sin(\theta) - p' \cdot sin(\phi). \tag{5.5}$$

The solution [60] of the set of equations leads to:

$$cos(\theta) = \frac{1}{n\beta} + \frac{\Lambda}{\lambda}\frac{n^2-1}{2n^2}, \tag{5.6}$$

where $\lambda = v_\gamma/\nu = c/(n\nu)$ is a wavelength of the photon, $\Lambda = h/p$ is a De Broglie wavelength. The Equation 5.6 is different with respect to the Equation 5.2 by an additional component which takes into account particle recoil during the photon emission. The order of magnitude of this quantum correction is around 10^{-6}. Therefore, usually for Cherenkov angle calculation is used Eq. 5.2.

According to Frank and Tamm [59], the total energy W radiated by a charged particle per path length of travel L in a single frequency region $\omega = 2\pi\nu$ is:

$$\frac{dW}{d\omega dL} = \left(\frac{e}{c}\right)^2 \left(1 - \frac{1}{n^2\beta^2}\right)\omega, \tag{5.7}$$

and it is only several keV per centimetre. Neglecting medium dispersion, the number of photons N emitted in path length L within the spectral region defined by the wavelengths λ_1 and λ_2:

$$N = 2\pi\alpha Z^2 L \left(\frac{1}{\lambda_1} - \frac{1}{\lambda_2}\right)\left(1 - \frac{1}{n^2\beta^2}\right), \tag{5.8}$$

where $\lambda_1 < \lambda_2$, $\alpha = c^2/(\hbar c)$ is the fine structure constant $\sim 1/137$, Z is a particle charge in electron charge units, and n, the average value of the refraction index in

that wavelength region. Frank and Tamm made some calculations for a 500 keV electron, which would correspond to $\beta = 0.75$, travelling in water, where $n = 1.33$, would produce approximately 10 photons per 0.1 cm within the visible region between $\lambda_1 = 400$ nm and $\lambda_2 = 600$ nm.

5.1.2 Refractive index and dispersion

Usually, to calculate the Cherenkov light properties (e.g. number emitted photons or radiated by a charged particle energy) it is enough to use the average value of the refractive index of the medium in which the particle is moving. However, for precise quantitative calculation it is necessary to take into account the dependence between medium refractive index and emitted photon wavelength (dispersion). In this case for a transparent optical material (glasses) in the wavelength range from ultraviolet through the visible to the infrared , it is widely used a so-called Sellmeier formula [61]:

$$n^2(\lambda) = 1 + \sum_{i=1}^{3} \frac{B_i \cdot \lambda^2}{\lambda^2 - C_i^2}, \tag{5.9}$$

where n is refractive index, which is a function of the phase velocity $v_{ph}(\lambda)$ ($n = c/v_{ph}(\lambda)$), λ is a wavelength (in μm), B_i and C_i are experimentally determined Sellmeier coefficients. For instance, for fused silica these coefficients can be taken from [62] and shown in Table 5.1. The role of phase and group velocities for Cherenkov radiation is well described in [63].

Coefficient	Value
B_1	0.6961663
B_2	0.4079426
B_3	0.8974794
C_1	0.0684043
C_2	0.1162414
C_3	9.896161

Table 5.1: The index of refraction of optical quality fused silica (SiO_2) was determined for 60 wavelengths from 0.21 to 3.71 μm at 20 °C [62].

5.1.3 Applications

Let discuss briefly the general applications for Cherenkov detectors. They are mainly used for particle identification (PID) and there are four main types: threshold

Cherenkov detectors, calorimeter, differential and Ring-Imaging Cherenkov Detectors (RICH). Cherenkov threshold detectors are used for fast time measurements and time of flight (TOF) technique. Using mass-dependent energy threshold gives a possibility to distinguish between a light particle (emits photons) and heavy particle (does not emit any light) with the same energy or momentum. Combining several threshold layers it is possible to increase the energy (momentum) region. Collecting the light produced by primary and secondary particles in the Cherenkov calorimeter one can measure the energy of the incident particle. Differential Cherenkov counter is used for PID in the beam with fixed momentum, selecting the special direction of light. RICH detectors use separated photon locations on the photodetector to recognize the Cherenkov angle and measure the velocity of the particle, and knowing the information about particle momentum allows to do a PID.

5.2 Cherenkov detector for UA9 experiment

In 2012 the UA9 collaboration started an R&D for the development of the detector for deflected by the crystal particle counting. The requirement of such device appears naturally due to the fact that the crystal characterisation in the circular machines like SPS or LHC needed a quantitative estimation of the channeling particle for the crystal collimation setup. There are several devices using different measurement technique for the beam intensity monitoring [64] (e.g. Beam Current Transformer, Secondary Emission Monitors, etc.). Unfortunately, due to their sensitive limitation (intensity should be larger that 10^9 particles with resolution of 5 % [65]) they are not suitable for the low particle flux measurements (the estimated number of the deflected particles per SPS revolution period of ~ 23 μs could be varied from 10 to 10^3) like UA9 experiment requests [66] for SPS beam in COAST (270 GeV/c proton beam with a single 3 ns bunch of up to 10^{11} particles). Therefore, it was decided to develop a new particle flux monitor for a low intensity with a precision of at least 15 %, which can be placed inside vacuum pipe without beam perturbation. More detailed description of the detector can be found in [65]. Here we will give a brief overview of the device, and in the next Chapters will be written in more concentrated way about its improvements and measurements at the SPS.

5.2.1 Detector description

Concerning particle counting in the accelerator machine like SPS or LHC, a detector, which will be operated in such environment, has to satisfy the following requirements:

- ▷ vacuum compatibility (10^{-9} mbar for SPS and 10^{-11} mbar for LHC) [67];
- ▷ fast enough detector response for the particle counting during a single bunch of 1-3 ns duration (it is not necessary to measure each bunch in a train) (with a revolution frequency of 43 kHz for SPS and 11 kHz for LHC);
- ▷ counting range of deflected by the crystal particles is from 1 to 10^3;
- ▷ radiation hardness (neutron flux of about $10^{12}/\text{cm}^2$ and $10^{15}/\text{cm}^2$ for SPS and LHC respectively with integrated dose up to kGy per year).

To be transparent for particles deflected by a bent crystal, to operate in a primary vacuum of the machine, and to resist a high radiation dose a Cherenkov detector based on a fused silica radiator was chosen. It was called Cherenkov detector for proton Flux Measurement (CpFM). The full development history with a precise prototypes description, performed tests and first SPS results can be found in [65]. Figure 5.3 shows the final design of the detector, which has been used for the 2015 – 2016 data-takings at the SPS.

The bent crystal, installed 58 m upstream the CpFM detector, deflects particles which are intercepted by the first detector bar producing Cherenkov light. The bars ($5 \times 10 \times 36$ mm^3) themself are used as radiators and light guides, placed on the motorized linear stage for the inserting and retracting from the beam. The first bar (Bar 1 in Fig. 5.3) is used for the incoming channeled particles counting, while the second one (Bar 2 in Fig. 5.3) monitors the background. The produced Cherenkov photons ($\sim$200 – 250 photons for 5 mm of bar thickness per incident proton) follow the bar and hit the fused silica viewport, which has the following functions: the light transportation and the primary vacuum separation from the air. Crossing the viewport (2 mm thick and 36 mm in diameter) photons are caught by two independent 4 m long bundles with 100 optical fibers in each (the numerical aperture is 0.22).

The radiation-hard bundles are attached to a pair of the Hamamatsu PMTs[1] (for Bar1: R7378A/BA1512, for Bar2: R7378A/BA1511), placed 1 m from the beam pipe and powered by a high voltage supply (ISEG T2DP050205EPU 2×5 kV/2 mA). To characterise the PMT (peak wavelength is about 420 nm) dedicated measurements of its gain with a LED and different supply voltages has been performed. A short blue (467 nm) light pulse of 10 ns with a frequency of 43 kHz (in order to simulate the SPS revolution frequency) was sent onto the PMT window. The results of the measurement of the gain are shown on Figure 5.4.

[1] http://www-eng.lbl.gov/~shuman/NEXT/MATERIALS&COMPONENTS/PMT/PMT_hamamatsu_R7378A%20.pdf

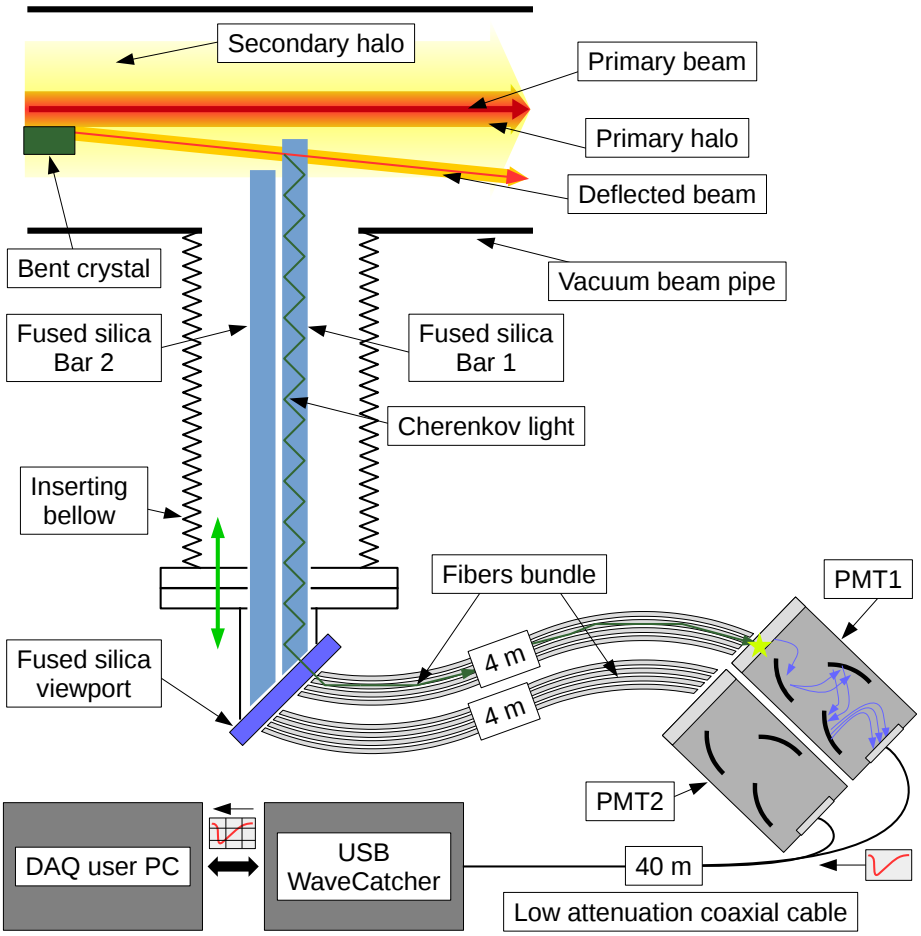

Figure 5.3: CpFM detector chain for 2015 – 2016 data-takings at the SPS. Not to scale. The bars are shifted by 5 mm with respect to each other in the direction to the beam.

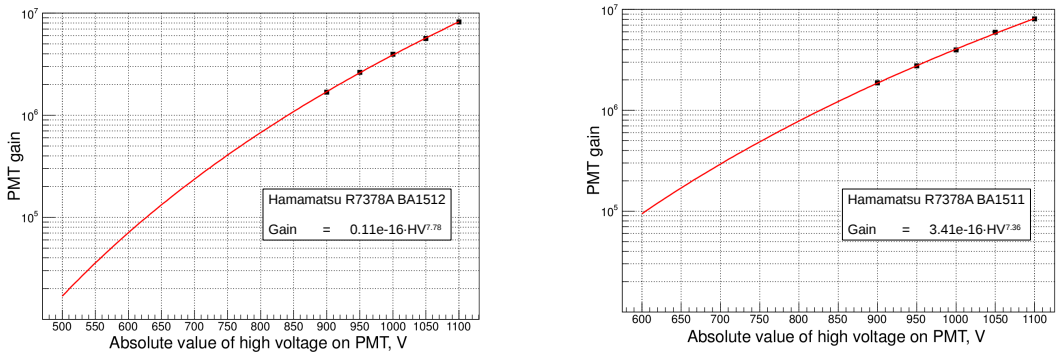

(a) R7378A/BA1512 for Bar1.

(b) R7378A/BA1511 for Bar2.

Figure 5.4: Measured gain for the Hamamatsu PMTs with a different applied supply voltage (HV), where BA1511 and BA1512 are their serial numbers.

The readout system of the PMTs consists of a 8-channel WaveCatcher module [68], connected to the detectors via low attenuation cables (40 m long).

In the present work we will speak about CpFM improvements and operation at the SPS for the deflected particle beam monitoring for 2016 – 2018 data-takings.

5.3 Semiconductor pixel detector

With the development of semiconductor electronics, a new direction in detector physics has appeared [69]. Pixel detector based on a semiconductor took the main place in high-energy particle tracking systems and particle counting. A detailed description of the pixel detector applications can be found in [70, 71]. In this section we will consider hybrid semiconductor pixel detectors for particle and radiation detection.

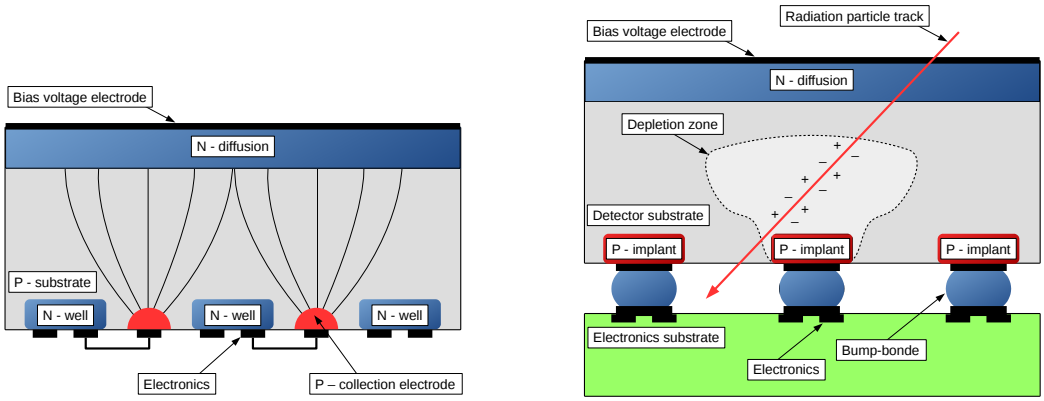

(a) Monolithic pixel detector.

(b) Hybrid pixel detector.

Figure 5.5: Difference between monolithic and hybrid pixel detector construction [72].

In general, all semiconductor detectors consist of two main components: sensitive (detection) layer and readout electronics. Detection layer is placed between two electrodes. A bias voltage (∼100 V) is applied to the electrodes and creates a depleted zone. An ionizing particle crossing a sensitive layer of a semiconductor detector creates an electron-hole pair in the detector material (Fig. 5.5b). As a result, freed electrons from the valence band are transferring to the conduction band, while the same number of holes is creating in the valence band. The charge carriers under electric field travel to the appropriate electrodes inducing a pulse,

according to the Shockley-Ramo theorem [73]. The number of pairs is proportional to the incident particle deposited energy in the material, therefore measuring the collected signal allows to determine the incoming particles flux.

A pixel (short for "picture element", the smallest distinguishable element of the image) detector is an ideal detector to work in a very extreme radiation hard environment like LHC. They can survive high integral flux of particles with a possibility to measure a position of the incident particle hit. The radiation damage of the semiconductor detectors is beyond the scope of this study, but the useful information can be found in [74]. Due to the construction difference we can split pixel detectors in two groups (Fig. 5.5): (1) monolithic and (2) hybrid pixel detector.

A monolithic pixel detector [70] is realized on a thin silicon layer (tens of μm) with low resistivity, which gives a possibility to produce very compact devices, due to the on-chip readout electronics with a high spatial resolution (few μm). On the other hand, it does not allow to make a large depletion zone (small amount of charge carriers $\approx 10^3 e^-$), fast charge collection ($\approx$ 100 ns with several ns of the time resolution) and due to the on-chip techniques of the readout electronics the number of sensors is very limited.

For a hybrid pixel detector a semiconductor sensor (hundreds of μm) is attached to the readout electronics using a bump bonding technique [72]. This method allows a using of the same readout electronics for different applications by changing the sensor to more suitable for the specific task. A good charge collection time (tens of ns with several ns of the time resolution) is possible with this type of detector, which has a large signal (for a full depleted detector it is more than $10^4 e^-$) due to the high resistivity. The spatial resolution of such devices is not smaller than tens of μm. The freedom in the choose of sensor materials makes this detector more favourable for different applications. Table 5.2 shows the main parameters for some detector sensor materials.

Material	C	Si	Ge	GaAs
Average atomic number $\langle Z \rangle$	6	14	32	31.5
Energy band gap [eV]	5.5	1.12	0.67	1.42
Electron-hole pair production energy [eV]	13.0	3.6	2.96	4.2

Table 5.2: Properties of the selected semiconductor materials. [75].

5.3.1 Medipix family detectors

The UA9 collaboration uses two different types of detectors for particle counting: CpFM (see Section 5.2) and Timepix detector. The Timepix [76] is the next generation of the pixel detector from the Medipix family developed at CERN by the Medipix collaboration with support of EUDET project[2]. The technology of Medipix is widely used in various field of human life[3]: medical imaging, space dosimetry, material analysis, education and high-energy physics. In a scope of the current work the operation of the Timepix detector for UA9 experiment is discussed. Detector calibration and tuning, a new cluster analysis and particle tracking will be described as well. Some useful information and links can be found in [76–79].

5.3.2 Detector overview

5.3.2.1 Hardware

Timepix (Fig. 5.6a) is a quantum imaging pixel detector of area ~ 2 cm^2, consisting of a monolithic silicon pixelated matrix of 256×256 sensitive elements, each 55×55 μm^2 and 300 μm thick, which is soldered together by 65536 metal bumps to a matching a Complementary metal–oxide–semiconductor (CMOS) read-out chip with identical dimensions. Each pixel is a rectifying Si diode, with its volume depleted from free charge carriers by the application of a reverse bias voltage, typically 20 V – 100 V, so that charge generated by an incident radiation quantum can be collected and measured. Detailed information about charge generation and collection in the pixel is also given in [80]. Each pixel is connected to its respective preamplifier and discriminator forming an Analog part of the processing chain (Fig. 5.6b), while a Digital part is composed of a Timepix Synchronization Logic (TSL), 14-bit Shift Register (11810 counts), overflow control logic and local buffering (Clk_Count). Only if the signal exceeds the discriminator threshold value, a 'hit' is recorded by the pixel, and then the signal is processed as indicated below. The innovative feature of the pixels in the Timepix chip is the use of the threshold in combination with a MHz clock that is distributed to all pixels. The pixel can record a timetag for the moment that a signal passes the threshold in one direction: up, or the other: down. This allows to count the number of clock-pulses while discharging the signal charge via the amplifier feedback, and offers a measure of the signal amplitude, as it was proposed in 1948 by Wilkinson [81].

[2] https://medipix.web.cern.ch/technology-chip/timepix-chip

[3] https://medipix.web.cern.ch/application-areas

[4] https://twiki.cern.ch/twiki/pub/BL4S/TimePix/Timepix_Manual_v1.0-1.pdf

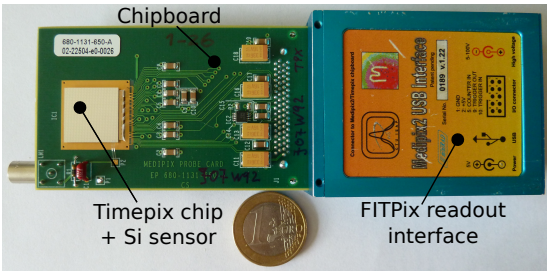

(a) Timepix detector connected to the FITPix readout electronics.

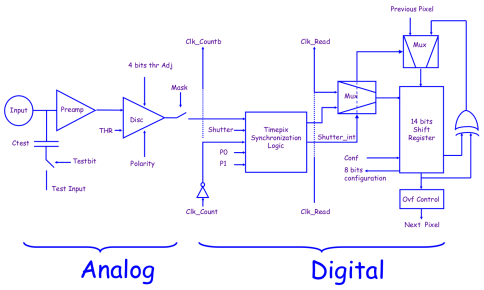

(b) Timepix pixel cell blocks diagram[4].

Figure 5.6: Timepix detector photo with its pixel electronics diagram.

The readout chip further contains the Digital-to-Analog DAC power regulators with 4 bits, programmable parameter tuning and I/O drivers. The on-pixel threshold adjustment has 4 bits, so that a natural dispersion of the threshold values between the pixels can be precisely equalized to achieve a minimum operating threshold for all pixels of ∼600 electrons [82]. This results in practically noise-free data.

According to the TSL configuration and P0/P1 bits (Fig. 5.6b) each pixel can be setted to one of the following modes in the next way:

⋆ P0 = 0 and P1 = 0: Medipix mode;

⋆ P0 = 1 and P1 = 1: Time of Arrival (ToA) mode;

⋆ P0 = 1 and P1 = 0: Time over Threshold (ToT) mode;

⋆ P0 = 0 and P1 = 1: Timepix-1hit mode.

The full matrix can be reset, and by opening the global shutter (acquisition time window) it is switched to exposure for a programmable period, ranging from μs to hours. After the shutter has closed again, the data from all pixels are sequentially transferred off-chip, and these represent one image 'frame'. Figure 5.7 shows different pixel acquisition modes within a given shutter:

- **Medipix mode** – Counter counts the incoming particles which have generated an above-threshold signal.
- **Time of Arrival (ToA) mode** – The counter receives clock pulses, e.g. at 5 MHz and measures the time interval, starting from the opening of the shutter until the arrival of the first signal from an incident quantum above threshold. Then the clocking is stopped for this pixel, so that only the time for the first incident particle can be recorded.

- **Time over Threshold (ToT) mode** – In a similar way, the counter receives clock pulses, but these are enabled only as long as there is a signal above threshold, which is similar to the Wilkinson type ADC. This measurement provides the amplitude of the particle energy released in the pixel, and signals from successive quanta during the exposure are summed.

- **Timepix-1hit** – Takes only one count per shutter if there is at least one hit.

The Fast Interface for Timepix Pixel detector (FITPix, see Fig. 5.6a) readout board [83] is using for the communication and data transferring between a user's PC and device via a USB 2.0 interface chip. It based on a FPGA circuit to archive the high data frame rate (up to 90 frames per second). The interface supports all operational modes of the Timepix and allows a hardware triggering for the multiple devices synchronization. The FITPix board is fully powered through the USB bus, and in case of a several detectors in chain readout the external power supply is needed.

5.3.2.2 Software

The Pixelman [84] software package developed in Prague University is designed to readout the chip. The package has a very flexible modular architecture that can be extended by software plugins (i.e. additional software that extends functionality). In our project we used two ways to communicate and control detector:

1. Pixelman Graphical User Interface (GUI) (allows to visualize the acquired frames and to write data into the text files)(Fig. 5.8);

2. Python scripting plugin (gives a possibility to integrate Pixelman libraries inside other DAQ systems).

With a developed Python script we can run a DAQ for several devices with a synchronization in time within 1-2 ticks of the internal clock and save the data on the disk.

5.3.2.3 Threshold equalization

Due to a natural contradiction, which appears during manufacturing, some parameters of identical Timepix pixels can be different. Usually, the common value of the threshold is varying from pixel to pixel. To take into account this effect Pixelman has a function Equalization to adjust the level of the threshold for each individual pixel using a Noise Floor Equalization method [85]. After this procedure

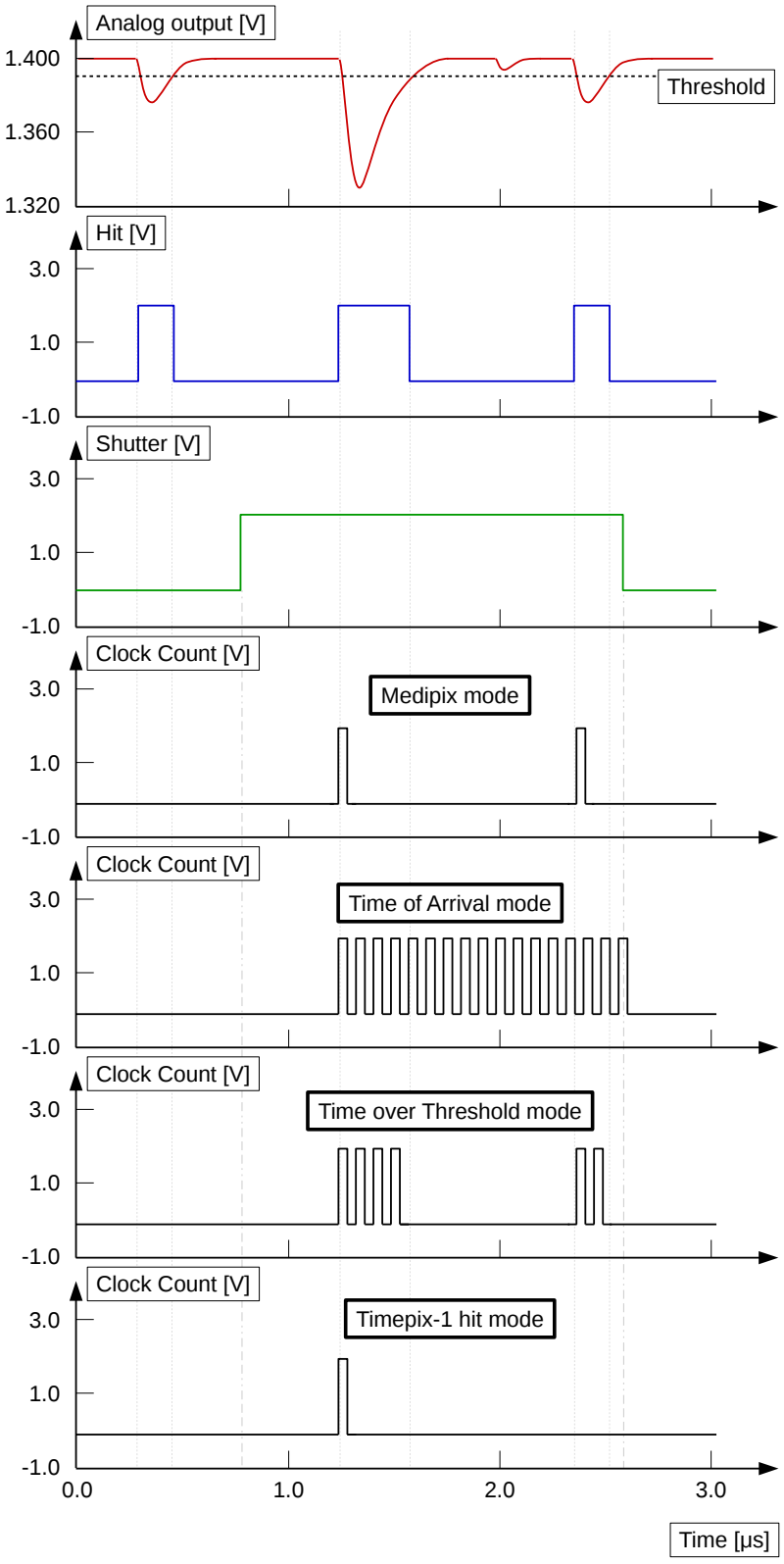

Figure 5.7: Timepix pixel acquisition modes.

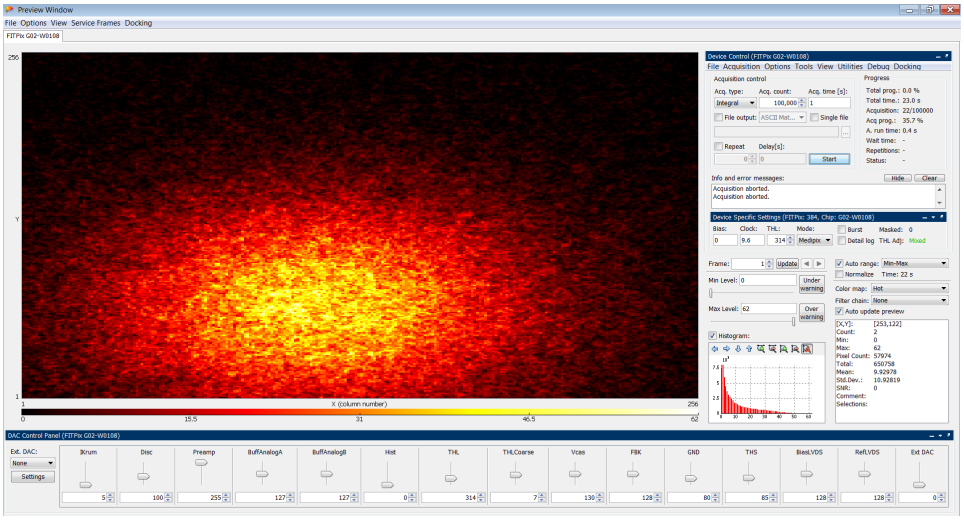

Figure 5.8: Pixelman GUI window with an event display. Timepix integrated image of the electrons from the Sr-Y source (∼37 MBq), 22 frames in the Medipix mode, 9.6 MHz clock with 1 sec of acquisition window for each frame. The number of hits is indicated in color (Z-axis).

a common threshold can be applied to all pixels for the electronic noise suppression. As consequence typically no pixels is fired if there is no particle incident on the silicon sensor.

To correct pixel disparity for the signal threshold, the Timepix uses 4 bits for pixel threshold tuning, while the THL offset is adjusted in 16 steps. Through the dedicated input (4 bit thl Adj) of the Analog part (Fig. 5.6b) the steps are applied to the discriminator. All parameters of the scanning (e.g. adjustment step) can be set up in advance using the GUI corresponded fields. Constantly moving the THL value into the noise the NFE requires a given criterion in photon counts. When the benchmark has been met the value of the THL is indicated on the equalization graph (Fig. 5.9). The same procedure is applied for each pixel with plotting the THL distribution. To extrapolate the THL value for all steps it is enough to do only the first (Fig. 5.9, blue bars) and the last step (Fig. 5.9, red bars). The proper adjustment step for each pixel leads to the THL distribution minimization (Fig. 5.9, black bars). The mean value of the latter is taken for the electronic noise suppression.

5.3.2.4 DAQ settings

Before any detector operation, a set of the Timepix parameters has to be applied: discriminator threshold value (THL) received from the equalization function, value of the bias voltage (the capacitance of each sensor pixel depends on the applied

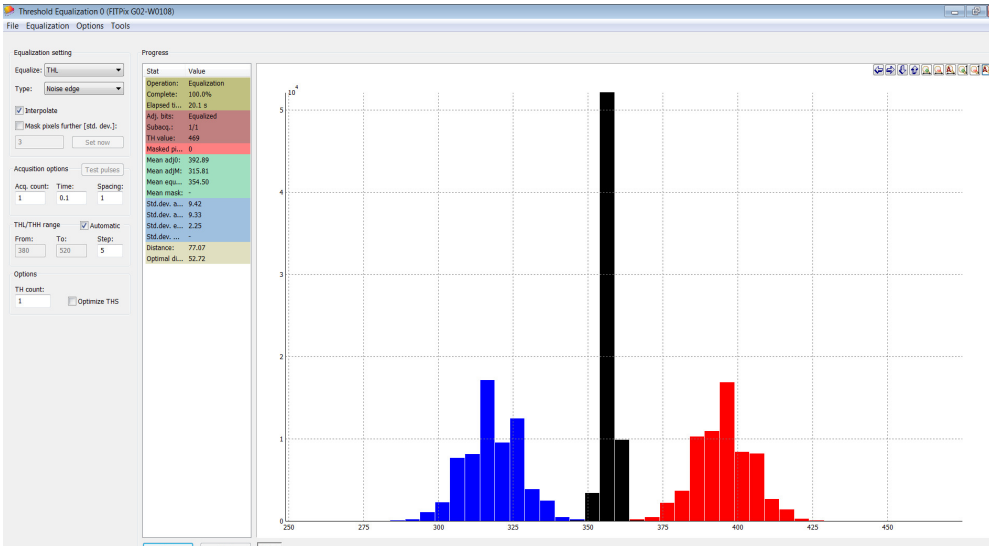

Figure 5.9: Typical results of the Timepix threshold equalization from the Pixelman interface. For a 100 V bias applied, the centroid is at 354.5, while the standard deviation is 1.02

bias voltage which affects depth of depleted zone), Ikrum (The parameter controls a discharging current in the preamplifier, i.e. the slope of a falling edge of the pulse), number of frames, time of each frame, acquisition mode (Medipix, ToA, ToT or Timepix-1 hit), trigger type, frequency of the measurement clock ($\leq$96 MHz). The internal clock can be set to define the time granularity of the measurements; the maximum count of 11810 for each register attached to each pixel limits the performances of the readout. For example, for 48 MHz clock ($\sim$20.83 ns) in ToA mode the maximum frame duration cannot exceed $11810 \times 20.83\ ns = 246\ \mu s$. Similarly for a clock of 0.48 MHz, the time measurements up to 24 ms can be performed.

5.3.2.5 Detector setup at the SPS

Concerning the H8 beam line installation, simple metallic holders were used for a Timepix detector. They gave a possibility to fix the devices in a given position with respect to the beam direction. Most of the time the Timepix detectors were placed downstream the crystal (10 – 50 m) with no needs to move.

Another situation is for the SPS machine. Unlike the CpFM detector, the Timepix detector cannot be placed inside the primary vacuum close to the circulating high intensity beam without any shield from the electromagnetic interference from the beam. For this purposes the UA9 collaboration decided to use a Roman Pots [86]. The volume of the pot is filled with a secondary vacuum ($\sim 10^{-6}$ mbar). There are

a detector sensitive board (Fig. 5.10a, right) with all necessary cables (bias voltage, sensor readout chip low-voltage supply) connected via a couple of feedthroughs to the extenders for the power supply and readout electronics (Fig. 5.10a, left), which are placed away 1 m from the beam pipe. The beam coupling impedance measurements of the Roman Pot (RP) are well described in [87].

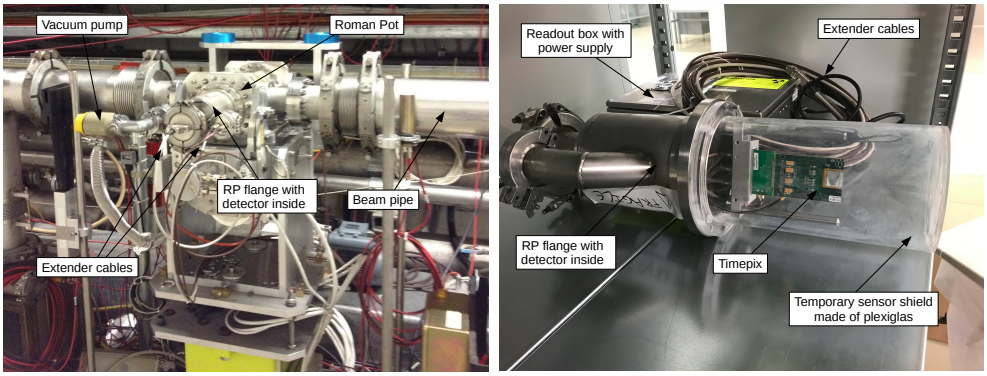

(a) Roman Pot at the SPS with a Timepix detector installed inside.

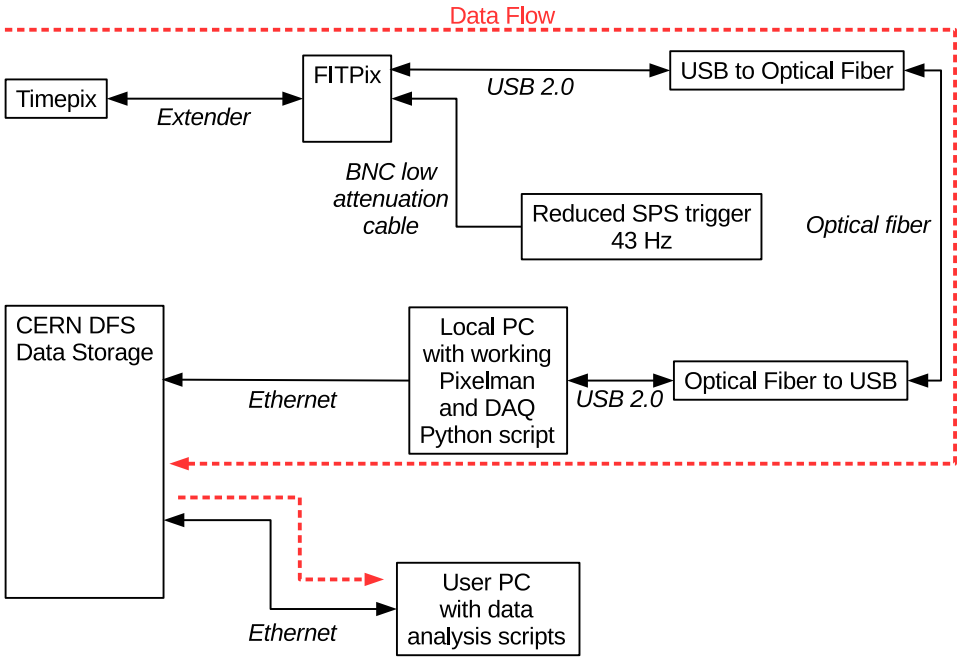

(b) Timepix data acquisition network. Red dashed line indicates data flow direction.

Figure 5.10: SPS acquisition setup for a Timepix detector.

Figure 5.10b shows the scheme of the data transferring. Using a DAQ Python script the data from the FITPix (fired pixel coordinates and number of counts)

frame by frame is transferred each minute to a new data file to the CERN-DFS storage. With a BASH script running on the user PC a quasi-online analysis can be performed producing about each minute a suitable information for the experiment: analyzed data is converted into the beam images and profiles, and saved on the user PC. Thus we were able to have the image of the detector frame almost immediately (the delays came only from the USB/Ethernet/Optical connection speed limits), which is the most important information needed during the measurements.

Chapter 6

UA9 experiment applications

Concerning the aim of the UA9 experiment, high-energy particle beam collimation, the majority of its fields of investigation were dedicated to this subject. Nevertheless, the collaboration was focused on several aspects of the beam manipulation with bent crystal, like beam extraction and fixed-target experiments. At the same time, a bent crystal physics of the particle channeling is continued to be examined using different particle beams. Obviously, each crystal before to be used at the SPS or LHC accelerators has to be tested and checked several times for the deflection stability in time, defects concentration, hitting (baking) or bending angle changing. All these tests have been performed at H8 beam line using proton, pion or ion beams with different energies.

The detailed information and important references about crystal-based beam collimation results can be found in [25, 42, 43]. The main idea of the experiment is to use a bent crystal as a primary collimator to deflect particles from the beam halo onto the secondary collimator or absorber. Such technique gives a possibility to increase the intensity of the main beam due to the low rate of inelastic nuclear interaction in the crystal comparing to the standard collimator jaw (about 1 m of high-Z material, e.g. tungsten), and to protect LHC superconductive magnets from the quenches.

A high-energy beam extraction was investigated during the last decades. The first successful experiments in this direction were carried out at the SPS CERN accelerator by the RD22 Collaboration [88], U-70 IHEP-Protvino accelerator [89] and Fermilab Tevatron accelerator in the E853 experiment [90]. The main result of these experiments is that a high channeling efficiency (10-85 %) was reached for high-energy proton and ion beams (70-900 GeV).

In this Chapter we will discuss recent experimental results of the UA9 collaboration for the crystal characterisation, detectors calibration and beam extractions

using bent crystal at the SPS accelerator.

6.1 Crystal characterisation at H8

As it was mentioned above, before to use a bent crystal for collimation or extraction purposes it has to be checked and tested in advance. To do so the UA9 collaboration uses an H8 beam line in the SPS North Area at CERN. The experimental setup for the crystal characterisation is described in Subsection 4.1.1. Here we just briefly remind the main parts of the experimental chain. The bent crystal itself is place between two tracker arms of 10 m each composed of 5 silicon planes for measuring incoming and outgoing particle tracks. The common trigger signal is produced by a plastic scintillator located upstream the tracker. The origin of the coordinate system for the setup is located in the middle of the crystal, where the Y-axis (Vertical) goes along the crystal high, while the X-axis (Horizontal) lies in the deflecting plane, transversally to the beam axis (Z-axis). For the investigation of the inelastic nuclear interactions in a bent crystal there is a linear motorized stage with two small ($10 \times 20 \times 4$ mm^3) plastic scintillators, working in a short (~ 3 ns) coincidence time gate for the background suppression. The INI scintillators are integrated in the tracker DAQ system and used for the secondary particles counting within a given tracker event. Placing them around 20-25 cm downstream the crystal, symmetrically with respect to the beam axis (with a gap of 10-20 cm in X-axis), we can measure the number of events when a single particle enters to the crystal and interacts inelastically with it, producing secondaries (Fig. 6.1).

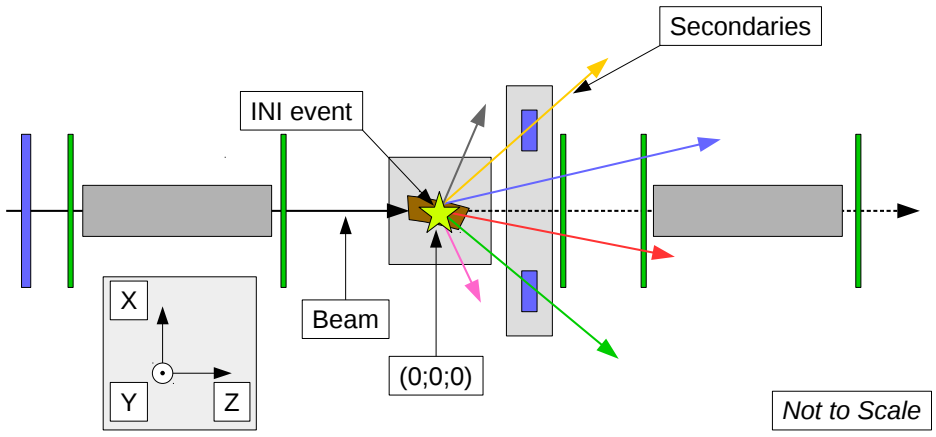

Figure 6.1: Scheme of the INI measurement principle (see Fig. 4.2 for details).

6.1.1 Data analysis algorithm

Now we are going to describe the methodology of the data analysis for the bent crystal characterisation at H8 beam line. Table 6.1 shows the main parameters of the particle beams, which were used for the measurements discussed later in the text. Along 5 s of the SPS Spill an extracted beam has an intensity of about 10^5 particles per second with an average time distance beam each particle of $\sim$10 μs.

Type	Momentum, GeV/c	σ_x, mm	σ_y, mm	σ_{θ_x}, μrad	σ_{θ_y}, μrad
proton	400	1	1	10	10
π^+	180	2	2	30	40
^{129}Xe ion	150A	2	2	15	22
^{129}Xe ion	40A	5	5	42	29
^{208}Pb ion	150A	7	5	25	40

Table 6.1: H8 beam characteristics.

During the experiment an operator in a control room, using a remote controlled 6-axis goniometer, aligns the crystal with the center of the beam and performs an angular scan to find the optimal crystal orientation for channeling. Figure 6.2 shows a detailed experimental angular scan of the silicon crystal with 400 GeV/c proton beam, where it is possible to define each region of the particle interaction with a bent crystal:

AM A particle with beg incoming angle interacts with a crystal like an amorphous material, obtaining a multiple scattering deflection of few microradians.

VR During the long angular range ($\sim$300 μrad), which is equal to the deflection angle of the crystal, the particle undergoes a volume reflection process with around one critical angle deflection in an opposite direction to the channeling.

VC At the same time, there is a probability to be capture in a channeling regime at different position along the crystal, obtaining a correspondent deflection angle. The volume capture process takes place.

CH At certain orientation the particle starts to be channeled within $\pm$ critical angle region.

DCH Due to the dechanneling process particle leaves the channeling regime and deflects with a smaller angle.

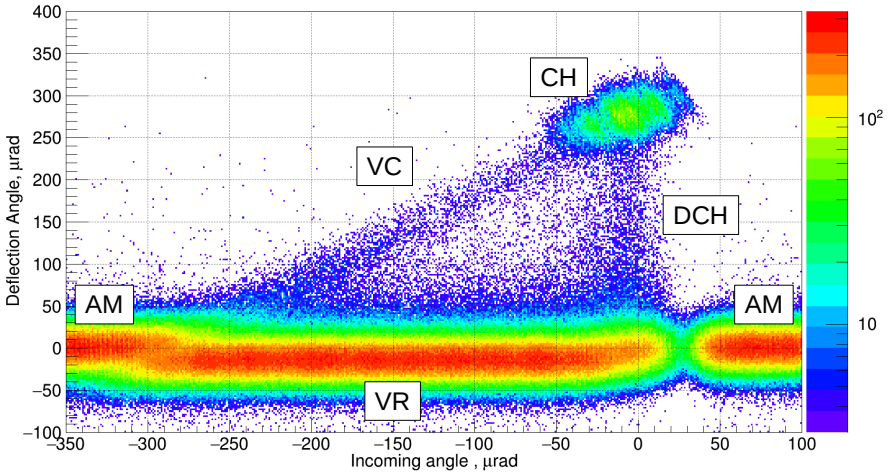

Figure 6.2: Deflection angle as a function of the incident angle with respect to crystalline planes for 400 GeV/c proton beam. The data refers to the detailed angular scan for a silicon crystal with an anti-clastic bending of about 290 μrad.

After an angular scan the operator puts the crystal in the optimal orientation for the given process (e.g. CH, VR, etc.) and starts an acquisition for a high statistical run. In particular cases (e.g. for INI investigation), there is a need to have a run without crystal on the beam line, called background run (BKG). In this way, the crystal is retracted from the beam using one of the linear axes of the goniometer.

The basic idea for the channeling efficiency calculation is: (1) to apply geometrical cuts, taking only that part of the beam, which is hitting the crystal; (2) define the optimal crystal orientation with respect to the incident beam; (3) for a given angular region calculate the ration (Eq. 2.26) between the channeled particles number (N_{ch}) and the total number of incident particles (N_{tot}).

6.1.2 Single-pass channeling efficiency calculation

Before to start we have to introduce a crystal torsion effect, which is one of the most important crystal imperfections. It appears during the bending of the crystal and arises as a deviation from the cylindrical bending. The torsion leads to a dependence between a vertical position on the crystal and input orientation of the atomic planes: $\theta_X^{IN} = f(d_{0Y})$, where θ_X^{IN} is an incoming horizontal angle of the particle with respect to the crystalline plane, and d_{0Y} is an impinging vertical position of the particle.

Lets take a bent crystal ($2\times55\times4$ mm^3) with 46 μrad deflection angle in the (110)

plane orientation. The total number of events for the run is about 10^6 pions (π^+) with momentum of 180 GeV/c. To find the best crystal orientation for channeling and to calculate the torsion we can follow the next steps:

1. Plot a distribution of the deflected angle ($\Delta\theta_X$) and impact parameter to define the geometrical cuts as a visible region of the particle channeling (Fig.).

2. Applying geometrical cuts and splitting vertically by 0.2 mm (assuming that the torsion is negligible for this slice) plot the angular distribution of the deflected particles for each slice (Fig.).

3. Plot the deflection angle for particles with an incoming angle in the range (Fig.) of mean ± 1.5·rms (can be adjusted for different beams). Fit the channeled and not channeled fractions of the beam using a double Gaussian function (Fig.).

4. Calculate the following value: (1-η_{nch}), as a function of the particle incoming angle and vertical impact parameter, where $\eta_{nch} = N_{nch}/N_{tot}$ is an efficiency to be not channeled, N_{nch} and N_{tot} are the numbers of the not channeled and total incident particles, respectively. (Fig.).

5. Plotting the incoming angle as a function of the impact position for the maximum channeling efficiency we get a torsion parameter of the crystal, fitting with the first order polynomial function (Fig.).

6. Taking into account the obtained torsion parameter we can plot an angular distribution of the deflected particle, the same as (Fig.) but for the full vertical crystal range within geometrical cuts. Calculating (1-η_{nch}) it is easy to find an optimal crystal orientation for channeling as an angular position with the maximum deflection efficiency (Fig.).

7. Plot deflection angle distribution for all events with single incoming and outgoing tracks, applying the torsion correction for the optimal crystal orientation. Fitting by the double Gaussian function we can calculate the channeling efficiency ($\eta_{ch}(\pm\theta_{cut}) = N_{ch}(\pm\theta_{cut})/N_{tot}(\pm\theta_{cut})$) for a given incoming angle range ($\pm\theta_{cut}$) and deflection angle of the crystal (θ_{def}) (Fig.).

Table 6.2 shows a single-pass planar channeling efficiency of different crystals with their torsion parameter and deflection angle. The meanings of the crystal names are the following: QMP - Quasi-Mosaic (quasi-mosaic bending) crystal from the Petersburg Nuclear Physics Institute (PNPI), STF - STrip (anti-clastic bending)

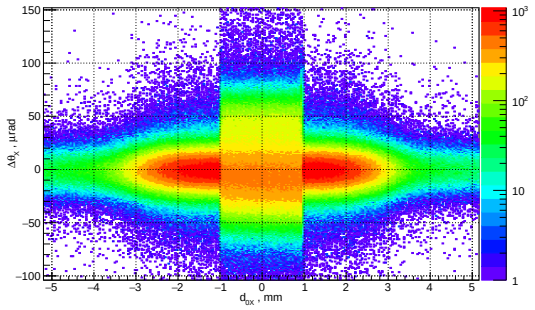

(a) Deflection angle as a function of an impact parameter in X-axis. Geometrical cuts: $-1 < d_{0X} < 1$, corresponds to the crystal edges.

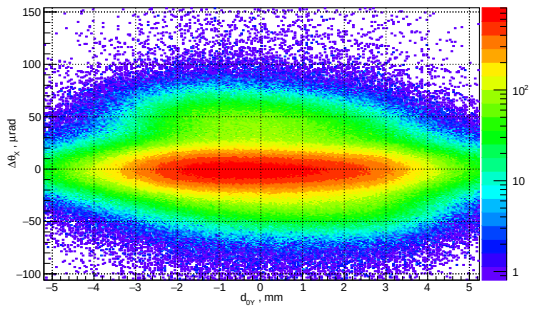

(b) Deflection angle as a function of an impact parameter in Y-axis. Geometrical cuts: $-3 < d_{0Y} < 3$, corresponds to the crystal edges.

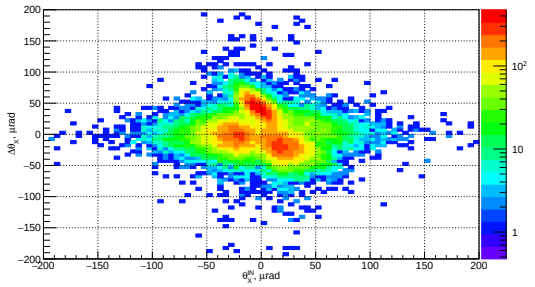

(c) Deflection angle as a function of the incoming angle in X-axis for a single slice of 0.2 mm in Y-axis. It is clearly visible a CH region with 50 μrad of deflection in the center, AM on the left and VR on the right from the CH with a small negative deflection.

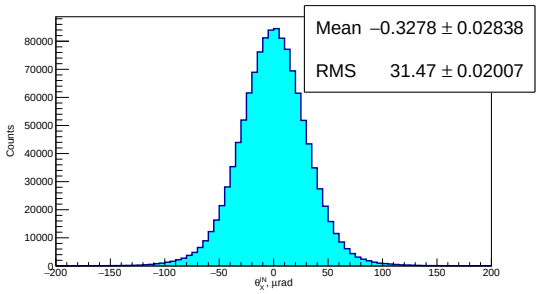

(d) Angular distibution of the incoming angle of the particles in X-axis. Mean value of the distribution is about -0.33 μrad with 31.47 μrad of the standard deviation.

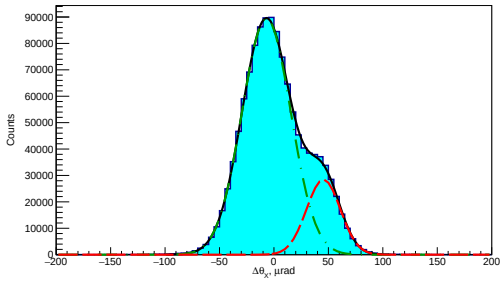

(e) Deflection angle in X-axis for a slice of 0.2 mm in Y-axis. A green dot-dashed line is a Gaussian fit of the not deflected beam part; a red dashed line is a Gaussian fit of the deflected part of the beam; a black solid line is a double Gaussian fit of the distribution.

Figure 6.3: Illustration of the data analysis steps for a single-pass crystal channeling efficiency calculation (Part 1).

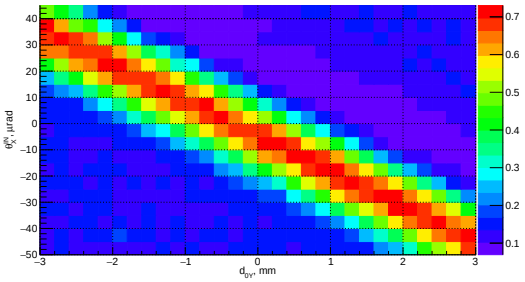

(a) Deflection efficiency $(1 - \eta_{nch})$ (indicated in color) as a function of the incoming angle and impact parameter in X-axis.

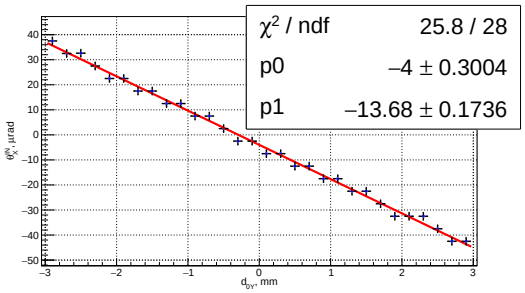

(b) Incoming angle as a function of the impact parameter in X-axis for the maximum deflection efficiency. Red line is the first order polynomial fit, where $p1$ is a slope (torsion, μrad/mm), and $p0$ is an offset (μrad).

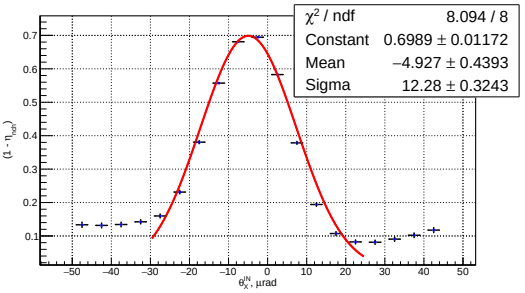

(c) Deflection efficiency as a function of the crystal orientation (or incoming particle angle) with applied torsion correction. Mean value of -4.9 μrad corresponds to the optimal angle for the channeling.

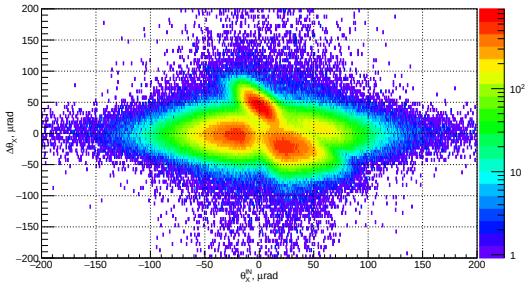

(d) Deflection angle as a function of the incoming angle in X-axis for the whole crystal within geometrical cuts, the torsion correction and optimal crystal angle are applied.

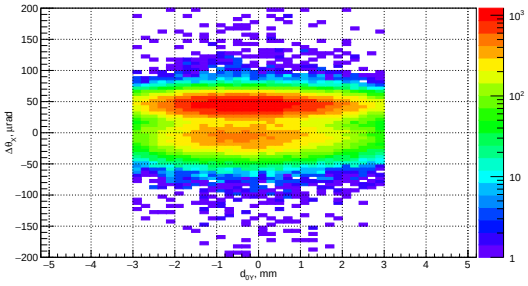

(e) Deflection angle in X-axis as a function of the impact parameter in Y-axis. The top region (around 50 μrad) corresponds to the deflection beam fraction, while the bottom one (around 0 μrad) is a not deflected part of the beam.

Figure 6.4: Illustration of the data analysis steps for a single-pass crystal channeling efficiency calculation (Part 2).

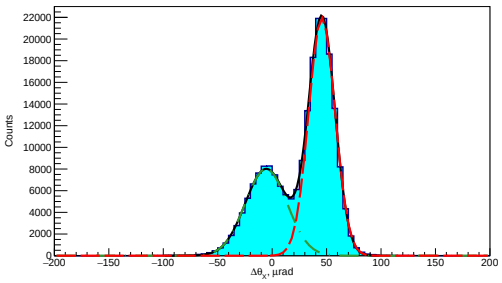

Figure 6.5: Deflection angle distribution with torsion and optimal angle corrections applied within geometrical cuts for the incoming angle in X-axis of $\pm\theta_c/2$, where θ_c is a critical angle (13.3 μrad for 180 GeV/c pions in Si(110) crystal, Table 2.2). A green dot-dashed line is a Gaussian fit of the not deflected beam part; a red dashed line is a Gaussian fit of the deflected part of the beam; a black solid line is a double Gaussian fit of the distribution. The calculated channeling efficiency (η_{ch}) in this case is around 68 %.

crystal from the Istituto Nazionale di Fisica Nucleare (INFN) section of Ferrara, TCP - Test Crystal from the PNPI (anti-clastic bending) with high stability bending device, GE - GErmanium crystal (anti-clastic bending) from the INFN Ferrara, PL - Plate Long crystal (anti-clastic bending) from the INFN Ferrara.

6.1.3 INI rate measurements

To use a bent crystal for a particle beam collimation and extraction in the accelerators like the SPS or LHC, the beam losses produced by the bent oriented crystal has to be estimated. The important value is the inelastic nuclear interaction probability for a given crystal orientation. A detailed information about the measurements done by the UA9 collaboration is well described in [51, 52]. Here we will just briefly overview some very important results from the H8 beam line measurements with 400 GeV/c protons.

For these dedicated measurements a pair of plastic scintillators (lets call them scintillator 1 and scintillator 2) was use in time coincidence for the INI events registration. Due to the geometrical acceptance of the scintillators, they were able to cover only a part of the solid angle of the secondaries produced in the crystal. Therefore a Monte-Carlo based routine was needed to calculate the geometrical factor for each INI measurements, taking into account the distance between detectors and position with respect to the crystal. For this purpose a GEANT4 [91] and FLUKA [92] software were used to simulate an experiment, calculating the number of INI events occurred in the crystal (N_{INI}) and the number of corresponding events, when both

Crystal name	Material (Plane)	L [mm] ($\pm$0.02)	Torsion [μrad/mm] ($\pm$0.8)	θ_{def} [μrad] ($\pm$1)	R [m] ($\pm$1)	η_{ch} [%] ($\pm$2)	P [GeV/c]
QMP46	Si(111)	4.0	1.0	48.8	82	70	proton, 400
QMP54	Si(111)	4.0	0.0	57.2	70	61	π^+, 180
QMP46v2	Si(111)	4.0	0.0	57.3	70	63	π^+, 180
QMP25	Si(111)	2.1	1.1	166.0	13	49	π^+, 180
STF105	Si(110)	4.07	1.8	49.4	82	78	proton, 400
STF103	Si(110)	1.88	15.7	56.0	34	80	proton, 400
STF18	Si(110)	2.0	0.6	176.0	11	78	proton, 400
STF81	Si(110)	1.87	–	165.0	11	–	–
TCP72	Si(110)	6.0	1.3	203.8	29	64	^{129}Xe, 150A
TCP74	Si(110)	4.0	0.7	52.0	77	72	^{129}Xe, 150A
TCP75	Si(110)	6.0	4.6	196.8	30	48	^{129}Xe, 40A
GE01	Ge(111)	3.0	26.4	333.6	9	46	π^+, 180
PL08	Si(111)	56.8	2.6	1064.0	53	49	π^+, 180
PL10	Si(111)	79.7	1.6	3453.2	23	27	π^+, 180
PL11	Si(111)	80.0	26.8	12043.2	7	13	π^+, 180

Table 6.2: Crystal parameters, where P is a particle momentum, the nominal dislocation density of crystals is about 1 cm^{-2} and 300 cm^{-2} for silicon and germanium crystals, respectively, η_{ch} is a single-pass planar channeling efficiency within $\pm\theta_c/2$ incoming angle region, L is a crystal length along the beam, while R is a bending radius.

scintillators detect secondaries (N_{SCINT}). The required geometrical factor (F_{GEOM}) of the setup is the ratio between these two numbers:

$$F_{GEOM} = \frac{N_{SCINT}}{N_{INI}}. \tag{6.1}$$

After the threshold adjustment to the minimum ionizing particle (MIP) signal the efficiency of the plastic scintillators can be consider as 100 %. It is also necessary to calculate the background rate of the INI events which are coming from the beam interactions with air and second tracker plane. The nuclear rate (I_{INI}) for the INI invesigation is calculated in the following way:

$$I_{INI} = \frac{N_{12}}{N_0}, \tag{6.2}$$

where N_0 is a total number of incident particles to the crystal, while N_{12} is a number of the plastic scintillators coincidences for the corresponding event. Then the INI probability (P_{INI}^{CH}) in the channeling (CH) orientation (planar or axial) can be easily calculated subtracting the background (I_{INI}^{BKG}), taking into account the acceptance of the detectors (F_{GEOM}), received from the simulation:

$$P_{INI}^{CH} = \frac{I_{INI}^{CH} - I_{INI}^{BKG}}{F_{GEOM}}. \tag{6.3}$$

Figure 6.6a shows a normalized interaction probability (i.e. $P_{INI}^{PCH}/P_{INI}^{AM}$) for planar channeling comparing with simulation results done by the Planar Channeling full analytical routine [6] (PCH sim.) and SixTrack Crystal routine [42] (SixTrack sim.), which show a good description of the experimental data for the STF105 and QMP46 crystals (Table 6.2). According to the plot, there is a difference between two crystals with the same bending angle and length, which is only due to the crystal lattice orientation for planar channeling. The quasi-mosaic crystal (QMP46) uses (111) plane for particle deflection, while the anti-clastic crystal (STF) is bent along (110) crystalline plane. The interplanar distance for (111) is around 1.565 Å (averaged for (111)L and (111)S, Table 2.1), and for (110) is around 1.92 Å, which is smaller and leads to the lower probability for the incident particle to interact with a nuclear plane.

In addition, we can see, that within 5 μrad angular acceptance, in a perfect aligned planar channeling orientation, the interaction rate (i.e. beam losses) is only 26.9±1.8 % and 35.9±2.9 % of the amorphous rate for STF105 and QMP46 crystals, respectively.

The asymmetry of the inelastic nuclear interaction probability dependence on the crystal orientation in the vicinity of the planar channeling minimum has been precisely measured for the first time (Fig. 6.7) [93]. For the inspected crystal, this

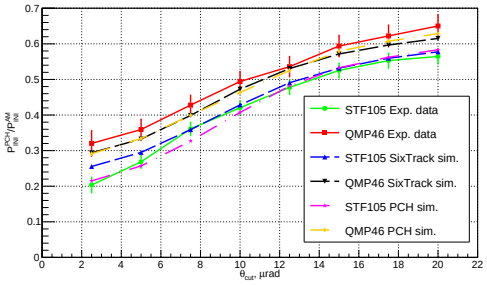

(a) Experimental and simulation results of the INI probability measurements in PCH orientation (normalized to the corresponded value in AM orientation) for a quasi-mosaic (QMP46) and anti-clastic (STF105) crystals as a function of the angular cut ($\pm\theta_{cut}$) applied on the incident particle beam.

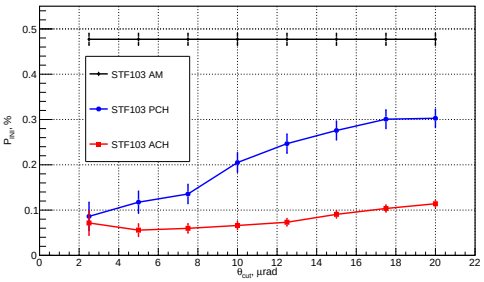

(b) Absolute INI probability for planar (PCH), axial (ACH) channeling and amorphous (AM) bent crystal orientation as a function of the angular cut ($\pm\theta_{cut}$) applied on the incident particle beam.

Figure 6.6: Inelastic nuclear interaction measurements for 400 GeV/c protons in bent silicon crystals.

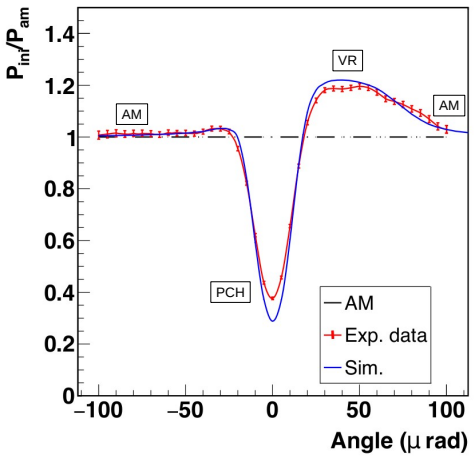

Figure 6.7: In red the observed dependence of INI rate for 180 GeV/c π^+ mesons on the orientation angle of a silicon crystal ($\theta_{def} \approx 61\ \mu rad$, length along the beam is about 4 mm) bent along the (110) planes. The blue curve shows the full analytical simulation results. Both are normalized to the AM level (black dashed line).

probability was about ∼20 % larger than in the amorphous case because of the atomic density increase along the particle trajectories in the angular range of volume reflection, whose dimension is determined by the crystal bending angle. Instead, for the opposite angular orientation with respect to the planar channeling, a smaller probability excess of ∼4 % has been measured. Such an increase of the yield at the crystal turn is caused by the peculiarities of interaction of above-barrier particles with an atomic plane: the effect of particle hovering over potential barrier of the continuous potential of atomic plane. A particular role of the above-barrier particles at the interaction with atoms of a straight crystal was noted yet in the work [94].

Accompanying to the planar channeling, we can take a look on the axial channeling situation. Figure 6.6b shows an absolute probability for STF103 (anti-clastic bent), which is oriented along < 110 > atomic axis (Fig. 6.8). In [24] was shown, that for the axial orientation INI rate is smaller compare to the planar one, like it was predicted in [95]. In our case, for the 5 μrad angular acceptance we have about 4.1 and 8.6 times of INI reduction in PCH and ACH with respect to AM orientation [52].

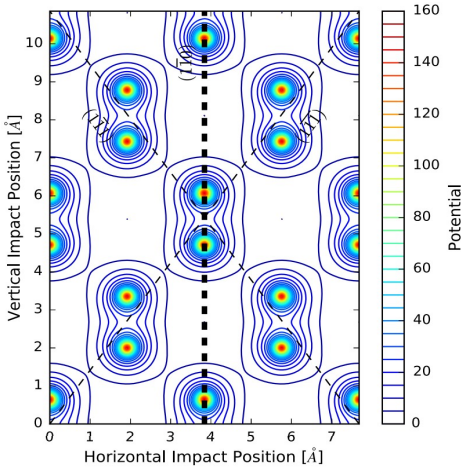

(a) Potential averaged along the < 110 > axis of a silicon crystal. The directions of the skew (111) planes are shown. From [24].

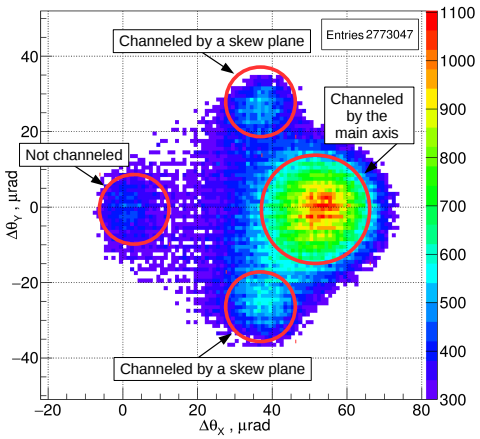

(b) Measured distribution of the vertical and horizontal deflection angles of 400 GeV/c protons interacting with a < 110 > crystal (STF103), oriented for the axial channeling.

Figure 6.8: Axial channeling in the silicon crystal for charged particle beam.

6.2 Detectors calibration on the beam line

In parallel to the crystal characterisation measurements at H8 extraction line, 50 m downstream the beam CpFM and Timepix detectors tests were conducted. In this Section we will describe detectors calibration parameters and experimental results.

6.2.1 CpFM

In 2015 the first calibration of the CpFM (see Subsection 5.2.1) was done on the Beam Test Facility (BTF) at Frascati with 449 MeV/c electrons [96]. A good signal linearity with a number of incoming electrons was observed for CpFM placed on the beam (Fig. 6.9a). The measured resolution of the detector is 15 % for 100 electrons (or 150% for a single proton) with a calibration value of about 0.62 photoelectrons (p.e.) per incoming particle (Fig. 6.9b).

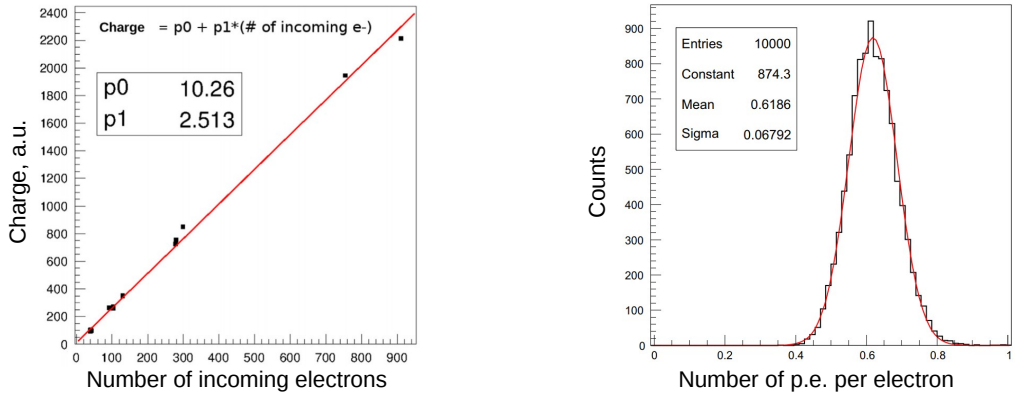

(a) Charge measured by CpFM as a function of the number of incoming electrons. Red line is the first order polynomial fit.

(b) Distribution of the p.e. number measured by CpFM, normalized by the number of incoming electrons.

Figure 6.9: CpFM detector calibration results of the measurements done at the BTF beam line with 449 MeV/c electrons.

From the H8 test-beam with 400 GeV/c protons the calibration factor of 0.63 photoelectrons/particle has been obtained [65].

Unfortunately, due to the designed geometry of the tank for the detector, the length of the bar of 36 cm has been considered too short to reach the middle of the beam pipe, which is needed for the device alignment with respect to the circulating beam. Therefore, right before the installation on SPS, the bars have been replaced

by two new fused silica bars 40 cm long. To avoid to postpone the installation of the detector on the accelerator, we did not test the new bars before the installation, assuming their identity to the previous ones.

6.2.2 Timepix

6.2.2.1 Detector sensibility

To provide the highest efficiency of the particle detection (sensibility to the incoming particle), it is important to apply the optimal value of the bias voltage. Under influence of the bias voltage the charge carries travel toward different electrodes. The detector used in the UA9 experiment is set to collect holes, i.e. the pixels have positive polarity.

In 2016 a test with 3.7 MBq Sr-Y beta-source has been done to evaluate the optimal value of the bias voltage. Figure 6.10a shows a picture of the experimental setup. The radioactive source was placed in front of the Timepix detector. Varying the distance between the source and the detector we measured the dependency between number of the total hits and different applied bias voltages. Assuming that the flux of the particles from the source is constant during the measurements, we reached the full efficiency with a bias of 40 V with silicon thickness of 300 μm (Fig. 6.10b).

(a) The Sr-Y source in front of the Timepix detector.

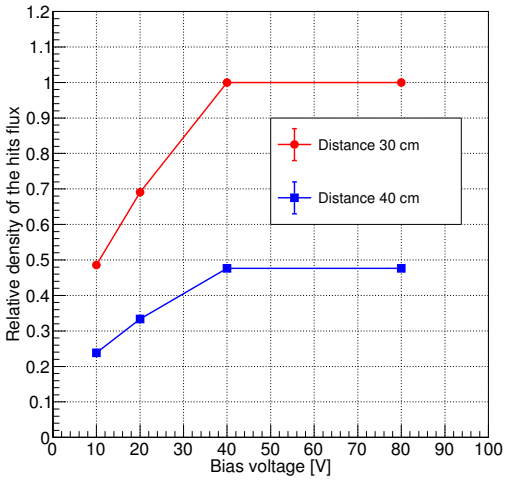

(b) The dependency between the total number of hits and applied bias voltage for different distances between the source and detector. The relative error of the values is less than 1%.

Figure 6.10: Detector efficiency measurements.

6.2.2.2 Cluster Analysis improvements

For analysis of the 2016 data we used the standard Cluster Analysis [97] (CA) to identify the particle type. With this CA the cluster is recognized as the region of the fired neighbor pixels, which bring rapidly to a saturation of the particle counting caused by clusters overlapping. To solve this problem we decided to write a New (Improved) Cluster Analysis to use the information about time of arrival in each pixel.

The time distribution of the signal arrival time in a cluster exhibits a Gaussian with 60 ns of the standard deviation (Fig. 6.11a), compatible with the drift time of the holes inside the silicon sensor with 0.3 mm thickness for 40 V of bias voltage [98]. Figure 6.11b shows how the time difference inside each cluster behaves with cluster size.

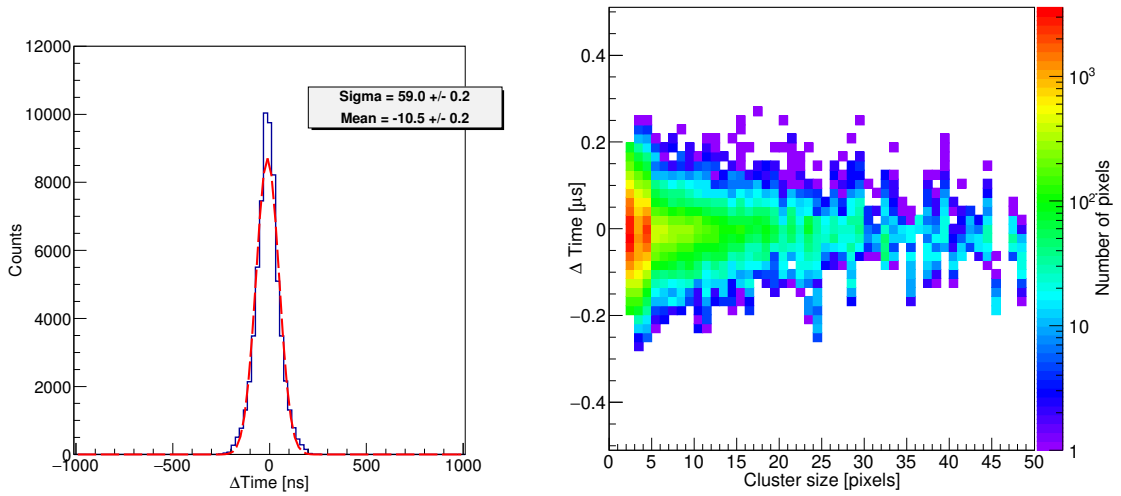

(a) Time difference of the pixels inside each cluster.

(b) Dependence between time difference of the pixels inside each cluster and the size of the cluster. In color (Z-axis) is indicated the number of pixels.

Figure 6.11: Distribution of the time difference inside the cluster, which is defined as the region of the neighbor fired pixels. H8 beam line data in ToA mode with 48 MHz clock.

Therefore, the algorithm for the new cluster analysis in ToA mode consists of the following steps:

1. Applying a cut of 200 ns (i.e. $\pm 3\sigma$ for 48 MHz clock) in a time difference between pixels, we split a given frame into several subframes, where all pixels will be within this time window.

2. For each subframe, we apply the standard cluster analysis, where a single cluster is defined as a region of the fired neighbor pixels.

With a new cluster analysis algorithm in 2017 we avoid the saturation of the particle counting in ToA mode and increase the maximum number of incoming particles per frame by factor 3 compare to the standard cluster analysis algorithm. Figure 6.12 shows the comparison between the results of the standard and improved cluster analysis done for the H8 beam line.

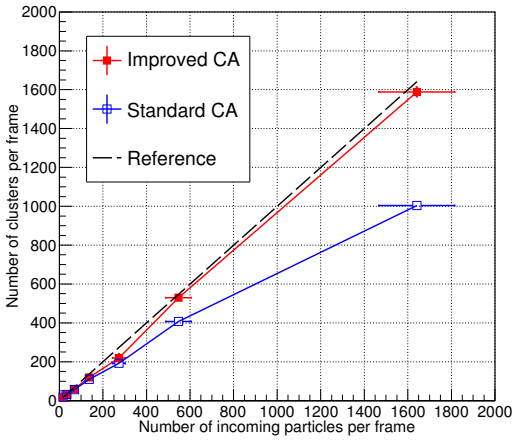

Figure 6.12: Comparison between two types of the Cluster Analysis (CA) for the H8 beam in ToA mode operation. The reference number of the incoming particles was taken with a plastic scintillator installed on the beam.

6.2.2.3 Detector calibration

To increase the statistics for particle counting per frame we have to use the Medipix mode. However, to calculate the number of crossing particle it is necessary to measure the number of fired pixels per cluster (particle), assuming that in most of the cases we have pions. Therefore, we plot the distribution of the cluster size, applying the cut of 200 ns ($\pm 3\sigma$ for 48 MHz clock, Fig. 6.11a) in the time difference between pixels inside the cluster. An expected cluster size for an incident high-energy pion is 1 pixel. However, due to the charge sharing between pixels, particle angular distribution and not ideally orthogonal orientation of the sensor with respect to the beam direction, a significant number of clusters has more than 1 pixel size. Calculating the most probable value (MPV) of the distribution we obtain $\sim$1.8 pixels/particle in ToA mode (Fig. 6.13a).

Taking into account received calibration parameter we can easily calculate the number of incident particles per frame (Fig. 6.13b). Using a Vavilov distribution

function [99] the MPV value is 12 particles per a frame of 246 μs, which is in a good agreement with the expected value of 0.1–1 particles per 10 μs (see Subsection 6.1.1). Switching to the Medipix mode we can measure the flux of the beam, which is about $0.6 \cdot 10^5$ pions/s or it is the same as 231 pions/(s$\cdot$mm^2) in the beam core for 196 mm^2 of the Timepix active area.

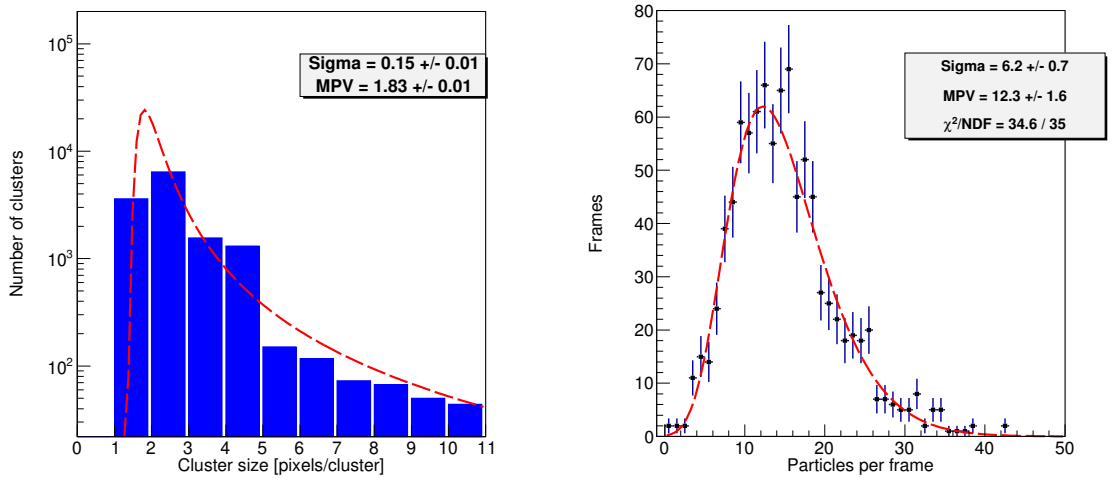

(a) Distribution of the fired pixels number per cluster. Red dashed line is a fit done with a Landau distribution function.

(b) Number of particles (clusters) per frame. Red dashed line is a fit done with a Vavilov distribution function.

Figure 6.13: Timepix measurements in ToA mode (246 μs of acquisition window with 48 MHz clock) for 180 GeV/c pion beam at H8.

Figure shows an integration image of the H8 beam with 180 GeV/c pions done by the Timepix detector in Medipix operational mode with 48 MHz of clock, while the measured number of detected particles per frame is illustrated in Figure 6.15.

6.2.3 Additional research

In addition to CpFM and Timepix calibrations several other measurements and tests have been performed at H8 SPS extraction beam line.

6.2.3.1 Beam profilometer

To perform an experiment on the beam line it is necessary to do an alignment of the system with respect to the beam axis. For this purposes an autonomous motorised system based on the scintillator detectors has been developed and tested. The detection chain consists of two plastic scintillator fingers ($3 \times 3 \times 50$ mm^3)

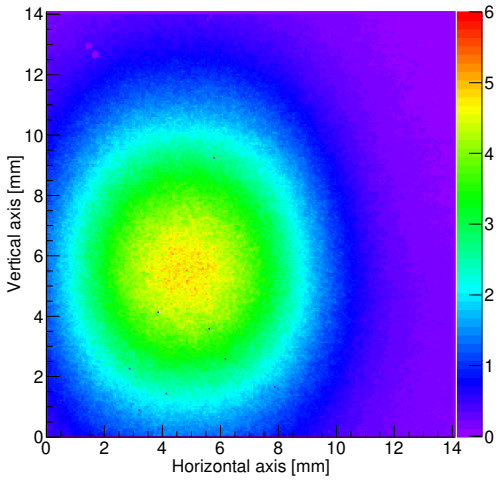

Figure 6.14: The image of the 180 GeV/c pion beam integrated within 1 second in the Medipix mode with 48 MHz clock. In color (Z-axis) is indicated the number of hits in each pixel per 1 second. White spots correspond to the masked pixels.

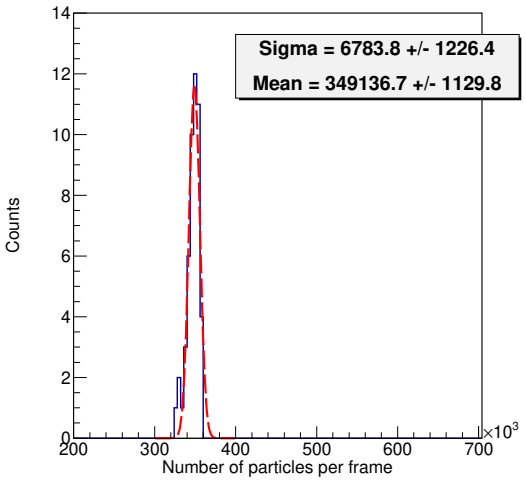

Figure 6.15: Number of particles per frame with 48 MHz clock in Medipix mode for 180 GeV/c pion beam at H8, an acquisition frame is 6 s. The fit (red dashed line) was done by means of the Gaussian distribution functions.

with a silicon photomultiplier (SiPM type PM3350[1]) attached to each side. The SiPM detectors were connected to the specific printed circuit board (PCB) for a bias voltage (Keithley 2410 source meter[2]) and readout (8-channel USB- WaveCatcher [68]). A UA9 upstream scintillator at H8 was used as an external trigger (see Subsection 4.1.1). One of the detector was oriented vertically, while another – horizontally (Fig. 6.16a). The detector system was located on the 3D translational stage (Fig 4.5) and was used as a beam profilometer. Doing a linear scan (vertically and horizontally) we were able to measure the beam profile in both directions, putting the corresponded signals from two sides of each finger in coincidences. The threshold of the output signals was applied in order to cut the noise pedestal.

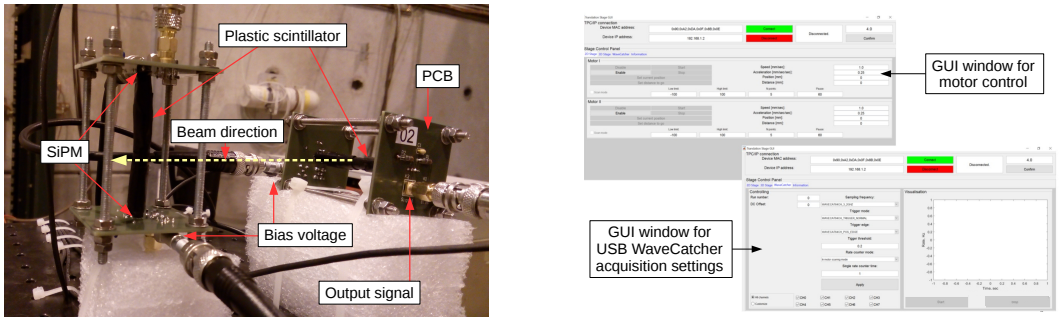

(a) Detector chain photo. Plastic scintillators are covered by a black tape from the outside light with SiPM sensors attached to each side.

(b) Graphical user interface of the acquisition system.

Figure 6.16: Experimental setup for the beam profile measurements.

A dedicated graphical user interface (GUI) based on Matlab and USB WaveCatcher libraries was developed in order to perform a remote control of the linear stages and data acquisition (Fig. 6.16b). After all setting the system made two linear scans (horizontal and vertical) in orthogonal directions to the beam axis in steps acquiring the number of coincidences between SiPMs at each pair.

The first alignment of the system was done by eye with respect to the beam pipe center. A 13 AGeV/c Xe ion beam with intensity of about 10^3 particles per SPS Spill (5 s of duration with 48 s of period) was used for the measurements in November 2016. Figure 6.17 shows the experimental results for each scan: 21 steps ($\pm$50 mm around the approximately beam center) with 120 sec of acquisition in each point. The mean values of the scans are equal to the beam center position in the

[1] https://www.ge.infn.it/~sicca/MegaMeg/SiPM_PM3350_STD_Trench_Datasheet_rev02.07.2012.pdf

[2] https://docs-emea.rs-online.com/webdocs/10eb/0900766b810eb7d7.pdf

translational stage coordinate system. The errors of the fit parameters affected by the low beam intensity and short acquisition time.

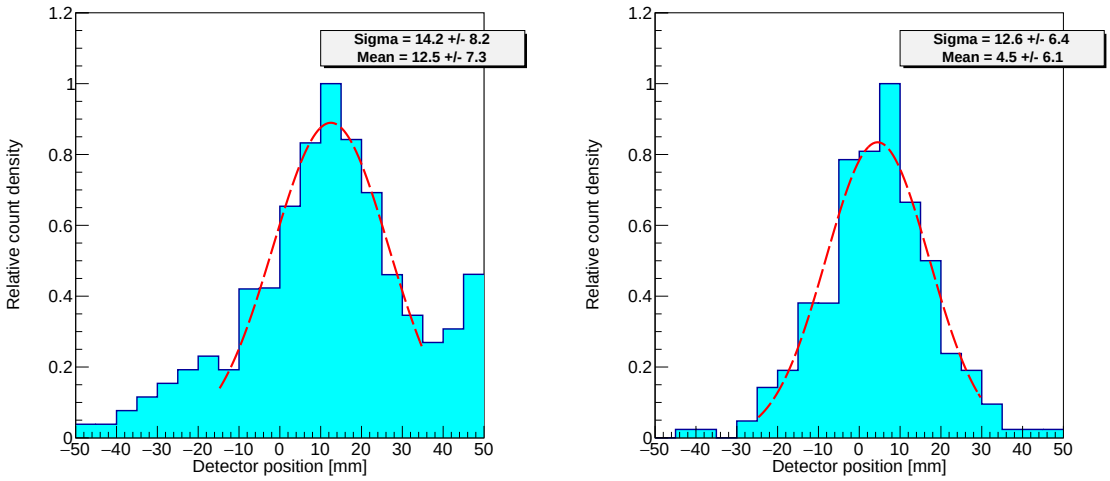

(a) Horizontal scan.

(b) Vertical scan.

Figure 6.17: Transversal profile of the 13 AGeV/c Xe ion beam at H8, measured by the profilometer. Red dashed line is a fit done with a Gaussian distribution function.

We have shown that using the system described above we are able to find a incident beam position (with a certain accuracy) for the fast detectors alignment.

6.2.3.2 Timepix and CpFM synchronization

To check the synchronization of the CpFM and Timepix detectors, a very fast test was performed at H8 beam line with 180 GeV/c pion beam. Both detectors were aligned with respect to the beam center, placed around 1 m from each other. A plastic scintillator located in front of the system was used as an external trigger. The Timepix detector used in ToA mode with 12 MHz (83 ns) clock and 1 ms of acquisition window, while the CpFM (Cherenkov fused silica radiator with attached PMT at the edge of the bar) was read by the GaGe COBRA electronics[3], operated with 1 GS/s sampling rate and 4 ms of acquisition window.

Figure 6.18a shows the time difference between each particle from the CpFM and every particle detected by the Timepix within correspondent frame (event). As a result one can see the Gaussian distribution with a standard deviation (sigma) of 180.5±11.6 ns, which corresponds to the detectors synchronization with a constant time delay of 8.88±0.02 μs (a mean value of the distribution). Due to the slightly

[3] `https://www.emona.com.au/products/electronic-test-measure/data-acquisition/`

misaligned (in space) detectors and different size of the sensitive area, the counted number of incident particles will be different with a linear dependency (Fig. 6.18b).

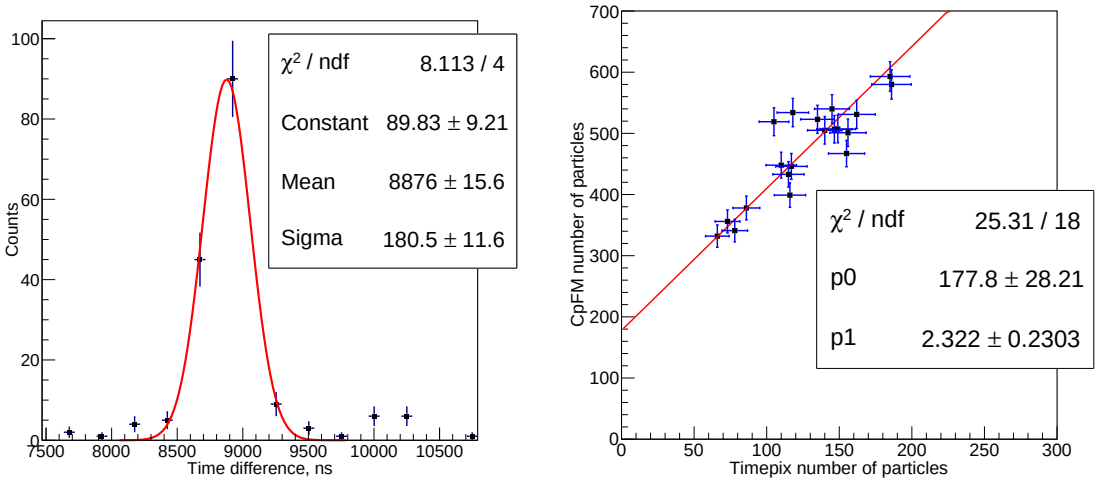

(a) Time difference between particles measured by the CpFM and Timepix detectors. Red line is a fit done with a Gaussian distribution function.

(b) Correlation between registered number of particles by CpFM and Timepix detector for 20 acquisition frames. Red line is a fit done with the first order polynomial function: CpFM=p0+p1·Timepix.

Figure 6.18: Timepix and CpFM detector synchronization at H8 beam line with 180 GeV/c pions.

6.2.3.3 Timepix telescope

The measurements of the crystal parameters, such as deflection efficiency, inelastic nuclear interaction probability, are very important for the future bent crystal applications and needs the track reconstruction. Thus, in April 2018 we decided to construct a short range (1.2 m long) tracker system based on 2 Timepix and 2 Quadpix (Timepix with the 4 times bigger sensitive area with 512×512 pixels) sensors to be compared with the main CMS like tracker system [46], already installed on the beam line. The idea to use the Timepix detector as a sensor for the particle telescope is not new [100, 101], but here the performances of our system are described. Figure 6.19 shows the experimental layout, which has been installed at the H8 beam line with a 180 GeV/c pion beam. The system was placed on the motorized translation stage (Subsubsection 4.1.1.1), which gave a possibility to align the telescope with respect to the particle beam.

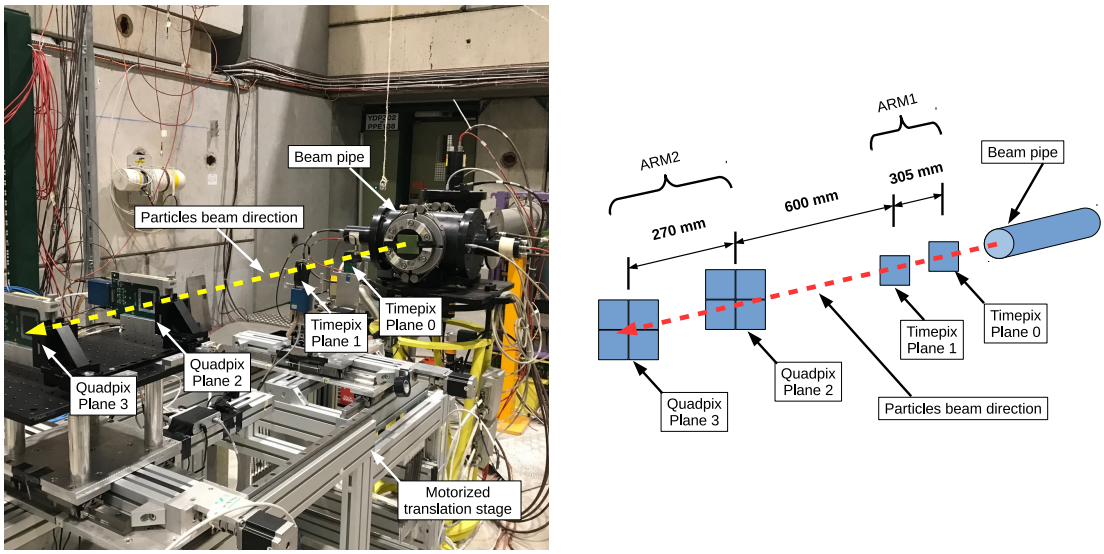

(a) A photo of the experimental setup.

(b) A principal scheme of the setup.

Figure 6.19: Experimental layout of the Timepix telescope.

Triggering and synchronization A plastic scintillator placed on the beam line was used as a trigger. The scintillator gave a signal per each crossing particle. The maximum DAQ rate of the system, which consists of 4 detectors, driven by the Python script, is about 2 Hz (2 acquisition frames per second for each detector) or 500 ms of the time delay between two consecutive frames, that can be improved for the future. To be sure that all detectors are starting from the same trigger signal and that they are all ready to collect the data a delay of 1 s between two trigger signals was applied. Once all Timepixes are configured, we send a command simultaneously to all detector to be ready for the acquisition and wait for the arriving of the trigger signal. In such a way we provide the time synchronization between detectors.

To estimate the order of the synchronization, we calculate the time difference between clusters from different sensors for the the same frame, taking one of them as a reference (e.g. the Timepix at the Plane 1 (see Fig. 6.19)). Figure 6.20 shows the typically distribution of the time delay between detectors in ToA mode with 48 MHz clock. Taking into account the mean value of each histogram, one can see that the time shift between Plane 1 and Plane 0 is ∼7.7 ns (Fig. 6.20a), between Plane 1 and Plane 2 is ∼30.2 ns (Fig. 6.20b), between Plane 1 and Plane 3 is ∼20.7 ns (Fig. 6.20c). Therefore, we can define that the synchronization between all 4 detectors is within 2 internal clocks for 48 MHz (∼20.83 ns).

Alignment A software alignment procedure based on particle tracks is used to calculate misalignments between sensors. In such a way the position of the hits

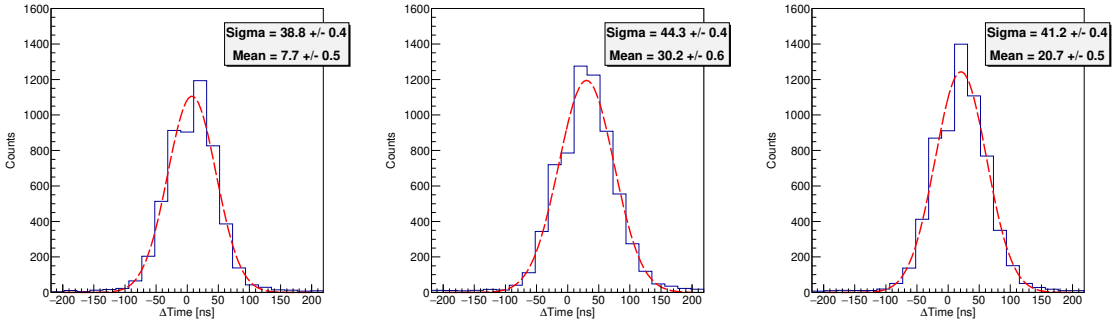

(a) Time difference between Plane 1 and Plane 0. (b) Time difference between Plane 1 and Plane 2. (c) Time difference between Plane 1 and Plane 3.

Figure 6.20: Time synchronization between 4 detectors. H8 beam line data with Timepixes in ToA mode and 48 MHz clock.

on each plane can be corrected. The (x,y) origin of the system was placed in the center of the beam spot. Fitting the track with the straight line we can calculate the residual (difference between hit position and interpolated position on the plane from the fit) of each sensor, taking into account the standard deviation in each pixel as $\sigma_p = p/\sqrt{12}$, where p means a pitch of the pixels (0.055 mm). Iterative position corrections are made in order to center the distribution of the residuals around zero (Fig. 6.21). To eliminate the rotational misalignment of the sensors around the axis of the beam direction (Z-axis) we use the correlation between residual position in X-axis and interpolated impact position in Y-axis for each plane.

Table 6.3 represents the iterative residual standard deviation (σ_r) and the twist angle (ϕ_{twist}) of each plane.

	Axis	Plane 0	Plane 1	Plane 2	Plane 3
σ_r [μm]	X	17.3	12.5	13.8	12.9
	Y	6.6	8.5	7.9	7.0
ϕ_{twist} [μrad]	Z	-141±85	-14±106	69±139	23±100
σ_d [μm]	X	17.7	12.5	13.8	13.3
	Y	7.3	8.5	7.9	7.9

Table 6.3: Standard deviation of the residual distribution (σ_r) in the plane transverse to the beam direction, the twist angle (ϕ_{twist}) around Z-axis of the tracker planes and the estimated resolution of each detector (σ_d).

Tracks reconstruction Following the alignment procedure and time synchronization discussed above, the particle track reconstruction has been performed.

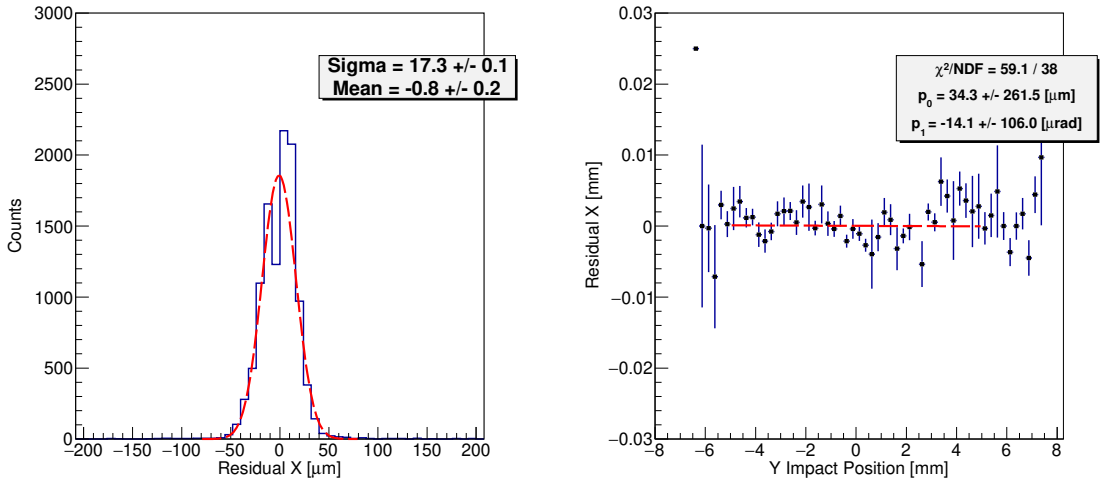

(a) Residual distribution in X direction for Plane 0 and the fitted Gaussian (red dashed line).

(b) The mean value of the residual in X-axis as a function of the estimated impact position in Y-axis for Plane 1. The fit (red dashed line) is done using the the first order polynomial function: $f(x) = p_1 x^1 + p_0$.

Figure 6.21: Spatial alignment characteristics of the telescope.

We may assume that in the future the crystal under investigation will be placed between Plane 1 and Plane 2, 300 mm from each plane (Fig. 6.22, a wide black solid vertical line). It means that the upstream section of the tracker (ARM 1), which consists of the Plane 0 and Plane 1, measures the incoming particles tracks, at the same time the outgoing tracks are measured using the downstream section (ARM 2), which is made of Plane 2 and Plane 3. To measure the error of the system in this configuration we have to take into account the not negligible scattering in the sensor and its resolution.

The estimated detectors resolution was calculated as $\sigma_d = \sqrt{\sigma_r^2 + \sigma_f^2}$, where σ_r is determined from the residual distribution, σ_f includes the errors due to the scattering as described in [102]. The results can be found in the Table 6.3. According to [100], each plane contributes 300 μm thick silicon sensor, a Timepix chip (700 μm thick) and a PCB with 100 μm of copper and 1.3 mm of FR4, the angular error per plane due to the scattering is ~10.5 μrad for a 180 GeV/c pion beam. The spatial resolution of the detectors is very close to the digital resolution of $\sigma_p = 15.88$ μm.

The main parameters of the track reconstruction (Fig. 6.22) are θ_{in} (incoming angle), θ_{out} (outgoing angle) and d_0 (impact parameter at the crystal position).

Figure 6.23 shows the angular resolution of the telescope for both horizontal and vertical projections, measured as the angular deviation between incoming and

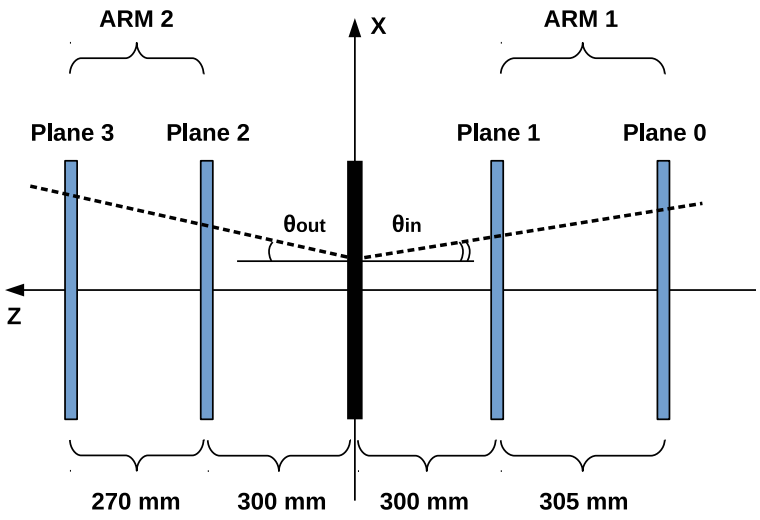

Figure 6.22: Track reconstruction scheme. θ_{in} and θ_{out} are the incoming and outgoing angles, respectively, at the crystal position (black rectangle).

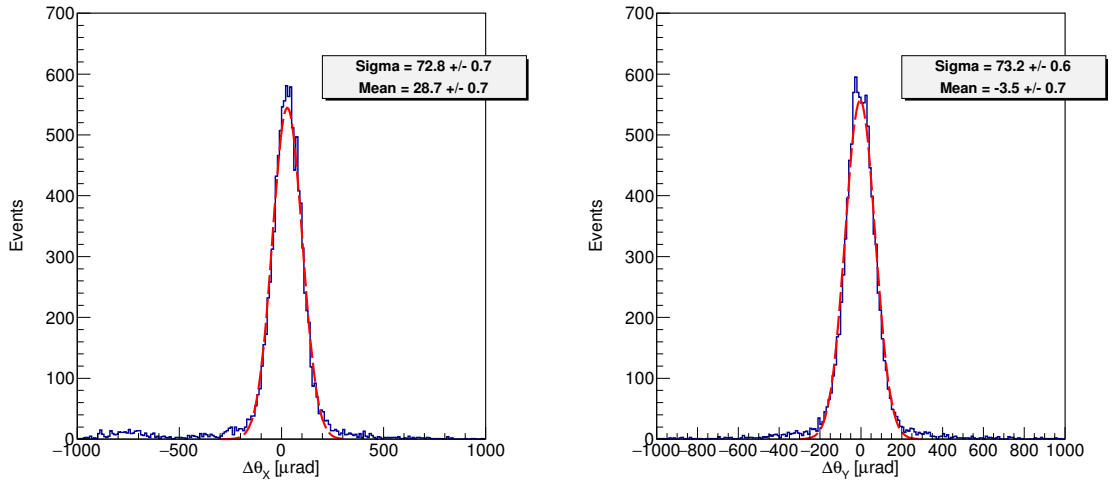

(a) In horizontal plane.

(b) In vertical plane.

Figure 6.23: Angular resolution ($\Delta\theta = \theta_{out} - \theta_{in}$) of the telescope in the plane transverse to the beam direction. Red dashed line is a fit done with a Gaussian distribution function.

outgoing tracks, reconstructed by the upstream (ARM 1) and downstream (ARM 2) arms of the system. Only single track events were taken into account. The measured angular resolution (Sigma) is around 73 μrad in X and Y axes and the angular misalignment (Mean) between two arms of the telescope is around 30 μrad and 4 μrad in horizontal and vertical planes respectively. The increasing of the telescope length can linearly decrease the value of the angular resolution up to the physical limitation of about 10.5 μrad, which is related to the multiple scattering inside each sensor [100, 103].

To estimate the track reconstruction efficiency we can use the number of reconstructed tracks, number of recorded frames and DAQ rate (can be improved). Taking into account the flux of the particles ($\sim 10^5$ p/s), the calculated value of the efficiency is around 10 % of the total incoming particles.

Figure 6.24 illustrates a distribution of the detector efficiency as a function of the distance from the projected point, by means of the track reconstruction, and a real hit on the sensor (residual). It can be seen that at certain residual value (up to 0.5 mm) the efficiency of the detectors becomes to be higher that 90%. However, for one of the Quadpixes, the maximum efficiency is about 70%, which is due to the higher number of masked pixels and applied threshold, which was not optimized for such a measurement.

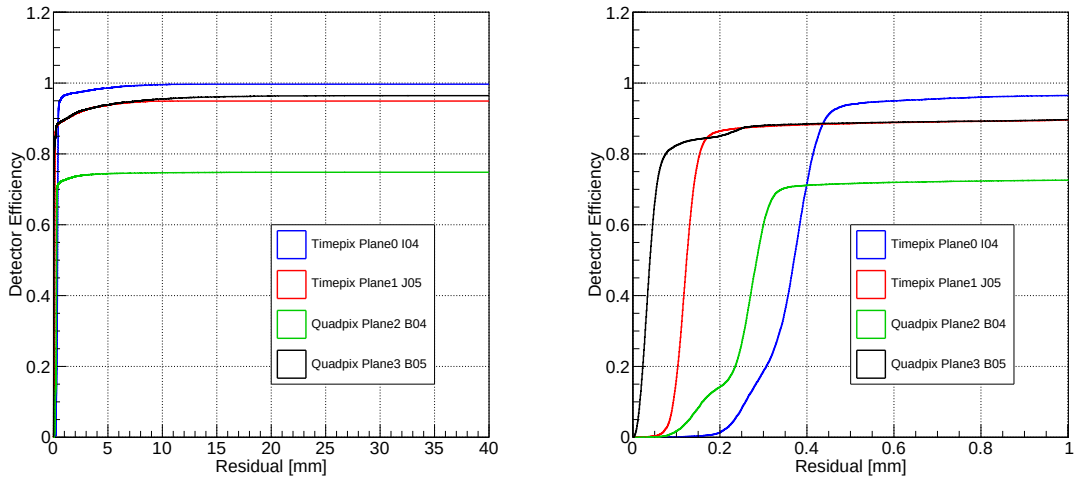

(a) Measured distribution.

(b) Measured distribution (zoomed in).

Figure 6.24: Timepix detector efficiency as a function of the residual value (distance from the projected point from the track reconstruction and a real hit on the sensor).

6.3 SPS beam extraction

Beam extraction from the accelerating machine is a well-known issue for physicists. A complicated beam transport system has to be used to inject and extract the particle beam from the accelerator, avoiding particle losses as far as possible [30] and place them onto the correct trajectory, with the right phase space parameters. Staying in front of these complexities, scientists and engineers have developed several techniques of the beam extraction. Hereby, we will briefly discuss only some of them [104]:

1. Single-turn (fast) extraction.
2. Non-resonant multi-turn extraction.
3. Resonant multi-turn (slow) extraction.

The fast extraction (Fig. 6.25a) of the beam is applied at the accelerator machines by powered a fast kicker magnet in about 10-100 ns rise and fall times. In such a way the entire beam is bumped into the extraction channel, where a septum (plural Septa) is located. The septum is a device which has two regions: a field-free and uniform field (electric or magnetic). The latter is used to deflect particles into the injection or extraction channel, while the field-free region does not influences the circulating beam at all. There are different types of septum, depending on the application: electrostatic septum, direct drive pulsed magnetic septum, direct drive DC magnetic septum, eddy current septum, Lambertson septum, etc.

Non-resonant multi-turn extraction (over a few turns (Fig. 6.25b) is used, for example, for the CERN SPS filling from the PS accelerator. The mechanism of the extraction is the following: a fast bumper magnet deflects the whole beam onto the septum and some part of the beam (e.g. 1/5 for CERN PS to SPS) is "shaved" off at each machine turn, while the machine tune is rotating the beam in the phase space. To minimize the losses during the extraction, a thin septum is required. The thinnest one is an electrostatic septum (ES) (Fig. 6.26). The circulating beam passes through the field-free part of the septum, while the extracted beam is moving on the other side of the septum, deflecting by an electric field in perpendicular to the initial direction. Usually the device is located in a vacuum tank, which is often fitted with a translational stages, which give a possibility to align it with respect to the beam direction. The typical electrode length of the septum is about 3 m, the electrostatic gap (d) is varying between 10 and 35 mm with a voltage up to 300 kV and field strength up to 10 MV/m. The septum foil can be done of Molybdenum (for CERN PS) or Tungsten wires (for CERN SPS) with a thickness less than 100 μm.

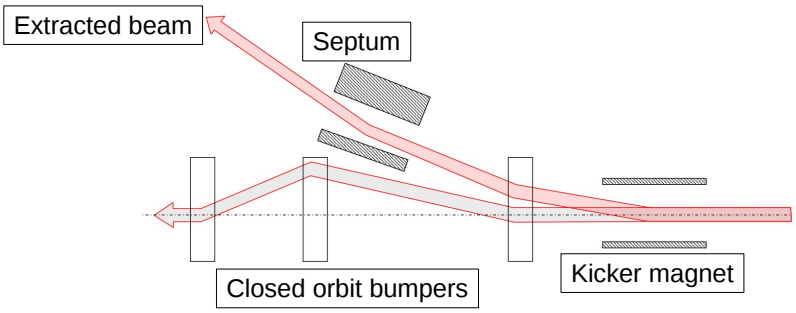

(a) Fast single turn beam extraction scheme.

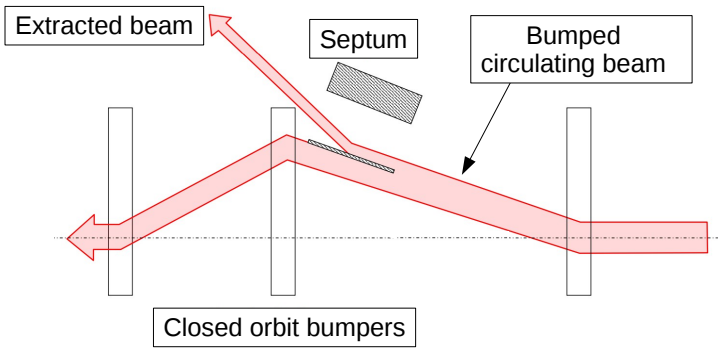

(b) Non-resonant multi-turn extraction scheme.

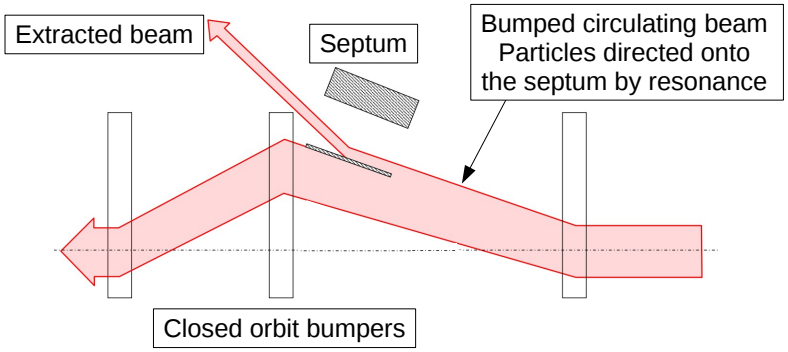

(c) Resonant multi-turn extraction.

Figure 6.25: Beam extraction technique.

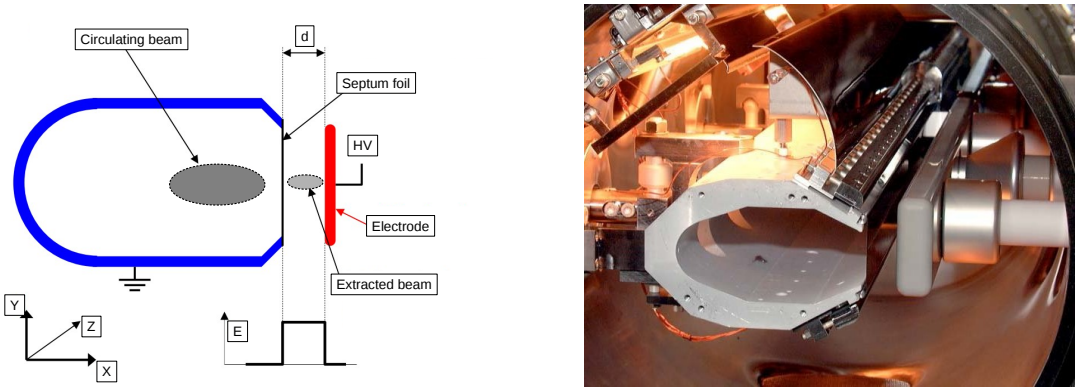

(a) Principal scheme.

(b) Photo of the CERN PS septum.

Figure 6.26: Electrostatic septum.

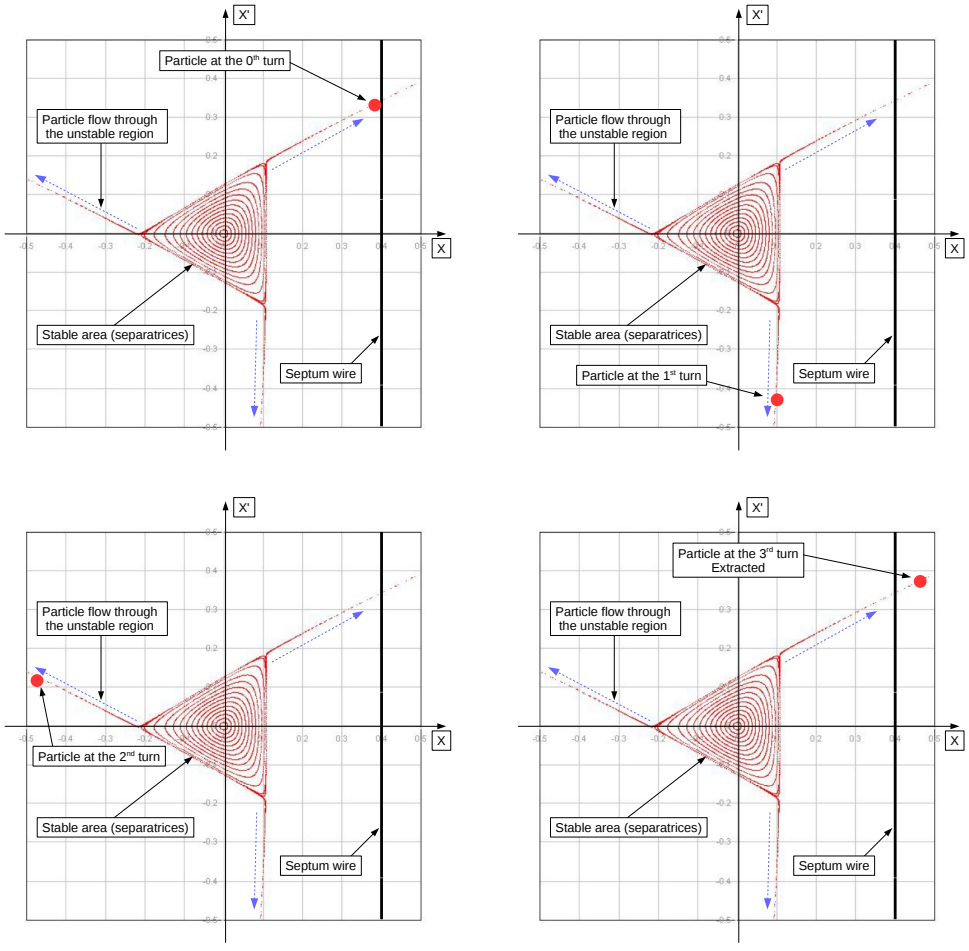

Figure 6.27: Phase space at the ES entrance.

To send a beam from the circular machine to experiments a resonant multi-turn extraction (Fig. 6.25c) is used. The time of the extraction can vary from 10^{-3} s to 10^4 s (which is called Spill). Slow bumpers excite betatron resonances with non-linear fields (sextupoles magnets) excite betatron resonances, which drive the beam (a bunch of particles) slowly across the septum: this is often a third-order resonance extraction of the large amplitude particles. For instance, at CERN SPS accelerator, to extract a constant flux of 10^{13} protons with momentum of 450 GeV/c to the fixed target experiment at North Area, it takes about 4.8 s, i.e. over 200000 machine turns. Figure [105] shows a typical phase space of the beam during the third-order of the resonance extraction. A triangular stable area (separatrices) in the phase space is produced by dedicated sextupole magnets, while through the unstable sections particles go with a large amplitude (Fig. 6.27). After the third turn they are captured by the septum and extracted from the machine. The part of the unstable beam, which interacts with septum wires, produces losses and leads to the inefficiency of the extraction.

6.3.1 Crystal-assisted beam extraction

Since 1990s the possibility of extracting high-energy particles from the accelerating machine by means of silicon bent crystals has been investigated. The main idea is to use a channeling effect to deflect particles from the main beam with further direction them onto internal components such as an absorber or additional deflecting devices for extraction from the machine. As reported in [106] by the RD22 collaboration, a diffusion extraction of 120 GeV/c coasting beam has been demonstrated at the CERN SPS. A demonstration of the TeV-scale particle beam extraction from a superconducting accelerator with a bent crystal in the course of collider operation has been done by the E853 collaboration at the Fermilab Tevatron in the early 2000s [107]. In the same time, a study of the high-efficiency beam extraction with a very short bent crystal has been carried out at the U-70 accelerator in Protvino, which provides a crucial support for implementing crystal-assisted slow extraction and collimation in the machine like the SPS or LHC [108].

In the last 3 years the UA9 collaboration studied a crystal based slow extraction technique for the SPS and LHC. The theoretical studies by simulation for the crystal based on the diffusive and orbit bump non-resonant slow extraction at the SPS for 270 GeV/c proton beam can be found in [109] for the experimental setup described in [110, 111]. The simulation has shown that the condition for the high efficient beam extraction from the accelerators with a bent crystal is a small divergence of the beam incident onto the crystal [109]. It can be fulfilled using the transverse

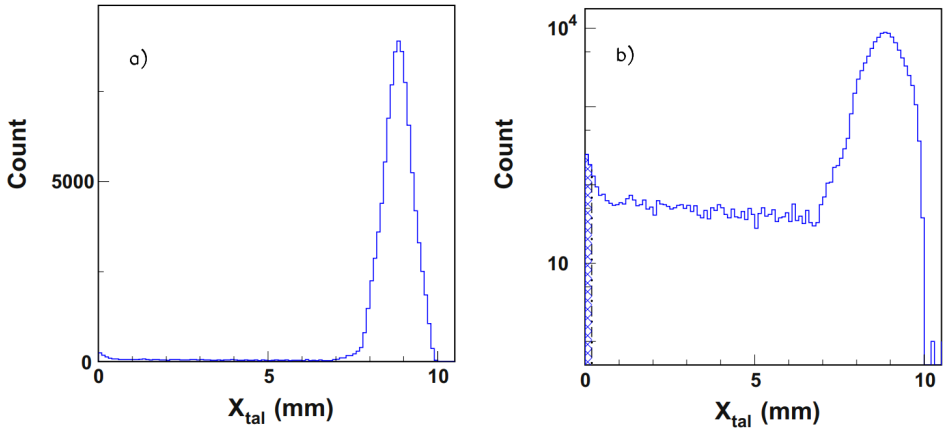

Figure 6.28: The case of the transverse diffusion. The distribution of protons in the impact parameters with the collimator-absorber (extraction septum). (a) linear scale, (b) logarithmic scale. The maximum on the right is the channeled fraction.The narrow dashed part on the left shows particles, which hit the septum wires (0.2 mm thick). The particles between are dechanneled ones, which obtained deflection angles in the crystal sufficient to be extracted. From [109].

diffusion (Fig. 6.28) or the optimal orbit bump (Fig. 6.29) for delivering the whole circulating beam onto the crystal. 99 % of the extraction efficiency can be reached with the considerably reduced irradiation of the septum wires.

A new technique of the resonant slow extraction assisted by a bent crystal is discussed in [112]. The idea is to use a bent crystal to shadow septum wires, installed immediately upstream of the SPS electrostatic extraction septum (ZS). The crystal intercepts particles in the separatrix that otherwise would hit the wires of the ZS (Fig. 6.30), and deflects them into the extraction channel, well inside the ZS aperture. The local beam loss and the debris produced by ZS wires will be thus reduced, and shifted in a safer area of the accelerator. In the same time, crystal can be used to deflect totally all the particles to be extracted, giving them a similar angle as the ZS.

6.3.2 Crystal-assisted slow extraction results

Since the beginning of the LHC operation in 2008, the SPS accelerator was working with the Q26 beam optics tune, and after a set of investigations and studies it has been switched to the Q20 tune since September 2012 [113]. This optics was applied in order to remove intensity limitation in the SPS. It opens the way for ultra-high brightness beams to be delivered in the high-luminosity LHC era for protons

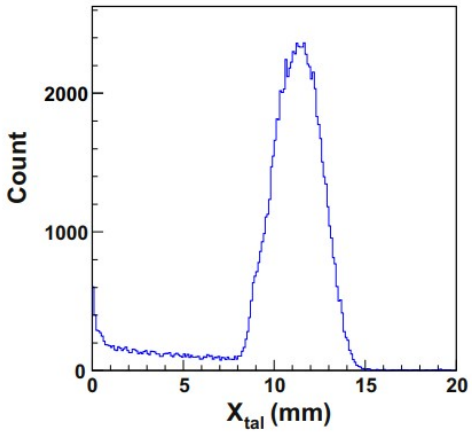

Figure 6.29: The case of the parallel bump. The distribution of protons in the impact parameters with the collimator-absorber (extraction septum). From [109].

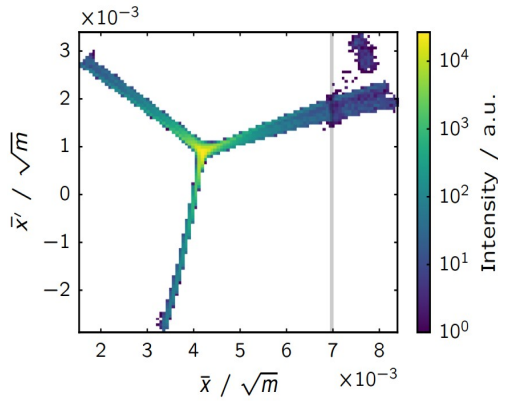

Figure 6.30: Simulations of the expected normalised phase-space at the ZS for a resonant crystal assisted slow extraction. A vertical grey line shows the crystal and septum wires position in the phase-space. From [112].

and eventually for ions [114, 115].

In 2016, for the first time at the SPS, the non-resonant crystal-assisted slow extraction of a 270 GeV/c proton beam from the accelerator into the extraction channel TT20 in the Long Straight Section 2 (LSS2) has been demonstrated by the UA9 collaboration and Accelerator Beam Transfer (ABT) group at CERN [116]. A silicon crystal with 175 ± 2 μrad of the bending angle was aligned at 6σ from the beam core. In the experiment a single-bunch with 1.6×10^{10} protons circulated in the machine with Q26 ($Q_x = 26.62$, $Q_y = 26.58$) optics, while the crystal deflected halo particles at the ZS on the second turn, with a fractional phase advance of 252°. Figure 6.31 shows the extraction scheme, where the channeled beam performs almost 41 betatron oscillations before reaching the ZS.

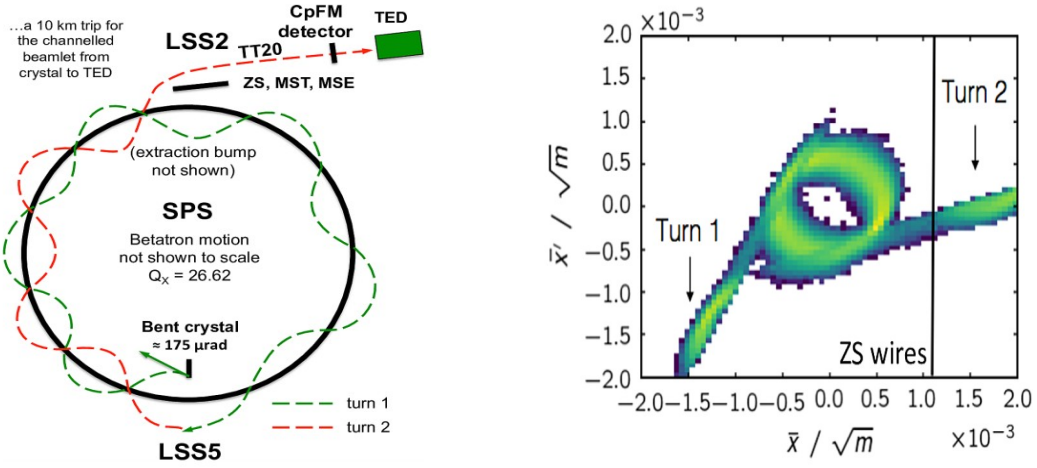

(a) Channeled beam trajectory drawing, where TED is an extraction dump.

(b) Simulation results of the beam distribution (hollow halo approximation) at ZS with normalised phase space.

Figure 6.31: Experimental setup of the crystal-assisted extraction scheme at the SPS. From [116].

A dedicated SE-CpFM (Slow Extraction-CpFM) detector [117], was installed in order to measure extraction rate in LSS2, while the indirect measurements carried out with the Timepix detector in LSS5. Figure 6.32 shows results obtained with SE-CpFM detector at LSS2. There are two position of the absorber (TACW) in LSS5, which is used for channeled beam stopping. When TACW is inserted the channeled beam is stopped at the first passage of the particles (Fig. 6.32a), while for the retracted position (parking position) of the TACW channeled particles at the 2nd turn reach the ZS and extracted in the TT20 beam line (Fig. 6.32b), where

they intersepted by the SE-CpFM detector. From Figure 6.32c it is clearly visible a changing of the extracted beam flux in LSS2 for different positions of the absorber in LSS5.

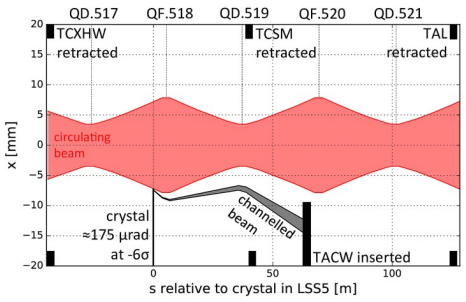

(a) LSS5 absorber configuration for the extraction: TACW in.

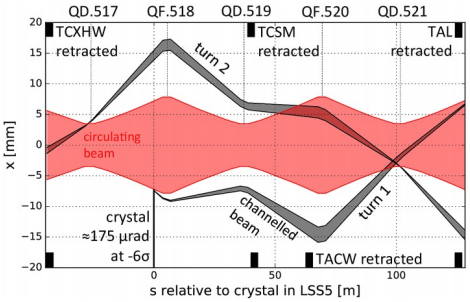

(b) LSS5 absorber configuration for the extraction: TACW out.

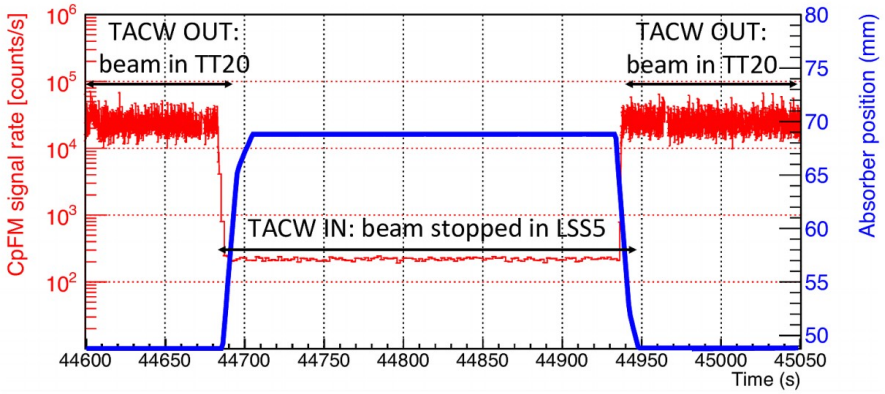

(c) TT20 SE-CpFM signal rate (red) versus TACW position (blue).

Figure 6.32: Extracted beam rate measurements at the TT20 line using SE-CpFM for two positions of the absorber. From [116].

To guarantee that the extracted beam was indeed channelled by the crystal, a Timepix detector in LSS5 has been used. Figure 6.32 shows experimental results obtained using the Timepix detector in LSS5, inserted in the channeled beam. For the turned off extraction bump and inserted absorber (TCXHW), which intercepts the deflected beam after its fourth pass, the channeled beam was captured by the Timepix detector on its third pass in LSS5 (Fig. 6.33a). After turning on the extraction bump, the channeled beam by the bent crystal disappeared from the Timpix image, which means that it was directed onto the septum and extracted into the TT20 (Fig. 6.33b). The Timepix results were confirmed also by the CpFM

detector.

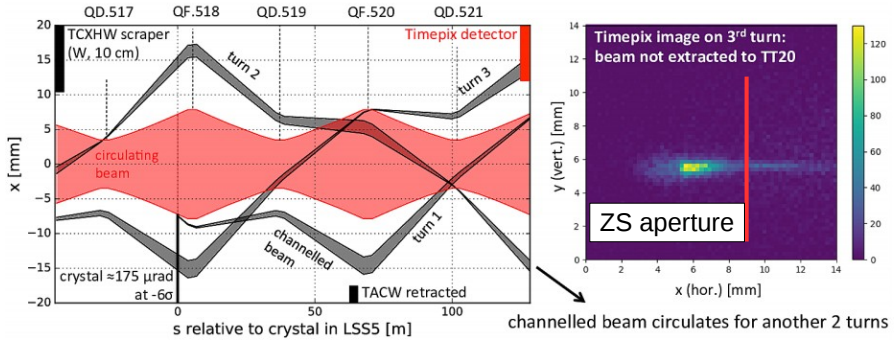

(a) Extraction bump OFF.

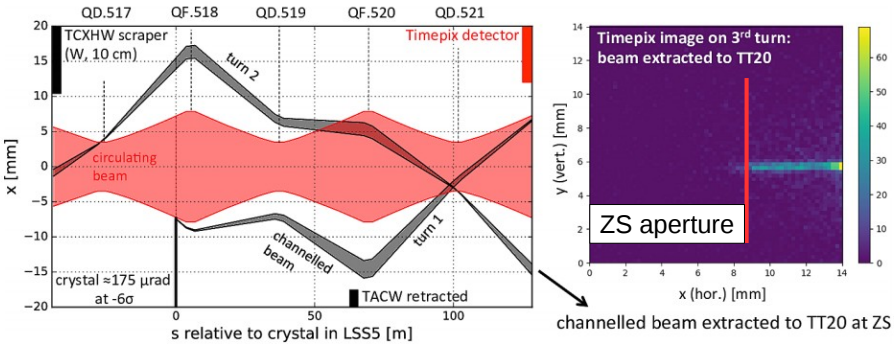

(b) Extraction bump ON.

Figure 6.33: Timepix images showing the disappearance of the channeled beam in LSS5, when extracted in LSS2. From [116].

Since the end of 2016 the UA9 experiment was mostly concentrated on the channeled beam characterisation in the LSS5 zone to improve the slow extraction technique at the SPS. Several MDs were dedicated for the measurements using the CpFM, Timepix and BLM detectors in the machine. The further materials in the Chapter will be focused on these measurements.

6.4 SPS crystals and channeled beam characterisation

6.4.1 Machine conditions and detectors operation

During specific MD runs UA9 experimental tests in the SPS are carried out several times per year. in this period the entire machine is devoted to the investigations of the collaboration. Usually the duration of each MD is not more than 24 hours, in which the accelerator is keeping in COAST (i.e. after the energy ramp there are no perturbations of the machine). The emittance of the beam is measured by a BWS as described above. The beam intensity and energy for each specific run will be listed below.

At the beginning of each run of the MD, with a new fill of the SPS, all devices, which take part in the measurements, has to be aligned with respect to the horizontal position of the beam core. After that all experimental devices are moving out to the parking position ($> 20\ \sigma$ from the main beam) with remaining only an oriented crystal in channeling as the first obstacle for the beam halo particles. Next, a linear scan of the CpFM is performed to measure the deflected particle beam profile and count the number of channeled high-energy particles. Considering the geometry of the detector, it will integrate the flux of particles crossing the bars during its movement from or to the main beam of the accelerator. A conceptual scheme of the linear scan is shown in Figure 6.34. Fitting the measured profile with an Error Function we can reconstruct the real beam profile and measure its size in the horizontal plane by a derivative of the distribution. In contrast, using the Timepix detector we can measure directly the profile of the deflected beam, like it was demonstrated for the Medipix detector in 2010 [118].

A reduced 1000 times common SPS trigger signal, which is synchronized with the machine RF cavities (43 kHz), is used by all UA9 experiment devices. The USB-WaveCatcher[4] connected to the PMTs for the CpFM readout, reads the detector output signal and every external trigger saves the software signal analysis results with the most important waveform parameters. Each channel includes a measurements block to extract signal properties online. It computes:

- the baseline which corresponds to the mean of the first 16 samples;
- the peak amplitude, relative to the baseline;

[4] `http://www.hep.ucl.ac.uk/pbt/wikiData/manuals/WaveCatcher/WaveCatcherFamily_V1.2.pdf`

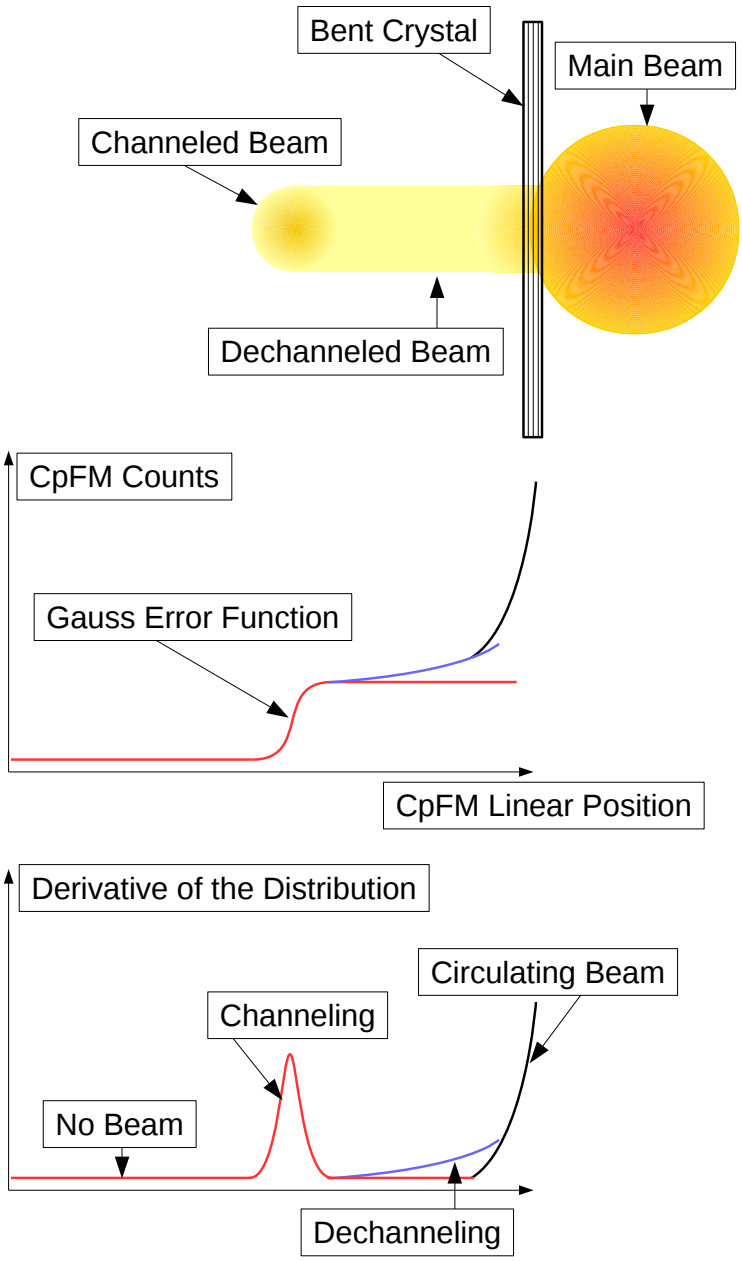

Figure 6.34: Conceptual scheme of the CpFM beam profile measurements. Top: the transverse XY-profile of the beam inside the beam pipe, where on the right is a main circulating beam, and on the left is a deflected particle beam by the bent crystal with a dechanneling region between the two. Middle: Counts of the CpFM detector along the linear scan. Bottom: A derivative of the measured distribution with reconstruction of the beam profile in the horizontal plane.

- the peak time (sample corresponding to the peak location);
- the charge contained in the signal (see below for the corresponding parameters);
- the time of the rising edge (can be the leading or the falling edge depending on pulse polarity);
- the time of the falling edge;
- the combination of the two edges gives the Time Over Threshold (TOT) of the signal;
- the rate of the signals (the absolute value of the pulses number per second), which exceed a given amplitude threshold. The rate counters work up to ∼400 MHz and, if this information is memorized long enough in the software along events, rate measurement can work as low as ∼0.1 Hz.

In the meanwhile, on each 10th trigger the device stores a whole waveform of the signal. Such a regime has been chosen for the reducing data storage space on a disk.

6.4.1.1 Waveform analysis

Since there are two possibilities of the data storing by using of the USB-WaveCatcher (USBWC), here we will briefly describe the analysis algorithm of the collected waveforms during the CpFM operation in the SPS. The logic of the waveform parameters computation is very similar to one, which is used for the DIRC-like TOF detector in [119]. At the first step of the analysis the polarity of each waveform is converted for convenience. Figure 6.35 shows an illustration of the signal with the most important computed parameters definition:

- The baseline is taken as the mean value of the first 16 samples.
- The amplitude (A) of the peak is computed as a maximum value of the waveform ($\max\{U(t_i)\}$) with a definition of the correspondent time: t_{max}.
- The time of the signal, which is corresponding to a constant fraction of 50 % from the peak amplitude: cft_{50}.
- The charge (Q) of the signal is proportional to the integral of the peak. The following formula [119] can be used for its calculation:

$$Q[in\ C] = \sum_{i=1}^{n} \Delta Q(t_i) = \sum_{i=1}^{n} \frac{U(t_i)}{R} \Delta t = K \frac{\Delta t[in\ ns]}{R[in\ Ohm]} \sum_{i=1}^{n} U(t_i)[in\ V], \quad (6.4)$$

where Δt is the USBWC time sampling, R is an input resistance of the device equal to 50 Ohm, $U(t_i)$ is the amplitude of the signal at a given time t_i, K is a dimensionless normalization constant (usually equal to about 10^{-15}), each waveform contains $n = 1024$ points. In our calculations we will just focus on the waveform integral for charge measurements ($\sum_{i=1}^{n} U(t_i)[in\ V] \cdot \Delta t[in\ ns]$) in arbitrary units (a.u.).

- The rise time of the signal, computed as the difference $cft^r_{90} - cft^r_{10}$ taken at the rising edge of the waveform.

- The fall time of the signal, computed as the difference $cft^f_{10} - cft^f_{90}$ taken at the falling edge of the waveform.

- The time width of the signal, computed as the difference $cft^f_{50} - cft^r_{50}$ taken at the falling and rising edges of the waveform respectively.

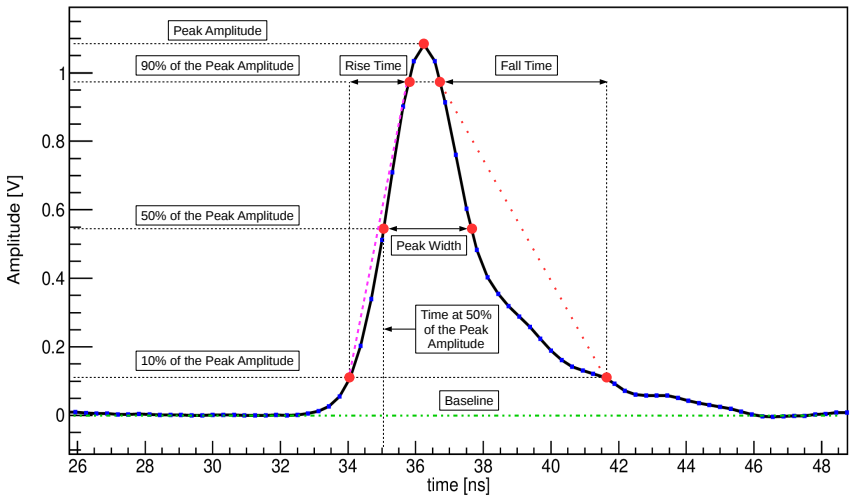

Figure 6.35: The most relevant waveform parameters definition (the signal is taken from the SPS run with 270 GeV/c channeled proton beam, USBWC time sampling is 312.5 ps). A black solid line with blue solid squares represents the signal waveform, while magenta dashed and red dotted lines illustrate rising and falling slopes of the signal respectively. A green dot-dashed line shows a level of the baseline defined as the mean value of the first 16 samples of the waveform. For the precise definition of the amplitudes and times (red solid circle), a linear extrapolation between two consecutive points of the waveform is used.

6.4.2 CpFM on SPS

6.4.2.1 Self-calibration with ions

Ion beam In 2016 a dedicated run with a Pb ion beam in the SPS has been conducted with CpFM detector to check its calibration parameters comparing with H8 and BTF beam lines results (see Section 6.2). The beam was done by 3 injections with 200 ns separation, each of which is consisted of 4 bunches with 100 ns spacing (Fig. 6.36).

The important parameters of the beam, which was used during the measurements, are listed in Table 6.4.

Beam	Momentum [ZGeV/c]	Intensity per bunch	Emittance [nm·rad]	Tune
Pb ion	270	$\sim 1.5 \times 10^8$	∼20	26.13

Table 6.4: Beam conditions during the measurements.

Data acquisition for the CpFM detector was performed in such configuration, where two fused silica bars intercepted the deflected beam (Fig. 6.37).

Due to the fact that PMT voltage supply polarity is negative, further in the text, we will indicate its absolute value for the convenience. Therefore, for the measurements, the operational high-voltage (HV) has been putted at 700 V on both PMTs with 163 μA of the flowing current. The second bunch of the first injection (Fig. 6.36b) has been chosen for the detector synchronization with about 30 ns offset, while 3.2 GS/s of the USBWC sampling frequency was setted for 320 ns of acquisition window, in order to see only three bunches of the first injection (Fig. 6.38).

Figure 6.39 illustrates experimental results of the CpFM detector measurements during UA9 MD at the SPS accelerator. The figure represents a measured charge of the waveform as a function of the input signal amplitude for both bars of the detector, subtracting the baseline according to Eq. 6.4:

$$\begin{aligned} &Amplitude = max\{U(t_i)\} - Baseline, \\ &Charge = (\textstyle\sum_{i=1}^{n} U(t_i) - Baseline) \cdot \Delta t. \end{aligned} \tag{6.5}$$

One can easily recognize several island-like regions on the distributions. Each region corresponds to the different amount of the Cherenkov light produced by charged particles in the fused silica bars:

- R0: for cases, when there is no incoming ion to the detector, the stored waveform corresponds to the electronics noise and a single photoelectron produced by the light from the environment.

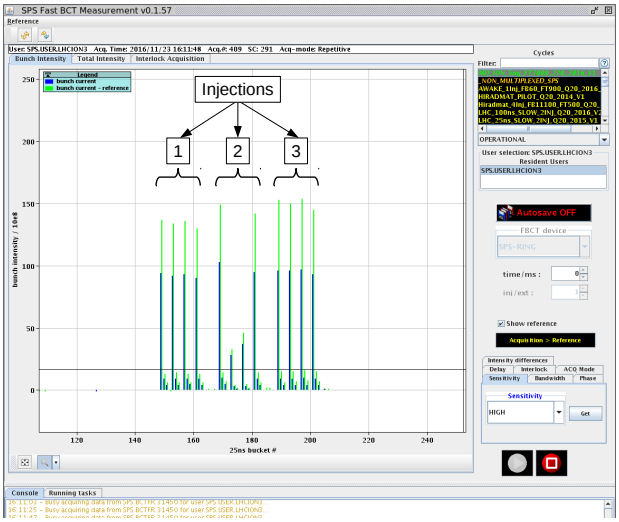

(a) A screenshot of the SPS operational Graphic User Interface (GUI) for the beam intensity measurements. SPS beam structure: 3 injections are formed of 4 bunches each with 100 ns spacing between each bunch and 200 ns between the injections. The results are received from the Fast BCT (FBCT) detector constructed to measure each bunch intensity circulating in the machine. Green columns represent a reference bunch structure, while blue columns correspond to the measured bunch intensity.

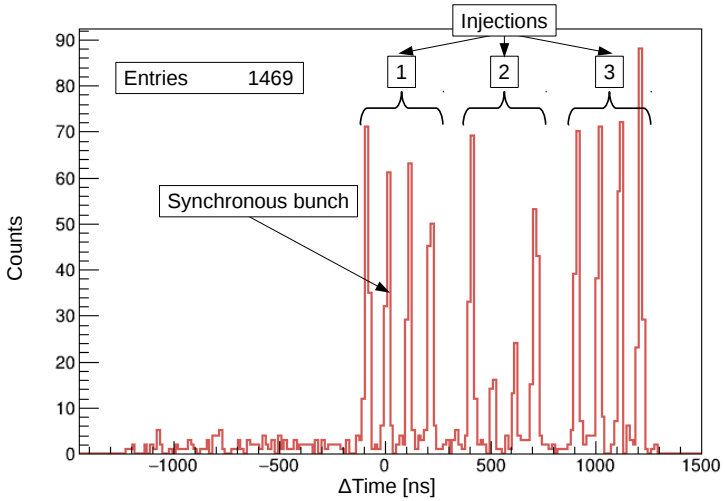

(b) Time difference between CpFM and trigger signals with applied cut of 6 mV for the amplitude. The measurements were conducted with 400 MS/s sampling frequency and 1 kV of the supply voltage for PMTs in the parking position.

Figure 6.36: SPS ion beam structure during the measurements. The time distribution obtained by the CpFM detector well describes the beam structure measured using the FBCT device.

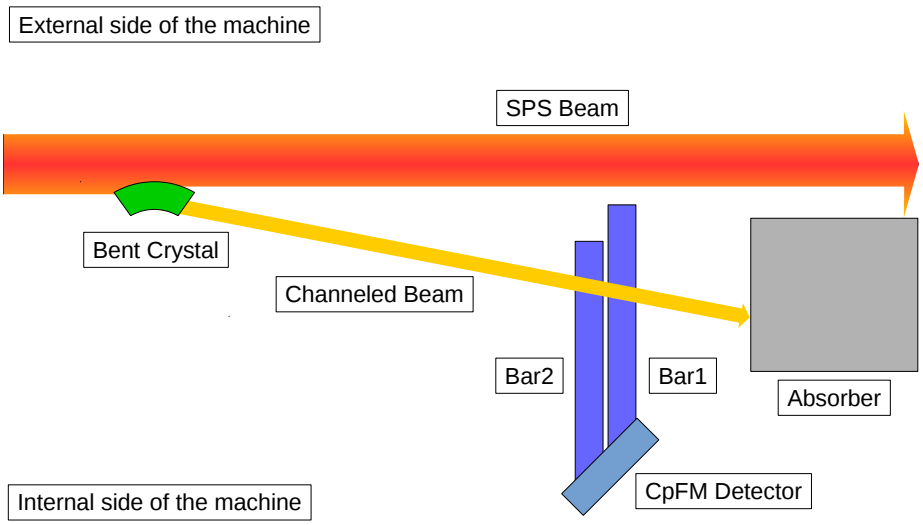

Figure 6.37: A scheme of the experimental configuration of the CpFM measurements in the SPS accelerator with lead ion beam in 2016. According to the detector geometry and position with respect to the main beam, the fused silica bar close to the beam is called Bar1 and another one is Bar2.

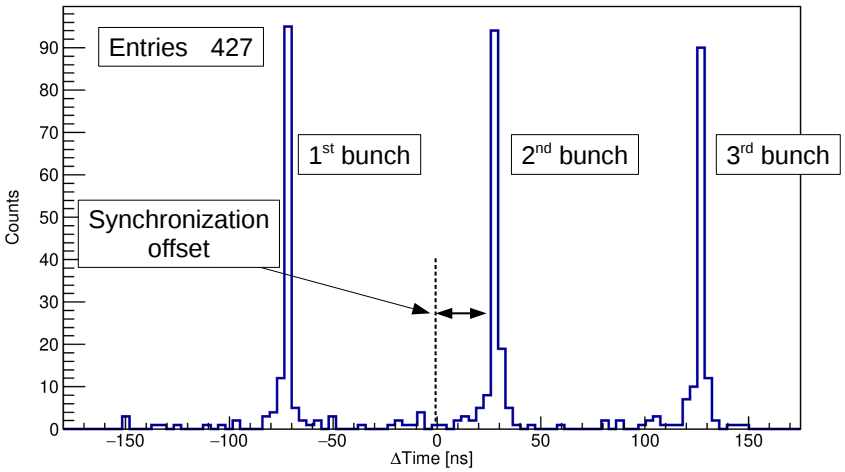

Figure 6.38: Time difference between CpFM and trigger signals with applied cut of 20 mV for the amplitude. The measurements were conducted with 3.2 GS/s sampling frequency and 700 V of the supply voltage for PMTs in a 320 ns acquisition time window.

- R1: a single ion per waveform. Due to the low intensity of the beam and short time acquisition window (covering only three consecutive bunches), the most probable value of the detected particles is one per machine revolution (23 μs).
- R2: two ions from the different bunches inside the same waveform (Fig. 6.40a). It is obvious, that for this case the amplitude belongs to one of the ions, while the charge is computed for the whole signal – doubling a single ion signal.
- R3: three ions from the different bunches during the same acquisition time window (320 ns). In this way, the amplitude remains unchanged, but the charge is tripled.
- R4: two ions per a waveform along the same bunch. Double of the amplitude and charge of a single ion signal.
- R5: three ions with a double and single peaks from different bunches (Fig. 6.40b).
- R6: one peak produced by three ions from the same bunch – tripling of the amplitude and charge.
- R7: four ions, where three of them are from the same bunch.
- R8: due to a large amount of the Cherenkov light and limited input dynamic range of the WaveCatcher, occasionally, a signal saturation happens. It leads to the cut shape of the waveform, constant value of the amplitude and charge.

The region between R0 and R1 islands belongs to different ion fragments with an atomic number smaller then Pb ion has ($Z = 82$), due to the smaller amount of the Cherenkov light produced in the radiator (Eq. 5.8): $N \sim Z^2$. This data can be used for beam contamination studies with different Z particles recognition. Due to the difference of the bars production quality, the amount of the light collected on each channel of the detector is not the same. It leads to different amplitude and charge for the same number of crossing ions. The mentioned issue will be discussed more detail later in the text.

Figure 6.41a shows a measured ion amplitude distribution for two fused silica bars. Due to the signal saturation on the CpFM Bar2 channel, a saturation peak of about 1.25 V is present as well. However, for Bar1 a two ions peak (at 0.544±0.004 V) is visible and its amplitude is about double of the single ion peak at 0.277±0.001 V (Fig. 6.41b), while for Bar2 the amplitude corresponds to one ion is about 0.989±0.001 V (Fig. 6.41c).

For better ions separation we applied an amplitude cut before to plot the charge distribution, in order to do not mix a single and double ion crossing through the bars

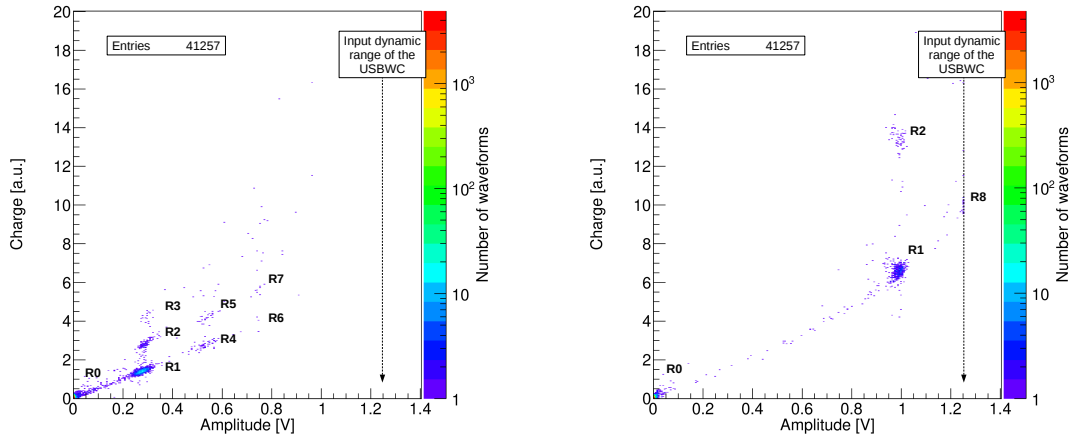

(a) CpFM Bar1.

(b) CpFM Bar2.

Figure 6.39: Waveform charge as a function of the maximum signal amplitude. Experimental results of the measurements done using the CpFM detector at HV = 700 V, inserted in the channeled ion beam during the SPS MD in 2016. The USBWC input dynamic range was setted from -1.25 V to +1.25 V. In color (Z-axis) is represented the number of the analysed waveforms. Regions definition: R0 – signal pedestal (no incoming ion); R1 – one incident ion per waveform per bunch; R2 – two ions from different bunches hit the detector within the acquisition window of 320 ns; R3 – three ions from different bunched on the same waveform; R4 – two ions from the same bunch (double amplitude and charge from R1); R5 – three ions: two of them are from the same bunch, and one from another bunch within a single waveform; R6 – three ions from the same bunch (three time of the single ion amplitude and charge); R7 – four ions: one is triple (R6), and one – single (R1); R8 – saturation region, where all signals are summed with the same amplitude, which is equal to the dynamic range of the USB-WaveCatcher (±1.25 V). Since CpFM Bar1 is located closer by 5 mm (6 σ) to the primary beam core with respect to Bar2, therefore the number of signals corresponding to a crossing ion for Bar1 is bigger.

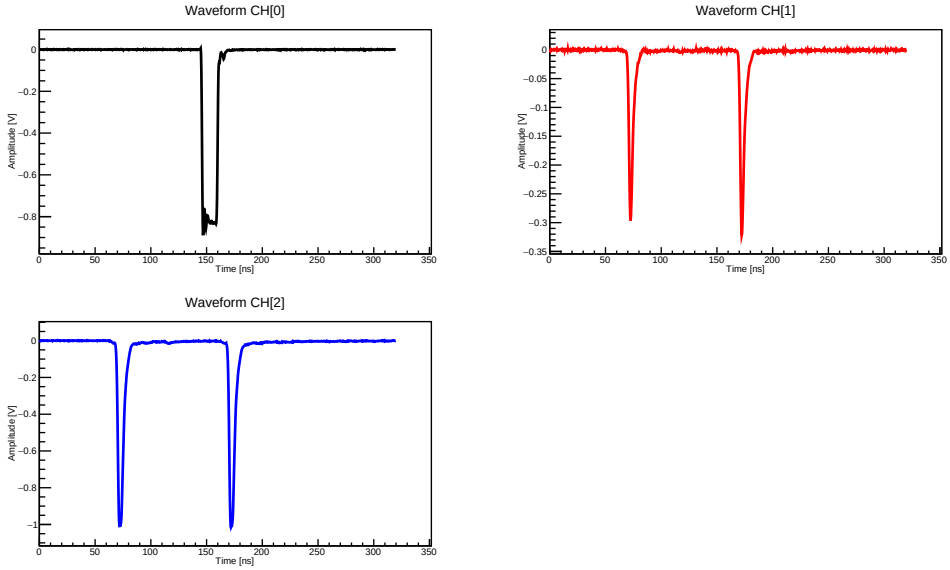

(a) The event, which illustrates the R2 region of the Charge-Amplitude distribution (Fig. 6.39). Each peak represents a single ion per bunch.

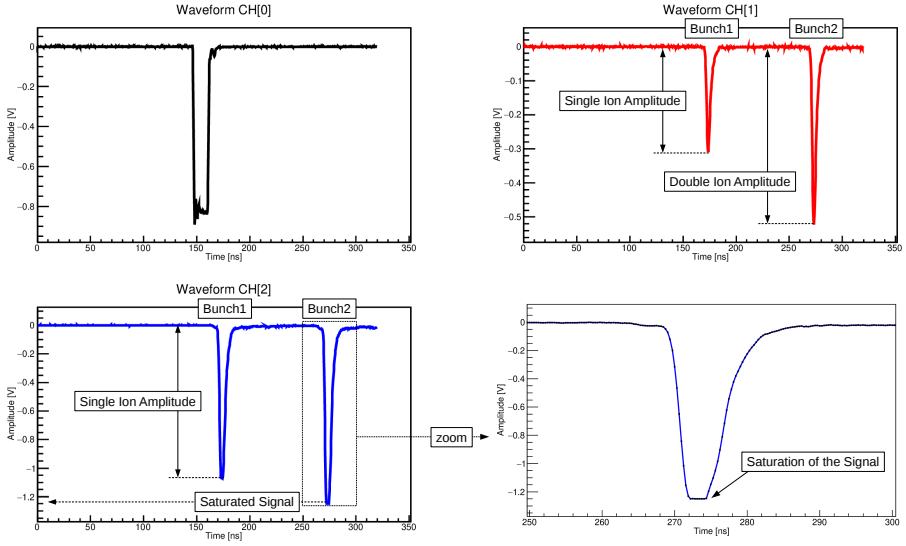

(b) The event of the R5 region, where there is a signal amplitude saturation on the CpFM Bar2 readout channel for the double ion beam. Bottom right plot shows a zoomed picture of the saturated peak waveform with a well visible flat shape (-1.25 V).

Figure 6.40: Raw data of the measured waveform for WaveCatcher channels, where CH[0] corresponds to the SPS trigger signal (top left), CH[1] – CpFM Bar1 (top right), and CH[2] – CpFM Bar2 (bottom left).

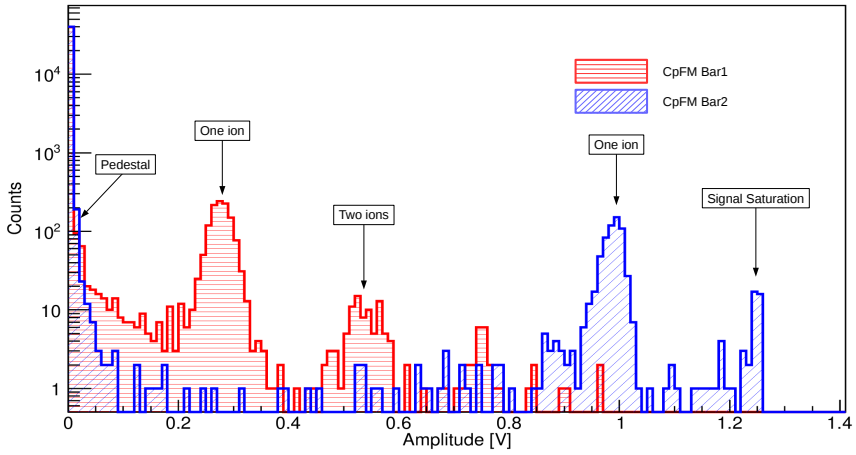

(a) Distribution of the amplitude for CpFM Bar1 and Bar2 signals (log scale in Y-axis).

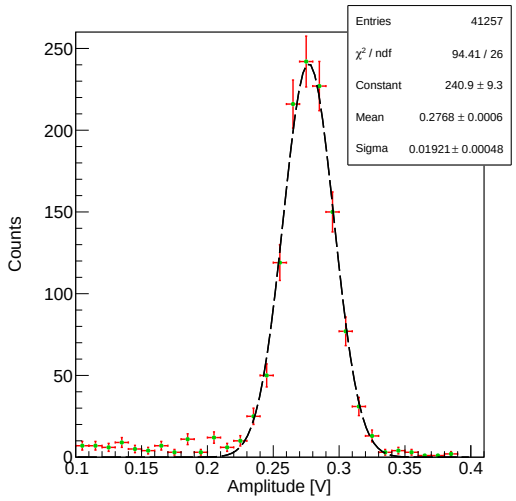

(b) Single ion amplitude distribution for CpFM Bar1.

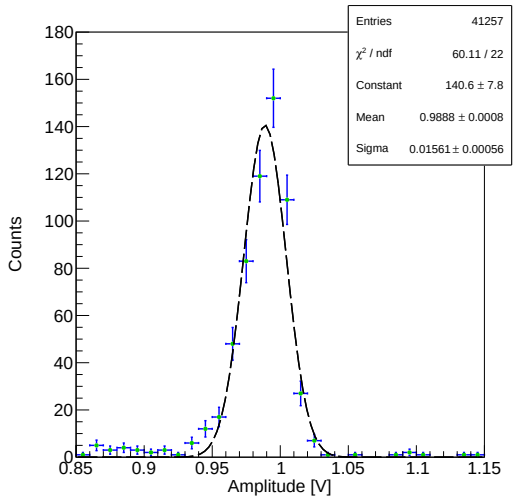

(c) Single ion amplitude distribution for CpFM Bar2.

Figure 6.41: Experimental results of the CpFM signals amplitude measurements, where HV = 700 V, sampling frequency = 3.2 GS/s, USBWC dynamic range = ±1.25 V. A Gaussian distribution function is used for the data fitting (black dashed line).

per bunch. Therefore, Figure 6.42a shows the charge for each waveform, where the amplitude (positive polarity) does not exceed a value of 0.4 V and 1.2 V for CpFM Bar1 and Bar2 respectively. For the value of the two ions charge (at 2.815±0.025 a.u. and 13.518±0.099 a.u) is about two times of a single ion, which is 1.362±0.004 a.u and 6.667±0.012 a.u. for CpFM Bar1 (Fig. 6.42b) and Bar2 (Fig. 6.42c) respectively.

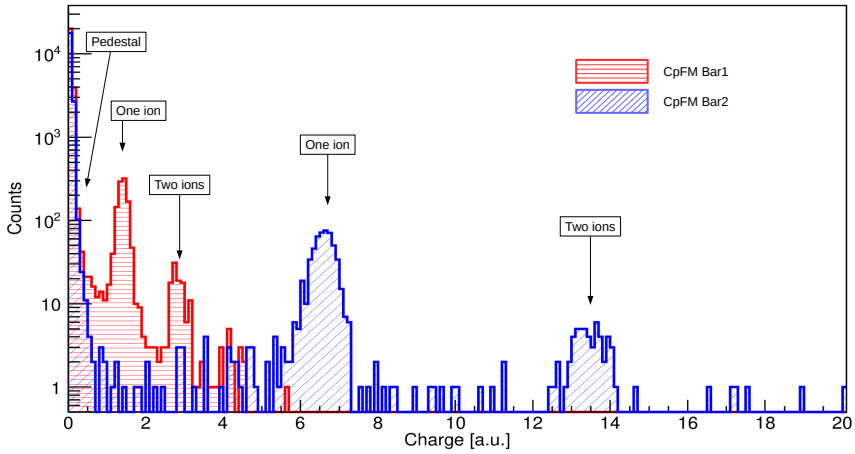

(a) Distribution of the charge for CpFM Bar1 and Bar2 signals (log scale in Y-axis).

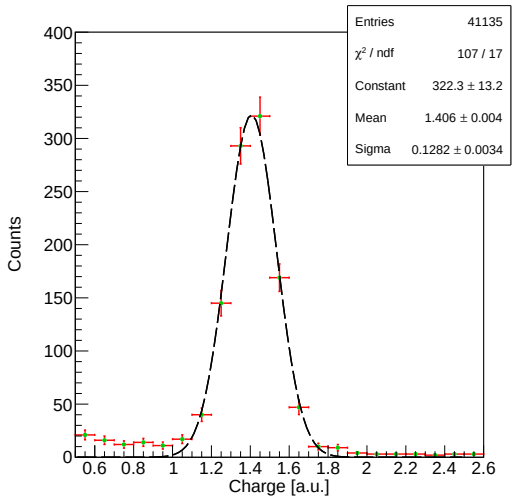

(b) Single ion charge distribution for CpFM Bar1.

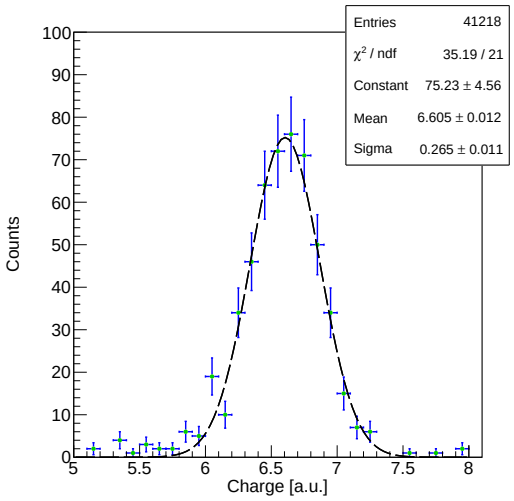

(c) Single ion charge distribution for CpFM Bar2.

Figure 6.42: Experimental results of the CpFM signals charge measurements, where HV = 700 V, sampling frequency = 3.2 GS/s, USBWC dynamic range = ±1.25 V. A Gaussian distribution function is used for the data fitting (black dashed line).

Single ion peaks of the amplitude and charge distributions are well separated from the pedestal and can be used for the detector recalibration (self-calibration on

the circulating beam).

To increase the statistics of the collected data we can use pre-analysed data from the WaveCatcher. We will be focused mainly on the signal amplitude and charge measurements calculated by USBCW software online (during the data acquisition). The only difference between offline waveform data analysis and online is the time window for the charge calculation. As it was mentioned before, in offline analysis we are computing the integrated charge of the full waveform during the acquisition window of 320 ns. In contrast, USBWC software[5] calculates charge for one peak with a maximum amplitude within a short time window (called Charge Length) predefined by the operator before the measurements (Fig. 6.43). Usually, we apply the following settings (Fig. 6.43): Precharge = 16 samples (e.g. for 3.2 GS/s – 16×0.3125[ns]=5[ns]), Charge Length = 6×16 samples (e.g. for 3.2 GS/s – 6×16×0.3125[ns]=30[ns]). In this way, we are measuring, only once per waveform, a charge of a single peak along 30 ns time window (Fig. 6.44).

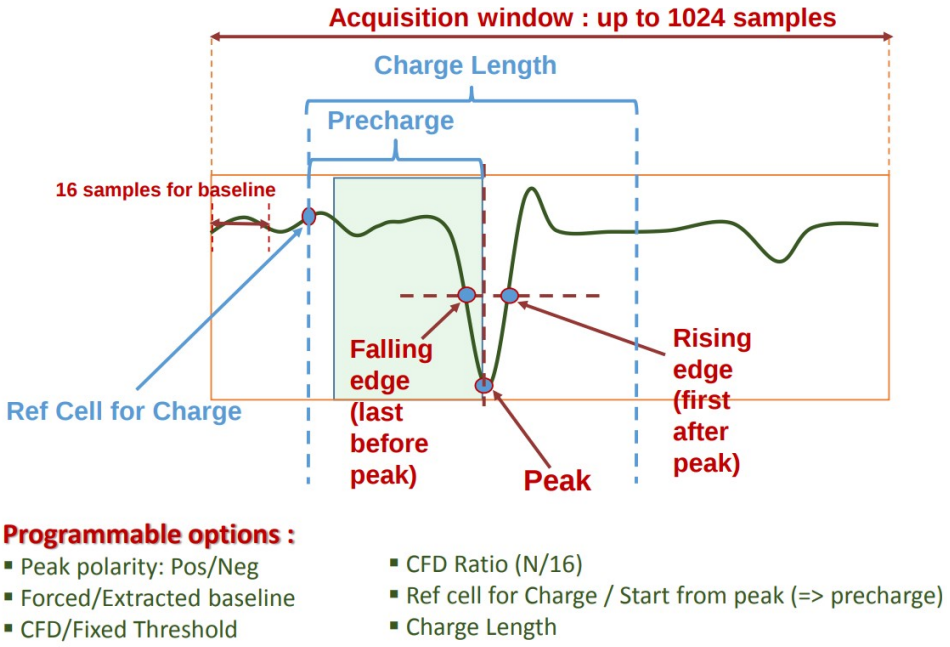

Figure 6.43: USB-WaveCatcher measurement parameters and results. From the WaveCatcher Family User's Manual.

Due to the fact, that USBWC software computes charge in 30 ns window, while offline data analysis integrates charge within whole time range of the waveform (320 ns), the difference in charge can be explained by means of the ion fragments.

[5] http://www.hep.ucl.ac.uk/pbt/wikiData/manuals/WaveCatcher/WaveCatcherFamily_V1.2.pdf

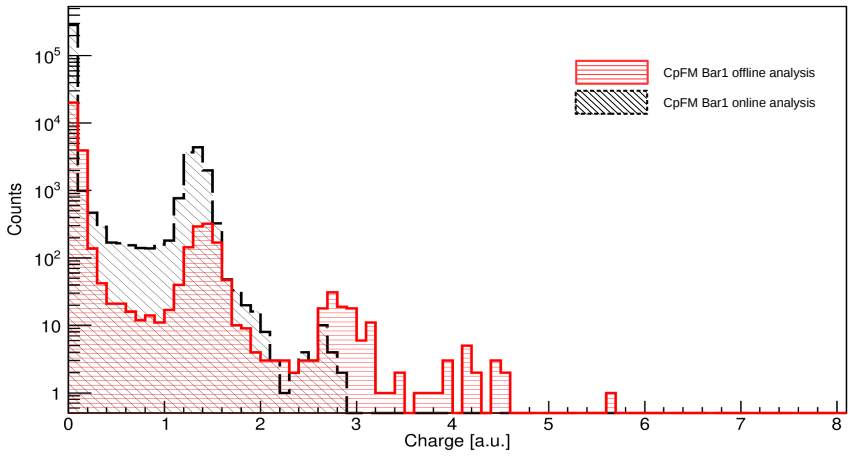

(a) Charge distribution for CpFM Bar1, calculated online (black dashed line) and offline from the waveform (red solid line).

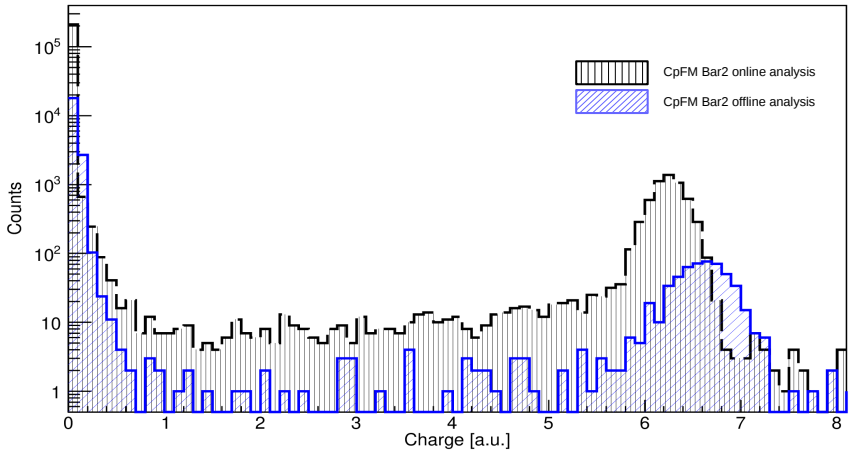

(b) Charge distribution for CpFM Bar2, calculated online (black dashed line,) and offline from the waveform (blue solid line).

Figure 6.44: Comparison between experimental results of the CpFM signals charge measurements calculated online using USBWC analysis software (dashed line, about $4 \cdot 10^5$ entries) and offline analysis from waveforms (solid line, about $4 \cdot 10^4$ entries), where HV = 700 V, sampling frequency = 3.2 GS/s, USBWC dynamic range = ± 1.25 V.

It leads to the additional small amount of the Cherenkov light detected along the 320 ns, while the online software takes into account the ion signal only.

The online computed values of the single ion amplitude and charge (Table 6.5) can be used for the self-calibration of the CpFM, in order to increase the statistics.

	Amplitude, mV	Charge, a.u.
CpFM Bar1	276.3±0.2	1.325±0.001
CpFM Bar2	990.3±0.2	6.247±0.002

Table 6.5: Single 270 ZGeV/c Pb ion parameters, computed by means of the USB-WaveCatcher software for 700 V of the CpFM PMTs voltage supply. Corresponds to $\sim 4 \cdot 10^5$ waveforms.

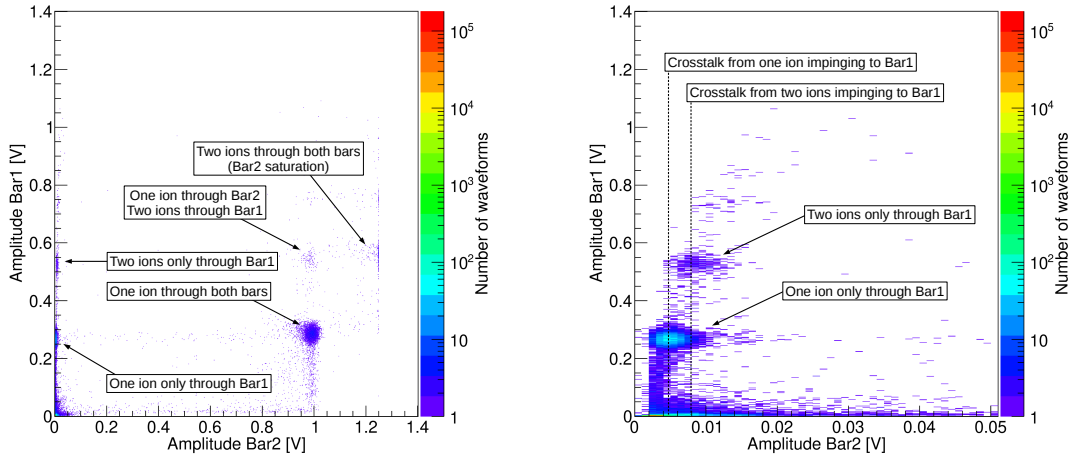

(a) Amplitude of the signal for Bar1 as a function of the amplitude for Bar2.

(b) Amplitude of the signal for Bar1 as a function of the amplitude for Bar2, which is less than 50 mV.

Figure 6.45: Cherenkov light crosstalk illustration between two bars of the CpFM detector.

Due to the specific structure of the detector, some Cherenkov light crosstalk can occur between two bars. To estimate the magnitude of this effect we can use a distribution of the amplitude for Bar1 as a function of the amplitude for Bar2 (Fig. 6.45). Each island-like region represents different region as it was shown in Fig. 6.39. Since Bar1 is closer to the primary beam and it completely covers Bar2 transversally (in XY plane), therefore there is almost no events with an incoming ion on Bar2 and not on Bar1. Instead, Bar1 has can detect single, double, etc. without

any hitting ion on Bar2. Figure 6.45b illustrates this situation. In this case when ion crossing Bar1 produces Cherenkov light, some photons escape the bar and hit Bar2 propagating up to the readout side. And obviously, the amount of crosstalk light is proportional to the initial number of photons generated in Bar1 (i.e. number of ions).

Thus one can see, that for a single ion the crosstalk amplitude value for Bar2 is about 4 mV, while for a double ion signal it is about 8 mV, which two times of one ion signal. According to the amplitude of the single ion (∼1 V) for Bar2 the amount of the crosstalk light is not greater than 1 % of the total light produced by means of one ion.

Proton beam At the beginning of the run with a 270 GeV/c proton beam at the SPS in 2016 (Tab. 6.6), the CpFM detector was acquired in the parking position, while there was no obstacle in the beam. We assume, that the crossing of the charged particle through the bar is very unlikely. Therefore, measured distribution of the amplitude is a typical single photoelectron (p.e.) spectrum (Fig. 6.46a, 6.46b). It contains two main peaks, the big one (pedestal) corresponds to the electronics noise, while the smaller one corresponds to a single p.e. For the charge distribution (Fig. 6.46c, 6.46d) an amplitude cut has been applied to remove the signal pedestal, which is lower than 6 mV. Computed values of the single p.e. are used for the further CpFM calibration (Tab. 6.7).

Beam	Momentum [GeV/c]	Intensity per bunch	Emittance [nm·rad]	Tune Q_h
proton	270	$\sim 1.1 \times 10^{11}$	∼6	26.13

Table 6.6: Beam conditions during the measurements.

	Amplitude, mV	Charge, a.u.
CpFM Bar1	10.8±1.0	0.045±0.001
CpFM Bar2	12.3±1.2	0.046±0.001

Table 6.7: Single photoelectron parameters of the signal distributions, computed by means of the USB-WaveCatcher software for HV = 1050 V, sampling frequency = 3.2 GS/s, and USBWC dynamic range = ±1.25 V.

Taking into account an equation (Eq. 5.8) of the produced number of the Cherenkov photons along 5 mm of the fused silica ($n \simeq 1.4585$) for 270 ZGeV/c lead ion

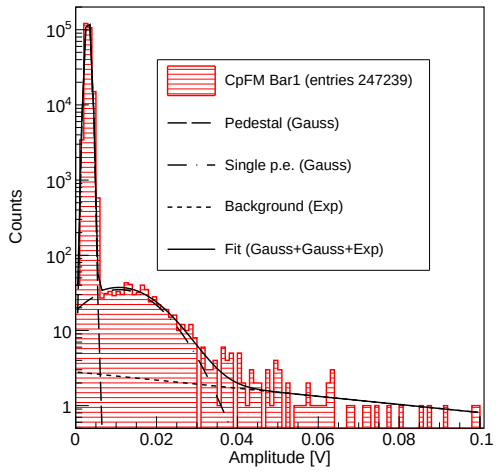

(a) Distribution of the Bar1 signal amplitude.

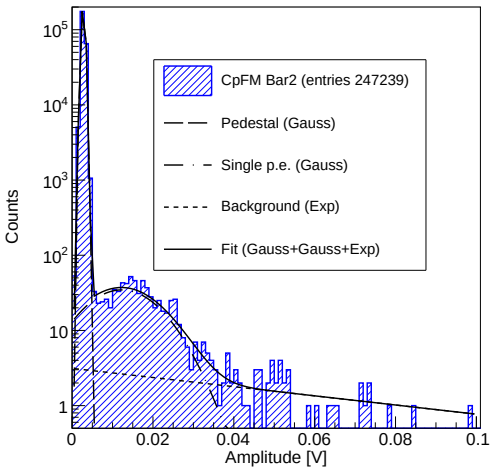

(b) Distribution of the Bar2 signal amplitude.

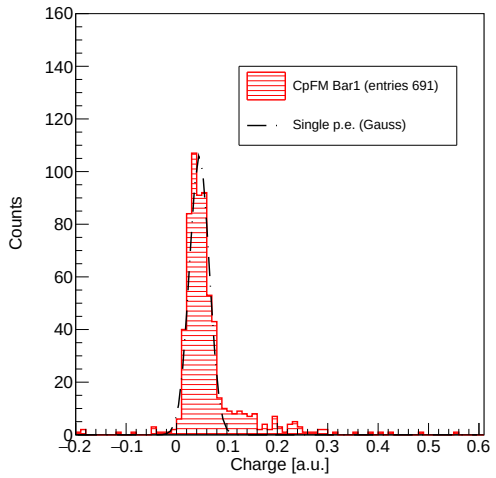

(c) Distribution of the Bar1 signal charge with applied amplitude cut of 6 mV.

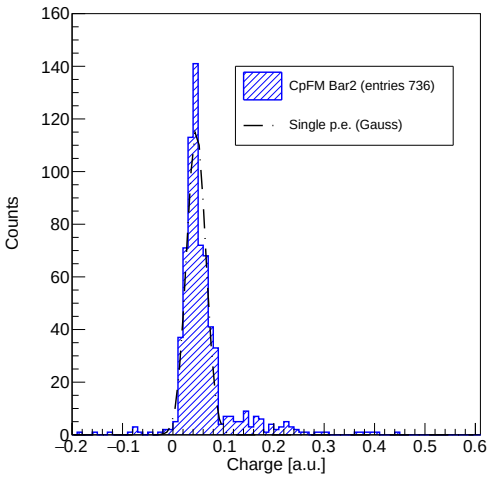

(d) Distribution of the Bar2 signal charge with applied amplitude cut of 6 mV.

Figure 6.46: CpFM single photoelectron distribution in the parking position. The data are collected with HV = 1050 V, sampling frequency = 3.2 GS/s, and USBWC dynamic range = ±1.25 V. Solid line is a fit of the amplitude distribution by means of the double Gaussian (Gauss) and Exponential (Exp) functions; dashed line – a signal pedestal fit; dot-dashed line – a single photoelecton peak fit; dotted line – a signal background fit.

($\beta \simeq 0.99996$) and 270 GeV/c proton ($\beta \simeq 0.99999$), we can easily calculate the amplitude and charge per proton:

$$N_{p.e.} \sim \frac{M}{G}, \tag{6.6}$$

$$K = \frac{N^p_{p.e.}}{N^i_{p.e.}} = \left(\frac{dN}{dx \cdot d\lambda}\right)^p / \left(\frac{dN}{dx \cdot d\lambda}\right)^i, \tag{6.7}$$

$$M^p = \frac{G^p}{G^i} \cdot M^i \cdot \left(\frac{dN}{dx \cdot d\lambda}\right)^p / \left(\frac{dN}{dx \cdot d\lambda}\right)^i, \tag{6.8}$$

where $N_{p.e.}$ is a number of p.e. per crossing particle, which is proportional to the amount of the Cherenkov light ($\frac{dN}{dx \cdot d\lambda}$), while indexes i and p indicate ion and proton respectively; M is a measured amplitude or charge per crossing particle; G is a gain of the PMT at a given supply voltage (Tab. 6.8); K is a ratio between numbers of p.e. per one crossing particle for ion and proton runs.

CpFM	PMT	Voltage, V	Gain
Bar1	R7378A/BA1512	600	$7.06135 \cdot 10^4$
		700	$2.36745 \cdot 10^5$
		1050	$5.70467 \cdot 10^6$
Bar2	R7378A/BA1511	600	$9.42513 \cdot 10^4$
		700	$2.93004 \cdot 10^5$
		1050	$5.78805 \cdot 10^6$

Table 6.8: Measured gain of the Hamamatsu PMTs, which have been used for the CpFM detector operation.

Taking into account all above, we can compute the amplitude and charge of a single proton crossing the bar. Table 6.9 shows the calculation results for $K = 0.00014873$.

	Amplitude, mV	Charge, a.u.
CpFM Bar1	0.990±0.001	$0.005 \pm 3.6 \cdot 10^{-6}$
CpFM Bar2	2.910±0.001	$0.018 \pm 5.9 \cdot 10^{-6}$

Table 6.9: Computed single 270 GeV/c proton parameters for 1050 V of the PMT supply voltage.

Considering the obtained results, the amplitude of a single proton for two bars is less than pedestal threshold of 6 mV. It means, that we are able to count starting

only from 6 and 2 incoming protons for Bar1 and Bar2 respectively, which defines our proton counting limitation.

To calculate the number of photoelectrons per proton we have to compute the ratio between the amplitude (charge) per p.e. (Tab. 6.7) and proton (Tab. 6.9). The results are listed in Table 6.10.

	From the Amplitude, p.e./proton	From the Charge, p.e./proton
CpFM Bar1	0.092±0.008	0.106±0.002
CpFM Bar2	0.237±0.023	0.399±0.009

Table 6.10: Calibration parameters of the CpFM detector for 270 GeV/c protons at 1050 V of the PMT supply voltage.

The difference between number of p.e. per proton, computed using the amplitude and charge, can be explained by the fact, that the values of the PMT gain have been calculated measuring only PMT anode current (i.e. charge), which contributes a systematic error to the amplitude calculation of the p.e. number per proton. On the other hand, due to the fact that before CpFM installation on SPS two calibrated fused silica bars were replaced by new ones, and the production company have prepared the bars within very tight time limits, the assumption about their identity was wrong. As a result, the SPS version of the CpFM has worse radiators, which leads to light losses. It can explain the difference between new results (∼0.1 and ∼0.4 p.e./proton) from the SPS and previous one (∼0.6 p.e./proton) from the BTF and H8 measurements (Subsection 6.2.1).

To estimate the resolution (R) of the detector for a certain number of incident protons, we can use the following expression:

$$R = \frac{1}{\sqrt{N_{p.e.}}}, \tag{6.9}$$

where $N_{p.e.}$ is a number of the produced photoelectrons. Therefore, the resolutions of a single proton detection are about 307% and 158% for CpFM Bar1 and Bar2, respectively.

6.4.2.2 Proton beam measurements

To follow particles, deflected by the bent crystal inserted in the halo of the SPS beam, and for a graphical view of the beam optics dynamics inside the machine, a dedicated script has been developed. For a given experimental layout and magnet strength of the SPS using MAD-X [120], an output file with twiss parameters is

generated. The tool takes the file and using Eq. 3.25 evaluates impact parameters of the channeled beam at a relative position along the beam.

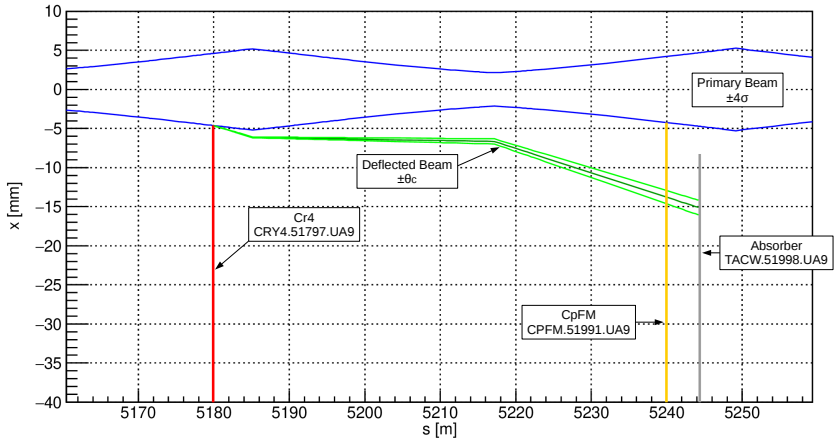

Figure 6.47: Horizontal projection (x) of the channeled halo particles as a function of the longitudinal coordinate (s) in LSS5. Blue lines represent the primary beam envelope with a 4σ size. A bent crystal (red line) deflects halo particles (green line) within $\pm\theta_c$ range (light green lines) onto the tungsten absorber (grey line). CpFM detector (orange line), located between the crystal and absorber, intercepts the channeled particles.

Figure 6.47 shows an experimental drawing of the horizontal projection for the beam optics at LSS5 zone of the SPS accelerator. According to the alignment procedure [54], a bent crystal (STF18, Table 6.2), inserted as a primary collimator into the halo of the beam (1 bunch with about $1.2 \cdot 10^{11}$ protons) 4σ from the core, deflects particles onto the 60 cm long tungsten absorber (TAL), which is placed 7σ from the beam core. Along the linear horizontal scan, the Cherenkov detector crosses the deflected beam and touch the primary beam at 4σ.

Figure 6.48 illustrates the linear scan of the detector from the parking position toward the primary beam. In each bin of the histogram (100 μm) an average amplitude (amplitude calibration) or charge (charge calibration) of the signal is multiplied by the revolution frequency of the machine (43 kHz), and divided by the amplitude or charge of a single proton. Due to the detector geometry, the CpFM Bar1 touched the primary beam first (Spike). The plot is following the shape of the beam profile crossing the channeled beam as it was mentioned before (Fig. 6.34).

The discrepancy between two plots (Fig. 6.48a and Fig. 6.48b) can be explained in the same way as it was done above: the gain of the PMTs (Tab. 6.8) was measured using an information about the anode signal charge, therefore the ion calibration

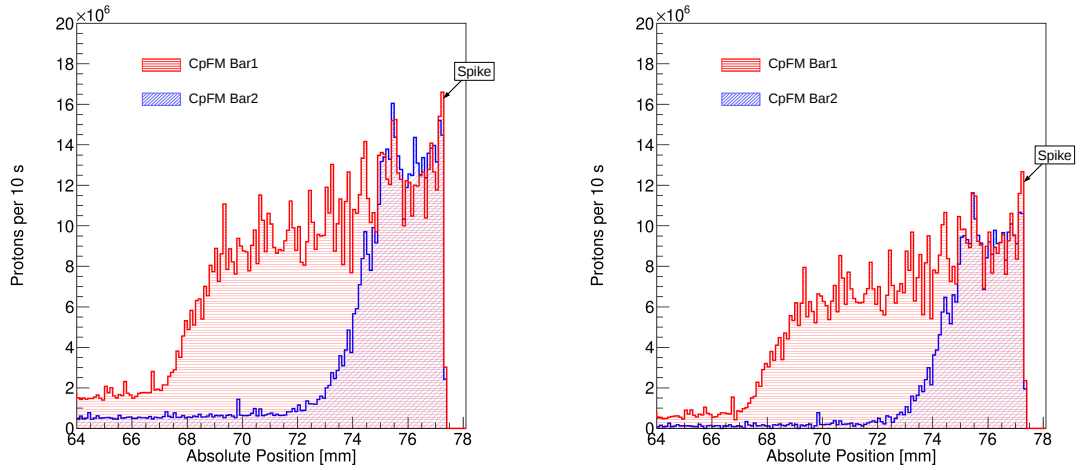

(a) From the amplitude calibration.

(b) From the charge calibration.

Figure 6.48: CpFM horizontal linear scan. Number of the detected protons as a function of the absolute horizontal motor position of the CpFM detector. A spike at CpFM Bar1 is due to the touch of the primary beam. The speed of the scan is 10 μm/s, while the binning of the histogram is 100 μm.

parameters (Tab. 6.9) of the CpFM with different gain values (700 V for ion run and 1050 V for proton run) is more reasonable for the proton calculation based on the charge measurement. Further in the text, we will concentrate only on the charge calibration results for the particles counting (Fig. 6.48b).

Figure 6.49 shows an integrated channeled beam profile along CpFM linear scan. Two histograms represents the counted number of protons as a function of the detector horizontal position. From the fit of these two distributions, using an Error Function, we are able to extract the channeled beam position (μ), and the standard deviation of its distribution in horizontal plane (σ). The difference between mean values for Bar1 and Bar2, which is equal to $\sim$6 mm, is close to the horizontal displacement of the bars (Fig. 5.3), equal to 5 mm.

The measured position of the channeled peak (68.48 mm) by means of the CpFM Bar1 is about 8.7 mm from the Spike ($\sim$77.20) (i.e. from the aligned position, which is equal to 4σ from the beam core), while its width is equal to the FWHM = 2.355×Std = 2.355×0.94 = 2.2±0.1 mm. From the beam optics routine, which we have used to follow the deflected beam trajectory (Fig. 6.47), the horizontal position of the channeled beam is about 10 mm, while the width is $\sim$2 mm.

To compare the measured distribution of the deflected particles number for the same bar position with respect to the main beam, a short region of the linear scan

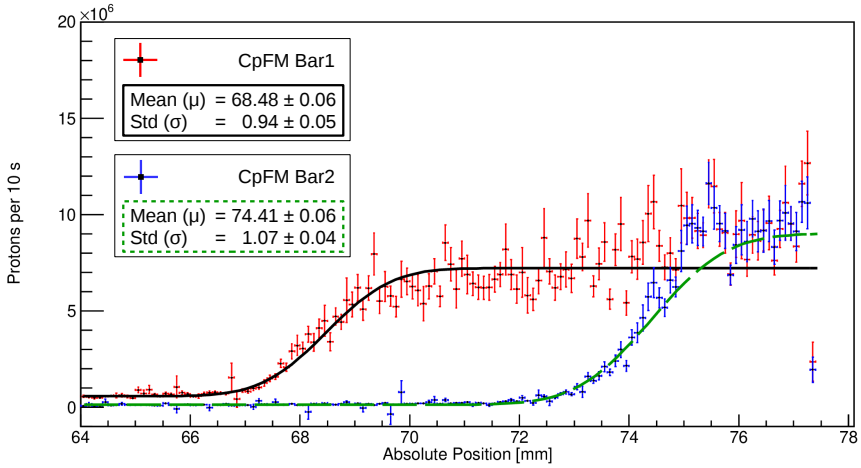

Figure 6.49: Distribution of the proton counting number as a function of the CpFM detector horizontal position. Two histograms represent the number of the detected protons using the charge calibration parameters. The fit was done by means of the Error Function for Bar1 (black solid line) and Bar2 (green dashed line). Sigma and mean values correspond to the standard deviation of the channeled beam and its position in the CpFM detector reference frame.

has been chosen (Fig. 6.49): 70-72 cm and 75-77 cm for Bar1 and Bar2 respectively. Figure 6.50 illustrates the number of channeled particle detected by the CpFM with an indication of the detector counting limitation.

Based on the results of the measurements, we can conclude the following:

- We have calibrated CpFM detector in its final configuration installed on SPS. The obtained values show us different particle detection sensitivity of the bars (Tab. 6.9) with a resolution of more than 100% for a single proton.

- Performed linear scan, by means of the detector crossing the channeled beam, has confirmed the estimated distance between the main SPS beam and deflected by the bent crystal (Fig. 6.49). We have measured the deflected beam profile and calculated the number of particles for channeled and dechanneled regions.

- The distribution of the channeled particles number (Fig. 6.50) is asymmetric and has a long tail with a counting limitation of 6 and 2 protons for the CpFM Bar1 and Bar2 respectively.

- Measured flux of the channeled particles is about 40 protons/turn, or in other words about $2 \cdot 10^6$ protons/s.

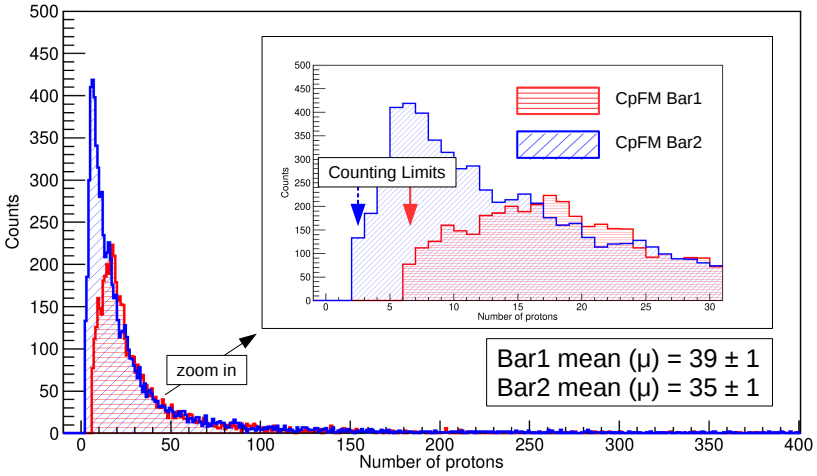

Figure 6.50: Distribution of the detected channeled particles number for same CpFM Bar1 and Bar2 distance with respect to the primary beam. Red solid and blue dashed arrows show the counting limitation (6 and 2 protons) for the Bar1 and Bar2 respectively.

6.4.3 Characterisation of the fused silica surface quality

To understand the source of the different light collection efficiency of two CpFM bars (i.e. for the same number of crossing charge particle a different amount of Cherenkov light is collected by CpFM Bar1 and Bar2 readout channels), we have developed a setup for characterisation of the bars surface quality and to estimate light losses due to the not 100 % probability of the total internal reflection and inefficient area at the edges of the bars [121] (Fig. 6.51). The main idea of the measurements it to perform a linear scanning of the radiator surface with a ^{90}Sr radioactive source and measure the Cherenkov light rate, detected by a PMT attached to the quartz bars.

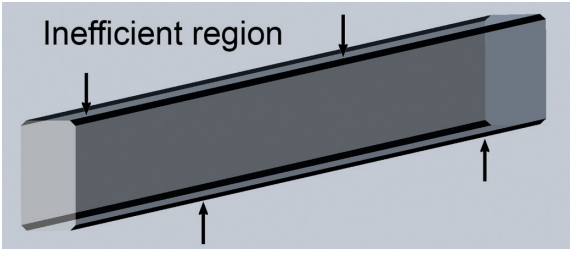

Figure 6.51: Bar drawing showing the inefficient area (black arrows) in the edge of the bar, which appears during the manufacturing process.

6.4.3.1 Experimental setup

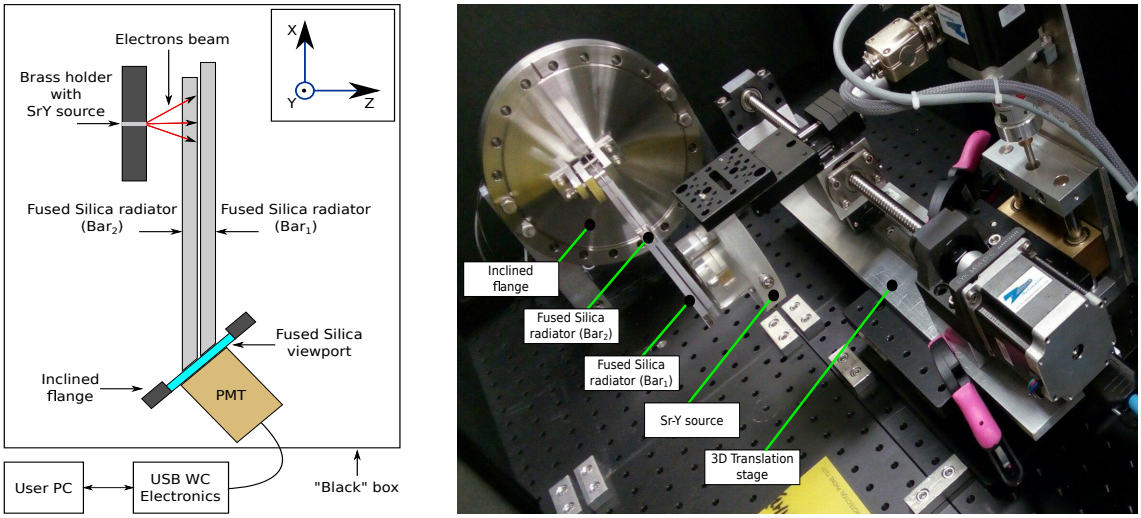

(a) Principal scheme.

(b) Photo.

Figure 6.52: Experimental setup: fused silica radiators, Sr-Y source, PMT, translation stage, readout electronics.

The scheme of the experimental setup is presented in Figure 6.52. It consists of two fused silica bars that are mounted parallel to the holder on the flange (non-magnetic 316NL Stainless Steel). The requested producer specifications of the bars are:

- the material is HPFC 7980 standard grade;
- all surface flat to 0.01 mm;
- all edges beveled with a diameter of 0.1–0.2 mm;
- surface quality < 1 nm;
- typical face to side squareness < 0.02 deg;

The two bars are optically independent and they are separated from the viewport by a 2 mm thick fused silica window and are 36 mm in diameter from the PMT (Hamamatsu R7378A), powered by a high voltage supply (ISEG T2DP050205EPU 2×5 kV / 2 mA). The PMT signal is read with the USB-WaveCatcher.

A 36.76 MBq Sr-Y radioactive source is positioned along the bars by a 3D motorised translation stage, with a position accuracy less than 100 μm. This assembly is similar to the setup installed in SPS. For the given energy spectrum of the electrons, the probability to penetrate 5 mm fused silica is about 10^{-5}; therefore, we can neglect the effect of the electrons crossing the two bars.

All components, except the readout electronics, were placed in a "black" box that was well shielded from the outside light. Figure 6.53 shows the scheme of the Sr-Y source container geometry.

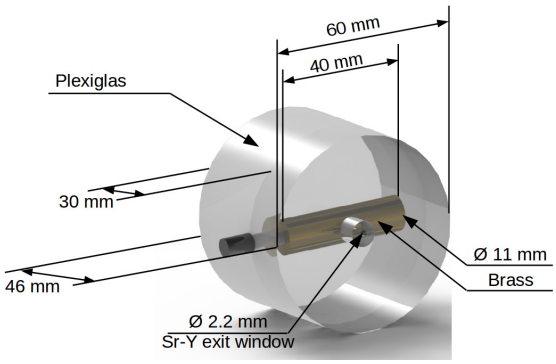

Figure 6.53: Scheme of the Sr-Y source container. The source itself is located inside a brass cylinder.

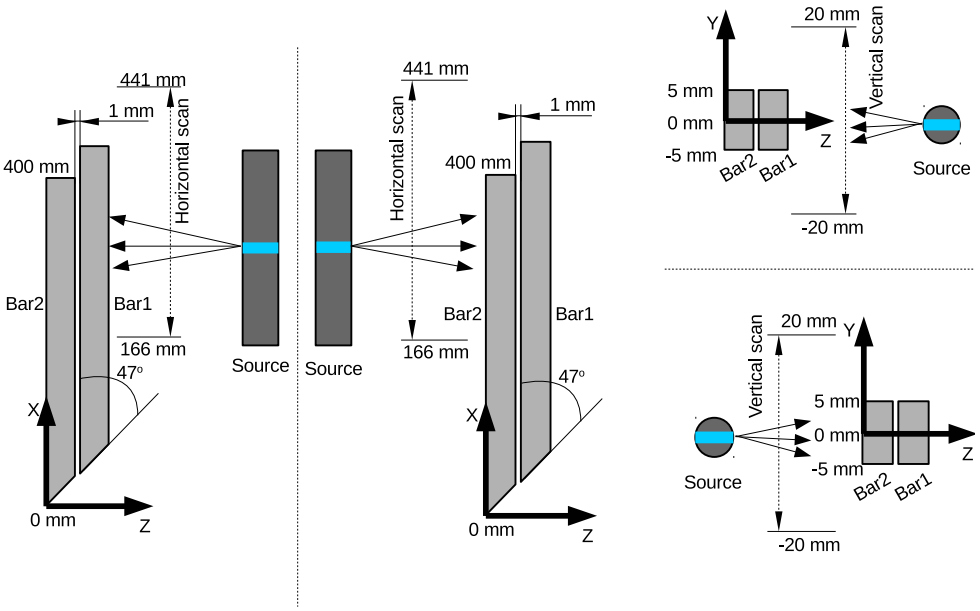

Figure 6.54: Definition of the coordinate system. Horizontal and vertical scans configuration. Left: horizontal cross-section of the bar; right: vertical cross-section of the bar.

Depending on the bar length, incoming angle of the electron and due to the multiple scattering inside the material [119], the photons will bounce $10 - 10^4$ times before exiting the bar. Therefore, the internal reflection coefficient must be close to one to have a good light collection at the end of the bar. For our setup the average

value is about 100 reflections. The experiment investigated the dependency between the light collection on the PMT, which is aligned to be able to collect the light from both bars, and the impacting position of the electrons. The measurements were performed in steps, scanning each bar in horizontal and vertical directions separately (Fig. 6.54).

During the horizontal scans, due to the mechanical limitation of our setup, it was impossible to move the source up to the edge of the bar closer to the PMT, which is the origin of our reference system (Fig. 6.54, left). The ranges for the scan are therefore from 166 mm to 441 mm in this reference system. The translation stage was moved over 270 points with a stop of 5 seconds at each point.

The vertical scan was perform in the range from -20 mm to 20 mm with respect to the middle of the bar. The translation stage was moved over 40 points with a stop of 20 seconds at each point.

6.4.3.2 Experimental results

The use of USB-WaveCatcher electronics provided the possibility to measure the rate (number of counts per second) of the signals from the PMT, which are due to the Cherenkov light produced by a β-electron. Given the 36.76 MBq source activity distributed over the 4π solid angle, it is unlikely that the pile-up of the signals originated from two different electrons. The results of the measurements are illustrated in Figure 6.55.

Figures 6.55a and 6.55b show a comparison of the rate between two bars for the vertical and horizontal scans respectively. In Figure 6.55c the data, relative to the rate for different distances between the source exit window and the surface of the bar, are reposted. To interpret the data, we fit them with the convolution function (F_{fit}) of a Gaussian and a box function (Fig. 6.55d):

$$F_{fit}(y) = (f * g)(y) \stackrel{\text{def}}{=} \int_{-\infty}^{\infty} f_{ab}(\tau) g(y-\tau) d\tau \Rightarrow \sum_{-20}^{20} f_{ab}(\tau) g(y-\tau) \Delta\tau \tag{6.10}$$

$$f_{ab}(y) = \begin{cases} 0 & \text{for } y < a. \\ 1 & \text{for } a < y < b. \\ 0 & \text{for } y > b. \end{cases} \tag{6.11}$$

$$g(y) = A e^{-\frac{(y-\mu)^2}{2\sigma^2}} \tag{6.12}$$

where f_{ab} is the box function (a and b are the left and the right edges of the bar respectively), g is the Gaussian function with amplitude A, mean value μ and standard

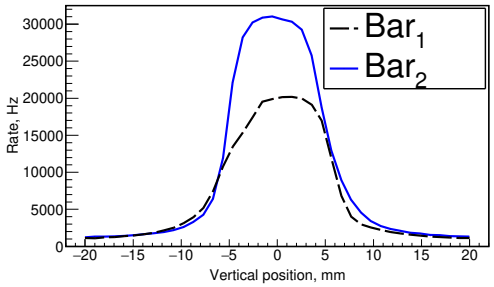

(a) Measured rates in a vertical scan for the two bars. The distance between the bar surface and the exit window of the source is 4.5 mm (along Z-axis) and the horizontal position is 385 mm. The black dashed line is for Bar1, the blue solid line is for Bar2.

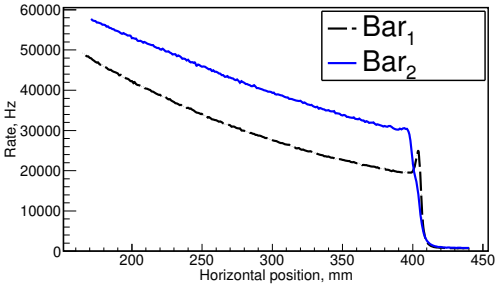

(b) Horizontal scan for two bars. Distance between bar surface and exit window of the source is 4.5 mm (in Z-axis). The black dashed line is for Bar1, the blue solid line is for Bar2.

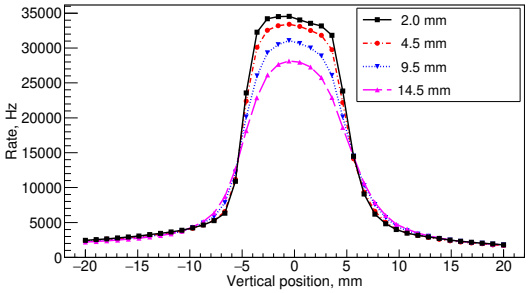

(c) Measured rates in a vertical scan for Bar_2. Different lines correspond to different distances between the bar surface and the exit window of the source (along the Z-axis): black solid with squares: 2 mm, red dash-dotted with circles: 4.5 mm, blue dotted with triangles down: 9.5 mm, pink dashed with triangles up: 14.5 mm.

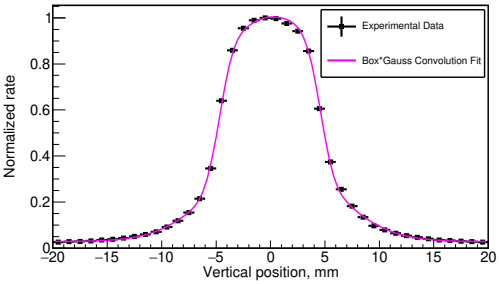

(d) Normalized (with respect to the maximum value) rate for a vertical scan (from -20 mm to 20 mm in Y-axis). The data were taken for Bar_2 at 210 mm along the X-axis and at a 4.5 mm distance between the bar surface and the exit window of the source (along the Z-axis). The pink solid line is a fit with the convolution function (F_{fit}).

Figure 6.55: Experimental results: Rate (Hz) as a function of the vertical and horizontal position of the source.

deviation σ. From the fit we derive the width of the radiator $\Delta_{ab} = 9.20 \pm 0.82$ mm and the sigma of the distribution of the particles exiting from the source $\sigma = 1.04 \pm 0.01$ mm.

6.4.3.3 Simulation

From Figures 6.55a and 6.55b one can see that there is a difference in the rate between the two fused silica bars. Since the same PMT was used to readout both bars, which are geometrically identical, we can conclude that the problem comes from the mechanical or optical properties of the bars, as follows: (1) different quality of the polishing of the sides of the radiator ("polishing effect"); and (2) different quality of the edges of the radiator, leading to a different extension of the ineffective area or non-homogeneities along the bar ("edge effect").

To estimate the quality of the bar we decided to use a method based on Monte-Carlo simulation algorithms. Our goal is to reproduce the experimental data using the simulation in an iterative process. Geant4 [122] software was chosen as the framework for our modelling.

The simulation is done in two main steps, as follows:

- Realistic modelling of the β-source and validation of the distribution of the electrons using data from the vertical scan;

- Iterative simulations of the horizontal scan varying the parameters describing the quality of the bars and comparison with the experimental results to assess the correct value of the parameters.

The physical processes which were implemented in the simulation code are: particle transportation, standard EM physics, Cherenkov light production, photon interaction with matter and the ^{90}Sr radioactive decay. Other features implemented in the code are: refractive index (Fig. 6.56a) and total internal reflection probability [119] behavior of the fused silica for different photon energies, and also quantum efficiency of the PMT Bialkali photocathode, taking into account dependence on the photon wavelength (Fig. 6.56b).

Sr-Y source There are several possible ways to model the Sr-Y source, as follows: (1) electrons with constant energy (0.5 and 2.2 MeV of kinetic energy); (2) electrons with Sr-Y decay spectrum (using Geant4 General Particle Source); and (3) real Sr-Y decay with secondary electron and neutrinos (using Geant4 Radioactive Decay Physics). We chose the latter, more comprehensive and precise method. Figure 6.57 shows the β-spectrum of Sr-Y source simulated with Geant4.

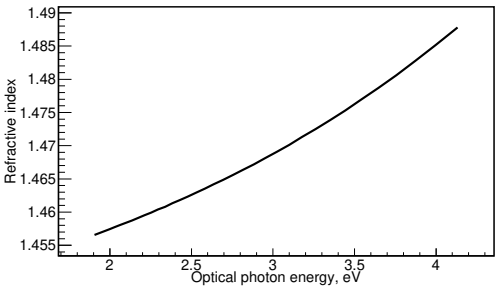

(a) Refractive index for fused silica as a function of the photon energy.

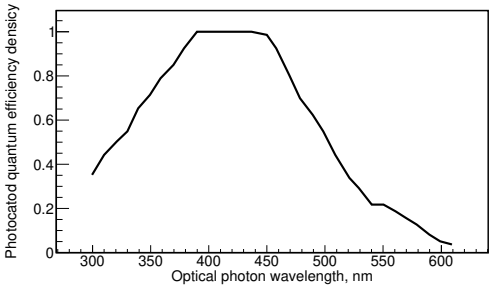

(b) Normalised Bialkali photocathode quantum efficiency as a function of the photon wavelength. Please note: 1.0 is corresponded to 24.25 %.

Figure 6.56: Optical properties of the fused silica and photocathode of the PMT used in the simulation.

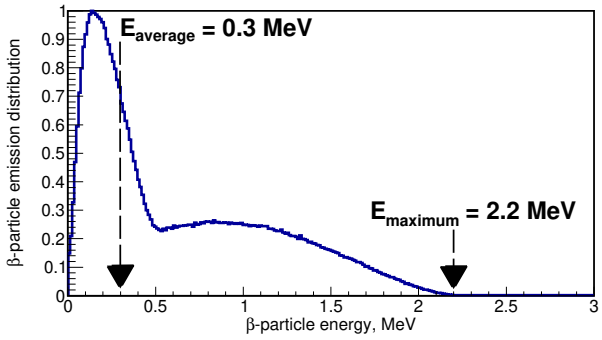

Figure 6.57: The spectrum of the Sr-Y source simulated with Geant4.

Using the Geant4 radioactive decay physics, we simulated the real energy spectrum of electrons with its angular distribution.

To cross check the accuracy of our simulation of the β-source we simulated the scan in the vertical direction. In Figure 6.58a, one can see a comparison of the normalized (with respect to the maximum value) rate distribution for experimental data and simulation. We fit the two distributions with the same function described previously (Eq. 6.10–6.12), adding a Gaussian and a constant term to take into account the effects due to electronics noise and light penetrating into the "black" box. From this procedure, we get the two following main parameters: (1) $\sigma = 0.996 \pm 0.001$ mm and (2) $\Delta_{ab} = 9.3 \pm 0.8$ mm.

Figure 6.58b shows the value of σ (which corresponds to the standard deviation of the distribution of the particles coming from the source) for different distances between the surface of the bar and the exit window of the source assembly. The value of σ linearly increases with the distance, as expected. The red curve on Figure 6.58b confirms that the fitted width of the bar is constant for all distances. Using σ, extrapolated on the distance of 0 mm between the bar and the exit window of the source, we can estimate the dimension of the source exit window: FWHM = $2.355 \times \sigma(0 \text{ mm}) \Rightarrow$ FWHM $= 2.052 \pm 0.037$ mm, which is close enough to the real value, 2.2 mm.

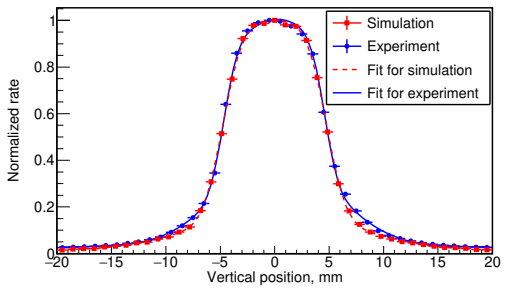

(a) Vertical scan for Bar2: Normalized (with respect to the maximum value) rate as a function of the vertical position of the source for data and simulation with the best fit function superimposed.

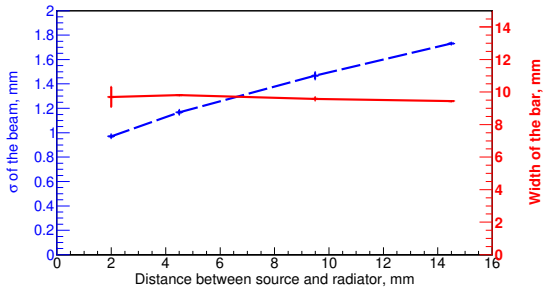

(b) The reconstructed standard deviation of a Gaussian distribution of the source particles (blue dashed curve) as a function of the distance between source and radiator (left axis); fused silica bar width (red curve) reconstructed from the fit of the experimental data as a function of the distance between source and radiator (right axis).

Figure 6.58: Validation of the Sr-Y source simulation in the Geant4, measurements - data comparison. Extraction of the bar width and electron spot size from the fit.

This test provides an exhaustive validation of the source modelling which was a

week spot of the proposed method.

Quality of the bars To describe the quality of the bars, we defined two parameters: the probability of total internal reflection (P_{IR}) and the fraction of ineffective area at the edges of the bars (F_{IA}).

We run the simulation by performing a scan on the values of the parameters in the following ranges: $95 < P_{IR} < 100$, $0 < F_{IA} < 0.32$ and we compared simulations and experimental data using the following χ^2 definition:

$$\chi^2 = \sum_{i=0}^{N} \left\{ \frac{(R_{exp.} - R_{sim.})^2}{(\Delta R_{exp.})^2 + (\Delta R_{sim.})^2} \right\}_i \tag{6.13}$$

where N is the number of measurements, which corresponds to the different positions along the bar; $R_{exp.}$ and $R_{sim.}$ are the normalized rate of the experimental and simulated events, respectively, with their errors $\Delta R_{exp.}$ and $\Delta R_{sim.}$. Figure 6.59 shows the χ^2 for both bars as a function of the F_{IA} and the P_{IR}. We found a global minimum for Bar1 at ($F_{IA} = 2.7 \pm 0.7$ %, $P_{IR} = 96.4 \pm 0.1$ %) and for Bar2 at ($F_{IA} = 0.0 \pm 0.7$ %, $P_{IR} = 95.9 \pm 0.1$ %). These values correspond to the simulation results that are shown in Fig. 6.59c and well-describe the data.

The simulation of the results obtained in the horizontal scan when the source is positioned at the edge of the bars (from 400 to 410 mm in our reference system) is more difficult and should take into account the different position of the edge of the bars (Fig. 6.60a), as well as photons that are produced in one of the bars and collected by the other (Fig. 6.60b). To take into account these boundary conditions, the χ^2 should be a function of the parameters of both bars simultaneously. Figure 6.60c shows that our simulation describes the data remarkably well, confirming a good understanding of the process described by the simulation.

6.4.3.4 Conclusion

To investigate the difference between light collection on the bars, we characterised the surface quality of fused silica bars with a β-source using a simple experimental setup and Monte-Carlo simulation. Our model takes into account the realistic electron distribution produced by the source and it well-describes the experimental data obtained by scanning the bars with the source and measuring the Cherenkov light signal output with a PMT. We estimated two parameters: the probability of total internal reflection and the fraction of ineffective area at the edges of the bars, which are different for each bar and leads to the different amount of Cherenkov light collected by PMTs. The surface properties in reality are position dependent but we

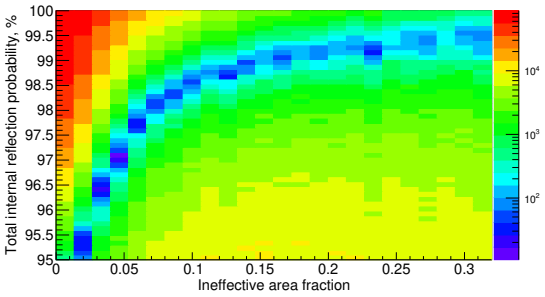

(a) χ^2 distribution of the difference between experimental and simulated data for the Bar1.

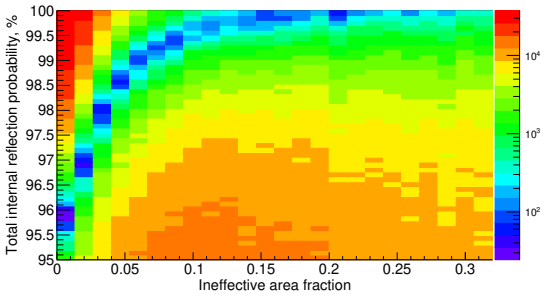

(b) χ^2 distribution of the difference between experimental and simulated data for the Bar2.

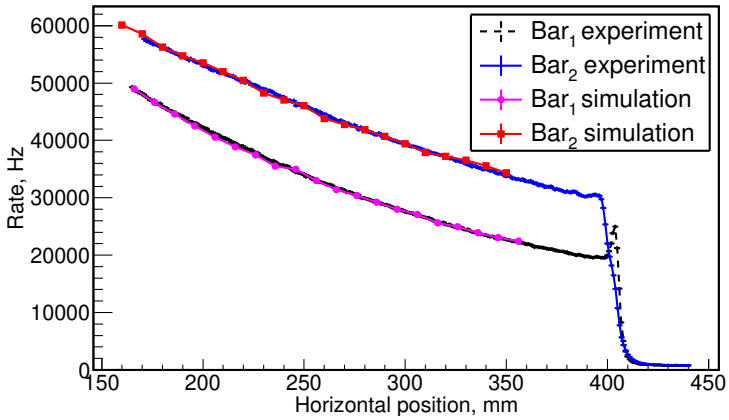

(c) Horizontal scan for Bar1 and Bar2. Rate (Hz) as a function of the horizontal source position, comparing between data and Geant4 simulation results. Experimental data: black dashed line is for Bar1 and blue solid line is for Bar2; simulation: pink solid line with circles is for Bar1 and red solid line with squares is for Bar2.

Figure 6.59: Experimental and simulation data comparison.

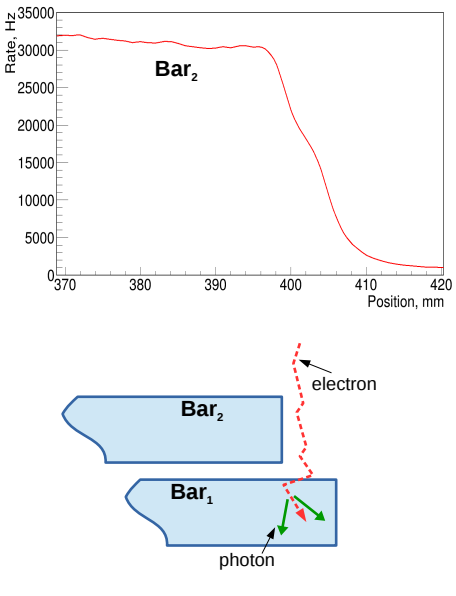

(a) Horizontal scan along Bar2 (experimental data). Top: rate as a function of the source position; Bottom: geometrical configuration in which electrons from the source hit the Bar1 during the scan along Bar2. Red dashed arrows – electrons, green solid arrows – Cherenkov photons.

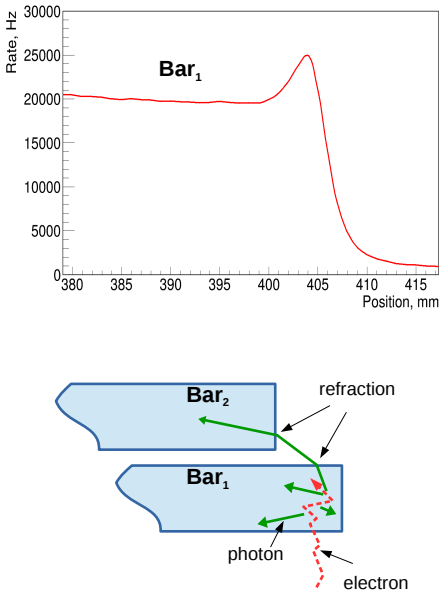

(b) Horizontal scan along Bar1 (experimental data). Top: rate as a function of the source position; Bottom: geometrical configuration of the light crossing between bars. Red dashed arrows – electrons, green solid arrows – Cherenkov photons.

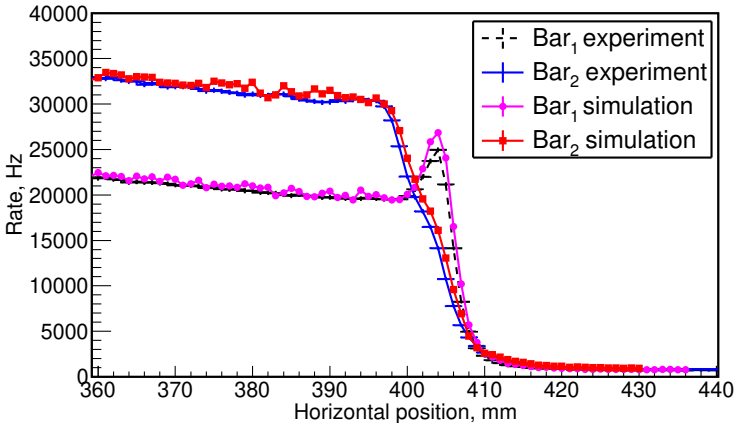

(c) Rate (Hz) as a function of the horizontal source position, comparing between data and Geant4 simulation results. Experimental data: black dashed line is for Bar1 and blue solid line is for Bar2; simulation: pink solid line with circles is for Bar1 and red solid line with squares is for Bar2.

Figure 6.60: Boundary effects on the ends of the bars.

have assumed their small variations and estimated averaged values.

Our simulation includes the dependency between the coefficient of the total internal reflection and photon wavelength, which is received for the BaBar DIRC bars with a very good surface polishing (P_{IR} = ∼99.92). We assume, that the behavior of this function is similar in our case, however, this uncertainty will contribute to the systematic error of our method.

6.4.4 Confocal laser measurements

Continuing the fused silica quality characterization research, an additional measurements have been performed by means of a 3D Laser Scanning Confocal Microscope VK-X210[6], based in the Institute of the Nuclear Physics at Orsay (IPNO).

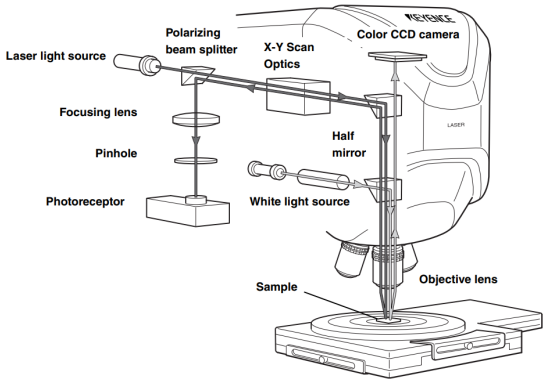

(a) The VK-X100K/X200K Series uses a two-way light source comprised of a laser light source and a white light source. The two light sources together provide the colors, laser intensity and height information necessary to create deep field color images, laser intensity images or height images.

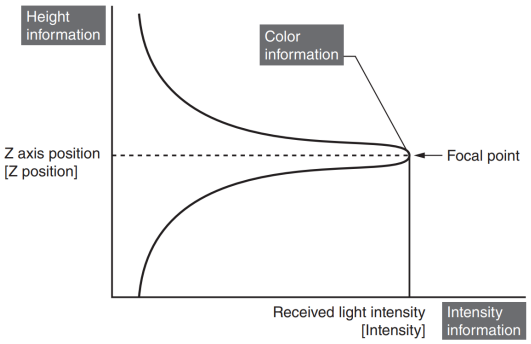

(b) The device reads the intensity of each Z position for each of the pixels on the screen (default: 1024×768 pixels; fine: 2048×1536 pixels; super fine: 3072×2403 pixels) and determines the Z-axis position (= focal point) of the maximum intensity, and records the intensity and color information for that position. Based on this information, three types of image data are constructed, a deep field color image, a laser intensity image and a height image.

Figure 6.61: Confocal laser measurement scheme. From a datasheet of the device.

The goal of the measurement is to verify, locally (i.e. at some fixed positions along the radiator), the order of magnitude for the fused silica bar roughness (i.e. P_{IR}) and edge quality (F_{IA}). We have chosen one of the fused silica bars, produced by the same company as the CpFM bars.

Combining the laser optics with a high-speed X-Y scanner we are able to create a high resolution focal image and gather height information (shape and roughness)

[6] `https://engineering.unl.edu/downloads/files/UserManual-KeyenceVK-X200K.pdf`

from the sample. To measure the infective area in the corner of the bar we have placed it in such a way, that one of its edges was faced in front of the laser beam (Fig.6.62).

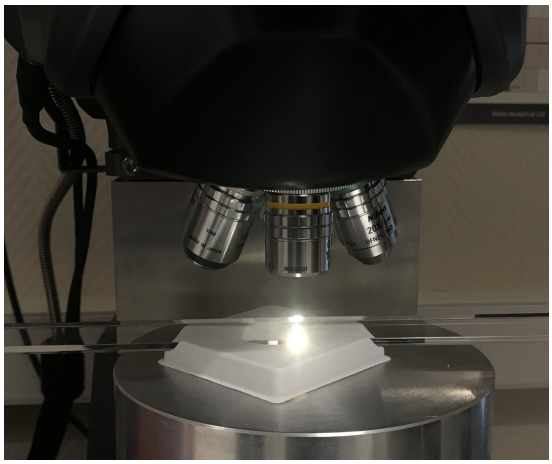

(a) A photo of the measurement setup. Small laser light reflection from the surface of the bar is visible.

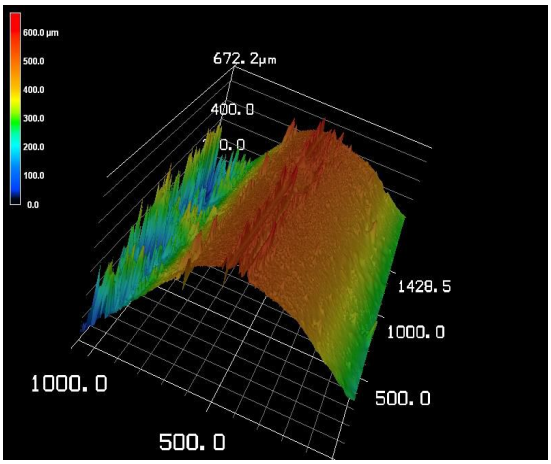

(b) A 3D image made by the laser software.

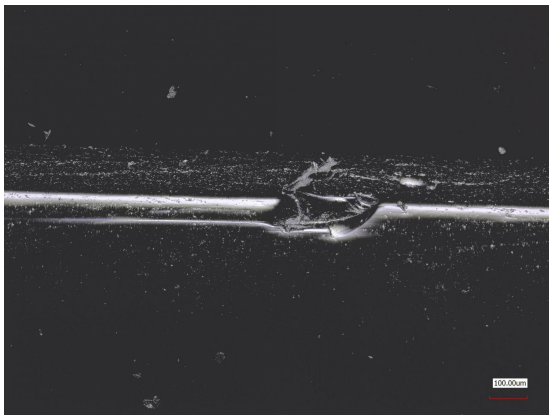

(c) Image of the bar edge with 10 times lens magnification.

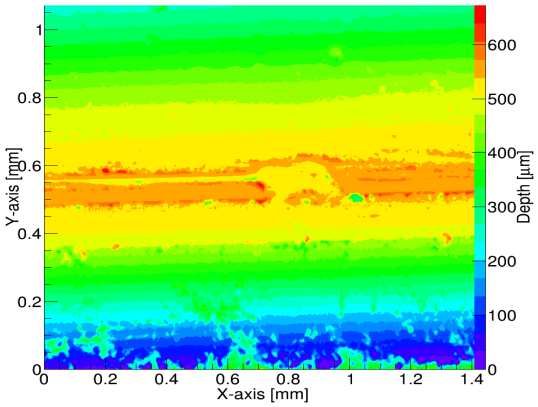

(d) A 3D color map of the bar edge.

Figure 6.62: Bar edge measurements with the confocal laser microscope. Small mechanical damage of the bar corner is visible. A blue zone of the color maps indicates a region of the bar, which is far enough from the focal plane of the microscope, therefore produces a lot of noise.

Taking a profile of the image in Figure 6.62d we can see the roundness of the bar corner (Fig. 6.63). By means of the linear fit we can reconstruct the expected shape of the bar edge (Fig. 6.62d, green dot-dashed lines).

From the measured profile of the bar corner, we can define the size of the ineffective area. It is approximately between 100 μm and 400 μm, depending on the

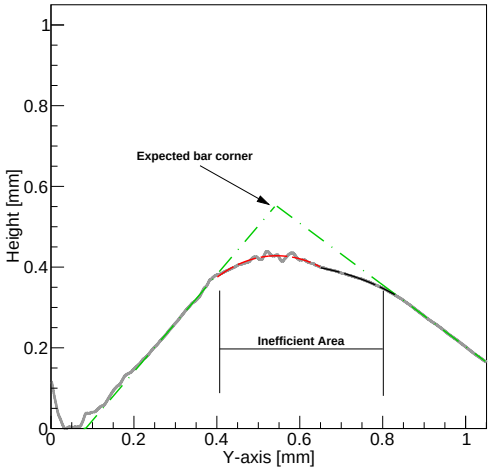

Figure 6.63: Projection of the bar corner image (gray line). Green dot-dashed lines illustrate the sides of the bar with a measured $\sim 90°$ degrees angle between them. Red and black dashed lines shows the round shape, fitted by means of an ellipse equation, of the corner with a radius of 0.3±0.1 mm. The roundness region of the bar introduces an inefficient area.

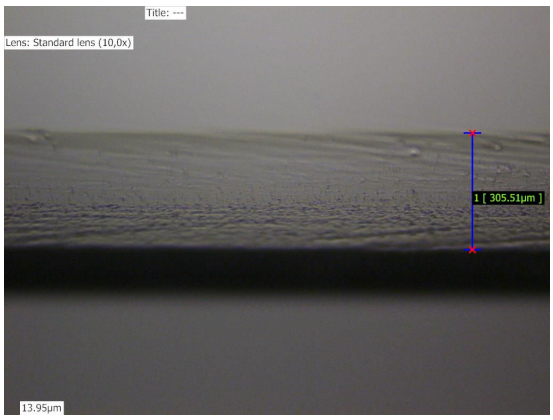

(a) Width of the ineffective region is about 306 μm.

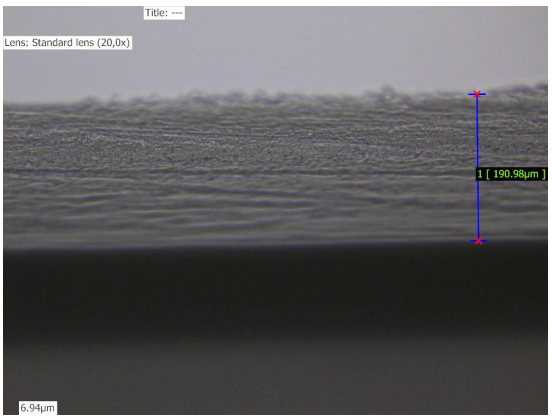

(b) Width of the ineffective region is about 191 μm.

Figure 6.64: Laser images of the bar corner, took in different positions along the radiator.

position on the bar (Fig. 6.64), while from the measurements done with a β-source, we have obtained for Bar2 $F_{IA} = 2.7 \pm 0.7\%$, which means 203 ± 52 μm.

To measure the roughness of the fused silica surface, the flattest and "clean" (in terms of scratches) region of the bar surface has been used (Fig. 6.65a, black dashed rectangle).

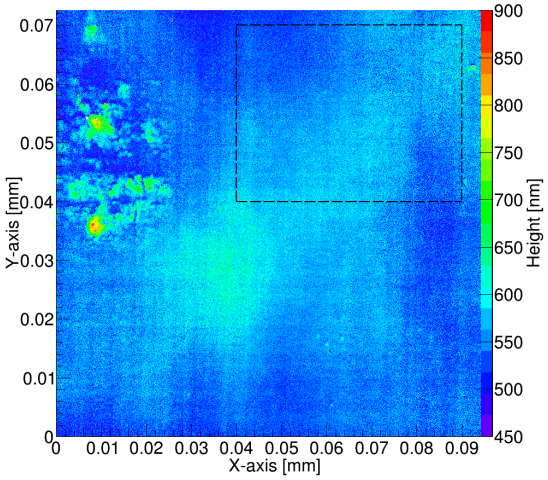

(a) A 3D Color map of the bar surface, measured by means of the confocal laser microscope. The region of the investigation (a flat area without scratches) is enclosed in a black dashed rectangle.

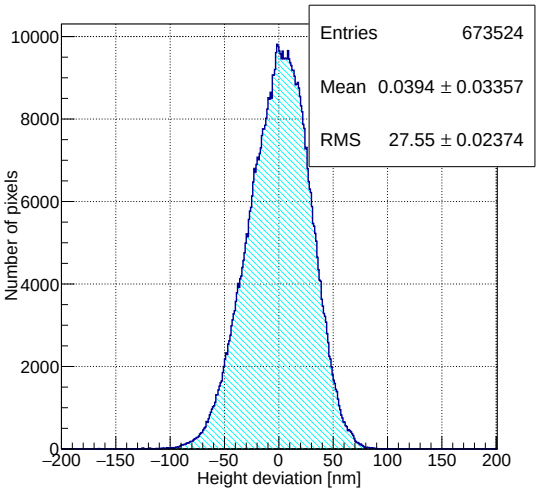

(b) Distribution of the height deviation from the average value within the defined surface area. The RMS of the histogram corresponds to the roughness of the bar surface.

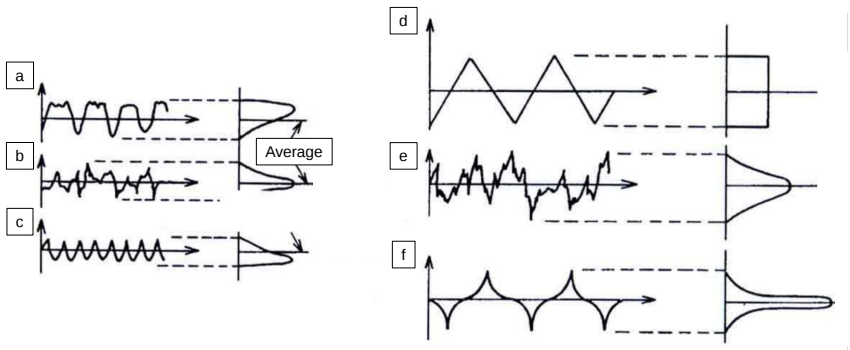

(c) Distribution of the pixel height as a function of the surface shape.

Figure 6.65: Distribution of the bar surface heights in each pixel (47.246×47.246 nm^2) of the microscope matrix.

Figure 6.65b shows a distribution of the surface heights for all pixels within the defined region of the bar. The RMS (Root Mean Square) of the histogram corre-

sponds to the roughness of the fused silica surface, and equal to $27.55 \pm 0.02^{stat} \pm 0.1^{syst}$ nm. An asymmetrical shape of the distribution shifted in a positive direction, indicates that on average the surface is more peak-like and edgy (Fig. 6.65c, cases c and e).

6.4.4.1 Conclusion

Considering obtained results of the fused silica surface characterization by means of the confocal laser microscope, which is precise ($\sim 0.1\ ns$) and accurate, we confirm previous bar surface quality parameters from the beta-source measurements. The ineffective area in the bar corners from the beta-source test ($\sim$200 μm) is within the laser values (100-400 μm); the measured probability of the total internal reflection from the beta source illustrates a bad quality of the polishing, while the laser measurements showed the same indication but with an absolute value for the local roughness of about 28 nm. Comparing with a requested specification for the bars produced, listed in Subsection 6.4.3, we have almost 20 times worse roughness, and about two times higher the edge beveled radius (corner roundness).

Thus we can state, that our method of the fused silica surface characterization with a β-source is well comparable with a precise measurement by means of the confocal laser microscope. The possible improvement can be achieved by means the laser microscope in a series of the linear scan along the whole bar surface, in order to fully characterize its properties, which is a perspective for future investigations.

6.4.5 Cherenkov detector improvements

6.4.5.1 Direct coupling

When the bar is connected to the bundle, only the photons within the numerical aperture of the fiber ($\sim 8°$) can be captured by the fibers. This limitation together with the fiber fill factor (the active area is not equal to the total one due to dead spaces between the fibers inside the bundle packing) reduce about 10 times the number of the Cherenkov photons [65]. Therefore, to increase the amount of light, which can reach the PMT window, we decided to remove bundles with optical fibers and attach a single PMT (R7378A/BA1512) to the readout side of the bars through the viewport (direct coupling, Fig. 6.66a). Taking into account the detection sensitivity of the bars, we decided to swap the bars, putting Bar2 in Bar1 place, and vice versa. To check an electromagnetic (EM) pick-up of the PMT, an additional PMT (blind, R7378A/BA1511) has been installed beside with an aluminum shield, covered both tubes (Fig. 6.66b).

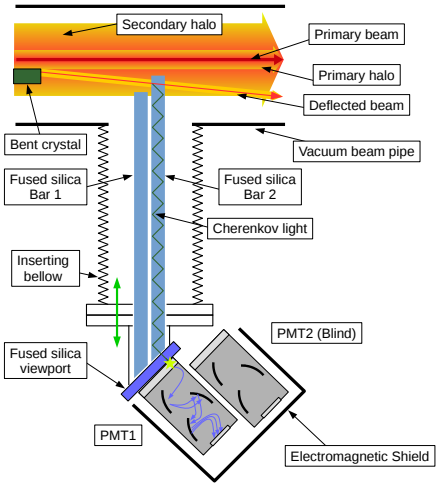

(a) Schematic drawing.

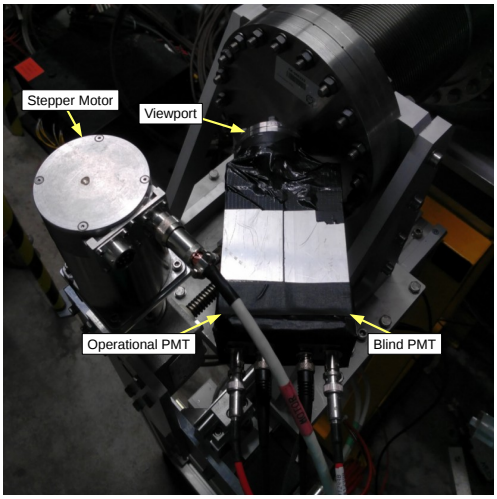

(b) Photo of the setup.

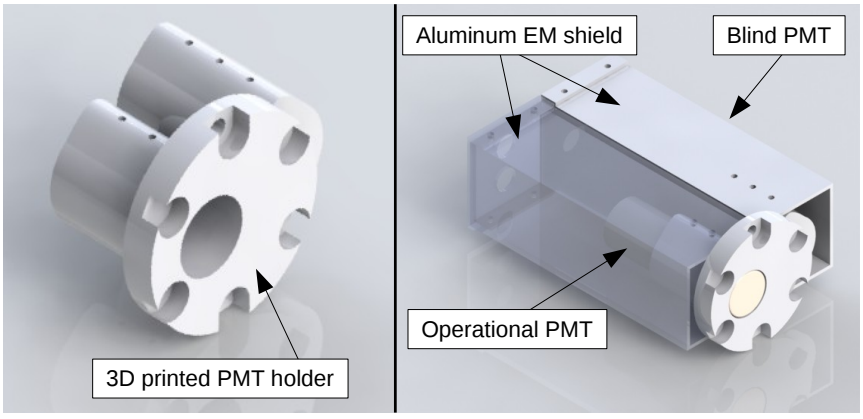

(c) Drawings of the 3D printed holder for PMTs, and aluminum EM shield.

Figure 6.66: New experimental configuration of the CpFM detector on SPS: direct coupling, blind PMT for the EM pick-up, and aluminum EM shield.

Due to the changed configuration of the detector (removed bundle), a self-calibration measurements were needed (Subsection 6.4.2). In 2017 a dedicated SPS MD has been conducted to recalibrate the detector using Xe ion beam with one 3 ns bunch (Tab. 6.11).

Beam	Momentum [ZGeV/c]	Intensity per bunch	Emittance [nm·rad]	Tune Q_h
Xe ion	270	$\sim 6.3 \times 10^{10}$	~19	26.13

Table 6.11: SPS beam conditions during the measurements.

Figure 6.67 shows the distribution of the CpFM charge and amplitude for only Bar2 inserted in the channeled beam, while Bar1 is working blindly. The histogram illustrates three regions, where one or two ions penetrate the fused silica bars. Due to a small linear shift of 5 mm between bars in horizontal plane, there is a probability for the deflected and scattered ions to hit both bars, which is clearly visible on the plot. As we defined above the different detection sensitivity of the bars (the Bar1 is less sensitive with respect to the Bar2), the amplitude (~0.8 V) and charge (~5.5 a.u.) for these two bars ion crossing are lower than the expected double amplitude (~1.2 V) and charge (~11 a.u.) values.

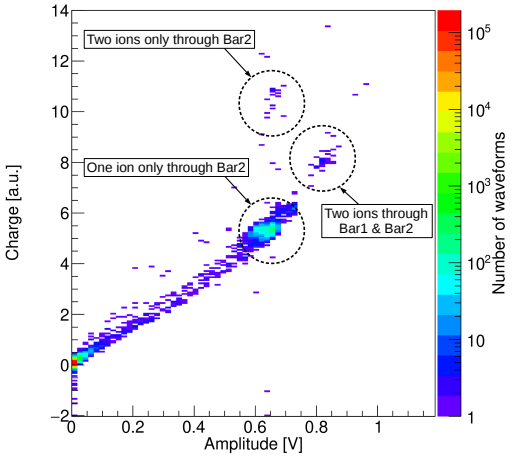

Figure 6.67: CpFM waveform charge as a function of the maximum signal amplitude for 2017 measuremets with 270 ZGeV/c Xe ions. Experimental results of the measurements, where only CpFM Bar2 intercepts the deflected particle beam. The PMT HV is 600 V, sampling frequency is 400 MS/s, while the charge integration window is 240 ns. In color (Z-axis) is represented the number of the analysed waveforms.

Considering only one ion peak of the amplitude and charge distribution, we can

easily compute the calibration parameter at a given voltage of the PMT (Tab. 6.12).

	Amplitude, mV	Charge, a.u.
CpFM Bar2	660.3±1.1	5.3723±0.0215

Table 6.12: Single 270 ZGeV/c Xe ion parameters, computed by means of the USB-WaveCatcher software for 600 V of the CpFM PMT voltage supply. Corresponds to $\sim 5.5 \cdot 10^5$ waveforms.

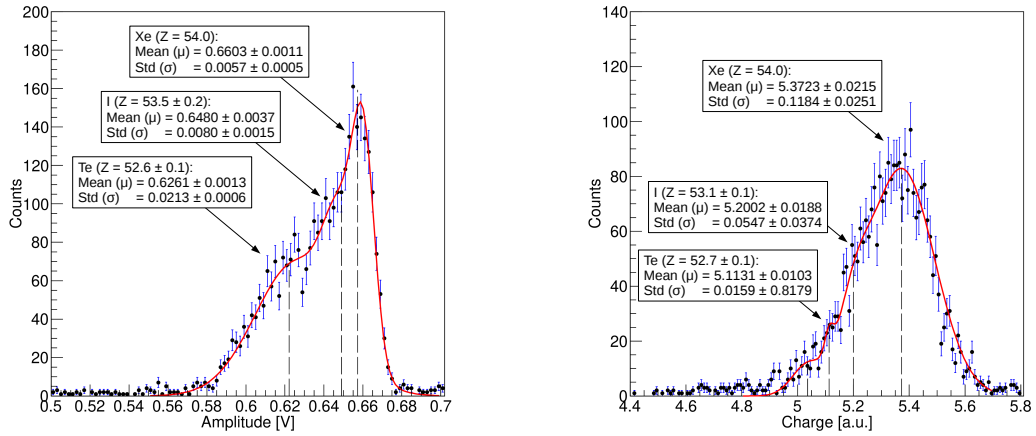

(a) Amplitude distribution.

(b) Charge distribution.

Figure 6.68: Single ion parameters for the CpFM Bar2 intercepting the channeled beam. Triple Gaussian fit introduces different Z ions distribution. The PMT HV is 600 V, sampling frequency is 400 MS/s, while the charge integration window is 240 ns. Corresponds to $\sim 5.5 \cdot 10^5$ waveforms.

Figure 6.68 shows amplitude and charge distributions for a single ion crossing the CpFM Bar2. Each distribution has an asymmetrical shape due to the different Z ions crossing the bar (beam contamination due to the inelastic nuclear interaction of the ions with surrounding obstacles). Taking into account the dependency between the number of the Cherenkov photons produced in the fused silica radiator and charge of the incident particle ($N \sim Z^2$, Eq. 5.8), we can define several peaks, which correspond to different charges. The amplitude distribution (Fig. 6.68a) has a more sharp shape compare to the charge distribution (Fig. 6.68b). This behavior can be explained, by the fact that the measured waveform charge is a sum of all Xe ion destruction products, while the measured waveform amplitude is just a value of the highest waveform peak, which corresponds to the highest Z ion. In such a

way, CpFM detector can be used for the beam contamination measurements using waveform amplitude information.

One of the main goals of the test was to check the EM pick-up of the detector PMT. An expected behavior of the PMT signal for the EM pick-up is big amplitude oscillations, while the integrated charge of the waveform is equal or close to zero.

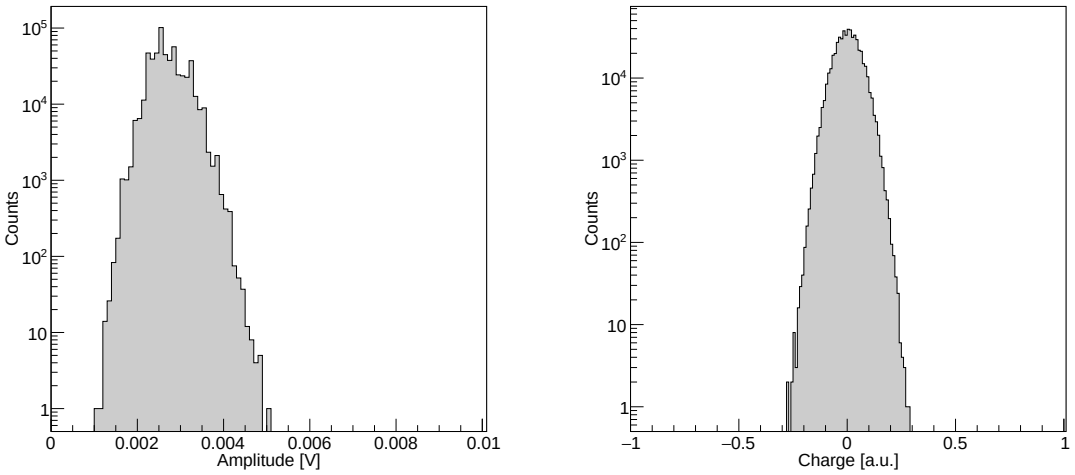

(a) Amplitude distribution.

(b) Charge distribution.

Figure 6.69: Waveform parameters for the CpFM Bar1 (blind), while Bar2 is intercepting the channeled beam. The PMT HV is 600 V, sampling frequency is 400 MS/s, while the charge integration window is 240 ns.

Figure 6.69 shows the amplitude and charge distributions for the blind CpFM Bar1, while Bar2 is intercepting the channeled ion beam. As one can see, the amplitude does not exceed the pedestal value of 6 mV, and charge value is equal to zero, like it was expected. Therefore, we can make a conclusion that in the direct coupling configuration CpFM detector is working properly without EM pick-up of the PMT attached to the viewport.

Continue the calibration procedure of the detector, we have collected data in the parking position, in order to measure a single photoelectron parameters (Fig. 6.70, Tab. 6.13).

Referring to a self-calibration technique (Subsubsec. 6.4.2.1), we can now calculate the amplitude and charge per a single proton in the direct coupling configuration using a single ion parameters (Tab. 6.12). Table 6.14 lists the obtained values, while Table 6.15 shows the number of p.e. per a single proton.

Considering the previous detector configuration results (Tab 6.10), the direct coupling setup improved the detection amount of light by factor ∼10. Therefore,

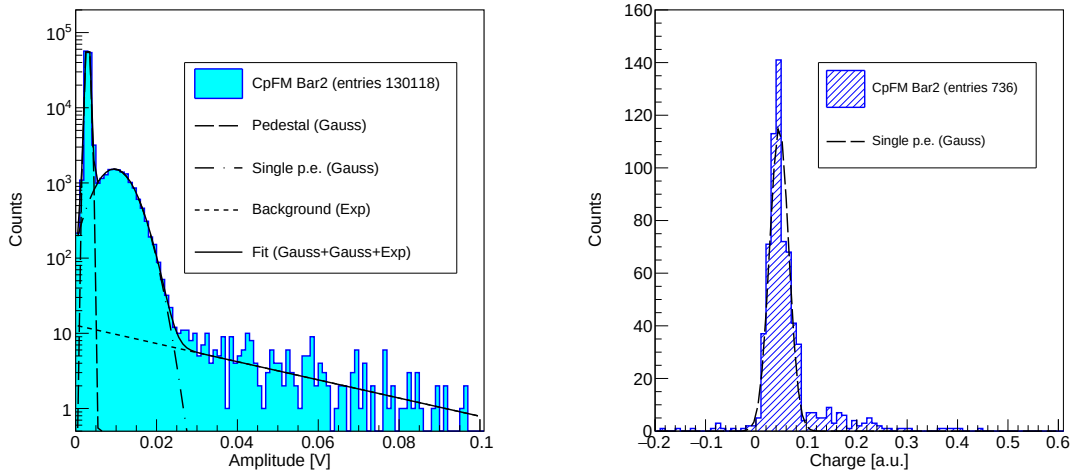

(a) Distribution of the Bar2 signal amplitude.

(b) Distribution of the Bar2 signal charge with applied amplitude cut of 6 mV.

Figure 6.70: CpFM single photoelectron distribution in the parking position with a derect coupling. The data are collected with HV = 1050 V, sampling frequency = 3.2 GS/s, and USBWC dynamic range = ±1.25 V. Solid line is a fit of the amplitude distribution by means of the double Gaussian (Gauss) and Exponential (Exp) functions; dashed line – a signal pedestal fit; dot-dashed line – a single photoelecton peak fit; dotted line – a signal background fit.

	Amplitude, mV	Charge, a.u.
CpFM Bar2	9.5±0.1	0.042±0.001

Table 6.13: Single photoelectron parameters of the signal distributions, computed by means of the USB-WaveCatcher software for HV = 1050 V, sampling frequency = 3.2 GS/s, and USBWC dynamic range = ±1.25 V.

	Amplitude, mV	Charge, a.u.
CpFM Bar2	18.294±0.0055	0.149±0.001

Table 6.14: Computed single 270 GeV/c proton parameters for 1050 V of the PMT supply voltage.

	From the Amplitude, p.e./proton	From the Charge, p.e./proton
CpFM Bar2	1.926±0.020	3.354±0.086

Table 6.15: Calibration parameters of the CpFM detector for 270 GeV/c protons at 1050 V of the PMT supply voltage.

our expectations, about the decreasing of the detected Cherenkov light due to the optical fiber acceptance, are confirmed.

Taking into account our calibration results (Tab. 6.15, From the Charge), the resolution of the detector for a single proton (Eq. 6.9) is about 55%. We can state, that we are still not 100% sensitive to a single proton with a bad resolution of a single proton. Therefore, an improved detector configuration is needed.

6.4.5.2 Radiator geometry

Requirements To increase the particle detection efficiency and to be sensitive to a single proton with a good resolution (10÷20%), the following steps for the detector improvements have to be done:

- Increase the number of the produced Cherenkov photons.
- Decrease the number of the photons internal reflections from the surface of the bar.
- Improve the quality of the fused silica bar surface.

Therefore, a new configuration of the detector has been developed (Fig. 6.71) with a direct coupling of the PMT.

The bar has a cut pyramid shape (square frustum) about 400 mm long to satisfy all listed demands. To increase the number of produced Cherenkov photons inside the bar, its width from the detection side was enlarged up to $d_0 = 10$ mm, due to the dependency between the amount of light and path length (Eq. 5.8). A small slant angle (θ_{sl} of a few degrees) leads to the gradual increasing of the reflected angle after each reflection from the bar surface. In the meanwhile, after a certain number of reflections, Cherenkov photon will propagate almost perpendicular to the readout side of the bar, which removes the needs of the 47 degrees of the bar readout end, like it was done for the previous version of the CpFM [65].

Simulation Several radiator geometries have been selected for the Monte-Carlo simulation with Geant4, in order to compare their benefits (Fig. 6.72):

- **GeaomID 0:** Current CpFM configuration with two bars (SiO_2 length=10 mm).
- **GeaomID 1:** Only one readout bar (SiO_2 length=5 mm).
- **GeaomID 2:** One wide bar (SiO_2 length=10 mm).
- **GeaomID 3:** One wide bar with a straight readout side (SiO_2 length=10 mm).

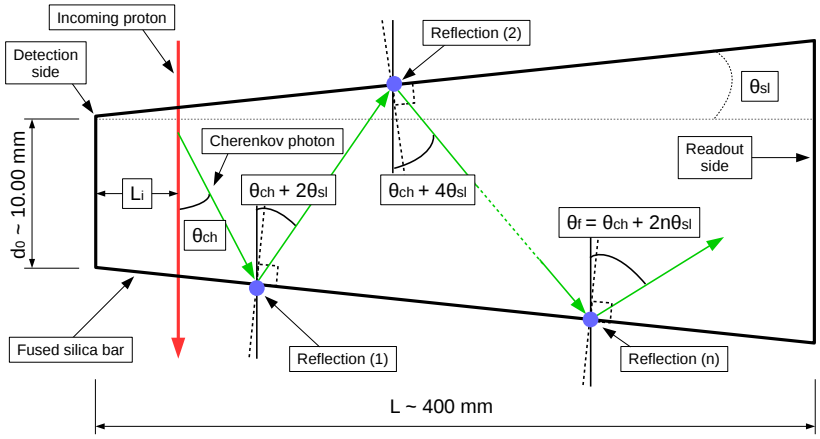

Figure 6.71: Schematic drawing of the pyramid fused silica bar. Charged particle (red arrow line) penetrates at L_i position the detection side (width of d_0) of the bar and produces Cherenkov photons (green arrow line) in the Cherenkov angle $\theta_{ch} \simeq 47°$. Each internal reflection (blue dots) from the bar surface, the photon will increases the reflection angle by $2\theta_{sl}$, where θ_{sl} is a slant angle of the pyramid. The final angle ($\theta_f = \theta_{ch} + 2n\theta_{sl}$) after a certain number of the reflections (n).

- **GeaomID 4:** One pyramid bar with $\theta_{sl} = 1°$ (SiO_2 length=10 mm).
- **GeaomID 5:** One pyramid bar with $\theta_{sl} = 2°$ (SiO_2 length=10 mm).

A pencil beam of 270 GeV/c protons has been sent onto each bar with perfect surface polishing ($P_{IR} = 100$). Figure 6.73 shows the simulation results for 1000 generated protons. It is evident, that for the 5 mm thick fused silica bar the number of photons (∼220 photons) is two times less than for the 10 mm bar (∼440 photons).

In the simulation, the number of the internal reflection from the surface of the bar for each Cherenkov photon has been calculated. Figure 6.74 illustrates the distribution of the photon reflections for different radiator geometries. As expected, in 5 mm thick bar the photon makes two time higher number of reflection with respect to the 10 mm thick bar. Due to the slant angle the number of reflection for pyramid bars is much lower compare to the straight one (2-4 times). The photon beam inside the pyramid bar becomes more orthogonal to the readout side of the bar (Fig. 6.75). These results are well comparable with an analytical approach, based on the pure geometrical calculation (Fig. 6.76).

On the other hand, the increase of the bar slant angle (θ_{sl}) leads to the loss of the Cherenkov photons, due to the critical angle effect inside the bar. Figure 6.77 demonstrates this effect: for the $\theta_{sl} = 1°$ (Fig. 6.77a), all produced photons are

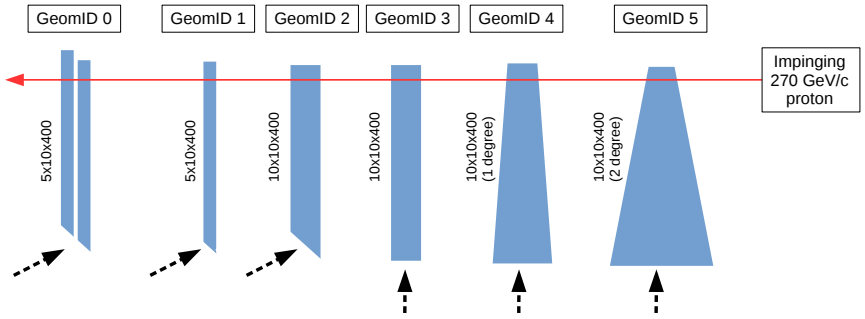

Figure 6.72: Different radiator configurations for the Geant4 simulation. Red solid line – incident 270 GeV/c proton, black dashed arrow – readout side of the bar.

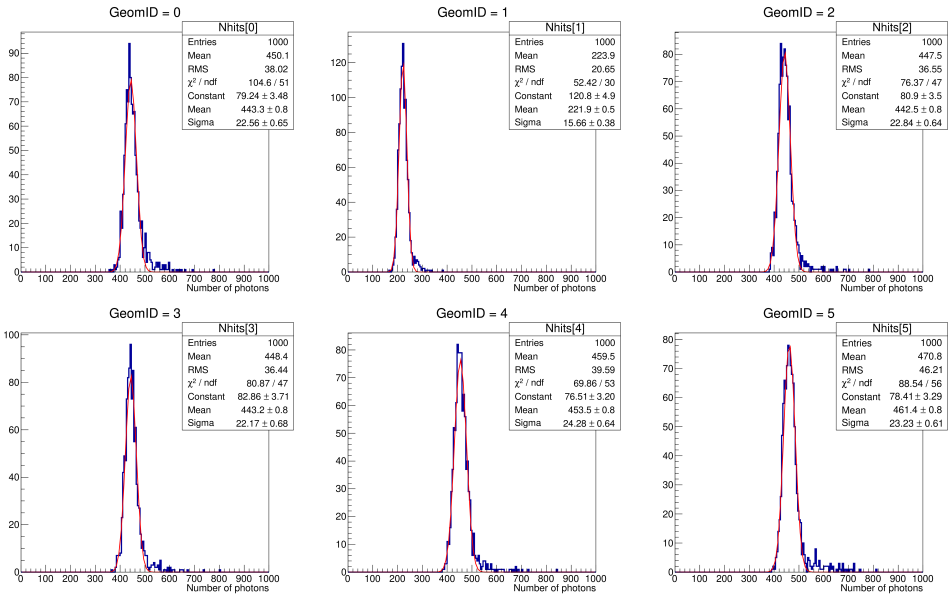

Figure 6.73: Geant4 simulation results of the Cherenkov photons, which have been produced by the interaction of the 270 GeV/c protons with the fused silica bar, and hit the bar readout side. Red solid lines is a Gaussian fit.

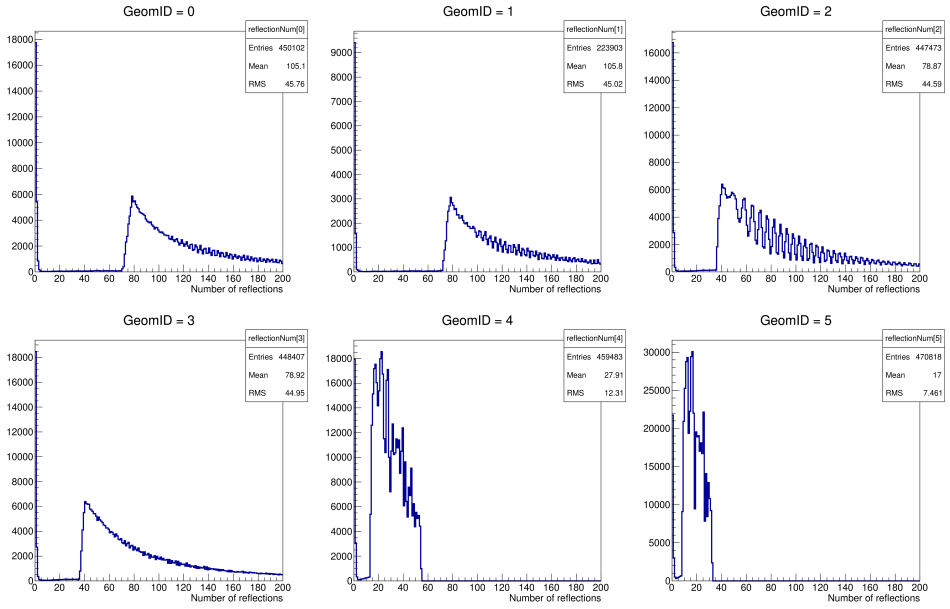

Figure 6.74: Geant4 simulation results of the Cherenkov photons internal reflection number.

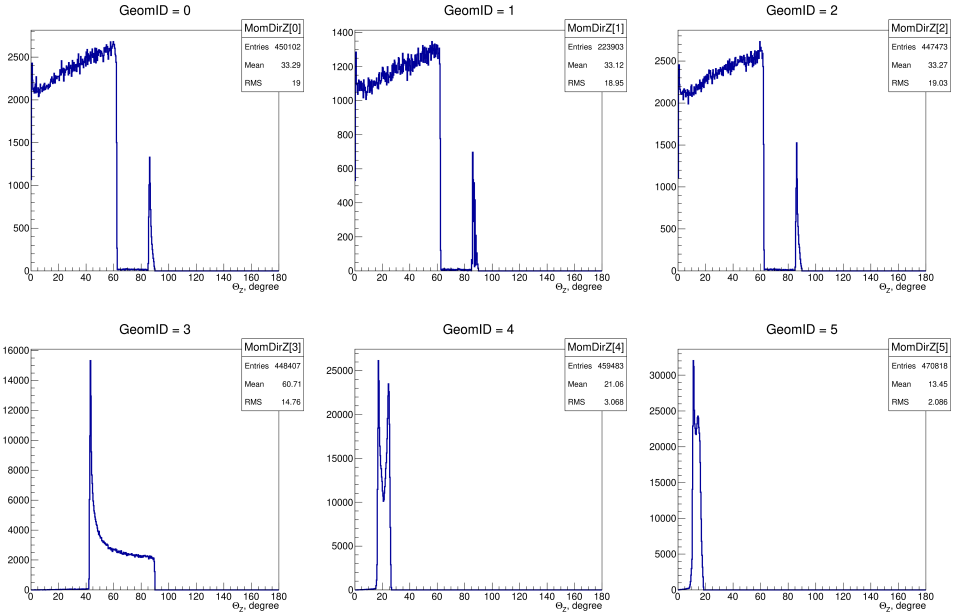

Figure 6.75: Geant4 simulation results of the angle between the normal vector to the readout side of the bar and direction of the Cherenkov photon.

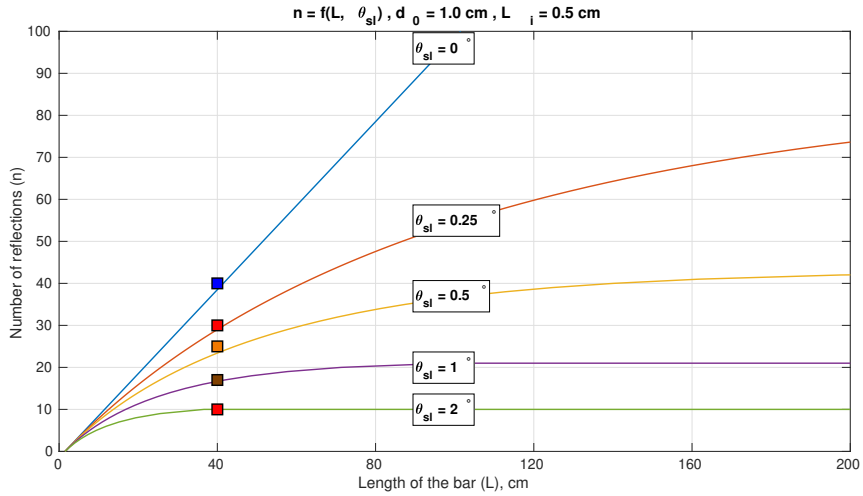

(a) Number of the Cherenkov photon reflections (n) as a function of the pyramid bar length (L) and slant angle (θ_{sl}). Coloured rectangles indicate Geant4 simulation results for ∼40 cm long pyramid bar.

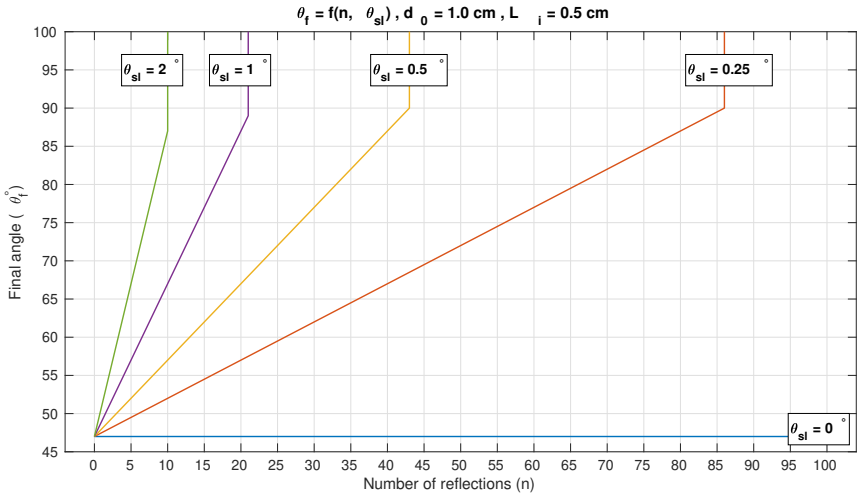

(b) Final angle of the Cherenkov photons (θ_f) at the readout side of the pyramid bar as a function of the reflection number (n) and slant angle (θ_{sl}).

Figure 6.76: Pyramid bar geometry optimisation using analytical approach (solid coloured lines) and Geant4 simulation (coloured rectangles) for $d_0 = 10$ mm of the detection side width at $L_i = 5$ mm position.

collected on the bar readout side, while for the $\theta_{sl} = 2°$ (Fig. 6.77b), some part of the Cherenkov photos is lost, due to their reflection angle, which is close to the critical angle of the total internal reflection (Eq. 6.14).

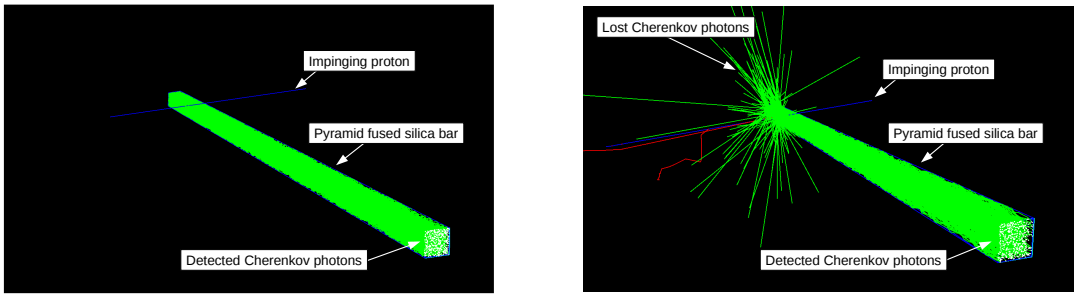

(a) $\theta_{sl} = 1°$. (b) $\theta_{sl} = 2°$.

Figure 6.77: Picture of the Geant4 simulation event, where an incident 270 GeV/c proton, crossing the fused silica bars with two different slant angles (θ_{sl}), produces Cherenkov light.

$$\theta_c = arcsin\left(\frac{n_2}{n_1}\right) \simeq 43°, \tag{6.14}$$

where n_1 and n_2 are the average refractive indexes of the fused silica ($n(SiO_2) \simeq 1.4585$) and vacuum ($n \simeq 1.0$), respectively.

Figure 6.78 illustrates the critical angle effect, where the number of the detected photons is increasing with the enlarging of the bar slat angle until $\sim 1°$, then the amount of the lost photons starts to grow, and at around 2° the detected amount of the Cherenkov light is decreased on $\sim 20\%$.

According to the results, the pyramid shape of the radiator with $\theta_{sl} = 1°$ has been chosen, avoiding the light losses due to the critical angle effect, with a high number of the detected Cherenkov photons (∼450 photons), and low number of the reflections ($N = 30$).

Concerning the investigation of the fused silica bar quality described before, we have asked the bar producing company for the best possible surface polishing quality and the smallest achievable ineffective area at the edges of the bar, in order to reduce Cherenkov light losses. Due to the space occupancy of the detector inside the SPS tank the length of the bar is limited to 40 cm, while the size of the readout side cannot exceed PMT (Hamamatsu R7378A) window diameter (25 mm).

H8 measurements To test the simulation results a set of three fused silica bars with different geometries has been prepared (Fig. 6.79): (1) a straight 10 mm thick

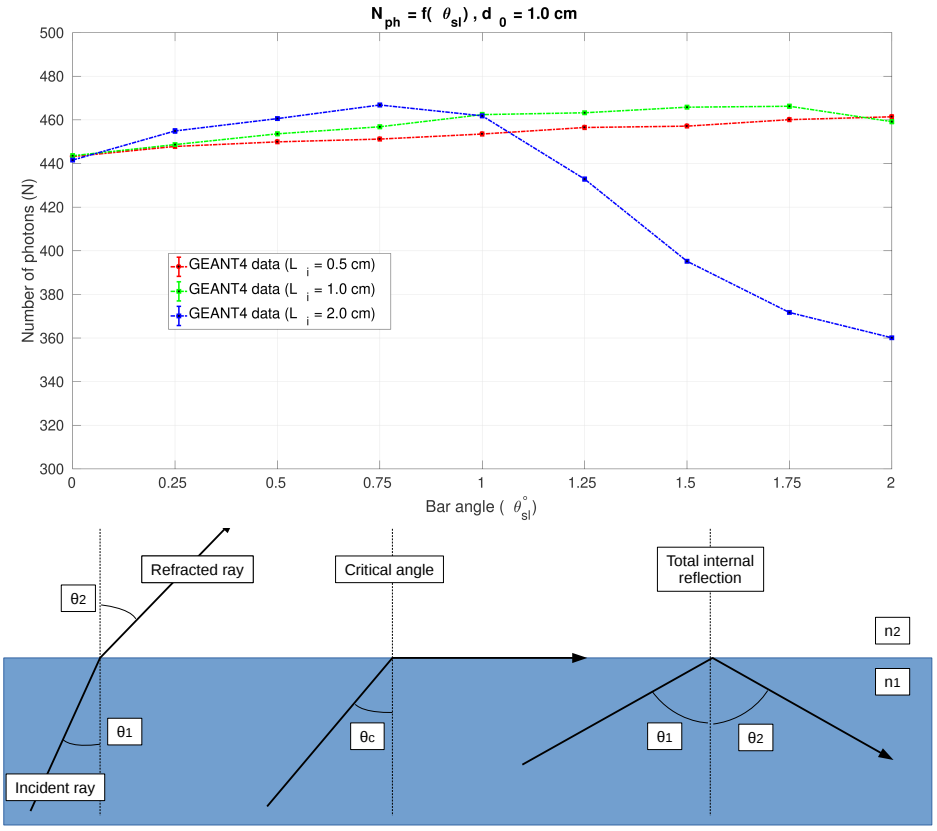

Figure 6.78: Geant4 simulation results of the Cherenkov photon number (N) as a function of the bar slant angle (θ_{sl}) and interaction position (L_i), for the thickness of the bar (d_0) of 10 mm. n_1 and n_2 are the refractive indexes of the fused silica (SiO_2) and vacuum. The critical angle (θ_c) effect starts to dominate after $\sim 1°$

.

bar (I-shape bar, GeomID 2), (2) banana bar of 5 mm thickness with a curved nose of 30 mm length, (3) pyramid bar with a slant angle of $\sim 1^\circ$ (GeomID 4). Each bar has been used with a viewport, and read by the Hamamatsu PMT R7378A.

Figure 6.80 demonstrates the experimental setup of the H8 measurements with a 180 GeV/c pions beam. Each bar has been inserted into the beam by several millimetres from the detection side. The banana bar has been used in two positions: (1) pion beam crossing the nose of 30 mm thick, and (2) pion beam crossing the bar outside the nose where the thickness of the bar is 5 mm.

Figure 6.81 shows the experimental results of the measurements. Due to the fact, that each PMT was working with different applied voltage, the data is presented with the PMT gain normalization.

As expected, the pyramid bar has shown the best detection efficiency. The banana bar has demonstrated almost the same high efficient light collection by means of its nose, which is 30 mm thick. Unfortunately, due to the banana-shape it is very sensitive to the interaction position along the bar, therefore it cannot be used as a beam monitor at the SPS configuration. The I-shape bar of 10 mm thick showed a higher counting efficiency, compare to the 5 mm of the banana bar (outside the nose), but it is much lower (3 times) than the pyramid bar did.

Detection efficiency as a function of the hit position An additional research has been done in order to investigate the detected amount of light as a function of the particles penetration position along the bar. Figure 6.82a illustrates the experimental layout of the measurements, which have been done on H8 beamline with a 180 GeV/c pion beam. Two plastic scintillators ($5 \times 10 \times 5$ mm^3), placed on the beam, have been used in the signal coincidence configuration as an external trigger for the USB-WaveCatcher. A horizontal linear scan of the bar has been done crossing the incident beam. Figure 6.82b shows the average signals amplitude along the scan. To find the edge of the bar an Error Function fit has been done, while a Constant Function fit defines the reference value, on which the distribution will be normalized.

Using a method of the fused silica surface quality characterization, well-described in Subsection 6.4.3, we have done a Geant4 simulation with different bar parameters: the probability of total internal reflection (P_{IR}) and the fraction of ineffective area at the edges of the bars (F_{IA}). Figure 6.83a shows a computed χ^2 (Eq. 6.13) for the pyramid bar as a function of the F_{IA} and the P_{IR}. We have found a global minimum at $F_{IA} = 0.006 \pm 0.006$, $P_{IR} = 96.0 \pm 0.5$ %). These values correspond to the simulation results that are shown in Fig. 6.83b and well-describe the experimental

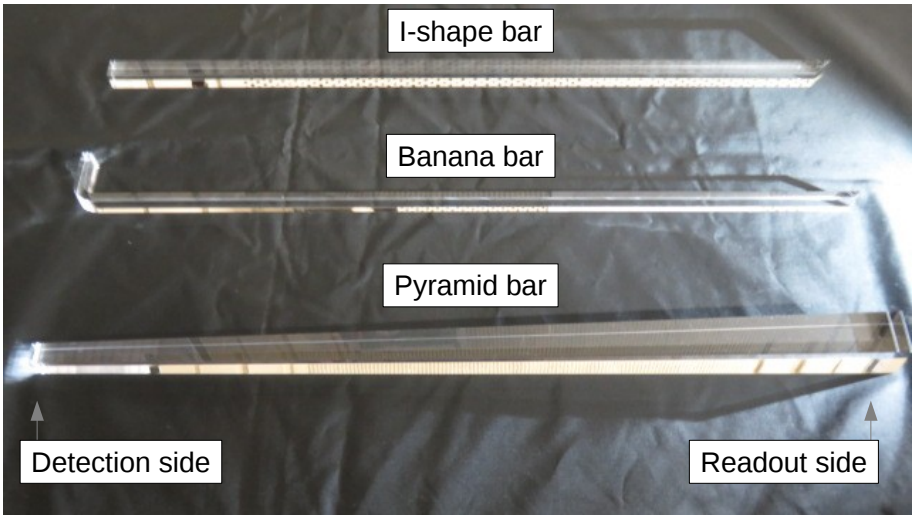

(a) Photo of the bars.

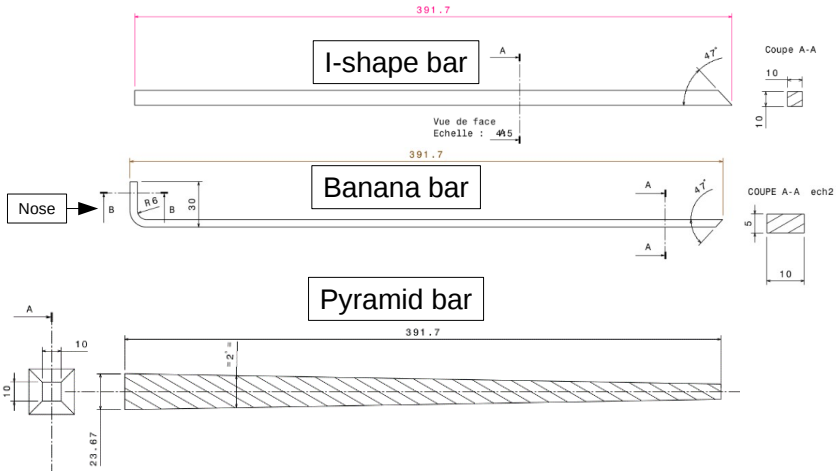

(b) Schematic drawing of the bars.

Figure 6.79: New geometries of the fused silica bars, which have been tested at H8 beam line.

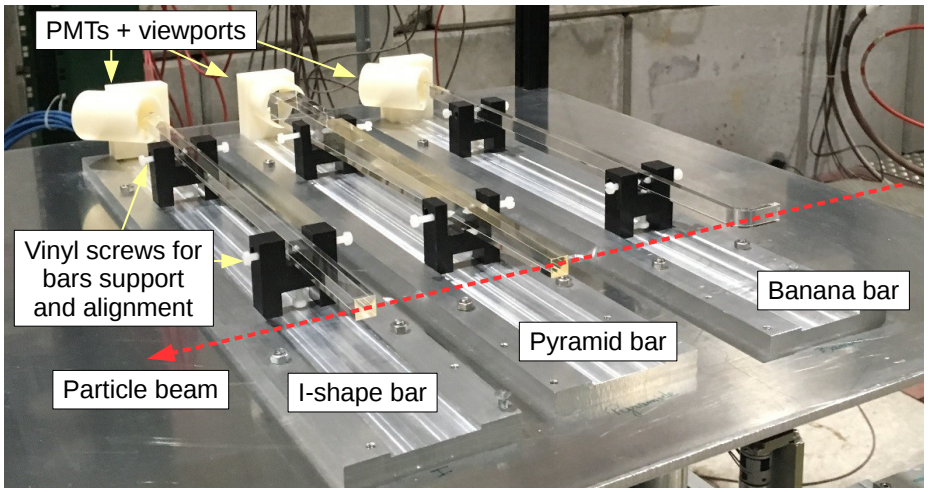

Figure 6.80: Experimental setup of the different CpFM radiators tested on H8 beam line with a 180 GeV/c pion beam.

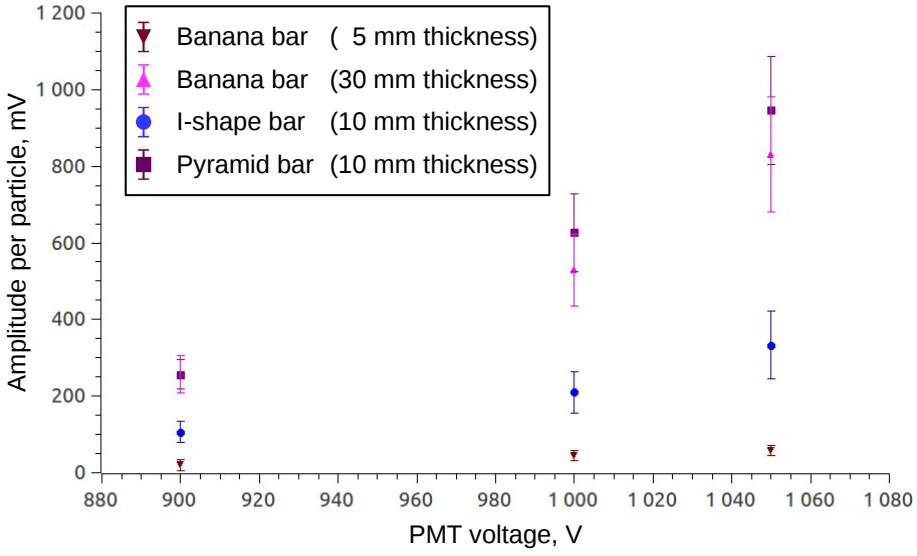

Figure 6.81: Experimental results of the CpFM signal amplitude as a function of the PMT voltage for different radiators tested on H8 beam line with a 180 GeV/c pion beam, normalized to the PMT gain.

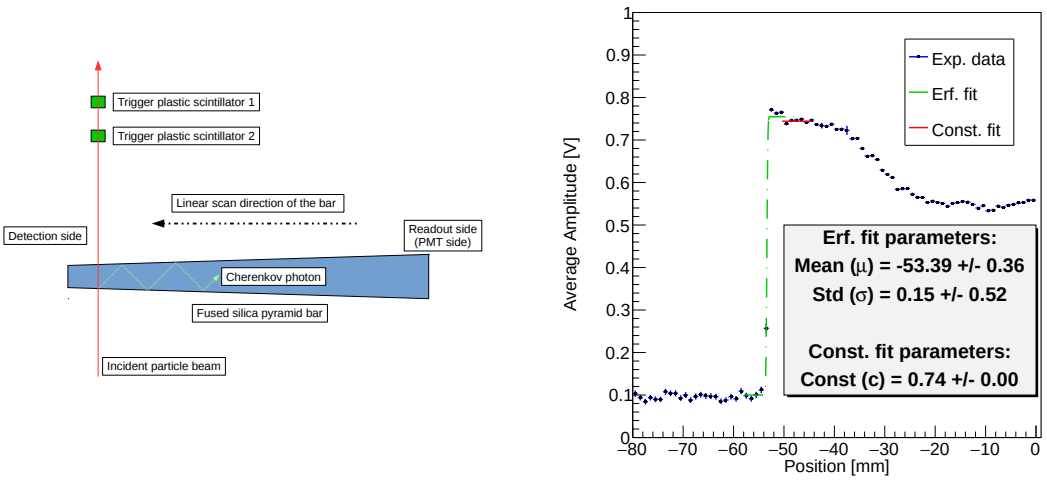

(a) Experimental layout. Each plastic scintillator is 5 mm thick along the beam, 5 mm of width (perpendicular to the beam), and 10 mm of height.

(b) Experimental data of the linear scan. Average signals amplitude as a function of the incident beam position along the bar. An Error Function fit (green dot-dashed line) defines the position of the bar edge, while a Constant Function fit (red dashed line) shows the normalization value of the amplitude.

Figure 6.82: CpFM linear scan at H8 beamline with a 180 GeV/c pion beam.

data.

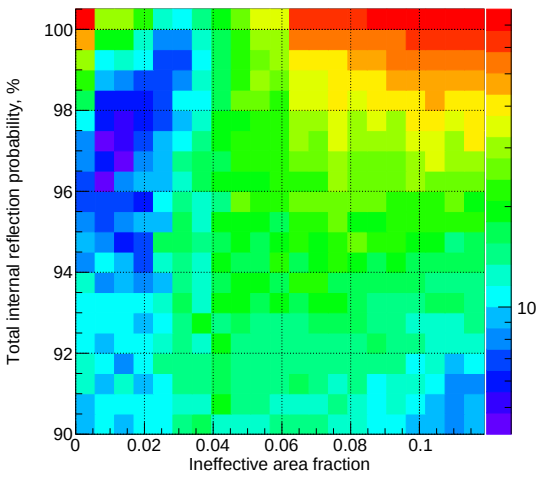

(a) χ^2 distribution of the difference between experimental and simulated data.

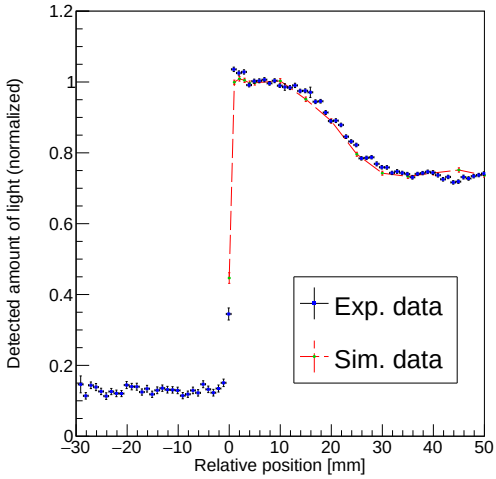

(b) Horizontal CpFM scan. Detected amount of the Cherenkov light as a function of the horizontal CpFM position with respect to the edge of the bar (0 mm), comparing between experimental data and Geant4 simulation results. Experimental data: blue squares with black error bars; simulation: green circles with a red dashed line.

Figure 6.83: Simulation results.

Due to some hardware restrictions, the linear scan of the CpFM detector has been performed only for about 50 mm region of the detection side. However, using the simulation routine we can investigate the behavior of the detected amount of the Cherenkov light for the whole bar length. Figure 6.84 illustrates the behavior of the detected amount of the Cherenkov light as a function of the beam position for boundary bar parameters ($P_{IR} = 90 \div 100\%, F_{IA} = 0 \div 0.12$).

Three regions of interest can be defined: $R1$ (0-30 mm) – all produced Cherenkov photons hit the readout side of the bar (then this number is reduced according to the quantum efficiency of the PMT) (Fig. 6.85a); $R2$ (50-150 mm) – only half of the produced photons can reach the readout side of the bar, due to the critical angle light losses discussed above (Fig. 6.85b); $R3$ (250-390 mm) – the focusing of the Cherenkov light due to the pyramid shape of the bar stops to work and large number of photons reflect from the readout side of the bar (Fig. 6.85c).

The surface quality of the bar plays an important role in the photon collection. The decreasing of the P_{IR} and increasing of the F_{IA} reduce the number of detected photons due to the high number of internal reflections. This is a more significant

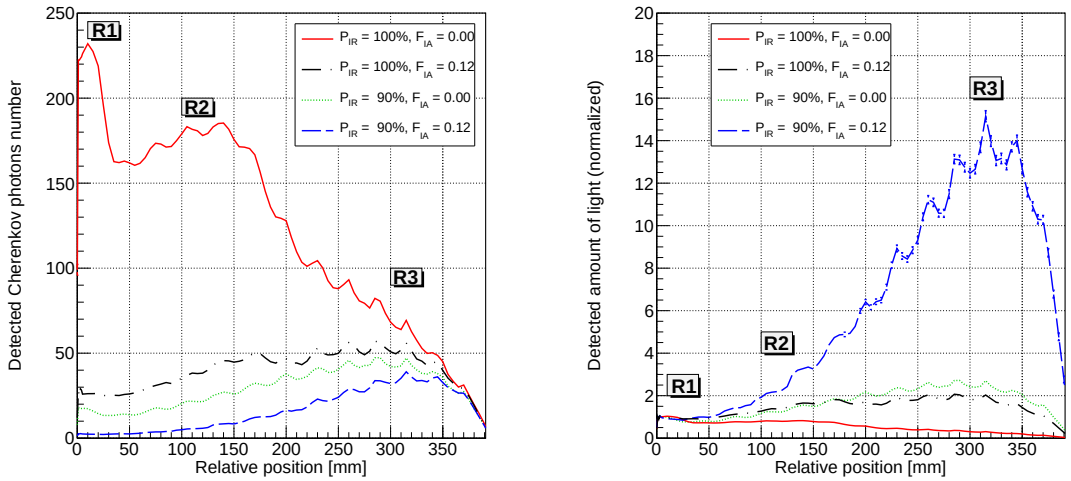

(a) Detected number of the Cherenkov photons as a function of the beam position and bar parameters.

(b) Detected amount of the Cherenkov light as a function of the beam position and bar parameters, normalized.

Figure 6.84: Experimental and simulation data comparison.

effect, when the beam is hitting the detection side of the bar (up to several cms from the edge). From the opposite side of the bar, the number of photon reflections is low, and the surface quality is not so important anymore (Fig. 6.84a). Due to the pyramid shape, the number of the produced Cherenkov photons is growing with the distance from the detection side of the radiator, therefore the relative number of registered amount of light (detected versus produced photons) is higher at the readout side of the bar (Fig. 6.84b).

A wave-like behavior in Figure 6.84 results from the fact, that depending on the incident beam position along the bar, a front of the produced Cherenkov photons hits different regions of the readout PMT window. In the meanwhile, the diameter of the PMT sensitive window is about 22 mm, while the readout side of the bar is about 24 mm. Therefore, when Cherenkov photons hit the corner of the readout side of the radiator, some amount of them becomes lost, which leads to the decreasing of the detected photons.

The obtained fused silica pyramid bar characteristics can be used during the further linear scans of the CpFM. Considering the detected photons dependency for different beam positions along the bar, it is necessary to use only about 20 mm of the radiator, in order to count the absolute flux of incident particles with the current detector calibration parameters. For the longer linear scans, the latter has to be corrected taking into account the obtained behaviors (Fig. 6.84).

Considering the detected number of photons as a function of the hit position

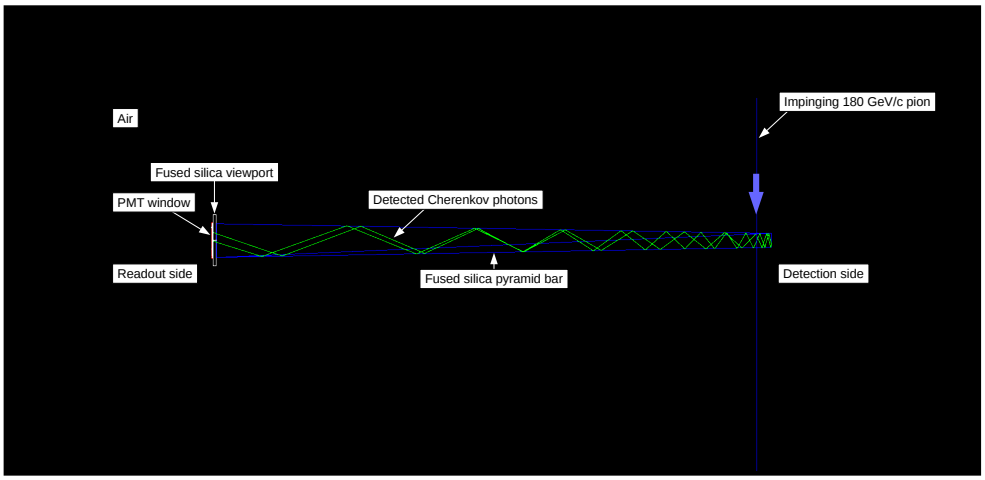

(a) Pion hits at 10 mm from the detection side.

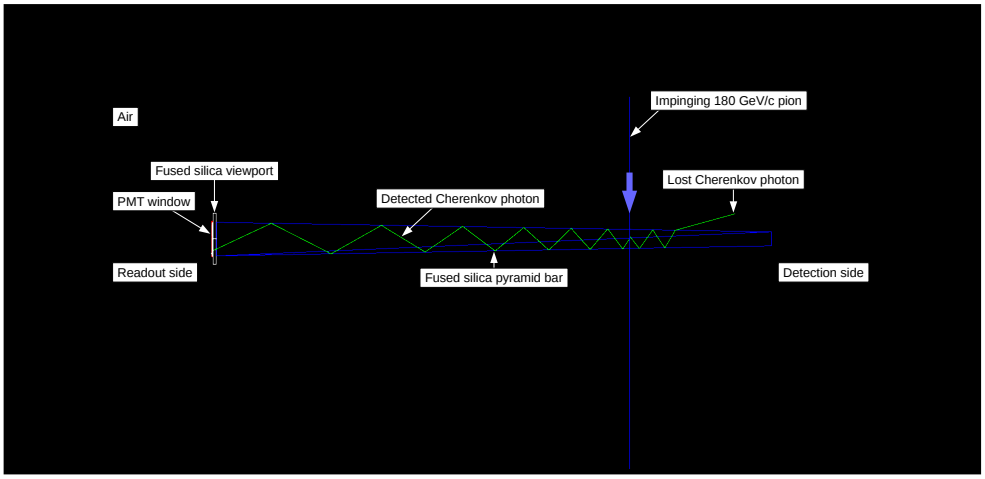

(b) Pion hits at 100 mm from the detection side.

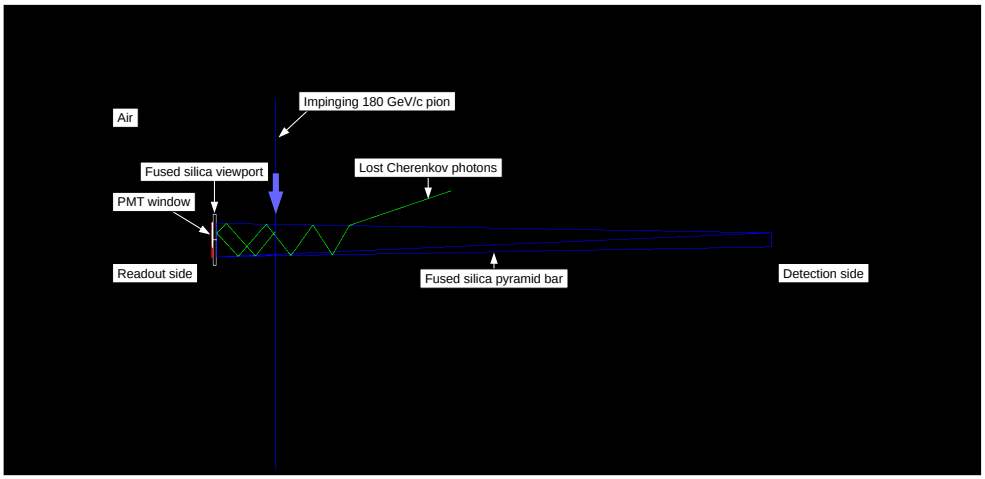

(c) Pion hits at 350 mm from the detection side.

Figure 6.85: Visualization of the Geant4 simulation.

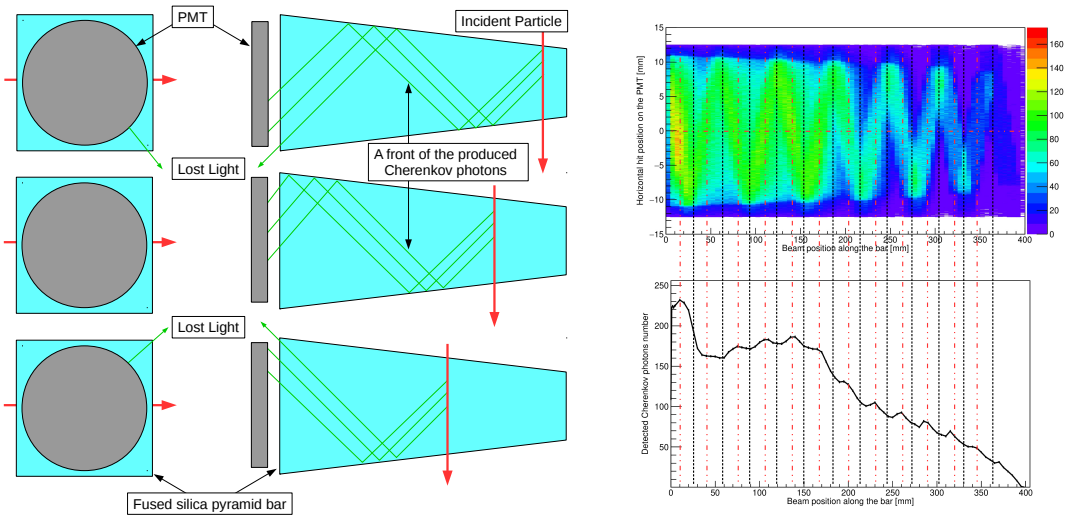

Figure 6.86: Simulation results of the horizontal Cherenkov photon hit position on the PMT window as a function of the incident particle position along the bar. Red dot-dashed lines correspond to the peaks of the photon number distribution (i.e. the maximum of the light detection), while black dashed lines illustrate valleys position (i.e. light losses).

along the bar, we can conclude the following: for a good quality ($P_{IR} \rightarrow 100\%$ and $F_{IA} \rightarrow 0$) fused silica radiator, the background signal (particles, which hit closely to the readout side) is suppressed about 5 times with respect to the measured signal (particles, which hit closely to the detection side); and the opposite situation for the bad quality radiator ($P_{IR} \rightarrow 90\%$ and $F_{IA} \rightarrow 0.12$) – background contribution is more than 10 times higher compared to the measured signal.

Installation on SPS Considering the simulation and H8 beam line measurements results, the final configuration of the new CpFM detector for the SPS accelerator has been defined (Fig. 6.87). The fused silica pyramid bar is attached to the Hamamatsu PMT R7378A/ZN2207 (Fig. 6.88) through the viewport. A monitoring system based on the calibrated LED diode to verify the CpFM operation regime has been installed in front of the bar inside the beam pipe.

6.4.5.3 Self-calibration with protons on SPS

The self-calibration of the new CpFM detector has been done at the SPS in 2018. The detector was inserted in the deflected 270 GeV/c proton beam. To avoid signal saturation, an offset of 1.130 V has been applied to the CpFM readout channel of the USB-WaveCatcher. The HV supply of the PMT was setted to 800 V, due to

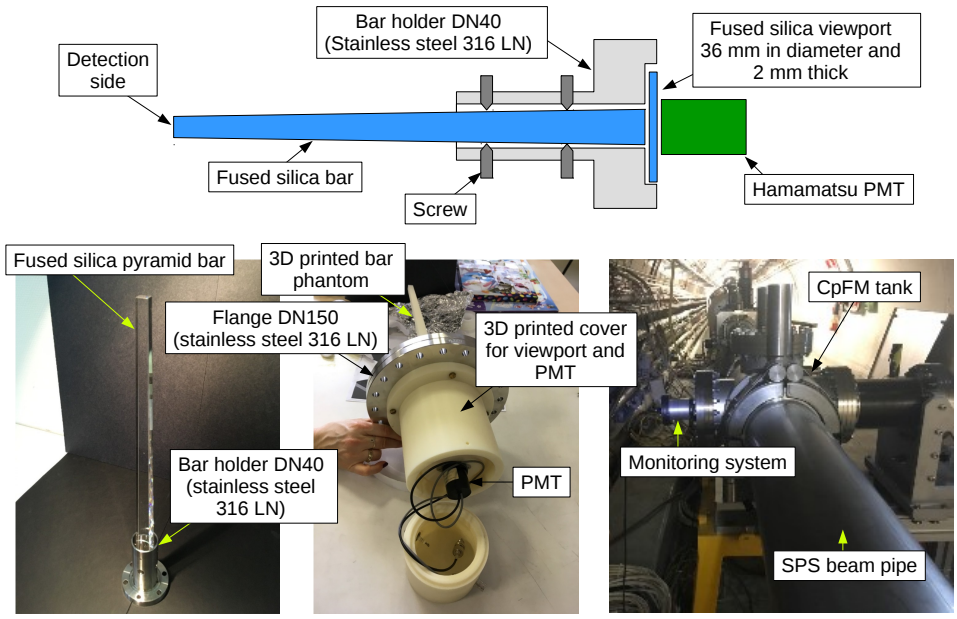

Figure 6.87: Upgraded CpFM detector configuration. Monitoring system installed in front of the CpFM bar is based on the calibrated LED diode.

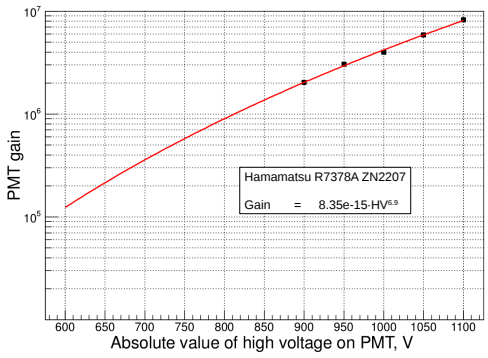

Figure 6.88: Measured gain for the Hamamatsu PMT R7378A/ZN2207 with a different HV.

the expected high flux of the Cherenkov photons produced by protons in 10 mm of the fused silica. Figure 6.89 shows the experimental results of the signals amplitude and charge distributions. The latter has been obtained applying the amplitude cut of 6 mV, in order to remove the pedestal signals. Each of the distributions has a peak-like shape, where it is clearly visible peaks from one, two, three and four protons crossing the bar. In such a way we can perform a self-calibration of the detector by using only a proton run.

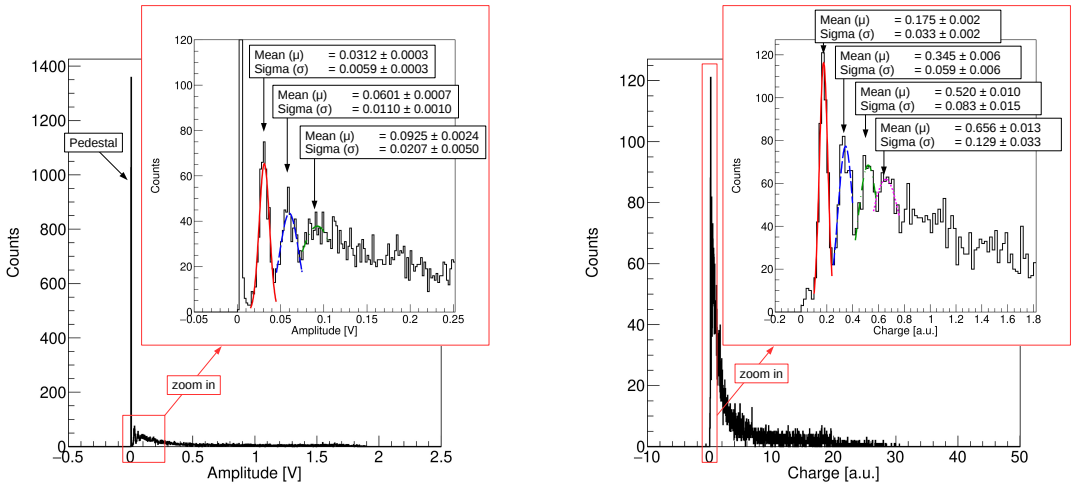

(a) Amplitude distribution of the signals. The pedestal indicates the number of the machine turns without particle extraction and makes up 24% of the total.

(b) Charge distribution of the signals with applied amplitude cut of 6 mV.

Figure 6.89: CpFM detector signal distributions for the 270 GeV/c channeled proton beam on SPS. The data are collected with HV = 800 V, and sampling frequency = 3.2 GS/s.

A single proton parameters for different PMT high voltages are listed in Table 6.16 and illustrated in Figure 6.90 with an exponential fit.

PMT voltage, V	Gain	Amplitude, mV	Charge, a.u.
700	$3.58226 \cdot 10^5$	11.7±0.1	0.069±0.001
750	$5.76659 \cdot 10^5$	19.2±0.4	0.114±0.002
800	$9.00185 \cdot 10^5$	31.2±0.3	0.175±0.002
900	$2.02914 \cdot 10^6$	77.8±1.3	0.407±0.004

Table 6.16: Measured CpFM signal parameters for a single 270 GeV/c proton.

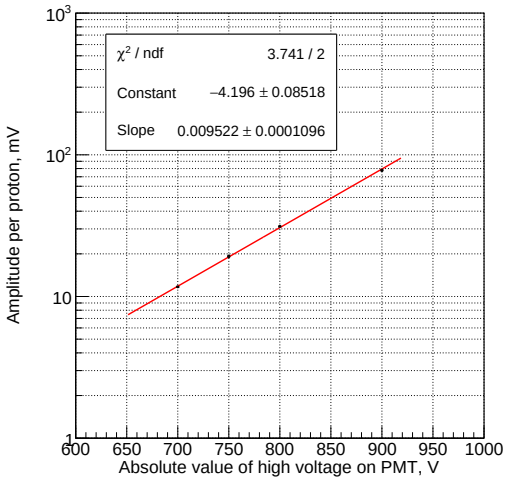

(a) Amplitude as a function of the PMT supply voltage.

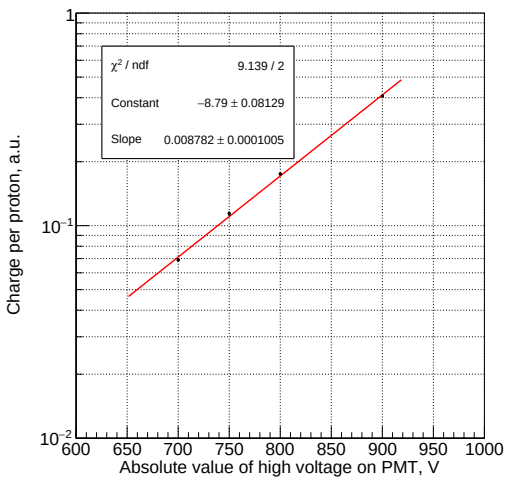

(b) Charge as a function of the PMT supply voltage.

Figure 6.90: Measured single proton parameters as a function of the PMT voltage. Red line is an exponential function fit: $f(x) = exp(Constant + Slope \cdot x)$.

Taking into account the obtained results, we can determine the detection limits of the CpFM detector. Due to the high flux of the Cherenkov photons produced by a charge particle in 10 mm of the fused silica, we are sensitive to a single proton. According to the PMT characteristics[7], the optimal range of the supply voltage between anode and cathode is 500÷1250 V, while the finite dynamic range of the USBWC is ±1.25 V (i.e. the maximum signal amplitude is 2.5 V), which leads to the maximum number of the detected protons for different HV. The calculated detection limits of the CpFM by means of the fit parameters (Fig. 6.90a) are shown in Figure 6.91.

Regarding the measured charge distribution (Fig. 6.89b), where we can clearly separate peaks from the different number of incident protons, the proton detection resolution can be defined as it was done for the first CpFM version in [65]:

$$R = \frac{\sigma}{\mu}, \tag{6.15}$$

where σ and μ are the standard deviation and mean value for a given proton peak. Figure 6.92 illustrates the detection resolution as a function of the incident protons. As expected, this value is proportional to $\frac{1}{\sqrt{N}}$, where N is a number of the detected particles (e.g. protons or photoelectrons).

[7] http://www-eng.lbl.gov/~shuman/NEXT/MATERIALS&COMPONENTS/PMT/PMT_hamamatsu_R7378A%20.pdf

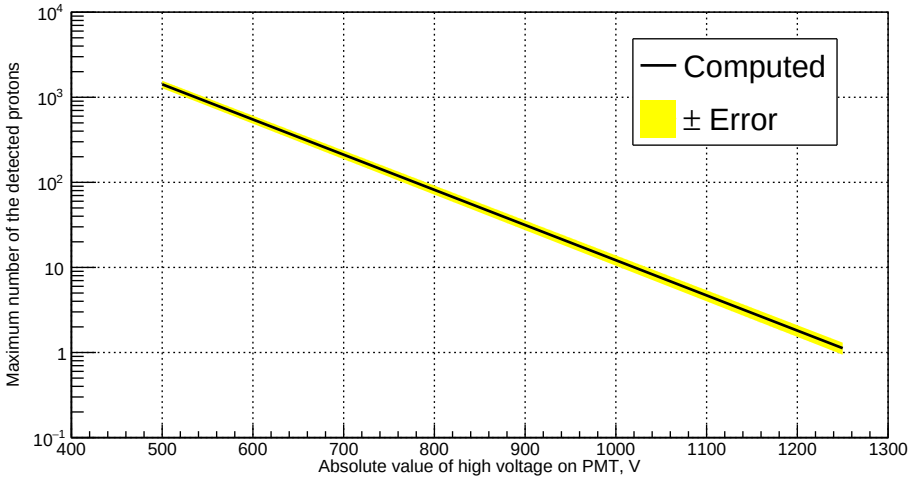

Figure 6.91: Maximum number of the detected protons using CpFM as a function of the PMT voltage supply.

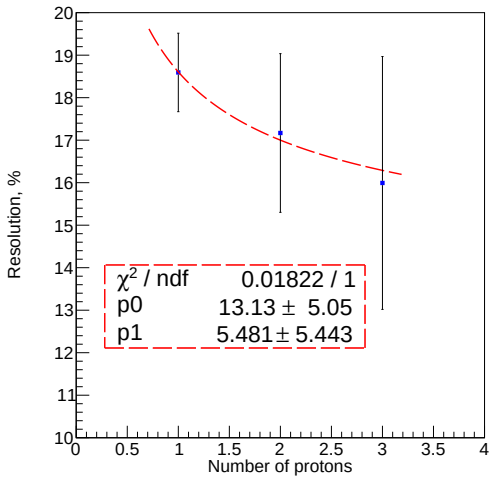

Figure 6.92: Measured CpFM detector resolution as a function of the incident protons. Red dashed line is the following fit function:
$Resolution = p0 + p1 \cdot (Number\ of\ protons)^{-0.5}$.

6.4.5.4 CpFM detection efficiency

Considering the old versions of the CpFM detector, where the Cherenkov radiator bars were 5 mm thick, the average photoelectrons number per proton (λ) is around one (Tab. 6.10,6.15, and Subsec. 6.2.1). Therefore, we can assume, that the probability (P) for a single proton to produce a certain number of the photoelectrons (N) can be described using a Poisson distribution function:

$$P(N) = \exp^{-\lambda} \frac{\lambda^N}{N!}. \tag{6.16}$$

Figure 6.93 shows the computed detection efficiency, which is calculated as a probability to detect a photoelectron per a given number of protons: $P(N > 0) = 1 - P(N = 0)$. The detection resolution of the detector is illustrated in Figure 6.94.

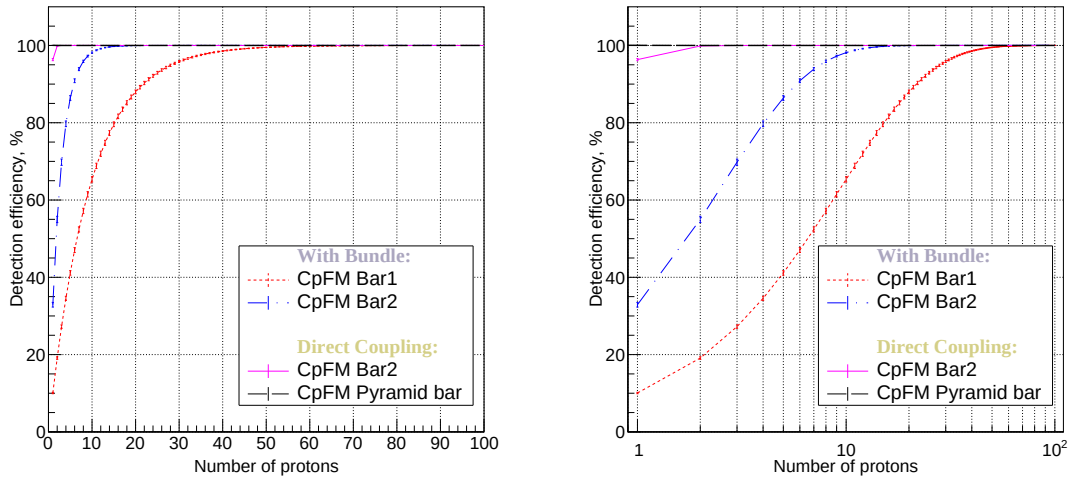

(a) Linear scale.

(b) Logarithmic scale in X-axis.

Figure 6.93: CpFM detection efficiency as a function of the incident protons number. Red dotted line – CpFM Bar1 with a optical fiber bundle, blue dot-dashed line – CpFM Bar2 with a optical fiber bundle, pink dashed line – CpFM Bar2 with a direct coupling, black solid line – CpFM pyramid bar with a direct coupling (final configuration).

Concluding obtained results for different CpFM versions, we can say, that the initial detector configuration, including the optical fibers bundle, was very inefficient for protons detection up to about 60 crossing protons, while the direct coupling has significantly improved this number (up to 1÷2 protons). Unfortunately, the detector configuration with a direct coupling and two 5 mm thick fused silica bars had a high particle resolution for a single proton (about 55%). Therefore, a new bar geometry has been proposed and made, in order to improve the resolution. For the final CpFM

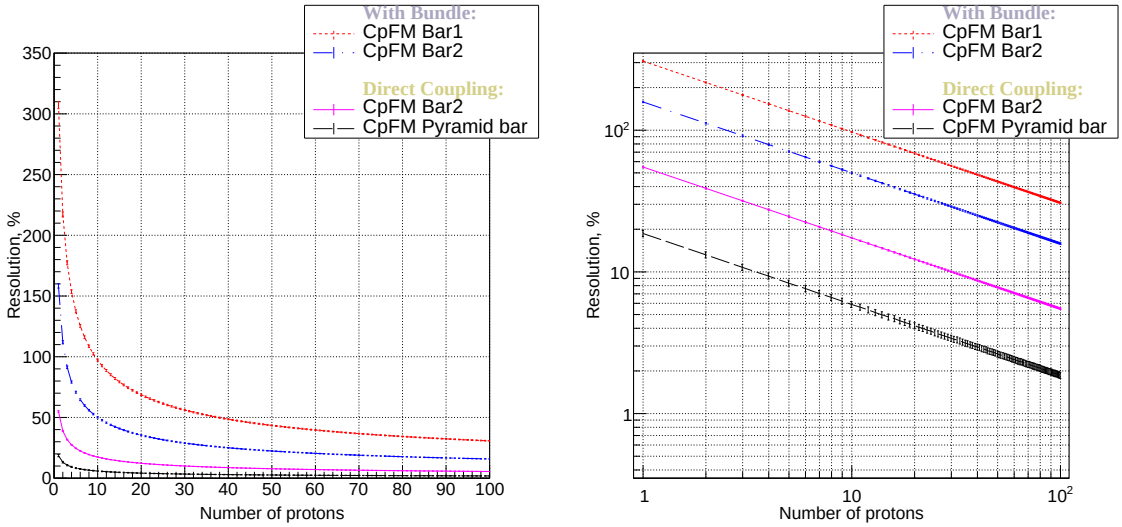

(a) Linear scale.

(b) Logarithmic scale in X-axis and Y-axis.

Figure 6.94: CpFM detection resolution as a function of the incident protons number. Red dotted line – CpFM Bar1 with a optical fiber bundle, blue dot-dashed line – CpFM Bar2 with a optical fiber bundle, pink dashed line – CpFM Bar2 with a direct coupling, black solid line – CpFM pyramid bar with a direct coupling (final configuration).

detector configuration, consisting of a pyramid fused silica bar and direct coupling, the detection efficiency and resolution for a single proton are about 100% and 19%, respectively. This configuration has been used for the further measurements on the SPS accelerator.

6.4.6 Timepix on SPS

Since 2017 the Timepix detectors are used during the SPS MDs. The main goal of the detector is to characterize the deflected by the bent crystal beam (Fig. 6.95). Therefore, the Timepix sensor has been placed in such a way to intercept the channeled protons and to measure their flux at a given position along the circulating beam.

Figure 6.96 shows the time distribution of the particles with the SPS periodicity (43 kHz or 23 μs), where 11 turns of the machine are visible, within a time window of 246 μs (Timepix in ToA mode with 48 MHz clock). With a clock set at 4.8 MHz 110 turns can be measured without dead time.

Due to the high flux of the particles at the SPS we have to define the maximum acquisition time window for each frame. We collected data putting the Timepix into the channeled beam (Fig. 6.97a) and plotting the total number of pixels (Fig. 6.97b,

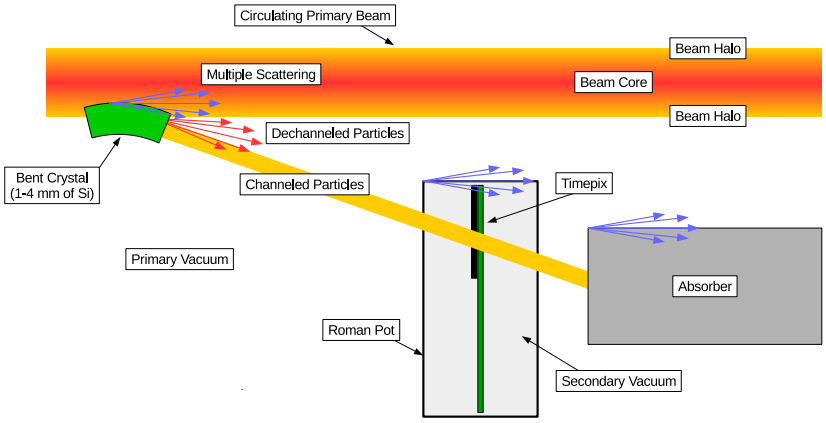

Figure 6.95: Conceptual sketch of the UA9 experiment with Timepix detector at the SPS accelerator. A bent crystal, inserted in the halo of the primary beam, deflects particles, while the Timepix detector, placed inside a Roman Pot cadge, intercepts the channeled beam before it will be captured by an absorber.

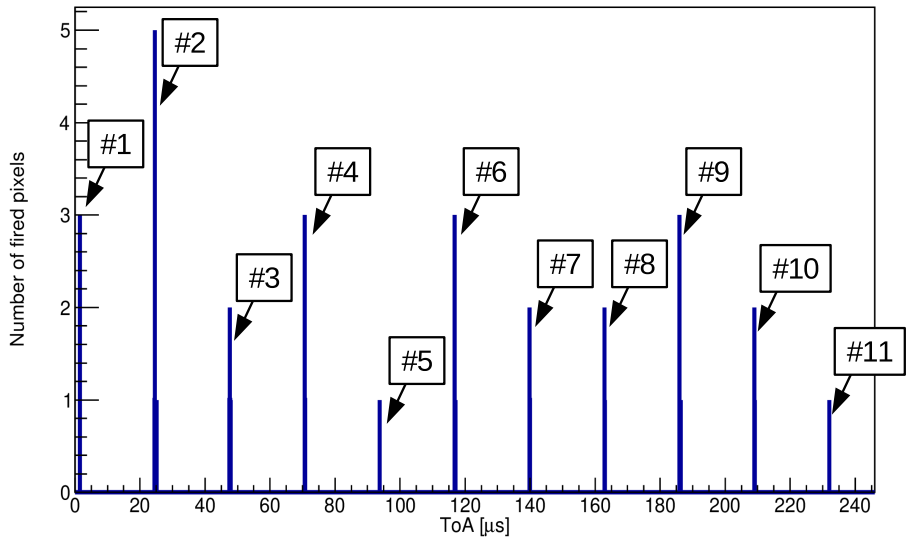

Figure 6.96: Distribution of the ToA for each fired pixel within one single frame of 246 μs (48 MHz clock). The distance between peaks is the period of the circulating beam in SPS, equal to 23 μs. One bin of the histogram corresponds to 20.83 ns.

Y-axis), which ToA is inside the specified time range (Fig. 6.97b, X-axis). For example (Figure 6.97b yellow rectangle), there are about 3800 pixels with a ToA less than 10 ms. For the case without clusters overlapping the dependency should be a straight line. Otherwise we should obtain a saturation behavior. From the Figure 6.97b we can see that starting from about 0.3 ms the behavior becomes to be not linear. Thus for the further analysis we decided to put the cut for the ToA of 0.246 ms with 48 MHz clock.

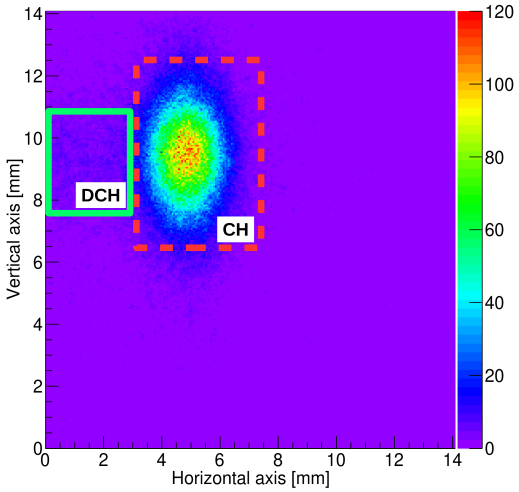

(a) Integrated image of the beam. Red dashed line – channeling (CH) region, green solid line – dechanneling region. In color (Z-axis) is indicated the number of hits in each pixel per 1 second.

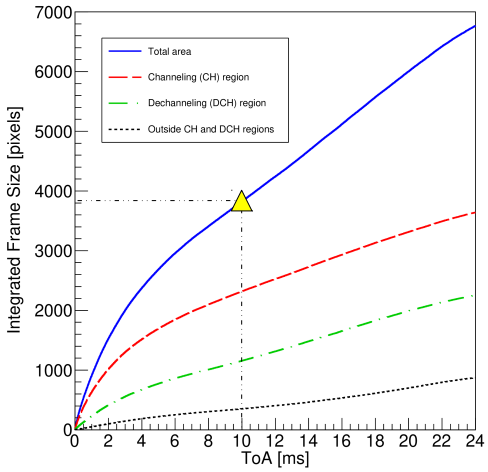

(b) Integrated number of the fired pixels as a function of the ToA. Clock is 0.48 MHz, acquisition time window is 0.0246 s. Blue solid line – total area of the sensor, red dashed line – channeling region, green dot-dashed line – dechanneling region, black dotted line – all others. A yellow triangle is an example point, in which there are 3800 pixels with a ToA less than 10 ms.

Figure 6.97: Saturation of the particle counting in the ToA mode for SPS data.

Following the detector calibration procedure, which has been done at H8 (Subsection 6.2.2), the number of fired pixels per particle cluster (Fig. 6.98a) and number of the particles per acquisition frame (Fig. 6.98b) have been measured at the SPS in ToA mode, and equal to ∼1.7 pixels/particle and 39 particles/frame respectively. It means about 3.6 particles are extracted by the bent crystal per each turn of ∼23 μs, or in other words $1.5 \cdot 10^5$ protons/s (4402 protons/(s·mm^2) in the beam core) for the active are of the Timepix sensor of 196 mm^2.

To increase the counting statistics, we can switch to the Medipix mode. Unfortunately, due to the high flux of the particle, deflected by means of the bent crystal,

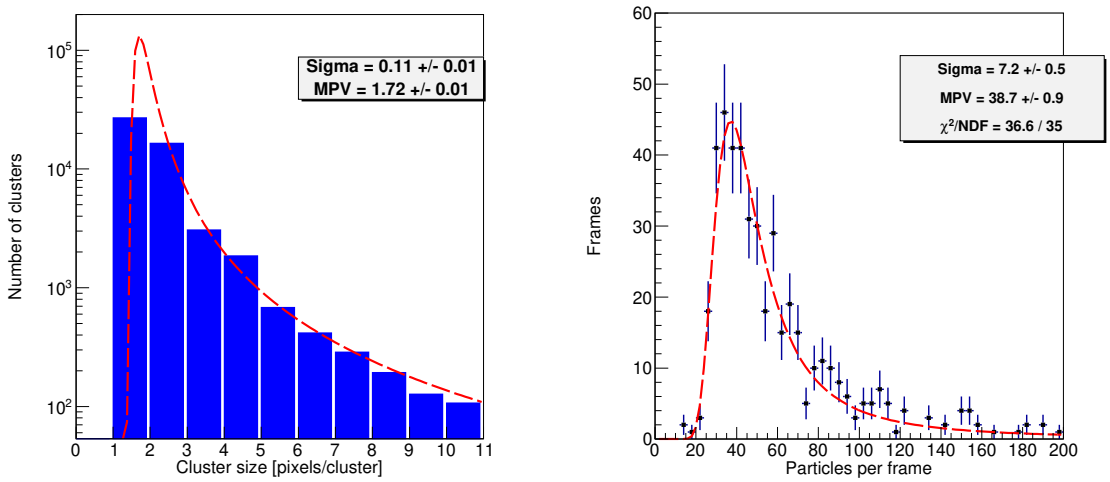

(a) Distribution of the fired pixels number per cluster. Red dashed line is a fit done with a Landau distribution function.

(b) Number of particles (clusters) per frame. Red dashed line is a fit done with a Vavilov distribution function.

Figure 6.98: Timepix measurements in the ToA mode (246 μs of acquisition window with 48 MHz clock) for 270 GeV/c proton beam at the SPS.

and high radiation environment of the device, there are noisy pixels (less than 1% of the total number of pixels), which distort the full image of the beam. It leads to single pixels with a high number of the counts (Fig. 6.99, red pixels). Thus, we decided to develop a filter routine, which will remove the noisy pixels using an averaging of the neighbor pixels counts.

The main problem with local averaging operations is that they tend to blur sharp discontinuities in intensity values in an image. An alternative approach is to replace each pixel value with the median of the color values in the local neighborhood. Filters using this technique are called median filters [123] (Fig. 6.100). For our filtering procedure we are following the next steps:

1. Sort the pixels into ascending order by counts (color).
2. If the noisy pixel has a value, which is ∼2 times (experimentally selected) bigger than the median pixel has, than replace it by the median pixel.

Figure 6.101 shows the image filter results. For further measurements, this filter is applied for each frame of the Timepix detector during the offline data analysis.

6.4.6.1 Fragmentation study

A ToT mode of the Timepix acquisition has been used in order to verify the detector response for different type of the incident particles at the SPS. A 270 ZGeV/c

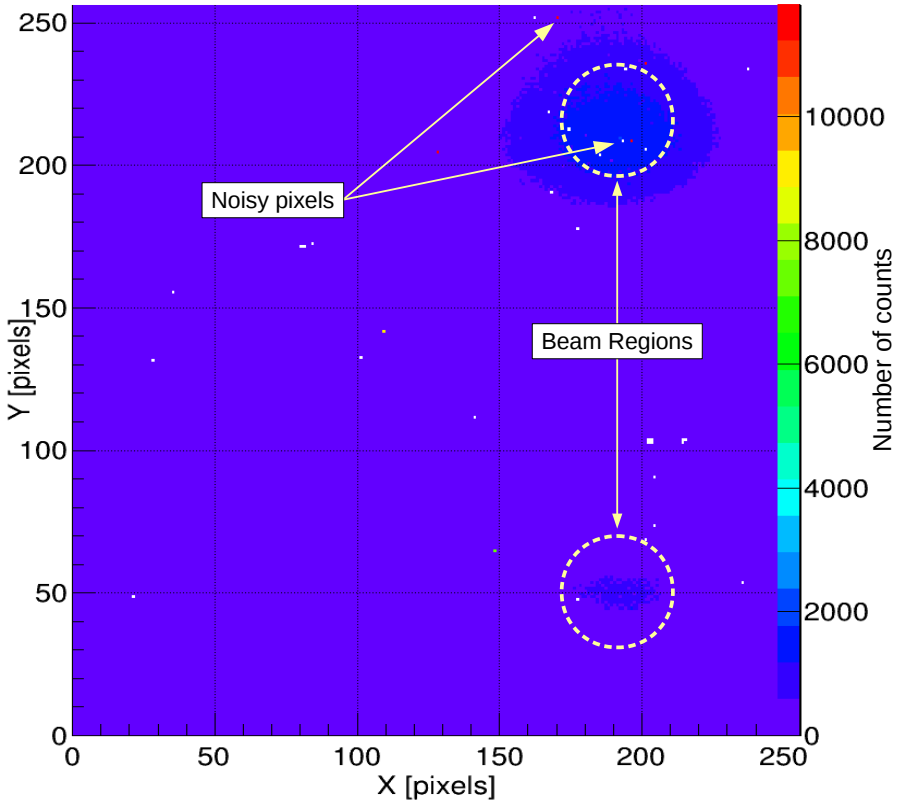

Figure 6.99: Integrated Timepix frame in the Medipix mode of 0.5 sec, and 48 MHz clock. The presence of noisy pixels distorts the full image of the beam.

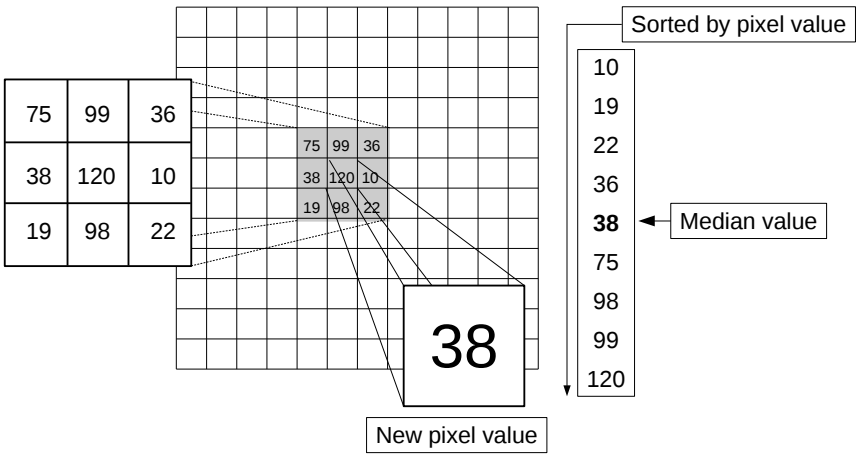

Figure 6.100: An example of the median filter illustration using a 3×3 neighborhood submatrix.

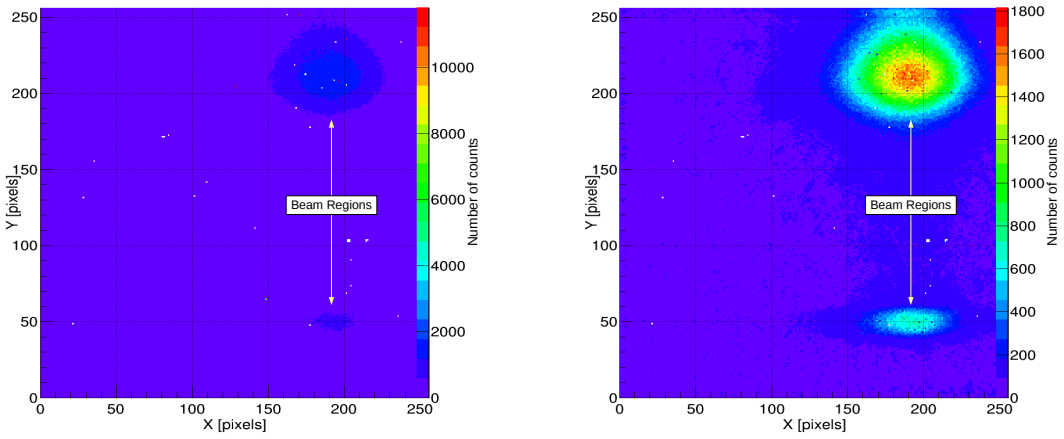

(a) Original frame image.

(b) Filtered frame image.

Figure 6.101: Timepix image of one frame in the Medipix mode with a channeled beam at the SPS. The developed image filter has been applied, in order to improve the picture and remove noisy pixels.

lead ion beam circulating inside the machine has been collimated by the bent silicon crystal, inserted into the primary halo. The Timepix detector has been placed in the secondary halo to do not intercept the channeled particle beam (Fig. 6.102a). In such a way registering scattered Pb ions and secondaries from the hadronic showers produced in the lead ions interactions with machine obstacles (crystal, collimator, beam pipe, Roman Pot, etc.).

Figure 6.102b shows the distribution of the cluster volume (CV) as a function of the cluster size (CZ). CV is a sum of the counts inside a cluster, which corresponds to the energy deposition of the incident particle in 300 μm of silicon. CZ is a number of the fired pixels of the cluster. It can be seen the island of the clusters with a size of about 1500 pixels, which are well-separated from the major part of the events. They correspond to the Pb ions interacting with the sensor. Taking into account obtained results and dependency between energy deposition and charge of the particle ($\sim Z^2$ [124]), we can recognize the rest of the islands as different Z ions (Fig. 6.102c) [125].

In analogy to the CpFM detector, Timepix can be used for a beam contamination study working in a ToT mode.

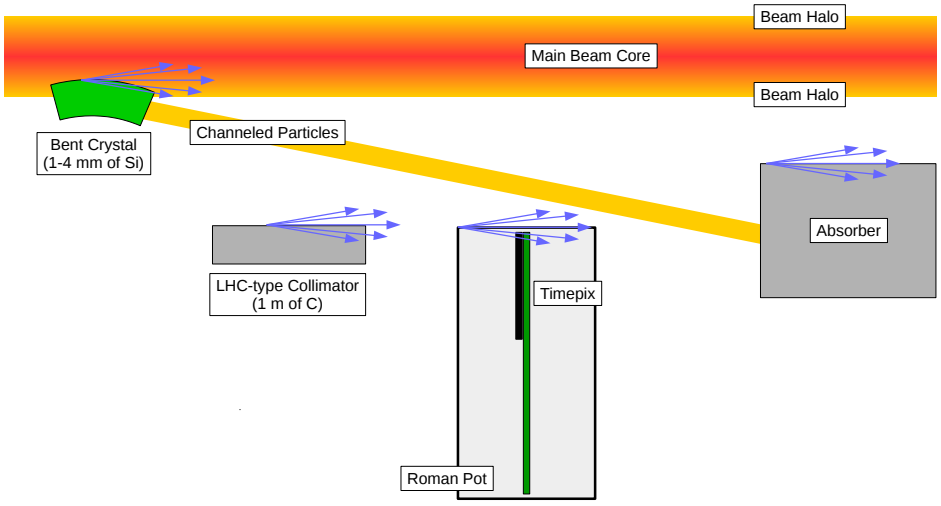

(a) Experimental layout.

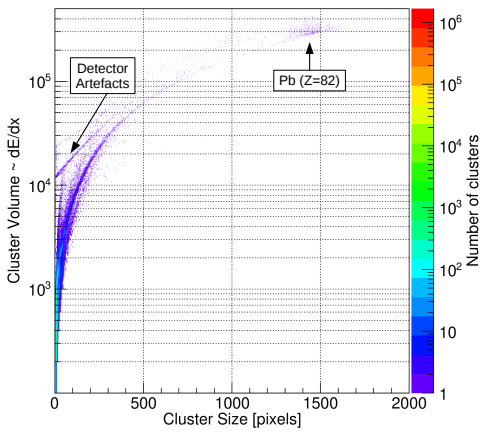

(b) Cluster volume as a function of the cluster size.

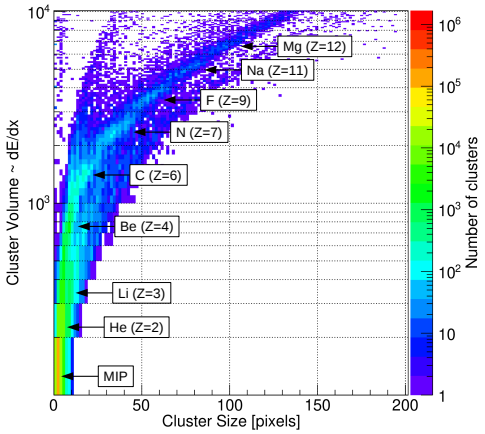

(c) Cluster volume as a function of the cluster size (zoomed in).

Figure 6.102: Fragmentation study using the Timepix detector and 270 ZGeV/c lead ion beam. Each cluster island corresponds to a different Z ion. Detector artefacts can be explained by the overshoots in the preamplifier output due to oscillations in the pixel electronics [126].

6.4.7 Deflected beam monitors

In 2018 the CpFM and Timepix detectors have been used at the SPS accelerator for the deflected halo particles counting. Table 6.17 shows the main parameters of the circulating proton beam (a single 3 ns bunch) during the measurements.

Beam	Momentum [GeV/c]	Intensity per bunch	Emittance [nm·rad]	Tune Q_h
proton	270	$\sim 0.9 \times 10^{11}$	~3.7	20.13

Table 6.17: SPS beam conditions during the measurements.

Figure 6.103 illustrates the beam optics of the setup. The bent crystal, named TCP78, is the same TCP74 (tested at H8, Tab. 6.2), but with a bigger angle of ~300 μrad.

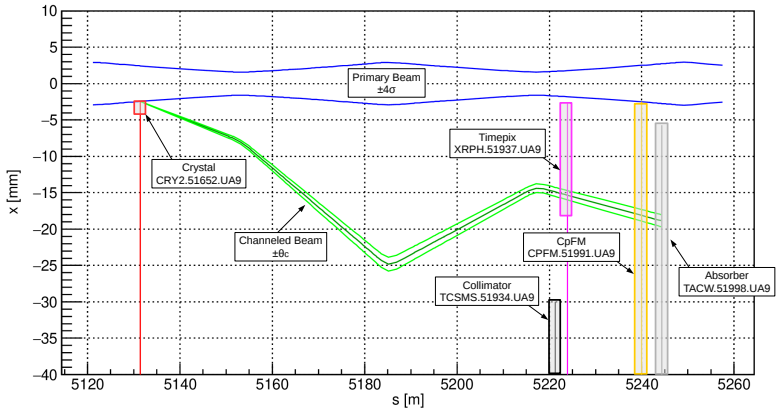

Figure 6.103: Horizontal projection (x) of the channeled halo particles as a function of the longitudinal coordinate (s) in LSS5. Blue lines represents the primary beam envelope with a 4σ width. A bent crystal (red line) deflects halo particles (green line), within $\pm\theta_c$ range (light green lines) onto the tungsten absorber (grey line). CpFM (orange line) and Timepix (pink line) detectors, located between the crystal and absorber, intercept the channeled particles, left and right jaws of the collimator (black line) are retracted from the beam.

Figure 6.104 illustrates a deflected particle beam, measured by a Timepix detector. The channeled particles are concentrated in a small spot around (8-12 mm;10-12 mm) position, while some part of the dechanneled particle interacts with a wall of the Roman Pot and produces a peak of secondaries in the left side of the image (0-2 mm;10-11 mm).

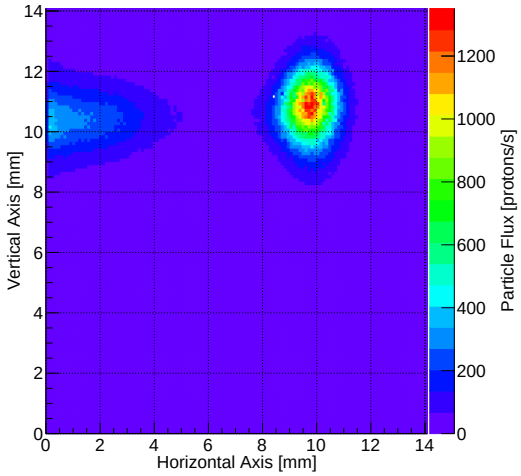

Figure 6.104: Integrated Timepix image of the channeled beam, normalized by the acquisition time of 198.7 s (1987 frames of 0.1 s). Medipix acquisition mode with 48 MHz clock. One 2D bin size is equal to 0.11×0.11 mm^2.

A linear scan has been performed in order to measure the channeled beam profile with the CpFM detector. It was moved with a speed of 0.1 mm/s from the parking position toward the primary beam, until it reached the alignment position, which corresponds to $\sim 4\sigma$ distance from the SPS beam core (Fig. 6.105a). According to Fig. 6.34, a horizontal beam profile can be reconstructed by calculating a derivative of the Error Function fit. The obtained beam shape is comparable with the Timepix data (Fig. 6.105b).

An equivalent crystal kick can be extracted from the obtained results by means of Equation 3.26. As expected, the computed from the experiment data crystal bending angle is about 300 μrad.

The measured flux of the channeled particles has been calculated for a region of $\pm 3\sigma$ around the peak position. It is equal to $(3.8 \pm 0.4) \cdot 10^5$ p/s and $(4.4185 \pm 0.0004) \cdot 10^5$ p/s for CpFM and Timepix detectors respectively. Taking into account the value of the beta function for the Timepix ($\beta_x^{TPX} = 40.1684$ m) and CpFM ($\beta_x^{CpFM} = 78.5522$ m) detectors, the measured standard deviation of the channeled beam from the CpFM is equal to $\sigma_x^{CpFM} \cdot \sqrt{\beta_x^{TPX}/\beta_x^{CpFM}} = 0.95 \pm 0.11$ mm in the reference frame of the Timepix detector. The obtained value is close to the measured standard deviation by means of the Timepix detector, which is about 0.72 mm.

6.4.7.1 Crystal orientation

To place a bent crystal in a perfect channeling orientation with respect to the incident halo particle at the SPS, the Beam Loss Monitors (BLM), placed outside

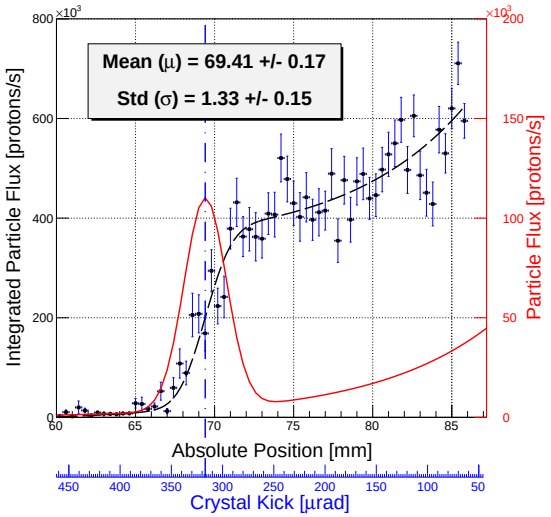

(a) CpFM particle integrated counts along the linear scan. One bin is equal to 0.4 mm. The fit was done by means of the Error Function + Exponential Function (black dashed line). Sigma and mean values correspond to the standard deviation of the channeled beam and its position in the CpFM detector reference frame. A derivative (red solid line) of the fit represents a profile of the beam, i.e. particle flux.

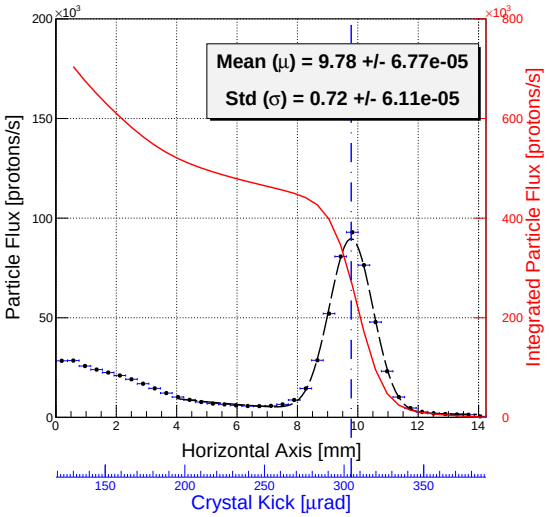

(b) Timepix horizontal axis projection. One bin is equal to 0.385 mm. The fit was done by means of the Gauss Function (channeling) + Exponential Function (dechanneling) (black dashed line). Sigma and mean values correspond to the standard deviation of the channeled beam and its position in the Timepix detector reference frame. An integral of the distribution (red solid line) represents an integrated beam profile along Horizontal Axis of the detector, i.e. integrated particle flux.

Figure 6.105: Deflected beam measurements using CpFM and Timepix detectors. Black markers with blue error bars represent experimental data. Bottom blue axis corresponds to the equivalent crystal kick at the position of the detector.

the beam pipe and close the crystal, are used in a proportional counting mode (i.e. BLM's counts are proportional to the incident particle number). After the crystal alignment during the measurements, an operator does an angular scan of the crystal to find a certain orientation, in which the local beam losses will be significantly reduced (∼10 times) with respect to the amorphous orientation. In a such configuration, halo particles, which should be scattered by the crystal, undergo the channeling effect, reducing the number of the nuclear interaction in the crystal. The precise description of the BLM signals behavior can be found in [25, 42, 43].

CpFM Figure 6.106 shows a typical BLM's response to the different crystal orientations with respect to the incident halo particles beam direction. When the crystal is in the amorphous (AM) orientation, the number of particles hitting the BLM is proportional to the number of the halo particles interactions with a crystal. In the channeling (CH) orientation, the crystal deflects halo particles reducing the nuclear interactions rate, i.e. BLM's counts drop down. Continuing the rotation a volume (VR) reflection effect becomes to dominate and particles are deflected in opposite direction to the crystal bending with a higher rate of the nuclear interactions (Subsec. 6.1.3). At the end of the VR region, the crystal becomes an amorphous piece of silicon. Therefore, an optimal channeling orientation can be found, measuring the BLM's counts along the angular scan of the crystal.

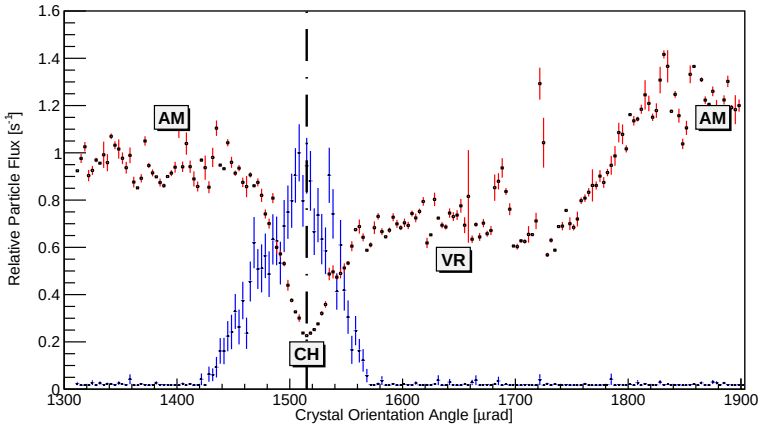

Figure 6.106: Relative particle flux as a function of the crystal orientation for $\sim 10^{10}$ particles in the main beam. A red line with an open square illustrates BLM's counts, while a blue line with a filled square represents CpFM detector counts. A black dot-dashed line shows an optimal crystal orientation for channeling. Different crystal orientations are labeled in the following way: AM – amorphous, CH – channeling, VR – volume reflection.

In the meanwhile, the CpFM detector can be used for the crystal angular positioning as well. Figure 6.106 illustrates how the detected particle flux behaves with different crystal orientations. Due to the fact, that CpFM can detect only channeled particles, in the optimal CH orientation the maximum counting rate is obtained.

Therefore, the CpFM detector can be used during the crystal orientation procedure, and it can be more efficient than the BLM detector, due to the high sensitivity to the low particle flux.

Timepix The functionality of the Timepix detector can produce more detailed information for the crystal orientation. During an angular scan of the QMP25 quasi-mosaic (111) crystal (Tab. 6.2), inserted into the primary proton beam halo at the SPS, the Timepix detector has been placed in a position of the deflected beam.

Figure 6.107 shows the BLM's counts behavior during an angular scan of a crystal. Three main regions of the particle interaction with a crystal are well visible. In the same time the Timepix detector was acquiring. Figure 6.108 illustrates the detector image projections on vertical and horizontal axes during the scan with a goniometer speed of about 1 μrad/s. The deflection effect of three crystalline planes can be defined: at the beginning and end of the scan two skew planes start to deflect particles within a certain angular range, which depends on the beam divergence and channeling critical angle; while in the middle of the angular scan the main crystalline plane, in which the crystal has been bent, deflects halo particles onto the sensor. This phenomenon can be explained by a given crystal orientation, which is very close to the axial orientation $< 110 >$ (Fig. 6.8). Therefore, the vertical and horizontal channeled beam movements are present for different crystal orientations with respect to the incident beam (Fig. 6.109).

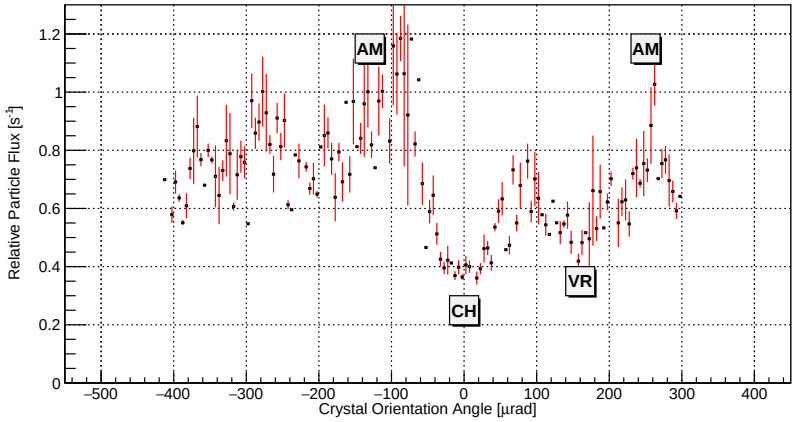

Figure 6.107: Relative particle flux as a function of the crystal orientation for $\sim 10^{10}$ particles in the main beam. A red line with an open square illustrates BLM's counts. Different crystal orientations are labeled in the following way: AM – amorphous, CH – channeling, VR – volume reflection.

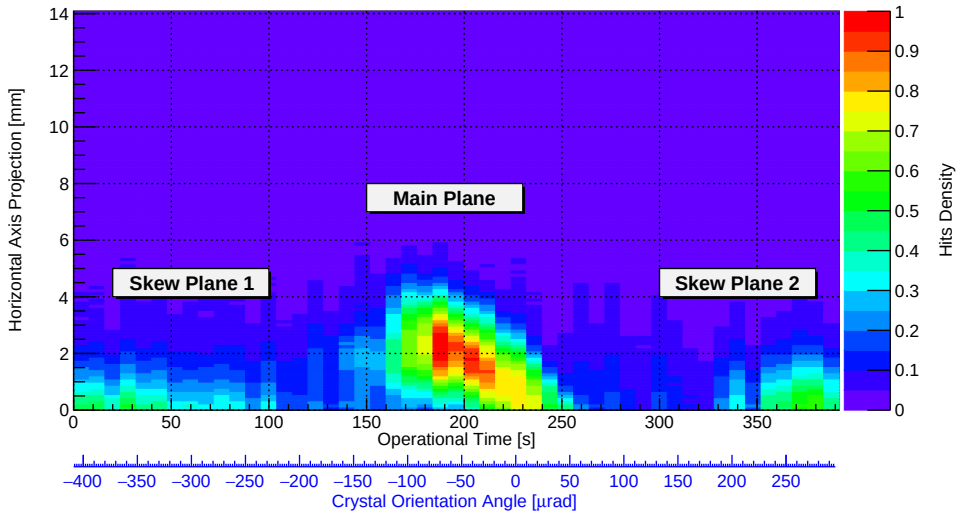

(a) Timepix image projection on a horizontal axis.

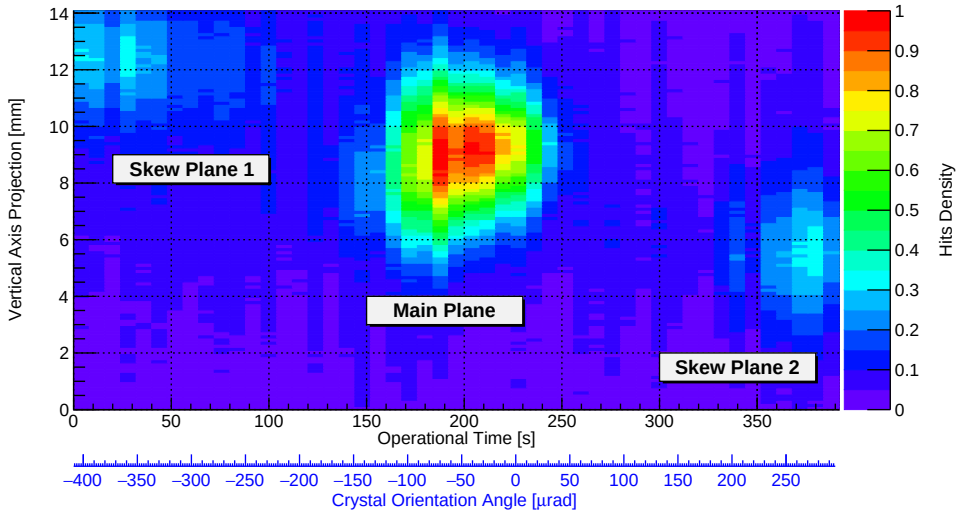

(b) Timepix image projection on a vertical axis.

Figure 6.108: Projection of the Timepix image during an angular crystal scan. Three regions of different crystalline plane deflection are visible: a skew plane 1 is around -400 – -300 μrad, the main deflection plane is around -150 – 50 μrad, and a skew plane 2 is around 200 – 300 μrad.

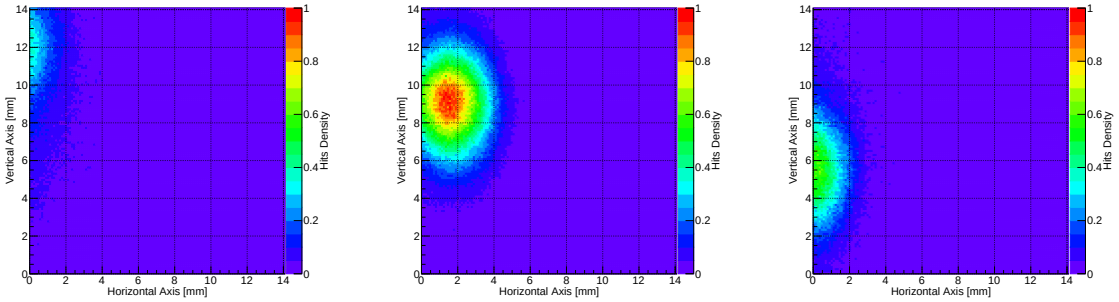

(a) Timepix image for the skew plane 1 deflection region (−260 μrad from CH).

(b) Timepix image for the main plane deflection region (around CH).

(c) Timepix image for the skew plane 2 deflection region (+260 μrad from CH).

Figure 6.109: Timepix images during the angular scan of the (111) quasi-mosaic crystal.

Chapter 7

Double-crystal setup

In September 2016 a new study of the opportunities offered by the CERN's accelerator complex and its scientific infrastructure has been launched. The aim of this project, called Physics Beyond Colliders (PBC) at CERN, is to target fundamental physics questions that are similar in spirit to those addressed by high-energy colliders, but that require different types of beams and experiments [127]. It will explore CERN's opportunities for a vision of some opened questions in high energy and particle physics.

In a frame of the PBC, and in order to collect different physical proposal for the LHC, a working group on fixed target physics has been created in 2017. The main idea of the most offers of the fixed target experiments is to re-use (probably, with small modifications) the existing detectors installed at the collider, without significant perturbation of the working conditions (in terms of luminosity, background, beam time, etc.) for the presently operating experiments (ATLAS, CMS, ALICE, LHCb, etc.).

At the moment, there are three main proposals for the implementation of the fixed target experiment [128]:

- Beam halo extraction, based on a bent crystal (Fig. 7.1, top).
- Use of unpolarized targets (Fig. 7.1, middle).
- Use of polarized targets (Fig. 7.1, bottom).

Further in the thesis, we will focus only on the crystal-based beam splitting technique. A detailed description of others can be found in [128]. The main idea is to use a bent crystal, which has been used for the primary LHC beam collimation studies, and direct halo particles onto the target, installed in front of the particle identification detector (like LHCb). In additional, another bent crystal with a higher

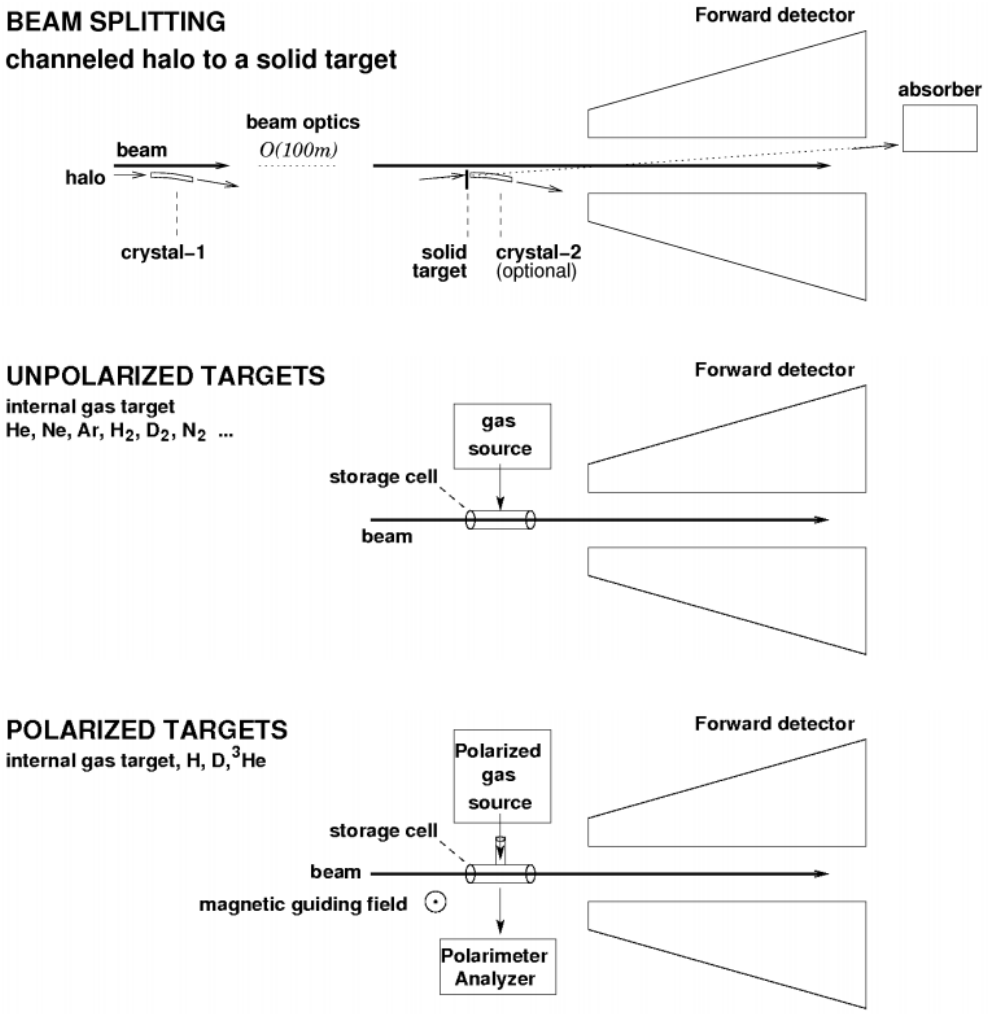

Figure 7.1: Illustration of three fixed target setups implementation. From [128].

deflection angle can be installed after the target in order to measure the magnetic and electric dipole moments of short living baryons (e.g. Λ_c) produced in the target (see Chapter 8). Such crystals configuration is called double-crystal setup, and before to be implemented at the LHC, it should be verified at the SPS machine. Therefore, in a frame of the UA9 collaboration, which has an experimental section of the SPS, these measurements have been planned for 2017 and 2018 [129].

7.1 The first alignment attempt

The aim of the UA9 experiments at the SPS, in a frame of the PBC program, is to demonstrate the feasibility of the double-crystal setup at the circular accelerator and its characterization in terms of the background and particle extraction efficiency and background production.

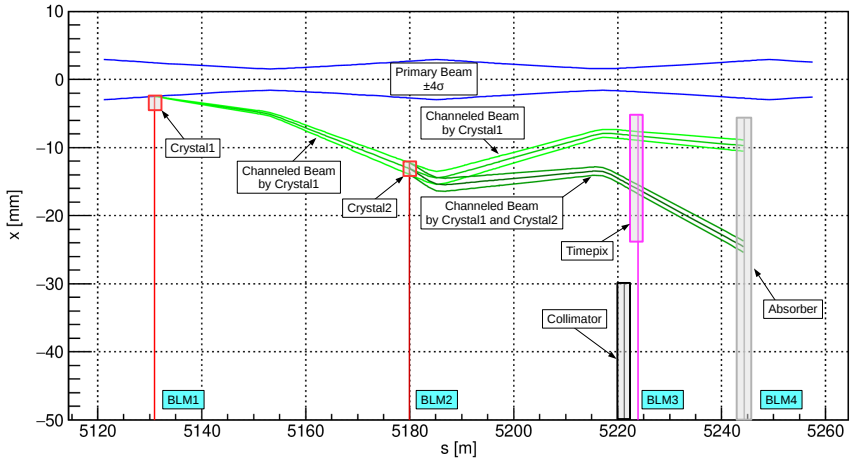

Figure 7.2: Horizontal projection (x) of the channeled halo particles as a function of the longitudinal coordinate (s) in LSS5. Blue lines represent the primary beam envelope with a 4σ width. An upstream Crystal1 (red line) deflects halo particles (green line), within $\pm\theta_c$ range (light green lines) onto the tungsten absorber (grey line), as well as channeled particles by the downstream Crystal2 (dark red line), inserted into the deflected beam by the upstream crystal with a phase advance of about 60°, in order to maximize the separation between channeled and primary beams (Eq. 3.25). Timepix (pink line) detector, located between the crystal and absorber, intercept the channeled particles, the collimator jaw (black line) is retracted from the beam. Each component of the setup is followed by the respective BLM counter, located outside the beam pipe.

In September (without Timepix) and October (with Timepix) 2017 two dedicated runs of 24 hours each have been performed for the double-crystal setup investigation [130]. Figure 7.2 shows the experimental layout of the double-crystal setup at the SPS. A single bunch, circulating in the machine, was collimated by the upstream Crystal1 (STF81) aligned at 4σ distance from the beam core, and fixed in the optimal channeling orientation. The alignment of the second Crystal2 (STF18), located 50 m downstream, with respect to the single-channeled beam, has been done along the linear scan toward the beam. It was expected to see a visible increase of losses, when the Crystal2 should cross the deflected beam. Unfortunately, this effect was not observed due to a low intensity of the particle beam impinging to the Crystal2. Therefore, the downstream crystal has been placed in a position, computed using a beam optics routine.

To find an optimal channeling orientation of the downstream crystal a series of angular scans have been conducted. For the first scan, when the collimator jaw was retracted ("Collimator OUT"), BLM counts did not show any significant changes. Therefore, the jaw has been moved in a position to intercept the double-channeled beam, but not a single one ("Collimator IN"). Figure 7.3 illustrates the behavior of the BLM counts during Crystal2 angular scan inside a single-channeled beam. It is clear visible, that at around 1500 μrad the number of losses on BLM3 (next to the collimator) increased due to the interaction of the double-channeled particles with collimator. The achieved configuration is called double-channeling, and it was repeated several time during the MD.

Beam	Momentum [GeV/c]	Intensity per bunch	Emittance [nm·rad]	Tune Q_h
proton	270	$\sim 10^{11}$	$\sim$5	20.13

Table 7.1: SPS beam conditions during the measurements.

To study the double-crystal setup a set of linear scans by means of the right collimator jaw have been performed. In analogy to the CpFM linear scan for a single-channeling configuration discussed before, the BLM3 counts are proportional to the particle flux scattered from the collimator jaw during the horizontal scan toward the beam. When the Crystal2 was retracted and Crystal1 was in amorphous orientation (orange line), an exponential-like profile has been obtained, due to protons diffusing mechanism into the halo from the circulating beam. When only the Crystal1 is in channeling orientation (green line), a typical profile is seen from -8 mm position. Putting Crystal2 in the deflected beam and orienting it in the channeling regime

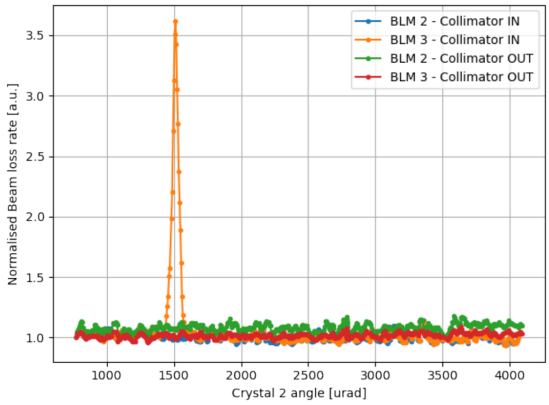

Figure 7.3: Beam loss rate as a function of the orientation of Crystal2 during two scans performed for its alignment. From [130].

(blue line), the profile starts to have an increase at around -13 mm, due to the crossing of the double-channeled beam, until -8 mm, where a single-channeled beam is located.

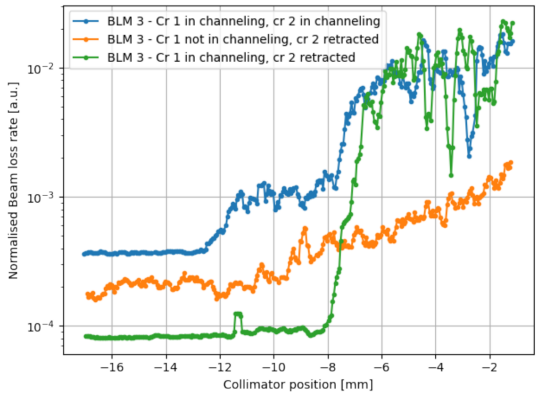

Figure 7.4: Beam loss rate as a function of the position of the collimator for different configurations of the crystals. From [130].

Accordingly to the obtained results, we have performed for the first time a double-crystal setup at the circular accelerator by means of the beam losses counters during a linear scan of the collimator jaw. Very low sensitivity of the BLM does not give a possibility to align the downstream crystal in an optimal configuration for the double-crystal setup. Therefore, the use of the position and flux sensitive device is needed (e.g. Timepix or CpFM).

7.2 Timepix measurements

7.2.1 Double-crystal alignment

Linear scan During the second run in October 2017, a Timepix detector has been used for the double-crystal setup investigation. The device was placed in a specific computed position, in order to intercept single and double-channeled beams (Fig. 7.2). At the first step an upstream Crystal1 (QMP25) was placed in a 4σ distance from the beam core, and oriented in the optimal channeling, deflecting particles onto the absorber. Then the downstream Crystal2 (STF18) was moved toward the main beam crossing a single-channeled region with a linear speed of 10 $\mu m/s$ (Fig. 7.5).

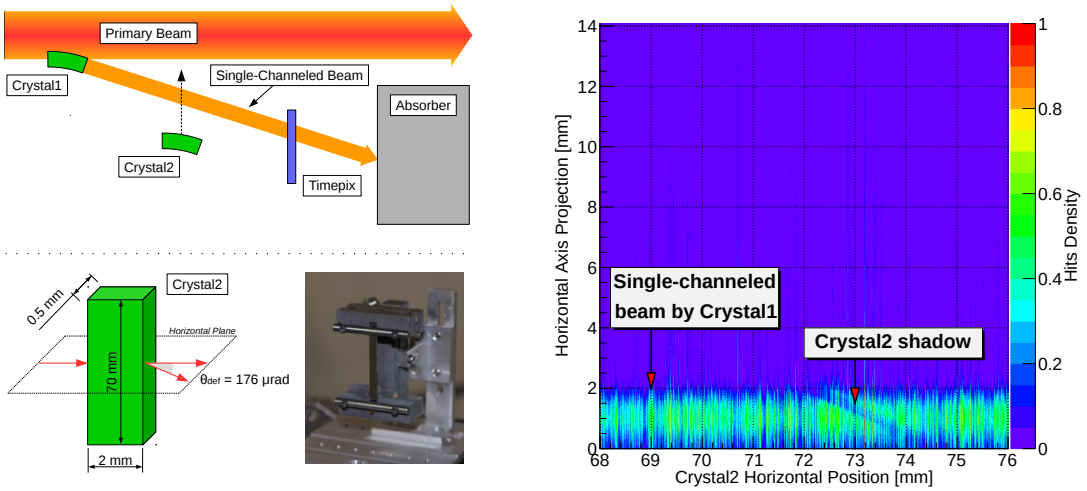

(a) Scheme of the Crystal2 linear scan across a single-channeled beam from the upstream Crystal1.

(b) Timepix image projection on a horizontal axis as a function of the Crystal2 horizontal position.

Figure 7.5: Horizontal scan of the Crystal2 crossing a single-channeled beam by the Crystal1. Timepix operation in a ToA mode with about 10 frames/s of the data taking for 5 MHz clock and ∼2.4 ms of the acquisition window.

From the horizontal projection of the Timepix image during the linear scan of the Crystal2, we could clearly see the shadow of the crystal crossing a single-channeled beam, due to the mostly elastic protons scattering. Therefore, we were able to align the downstream crystal, by means of the Timepix, in the optimal position with respect to the center of a single-deflected particle beam.

In the meanwhile, the linear scan gave us an information about the horizontal size of the beam (width) impinging to the Crystal2 (Fig. 7.6a). Figure 7.6b shows

a horizontal single-channeled beam profile at the Crystal2 longitudinal position, computed from the Timepix beam profile by means of the Crystal2 shadow trajectory function: (Timepix Horizontal Axis Projection) = -0.77·(Crystal2 Horizontal Position) + 57.49.

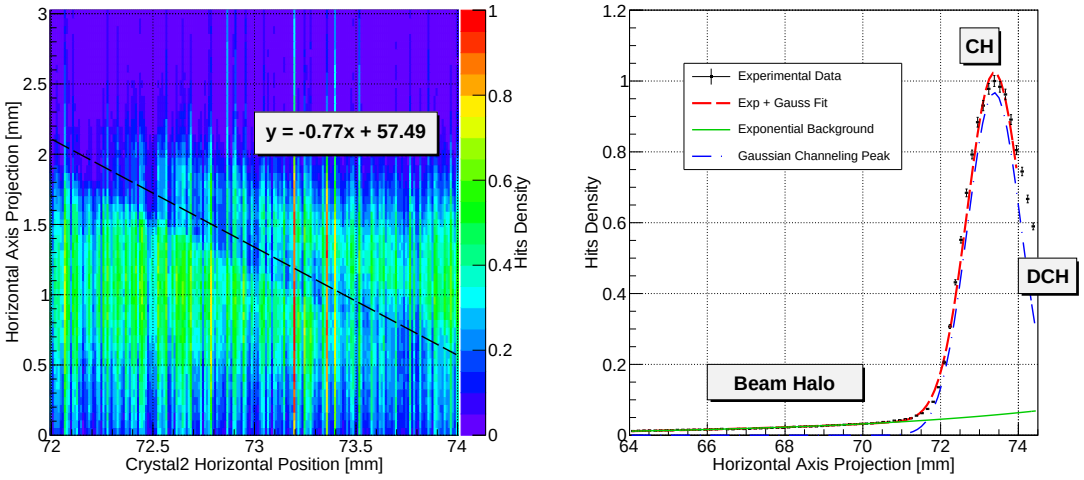

(a) Timepix image projection on a horizontal axis as a function of the Crystal2 transversal position. A shadow of the Crystal2 crossing the deflected beam by the Crystal1 is visible. Black dashed line illustrates the Crystal2 trajectory along the linear scan.

(b) Single-channeled beam profile at the Crystal2 longitudinal position, computed by means of the Crystal2 linear scan trajectory equation. Red dashed line shows a Gaussian + Exponential fit of the experimental data (black dots with error bars); green solid line – an exponential beam halo distribution; blue dot-dashed line – a Gaussian channeling peak distribution.

Figure 7.6: Reconstruction of a single-channeled beam profile at the Crystal2 longitudinal position.

To fit the beam profile an Exponential + Gaussian function has been used (Fig. 7.6b, red dashed line). Fairness of the use an exponential function for the diffusion beam halo particle region has been confirmed by means of the collimator linear scan without the Crystal2 and with the Crystal1 in AM (Fig. 7.7). To compare the obtained results, the collimator position has been displayed in the Crystal2 reference frame. From the fit of the data, the received exponential function parameters are: $p_0 = -15.38 \pm 0.46$ and $p_1 = 0.16 \pm 0.01$ [mm^{-1}], which are in a good agreement with the exponential fit results of the Timepix detector in the Crystal2 reference frame: $p_0 = -15.43 \pm 0.20$ and $p_1 = 0.17 \pm 0.01$ [mm^{-1}].

The measured single-channeled peak width (FWHM) at the position of the Timepix is 1.21 ± 0.01 mm, and Crystal2 – 1.63 ± 0.02 mm. The obtained values are in a good agreement with a beam optics routine calculation: 1.22 mm and

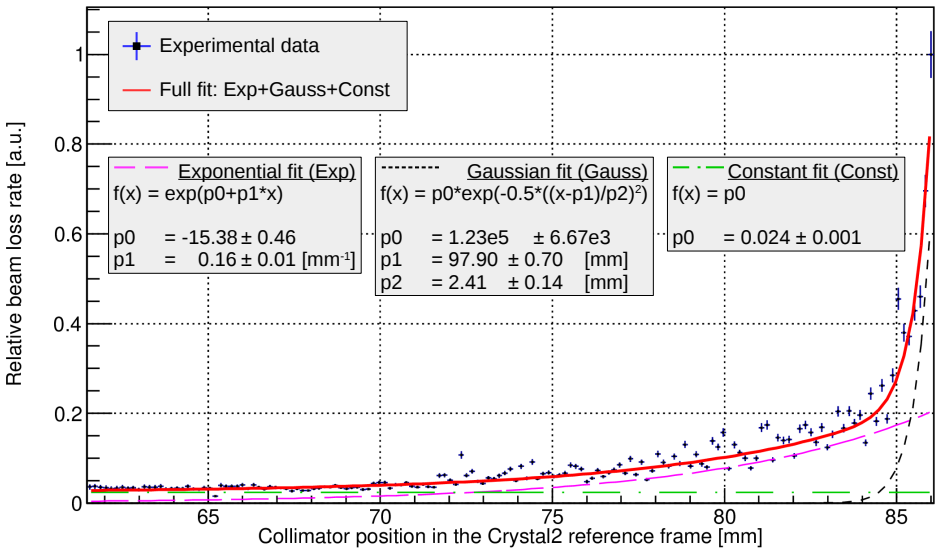

Figure 7.7: Relative beam loss rate as a function of the collimator position in the Crystal2 reference frame. BLM data during the linear scan of the collimator jaw while the Crystal1 is not in channeling and Crystal2 is retracted. The absolute collimator position has been converted into Crystal2 reference coordinate system in order to compare with the Timepix data. Red line represents full fit function which is composed of Exponential (pink line, diffusion halo particles from the main beam), Gaussian (black line, the edge of the main beam), and Constant (green line, background counts of the BLM) functions.

1.61 mm, for the Timepix and Crystal2 positions respectively.

Angular scan According to the Timepix data during the linear scan, the Crystal2 has been placed in the center of a single-channeled beam ($\sim$ 73.3 mm), which corresponds to the maximum beam intensity. At this position, an angular scan of the Crystal2 has been performed in order to find the optimal orientation for the double-channeled configuration. Figure 7.8 shows a Timepix image during the angular scan. It can be seen that within a certain angular range channeling (CH) and dechanneling (DCH) regions are visible. Since the deflection efficiency of the crystal is high (tens of percent), a decrease of the hits density during the channeling (1230-1330 μrad), in the region of the crystal shadow, is observed.

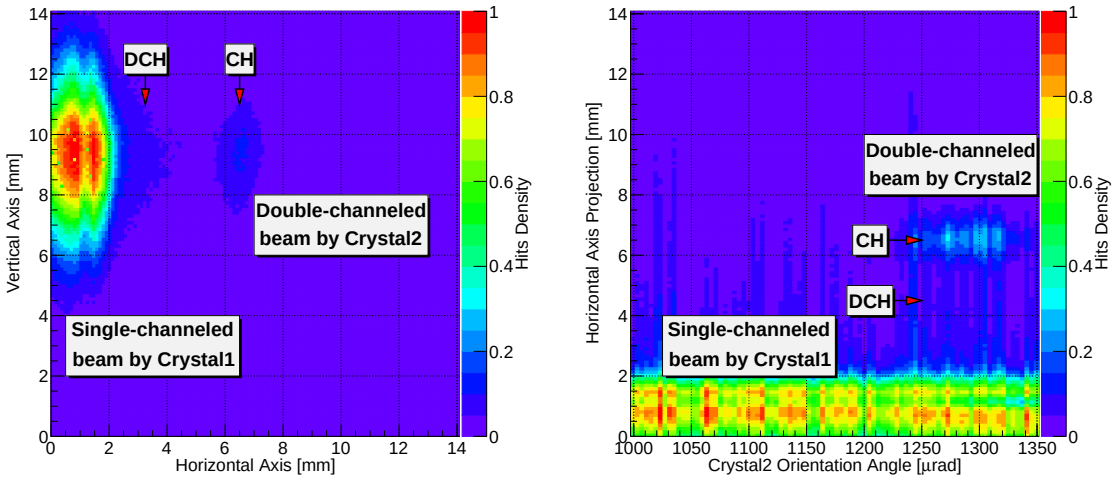

(a) Integrated Timepix image during the angular scan of the Crystal2.

(b) Timepix image projection on a horizontal axis as a function of the Crystal2 orientation angle.

Figure 7.8: Timepix image of the Crystal2 angular scan, placed in the center of a single-channeled beam from the Crystal1.

Crystal torsion Due to the presence of a significant crystal torsion, the angular range of the Crystal2 channeling is about 100 μrad. To measure this effect, a vertical projection of the beam profile during the angular scan was needed. Figure 7.9 illustrates a vertical movement of the double-channeled beam spot along the angular scan of the Crystal2. The profile of the distribution by means of the first order polynomial fit introduces the torsion of the crystal in the Timepix reference frame.

Figure 7.10 shows a vertical profile of the single-channeled beam. It is evident that the particle beam deflected by the Crystal1 is on top of the wide Gaussian

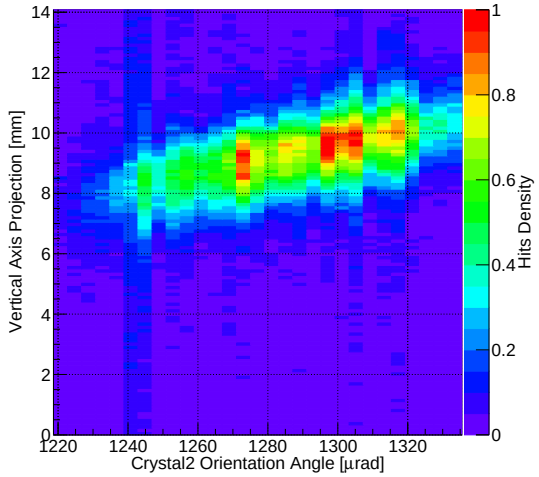

(a) Timepix image projection on a vertical axis as a function of the Crystal2 orientation angle. The projection has been done only for the double-channeled beam spot.

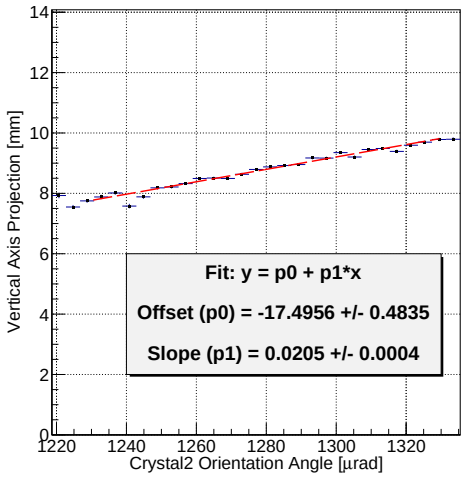

(b) The profile of the Timepix image projection on a vertical axis along the angular scan. Red dashed line illustrates the first order polynomial fit.

Figure 7.9: Vertical movement of the double-channeled beam spot during the Crystal2 angular scan.

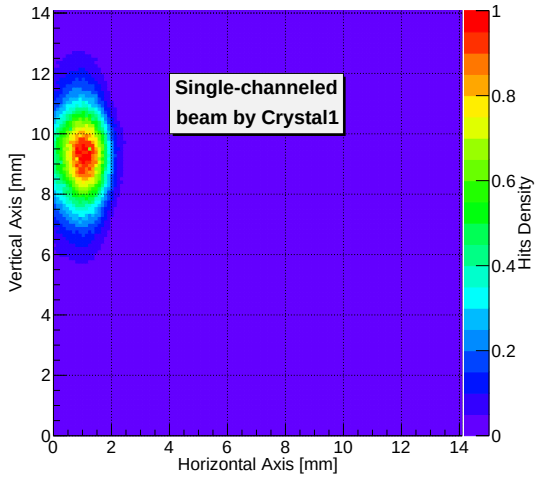

(a) Timepix image of the deflected beam by the upstream crystal.

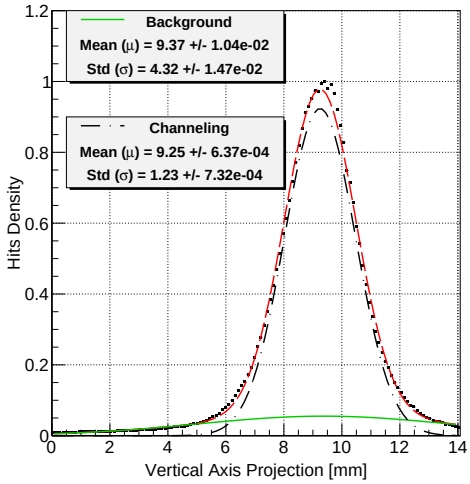

(b) Timepix image projection on a vertical axis. Red dashed line illustrates a Double-Gaussian fit, while green solid and black dot-dashed lines represent Gaussian fits of the background (the main SPS beam halo) and signal (a single-channeled beam) respectively.

Figure 7.10: Vertical single-channeled beam profile.

background produced by the main SPS beam. Assuming the decoupling between transversal coordinates of the beam, the size of the single-channeled beam impinging to the Crystal2 can be calculated as the follow:

$$S_y^{CR1/CR2} = S_y^{TPX} \cdot \sqrt{\frac{\beta_y^{CR1/CR2}}{\beta_y^{TPX}}}, \tag{7.1}$$

where $S_y^{CR1/CR2}$ is the size in Y-axis of the incident particle beam to the Crysta1/Crysta2, while $S_y^{TPX} = 6 \cdot \sigma_y^{meas.}$ is the measured size of the beam ($\pm 3\sigma$ to cover $> 99\%$ of the beam) by means of the Timepix detector (Fig. 7.10b); $\beta_y^{CR1/CR2}$ and β_y^{TPX} are beta functions in Y-axis at the Crystal1/Crystal2 and Timepix longitudinal position respectively (Tab. 7.2). Computed values of the beam size hitting each object are listed in Table 7.3.

Position	β_x [m]	β_y [m]
Crysta1	76.1635	45.4907
Crysta2	90.4735	37.3672
Timepix	40.1684	85.3640

Table 7.2: Beta function of the SPS beam optics in 2017.

Position	S_y [mm]
Crysta1	6.9487 ± 0.0041
Crysta2	4.8672 ± 0.0029
Timepix	7.3565 ± 0.0044

Table 7.3: Size of the incident particle beam S_y, assuming that the Crysta1 is the first obstacle which determines the fraction of the main beam to be channeled.

Considering a ratio ($k = S_y^{CR2}/S_y^{TPX}$) between beam sizes impinging to the Crystal2 and Timepix (Tab. 7.3), the torsion parameter of the crystal is equal to: $1/(k \cdot p1) = 73.7 \pm 1.4$ μrad/mm, where $p1$ is a Slope of the polynomial fit in Figure 7.9b. Such a high value of the crystal torsion can be explained by the fact, that the Crystal2 had been installed at the SPS since January 2010 with a torsion of about 1 μrad/mm but using an old version of the bending device (Fig. 7.5a, crystal photo), which has been later defined as unstable. Therefore, due to the particle beam (mainly protons and high-Z ions) interaction with a crystal material and more than 7 years under the high mechanical pressure of the bending device, the Crystal2 has increased its crystalline planes twisting.

7.2.2 Single-pass channeling at the SPS

For the quantitative double-crystal setup characterization we performed a set of measurements with different Crystal2 positions with respect to the center of a single-channeled beam. The procedure of the measurements is the following:

1. Collimator jaws are retracted ("Collimator OUT"), Crystal2 in the amorphous orientation, Timepix is acquiring only the single-channeled beam (Fig. 7.11a).

2. Linear alignment of the Crystal2 with respect to the center of the single-channeled beam (Fig. 7.11b).

3. Collimator jaw is inserted ("Collimator IN") in order to intercept a double-channeled beam.

4. Angular scan of the Crystal2, monitoring the beam losses at the collimator BLM (Fig. 7.11c).

5. Crystal2 is oriented in the optimal channeling orientation according to the BLM counts.

6. Collimator OUT and the Timepix is collecting data for a couple of minutes (Fig. 7.11d).

7. After the Timepix acquisition, a linear scan with the collimator jaw ("Collimator SCAN") is performing in order to reconstruct the profile of the beam by means of the BLM counts (Fig. 7.11e).

8. At the end of the scan, Collimator OUT and move the Crystal2 to a new linear position with a 200 μm step, repeating the previous operations.

Considering the above algorithm of the measurement, we have combined two techniques for the double-crystal setup alignment: use of the Timepix detector for the linear crystal alignment, and perform an angular scan with a downstream crystal, looking at the beam losses (BLM counts) near the collimator jaw, which intercepts the second deflected beam.

To compare beam profiles for different crystal orientations and positions, the background coming from the primary SPS beam has been to be subtracted. Figure 7.12a shows beam profiles with and without background, which has been estimated by means of an Exponential fit. Figure 7.12b illustrates beam profiles without Crystal2, Crystal2 in amorphous (AM) and in channeling (CH) orientations. It can be seen that regions around the crystal shadow are more populated compare to the

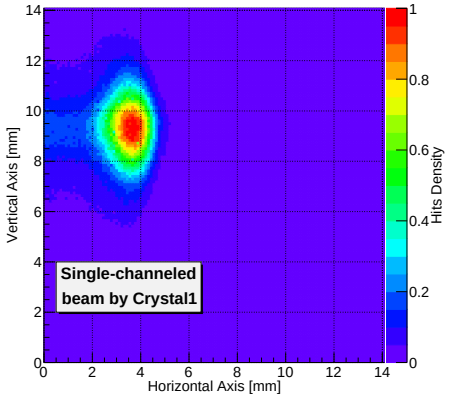

(a) Timepix image of the single-channeled beam by the Crystal1.

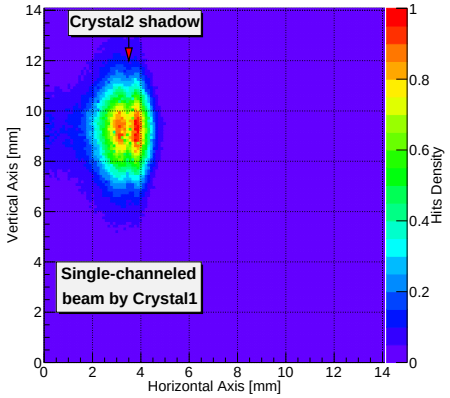

(b) Timepix image of the single-channeling with a shadow of the Crystal2 in an amorphous orientation.

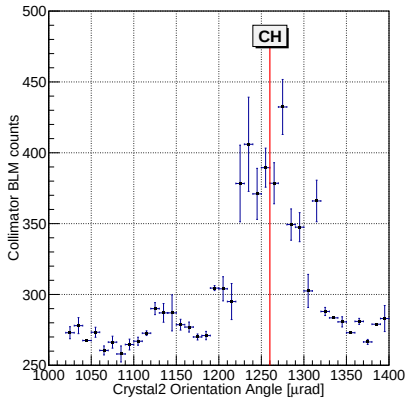

(c) Beam losses during the angular scan of the Crystal2. A vertical red solid line indicates the channeling orientation.

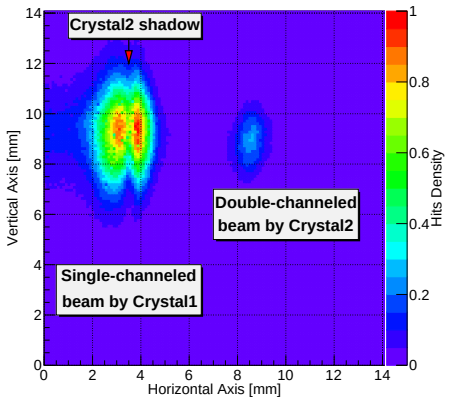

(d) Timepix image of the double-channeling.

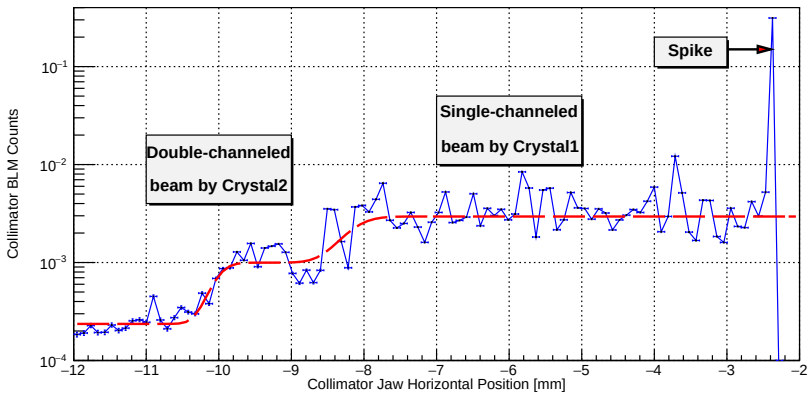

(e) Collimator jaw linear scan across single- and double-channeled beams. The spike is produced by the jaw touching the primary beam. Red dashed line illustrates a fit of the distribution by means of a Double-Error Function. BLM counts are normalized to the beam intensity.

Figure 7.11: Procedure of the measurements.

case, when the crystal is retracted. It is mainly due to the nuclear interactions of the incident particles with a material of the crystal. In the same time, in the CH orientation, we can observe the reduction of the amount of the scattered particles and a peak of the channeled beam around 6 mm from its shadow, which corresponds to the deflection angle of about 176 μrad.

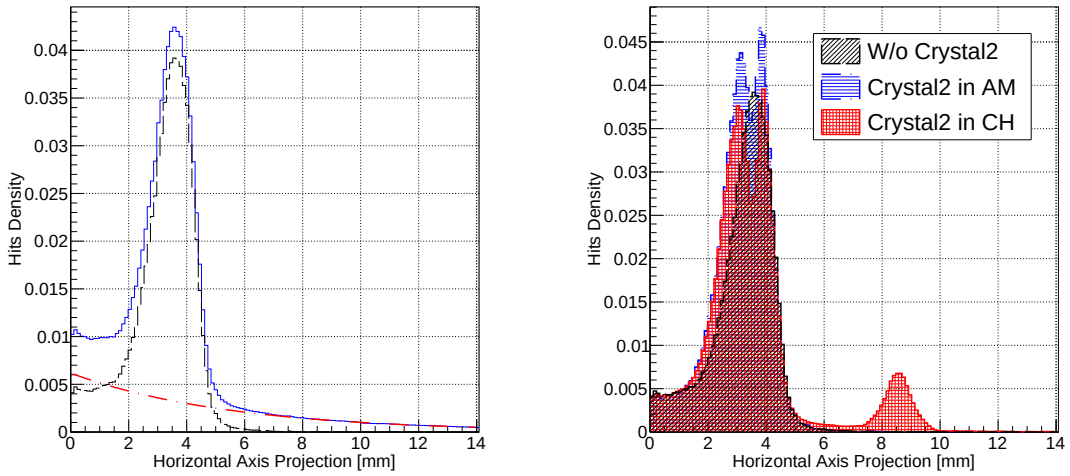

(a) Background subtraction from the horizontal beam profile. Red dot-dashed line illustrates an Exponential fit.

(b) Comparison between horizontal beam profiles for different crystals configurations.

Figure 7.12: Single- and double-channeled beam horizontal profile measured by means of the Timepix detector. The Timepix counts have been normalized by the total number of hits per acquisition frame.

To estimate the amount of particles, which have been scattered and deflected by the crystal, we calculated a difference between these three configurations. Figure 7.13 demonstrates the differences between Crystal2 in AM/CH and without the crystal. It can be seen that around the crystal shadow, there are two peaks due to the nuclear interactions (scattering and inelastic) of the incident particles with silicon. The asymmetry of their heights is due to the not centred position of the Crystal2 with respect to a single-channeled beam center, and some fraction of the volume reflection (VR) process. For the CH orientation the depth of the crystal shadow valley is more bigger compare to the AM, due to particles channeling.

Integrating the channeling peak we can calculate the fraction of the deflected particles, by doing this for different Crystal2 horizontal positions with respect to the single-channeled beam (Fig. 7.14). In such a way the distribution follows transversal shape of the single-channeled beam.

The calculated standard deviation of 0.71±0.03 mm is in a good agreement

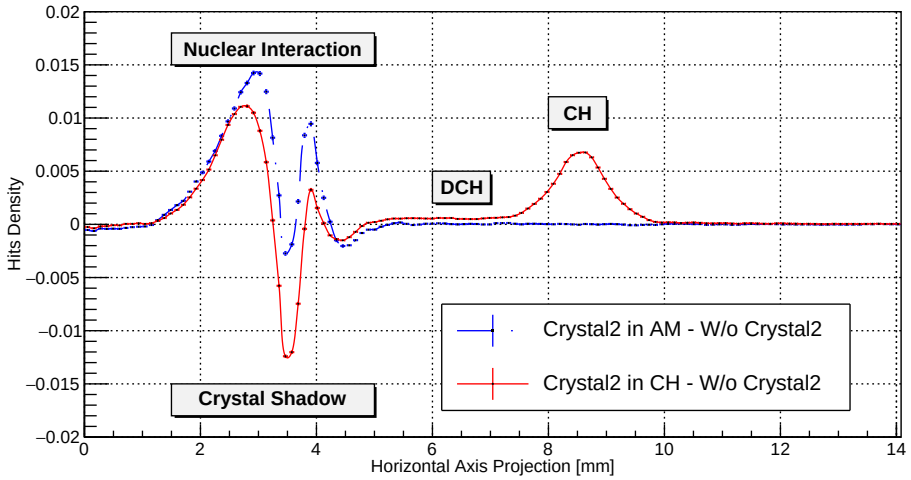

Figure 7.13: Differences between beam profiles: blue dot-dashed line – Crystal2 in AM orientation subtracted Without the crystal; red solid line – Crystal2 in CH orientation subtracted Without the crystal.

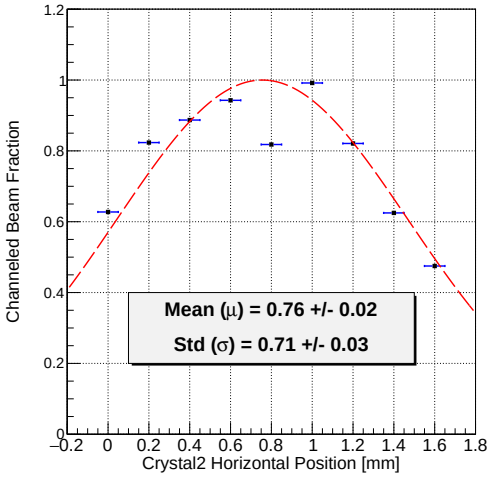

Figure 7.14: Distribution of the channeled beam fraction as a function of the Crystal2 horizontal position with respect to the single-channeled beam center. Red dashed line represents a Gaussian fit of the distribution.

with the measured values from the linear scan of the crystal in AM orientation: 0.69±0.01 mm (Fig. 7.6), and beam optics routine: 0.73 mm.

7.3 Upgraded configuration measurements

The main limitation factor of the test in 2017 was the too small cross-section of the available crystal in the downstream position. Therefore, during the 2017-2018 Winter Technical Stop an upgraded UA9 experimental layout included: optimized crystals, a new graphite absorber and a Roman Pot with Timepix detectors installed just upstream Crystal2 (Fig. 4.7b, highlighted in yellow).

The new crystals (Tab. 7.4, Fig. 7.15) are TCP78 (upstream Crystal1, upgraded TCP74, Tab. 6.2) and TCP75 (downstream Crystal2). A wide transverse aperture of the last provides a much larger fraction of incident beam undergoes through the double-deflection.

	Material (Plane)	L [mm] (±0.02)	W [mm] (±0.02)	Torsion [μrad/mm] (±0.8)	θ_{def} [μrad] (±1)
Crystal1 (TCP78)	Si(110)	4.0	1.5	3.0	301.0
Crystal2 (TCP75)	Si(110)	6.0	4.0	4.6	196.8

Table 7.4: Crystal parameters, where θ_{def} is a deflection angle of the crystal, L is its length along the beam, while W is a width of the crystal transversely to the beam direction.

In 2018 two dedicated runs in September and November for the double-crystal setup measurements have been performed. Table 7.5 shows the SPS beam conditions for the measurements, while particle trajectories are shown in Figure 7.16.

Beam	Momentum [GeV/c]	Intensity per bunch	Emittance [nm·rad]	Tune Q_h
proton	270	$\sim 10^{11}$	∼3.3	20.13

Table 7.5: SPS beam conditions during the measurements.

7.3.1 Upstream crystal alignment

At the first step of September run after the standard devices alignment with respect to the main beam, an angular scan of the Crystal1 (Fig. 7.17) has been

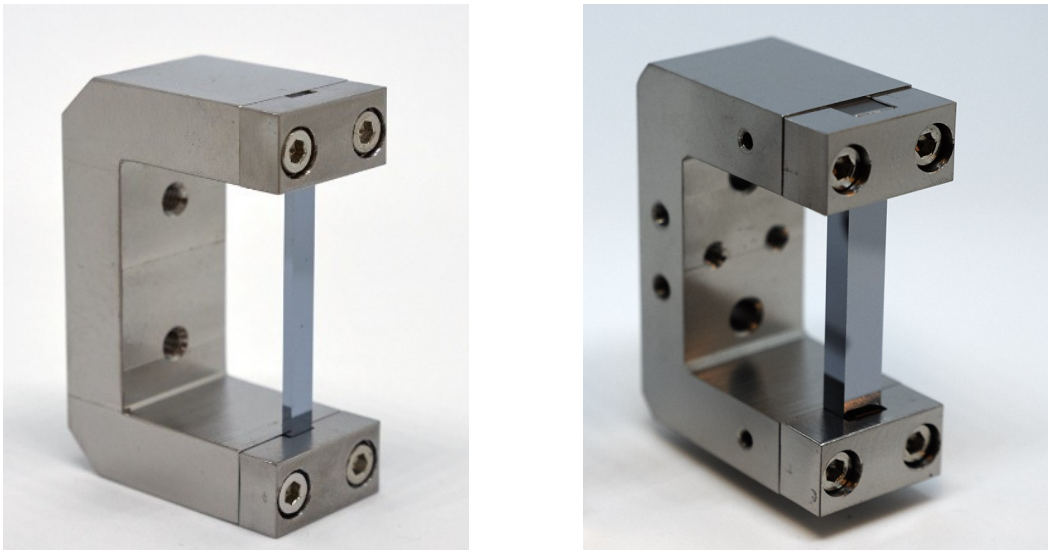

(a) Upstream Crystal1 (TCP78). (b) Downstream Crystal2 (TCP75).

Figure 7.15: New PNPI crystals for the double-crystal setup at the CERN SPS.

performed. Timepix detectors in the Roman Pot 0 (RP0) and Roman Pot 1 (RP1) were acquiring inside the deflected beam during the angular scan.

Figure 7.18 illustrates the Timepix images from the RP0 and RP1 during the angular scan of the Crystal1. As it is shown in Figure 7.18a, two shadows can be seen due to the channeled beam interaction with mechanical components of the Roman Pot 0 cage. The shape of the disturbed deflected beam is propagating along the machine and can be seen also on the Timepix in the Roman Pot 1 (Figure 7.18b). Such kind of beam interaction with the Roman Pot 0 is caused due to the vertical misalignment of the Roman Pot 0 with respect to the beam axis. The magnitude of the shift can be seen on Figure 7.18c, and can be compared with the image of the Timepix inside the Roman Pot 1 (Fig. 7.18d). The estimated vertical misalignment of the RP0 is about 4 mm, which leads to the beam position on the chip almost outside the sensitive area. Therefore, Timepix RP0 cannot be used for further measurements.

7.3.2 Downstream crystal linear scan

After the Crystal1 angular alignment, the downstream crystal in the AM orientation was moved toward the beam for the horizontal positioning into a single-channeled beam. A set of linear scans (Fig. 7.19) have been performed in order to measure an optimal horizontal position of the Crystal2 with respect to the center of

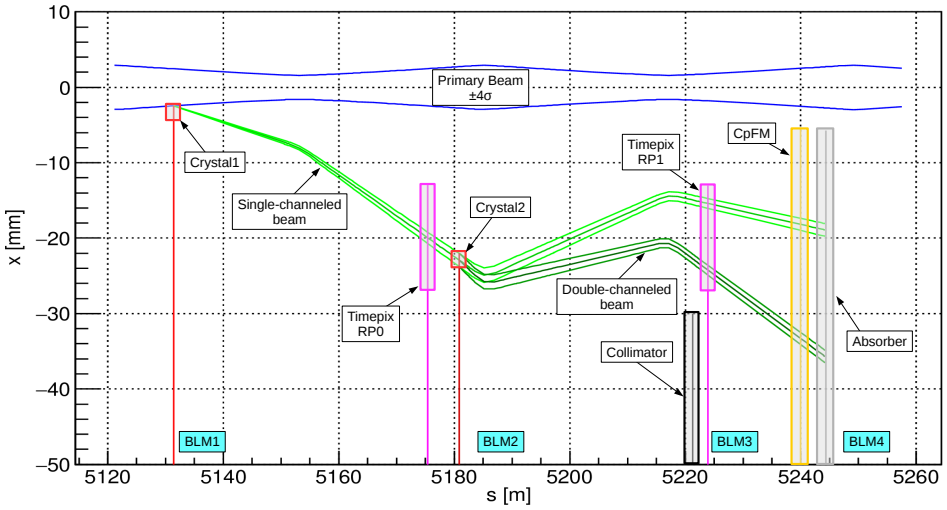

Figure 7.16: Horizontal projection (x) of the channeled halo particles as a function of the longitudinal coordinate (s) in LSS5. Blue lines represent the primary beam envelope with a 4σ of the width. An upstream Crystal1 (red line) deflects halo particles (green line), within $\pm\theta_c$ range (light green lines) onto the tungsten absorber (grey line), as well as channeled particles by the downstream Crystal2 (dark red line), inserted into the deflected beam by the upstream crystal with a phase advance of about 60°, in order to maximize the separation between channeled and primary beams (Eq. 3.25). Timepix (RP0 and RP1, pink line) and CpFM detectors, located between the crystal and absorber, intercept the channeled particles, while the collimator jaw (black line) is retracted from the beam. Each component of the setup is followed by the respective BLM counter, located outside the beam pipe.

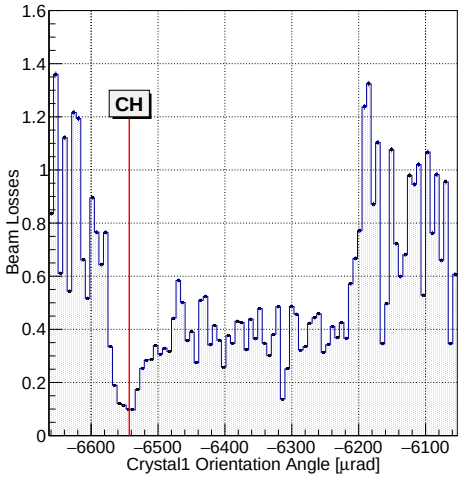

Figure 7.17: BLM1 relative counts during the angular scan of the Crystal1, normalized to the beam intensity.

the deflected beam. Figure 7.20b illustrates a fine horizontal scan, where the crystal shadow is crossing the single-deflected beam. The measured shadow width of $W_{sh} = 4.15 \pm 0.14$ mm is in a good agreement with a transverse size of the Crystal2 $W = 4.00 \pm 0.02$ mm, measured before the installation (Tab. 7.4).

Figure 7.21 shows two horizontal single-channeled beam profiles, when the downstream crystal was retracted from the beam ("Crystal2 OUT", horizontal position of 60-61 mm), and when it was perfectly aligned with respect to the center of the beam ("Crystal2 IN", horizontal position of 67-68 mm). For Crystal2 IN case, it can be seen an increase of the standard deviation (Std) compare to the Crystal2 OUT situation. However, due to the constant particle flux, the integrals (Int) of the counts within $\pm 3\sigma$ for two distributions are almost equal (about 1% of difference). It indicates that the inelastic nuclear interaction contribution is negligible. The angular distribution characteristics are listed in Table 7.6. The difference between the two cases can be explained by the multiple Coulomb scattering (MCS) of particles inside the downstream crystal. According to [124] the angular dispersion σ_{MCS} due to the MCS for a crystal, which contributes 6 mm of silicon, is about 11 μrad for a 270 GeV/c proton. Therefore, this value is in a good agreement with the measurements $\sqrt{\sigma^2_{Crystal2\ IN} - \sigma^2_{Crystal2\ OUT}} = 10.02 \pm 0.01$ μrad.

Taking into account the beta function value (β_x) at different positions along the beam (Tab. 7.7), the Std of the single-channeled beam in the Crystal2 reference frame can be computed as the follow:

$$\sigma_x^{CR2} = \sigma_x^{TPX} \sqrt{\frac{\beta_x^{CR2}}{\beta_x^{TPX}}} = 0.67 \pm 3 \cdot 10^{-4} \text{ mm}, \tag{7.2}$$

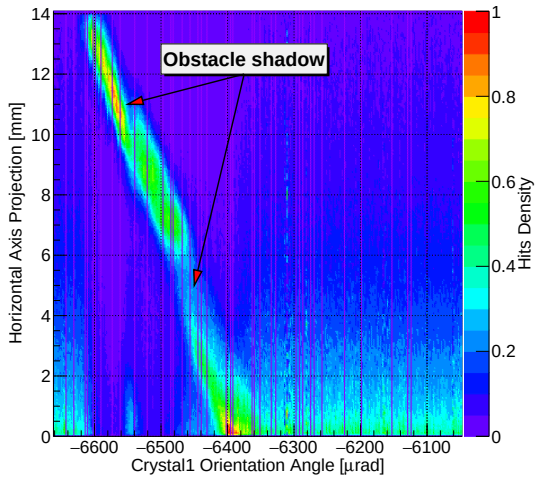

(a) Timepix RP0 image projection on a horizontal axis as a function of the Crystal1 orientation angle.

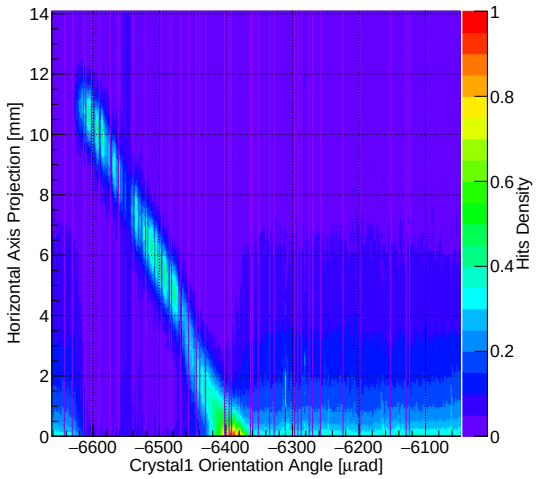

(b) Timepix RP1 image projection on a horizontal axis as a function of the Crystal1 orientation angle.

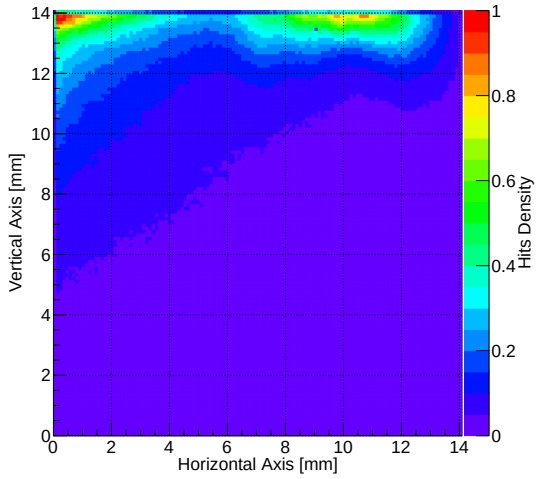

(c) Integrated image of the Timepix RP0 detector during the angular scan.

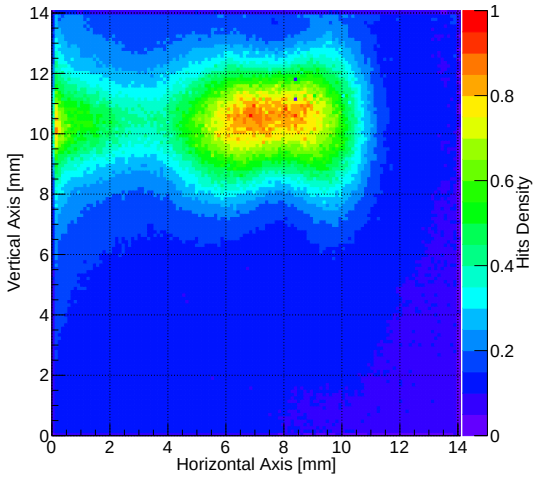

(d) Integrated image of the Timepix RP1 detector during the angular scan.

Figure 7.18: Images of the Timepix detectors during an angular scan of the Crystal1. The beam spot of a single-channeled beam is moving horizontally due to the crystal rotation. Shadows of the Roman Pot 0 mechanical components are visible on both Timepix detectors. The sensor inside the RP0 is shifted in a vertical direction due to the misalignment of the Timepix board with respect to the beam axis.

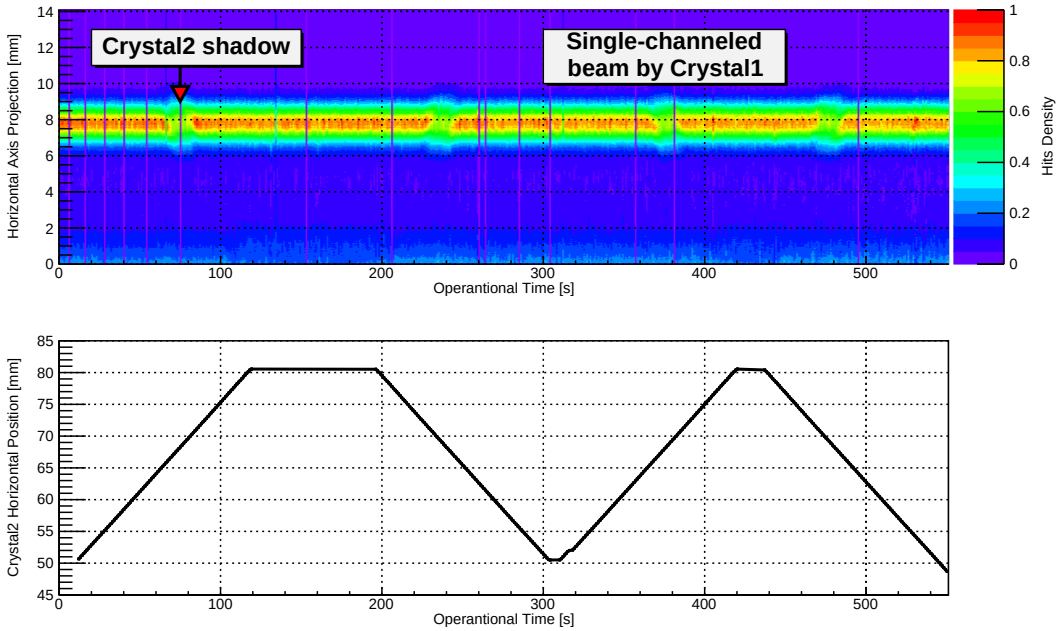

Figure 7.19: Timepix RP1 image projection on a horizontal axis as a function of the Crystal2 linear position.

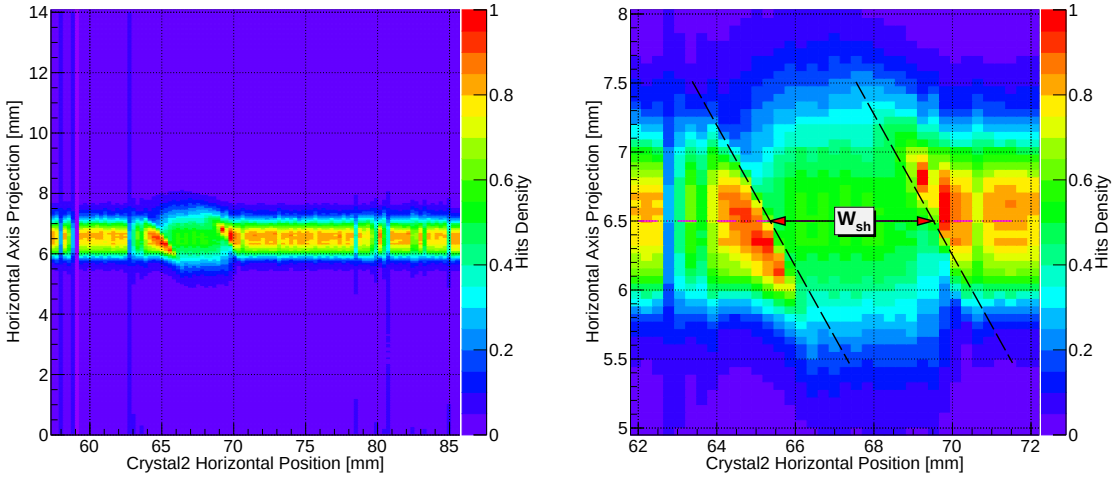

(a) Timepix horizontal projection. The movement of the Crystal2 shadow across a single-channeled beam.

(b) Zoomed In Timepix horizontal projection. The width (W_{sh}) of the shadow is measured between two edges of the particle scattered regions (black dashed lines).

Figure 7.20: Timepix horizontal projection during a fine linear scan of the Crystal2.

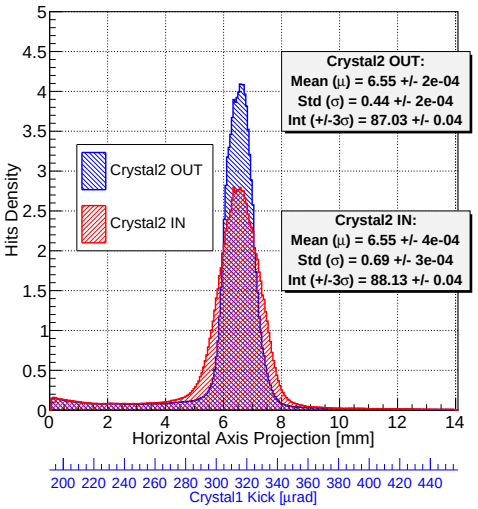

Figure 7.21: Horizontal single-channeled beam profile measured by means of the Timepix detector at RP1. Two distributions correspond to the following cases: the downstream crystal is retracted from a single-deflected beam ("Crystal2 OUT"), and the crystal is perfectly aligned at the center of the beam ("Crystal2 IN").

Configuration	μ [μrad]	σ [μrad]
Crystal2 OUT	315.34±4e-3	8.44±5e-3
Crystal2 IN	315.25±7e-3	13.10±9e-3

Table 7.6: Crystal1 kick angle characteristics, where μ is a mean value , while σ is a standard deviation.

Position	β_x [m]	α_x
Crysta1	74.6792	1.4887
Crysta2	93.5875	-1.73991
Collimator	35.9873	-0.739502
Timepix	40.1684	-0.852398
CpFM	78.5522	-1.54158
Absorber	92.9035	-1.73012

Table 7.7: SPS beam optics parameters in 2018.

where σ_x^{CR2} and σ_x^{TPX} are the standard deviations of the beam at the Crystal2 and Timepix positions respectively. Therefore, in a perfect aligned Crystal2 position, an almost entire single-channeled beam (within $\pm 3\sigma = 4.03 \pm 2 \cdot 10^{-3}$ mm, which means 99.7% of the total particles number) is intercepted by the downstream crystal ($W = 4.00 \pm 0.02$ mm).

7.3.3 Downstream crystal angular scan

To find the optimal Crystal2 channeling orientation, the Timepix detector has been operated during an angular scan. The downstream crystal has been placed in the center of a single-channeled beam, while the Roman Pot 1 was positioned intercept both beams (single- and double-deflected).

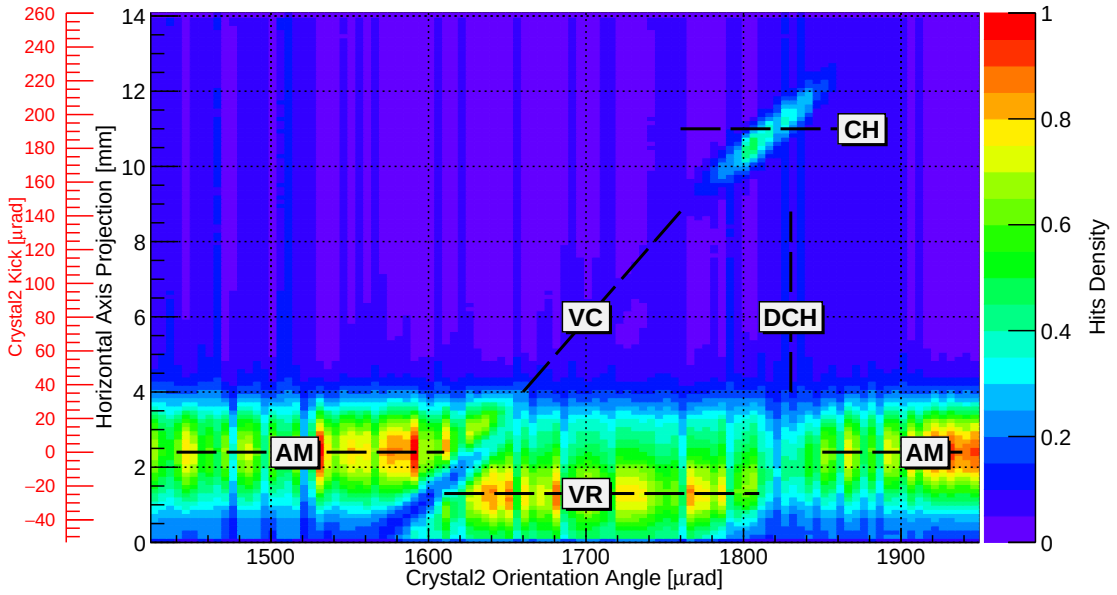

Figure 7.22: Timepix image projection on the horizontal axis as a function of the Crystal2 orientation angle, for 1 μrad/s of the goniometer rotational speed. Timepix detector has been operated in the Medipix mode with a 48 MHz clock, and 0.5 s of acquisition time window. Each Timepix image projection is normalized by the beam intensity. Black dashed lines represent different regions of the deflection angle distribution. Bin size is 0.11 mm$\times$5 μrad.

Figure 7.22 illustrates the Timepix horizontal axis projection during the Crystal2 angular scan. Due to the wide aperture of the crystal, it covers the entire single-channeled beam. Therefore, a typical particle deflection angle distribution (Fig. 6.2) can be recognized. The angular scan starts from the amorphous orientation (AM) of the crystal. At around 1600 μrad the volume reflection (VR) effect is starting to

dominate during about 200 μrad of the scan, which is close to the bending angle of the crystal (Tab. 7.4). The VR process is accompanied by the volume capture (VC), while at the perfect channeling orientation (CH) a deflected beam spot is located at around 1800 μrad with a low populated dechanneling region (DCH). Converting Timepix coordinates of the double-channeled beam projection into the Crystal2 kick angle (the second red vertical axis), the estimated deflection angles of the crystal are about 200 μrad and -20 μrad for CH and VR respectively.

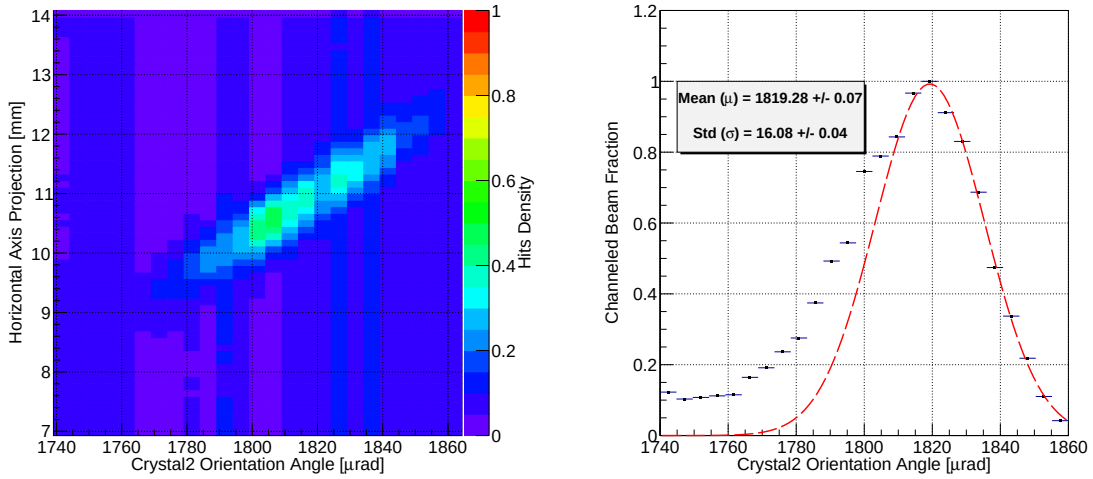

(a) Timepix image of the double-channeled beam spot projection on the horizontal axis as a function of the Crystal2 orientation angle.

(b) Double-channeled beam fraction as a function of the crystal orientation angle. Red dashed line illustrates a Gaussian function fit of the distribution.

Figure 7.23: Single-pass particle deflection as a function of the crystal orientation.

Performing a detailed analysis of the double-channeled beam spot during the scan, an angular distribution of the particles has been investigated. Figure 7.23 shows the behavior of the double-channeled beam spot as a function of the crystal orientation angle. The channeled beam fraction has been calculated as a ratio between counts integrals of the channeled peak (within $\pm 3\sigma$) and the entire frame, for each crystal orientation with a step of 1 μrad (Fig. 7.23b). By means of the Gaussian fit function the angular shape of the double-deflected beam has been reconstructed. Due to the significant influence of the volume reflection and volume capture effects, there is an increase of the counts for the Crystal2 orientation angle lower than $\sim$1800 μrad. The standard deviation (Std) of the distribution is equal to 16.08$\pm$0.04 μrad, while the expected value from the beam optics calculation is around 14.87 μrad. The discrepancy between measured and computed values of the angular standard deviation can be explained by the present of the Roman Pot 0

on the single-channeled beam, which leads to the increasing of the beam divergence due to the particle multiple scattering. In addition, the error of the beam optics parameters ($\Delta\beta/\beta$ ~10% for the SPS in 2009 [131]) can cause to the systematic error of the standard deviation estimation.

7.3.4 Channeling efficiency measurements at the SPS

To measure a single-pass channeling efficiency (ϵ_{SpCH}^{CR2}) for the Crystal2, a new machine fill has been used. The double-crystal setup has been repeated, while the orientation angle of the downstream crystal was setted to $\sim$ 1810 μrad.

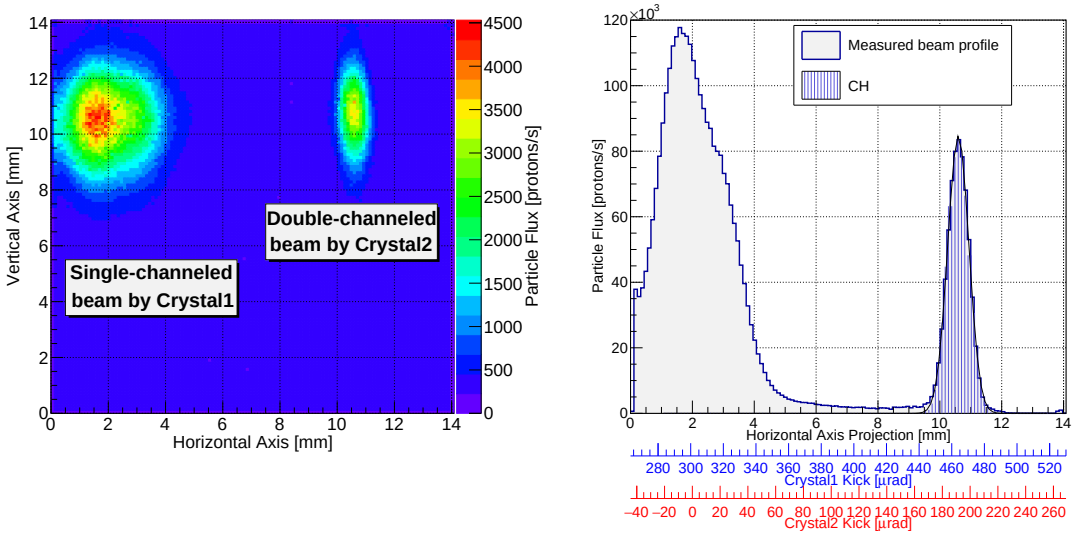

(a) Timepix integrated image of the double-channeling. Medipix mode, 0.5 s of the acquisition time window with 48 MHz clock, integration over 175 frames. Bin size is 0.11×0.11 mm^2.

(b) The horizontal projection of the Timepix integrated image. A Gaussian function has been used for the double-channeled peak fit. The correspondent crystals kicks at the Roman Pot 1 position is indicated. Bin size is 0.11 mm.

Figure 7.24: Timepix image of the channeled beam at the SPS.

Figure 7.24 shows an integrated 2D image of the double-channeled beam, measured by means of the Timepix detector. A not perfect crystal orientation for the particle channeling leads to the asymmetrical shape of the not channeled beam due to the volume reflection process. The measured channeling efficiency is equal to $0.188 \pm 3 \cdot 10^{-5}$, while from the H8 beamline measurements this value is about 48% (Tab. 6.2) for 40 AGeV/c ^{129}Xe ions (within $\pm\theta_c/2$).

The Timepix measurements have been followed by two linear scans of the collimator jaw (1 m of graphite, horizontal displacement $RMS_{MCS} \simeq 70$ μm and angular kick $\theta_{MCS} \simeq 121$ μrad due to the multiple Coulomb scattering [103]). Figure 7.25a

shows how the collimator shadow is crossing a single-channeled beam, while the Crystal2 in AM orientation. The same for a double-channeling configuration in Figure 7.25b. Multiturn and single-pass channeling efficiencies have been estimated by means of the beam losses at the collimator longitudinal position during the scans (Fig. 7.25c). According to [25], the BLM counts value at the moment when the jaw is touching the beam (i.e. it becomes the primary obstacle on the beam) is proportional to the incident particle flux onto the Crystal1. Therefore single- and double-channeling plateaus from the Error function fit, correspond to the deflection efficiency with respect to the incident particle flux. The calculated value of the multiturn channeling efficiency for the Crystal1 is $\epsilon_{MtCH}^{CR1} = 0.478 \pm 0.027$, while the double-channling deflection efficiency of the two crystals setup is equal to $\epsilon_{DCH} = 0.085 \pm 0.004$. In such a way, a computed single-pass deflection efficiency from the BLM measurements is: $\epsilon_{SpCH}^{CR2} = \epsilon_{DCH}/\epsilon_{MtCH}^{CR1} = 0.179 \pm 0.013$, which is in a good agreement with the Timepix measured value.

Due to the low flux of the beam circulating in the machine, a linear scan by means of the CpFM detector has been done with a new fill of the SPS. Figure 7.26 shows the number of detected particles as a function of the CpFM horizontal position (blue error bars). By means of the Double-Error function fit a differential beam profile is reconstructed (red solid line).

It can be seen that the ratio between double-channeled (57-67 mm) and single-channeled (75-82 mm) plateaus is about 0.5, which means that a single-pass channeling efficiency of the Crystal2 is about 50%, which is far away from the measured values by Timepix and BLM detectors. This beahaviour is explained by the present of the dependency between the incident beam position along the bar and CpFM detection efficiency (Fig. 6.84). Therefore, for long linear scans (more than 20-30 mm from the detection side of the bar) the CpFM detector becomes to be ineffective. However, it can be used for the beam parameters investigations (e.g. beam position, spatial width, crystal kick angle, etc.). Table 7.8 shows summarized information of the measured single- and double-channeled beams parameters.

7.4 Double-crystal setup with a target

During a technical stop of the SPS in September 2018, a tungsten target (3 mm along the beam, horizontal displacement $RMS_{MCS} \simeq 0.1$ μm and angular kick $\theta_{MCS} \simeq 46$ μrad due to the multiple Coulomb scattering [103]) has been installed in front of the Crystal2.

The goal of the measurement is to demonstrate a double-channeling of the pri-

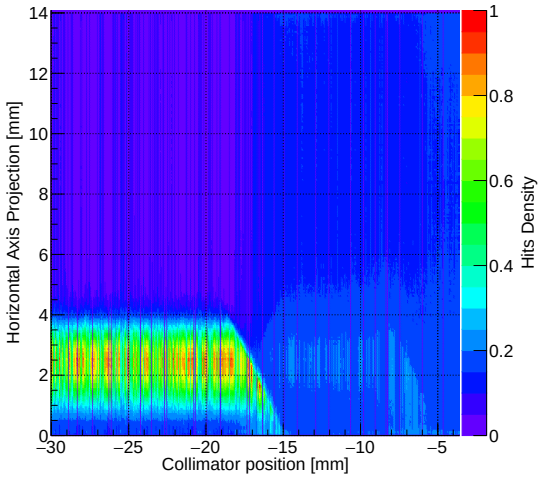

(a) The horizontal projection of the Timepix image as a function of the collimator position. Single-channeling configuration: Crystal1 in CH, Crystal2 in AM.

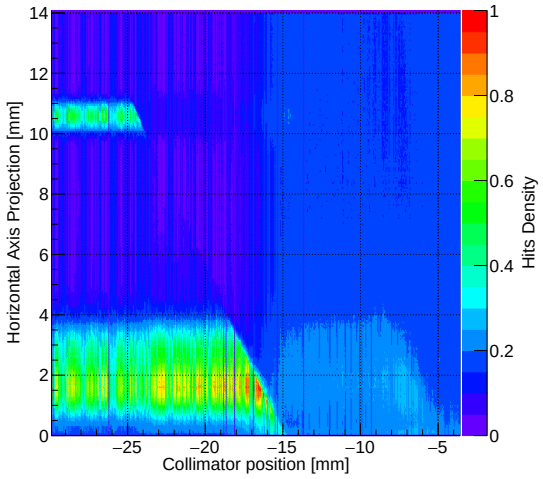

(b) The horizontal projection of the Timepix image as a function of the collimator position. Double-channeling configuration: Crystal1 in CH, Crystal2 in CH.

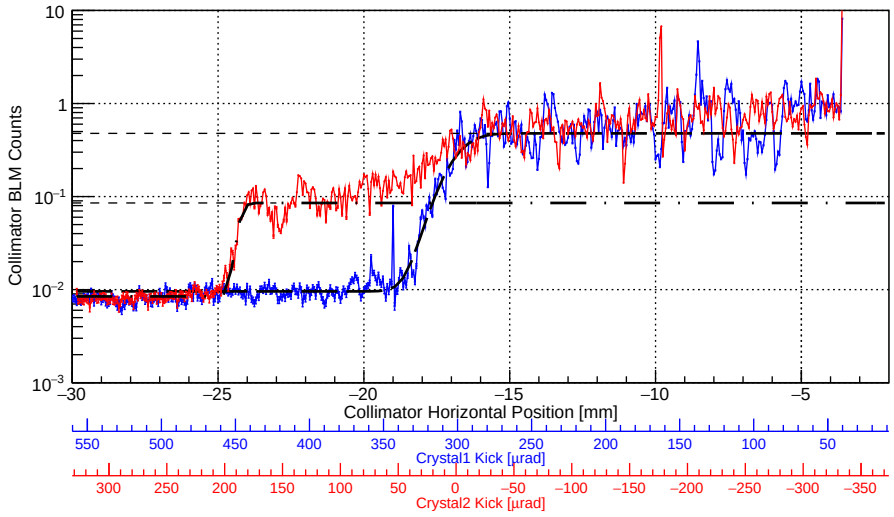

(c) Collimator jaw linear scan across single- and double-channeled beams. Linear speed of 50 μm/s. The spike is produced by the jaw touching the primary beam. Black dashed and dot-dashed lines illustrate a fit of the distributions by means of an Error Function for a single- and double-channeled beams respectively. BLM counts are normalized to the beam intensity.

Figure 7.25: Collimator linear scan.

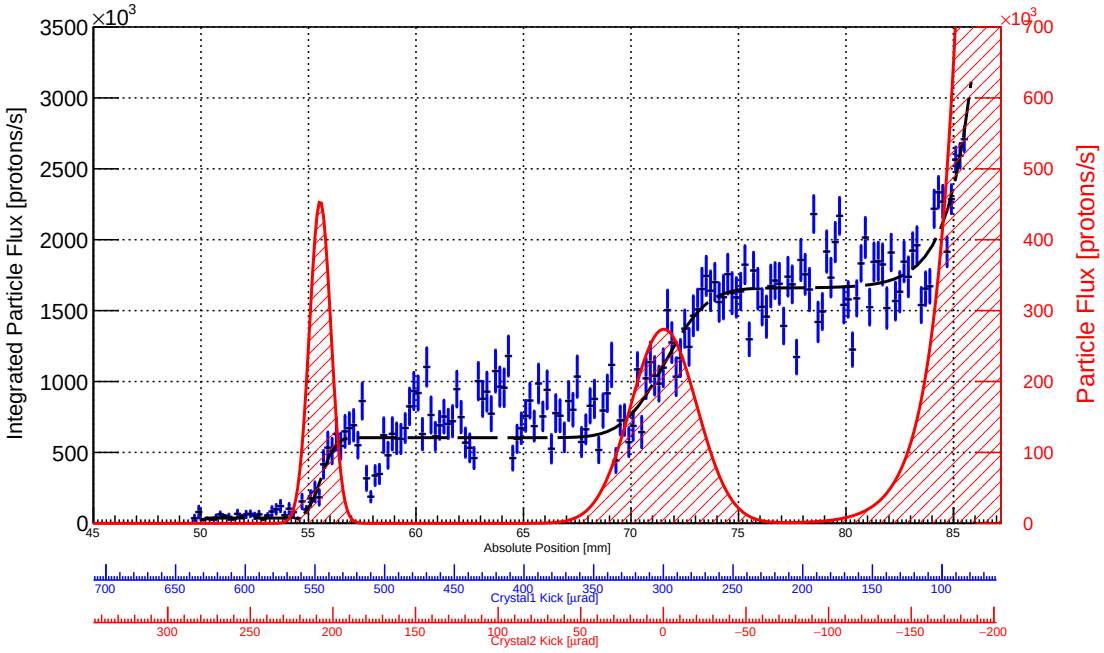

Figure 7.26: CpFM linear scan. Integrated particle flux as a function of the detector position. Black dashed line illustrates a Double-Error function fit of the distribution with an Exponential tail near the main beam edge. Red solid line is a differential of the fit function, represents the profile of the beam. Bin size is 0.2 mm.

Detector	$w_x^{coll.}$ [mm]	θ_{kick} [μrad]	
		μ [μrad]	σ [μrad]
Deflected beam by the Crystal1			
BLM Coll.	1.67±0.01	303.18±0.06	13.95±0.09
Timepix	2.05±0.01	299.83±0.01	17.43±0.01
CpFM	2.45±0.34	298.93±2.19	23.73±6.20
Deflected beam by the Crystal2			
BLM Coll.	0.45±0.01	188.16±0.09	4.78±0.16
Timepix	0.77±0.01	191.50±0.01	7.65±0.01
CpFM	0.79±0.10	207.05±0.99	6.46±1.62

Table 7.8: Parameters of the single- (by Crystal1) and double-deflected (by Crystal2) particle beams. $w_x^{coll.}$ is a width of the beam at the collimator longitudinal position, measured by different detectors taking into account beta function values; θ_{kick} is a measured deflection angle of the crystal, where μ is a mean value, and σ is a standard deviation. Parameters of the deflected beam by the Crystal1 are affected by multiple Coulomb scatterings inside the Crystal2.

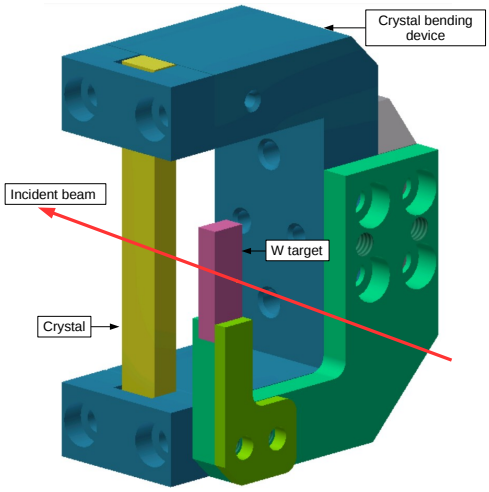

Figure 7.27: 3D drawing of the tungsten target ($width = 5\ mm \times thickness = 3\ mm \times height = 15\ mm$) installed in front of the Crystal2 at the SPS.

mary particles with a target.

7.4.1 Deflection efficiency at the SPS

Figure 7.28 shows a Timepix integrated image of a single-channeled beam by the Crystal1. The measured particle flux is about $5 \cdot 10^5$ protons/s. The Crystal2 with attached target is placed on the beam which leads to the increase of the beam spot size measured by the pixel detector. The measured horizontal beam size is $w_x = 2.355 \cdot \sigma_x = 4.95 \pm 2 \cdot 10^{-3}$ mm, which is almost 3 and 5 times higher than for Crystal2 IN and Crystal2 OUT cases respectively (Fig. 7.21). The computed kick angle of the Crystal1 is equal to 312.54 ± 0.02 μrad, with a divergence of 39.83 ± 0.03 μrad, which is affected by the multiple Coulomb scattering inside the target and Crystal2.

Due to the increase of the impinging to the Crystal2 beam divergence, the Timepix detector has been retracted by 7.5 mm, in order to intercept the double-deflected beam during Crystal2 angular scan. Figure 7.29a illustrates an evolution of the double-channeled beam spot during an angular scan of the Crystal2. The standard deviation of the channeled beam fraction distribution is equal to 42.05 ± 0.14 μrad (Fig. 7.29b), which is close to the incident single-channeled beam divergence (39.83 ± 0.03 μrad, Fig. 7.28b) obtained before.

Figure 7.30 shows a double-deflected particle beam by the Crystal2 at a fixed goniometer angle of about 541 μrad. The estimated single-pass channeling efficiency of the Crystal2 is about $\epsilon_{SpCH}^{CR2} \simeq 7\%$.

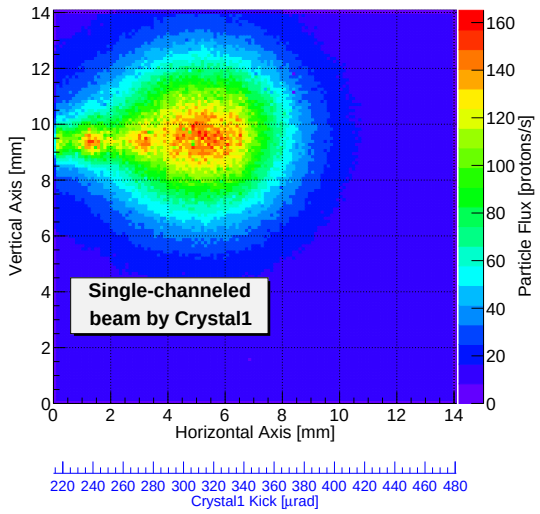

(a) Integrated Timepix image of a single-channeled beam. Medipix mode, 0.1 s of the acquisition time window with 48 MHz clock, integration over 970 frames. Bin size 0.11×0.11 mm^2.

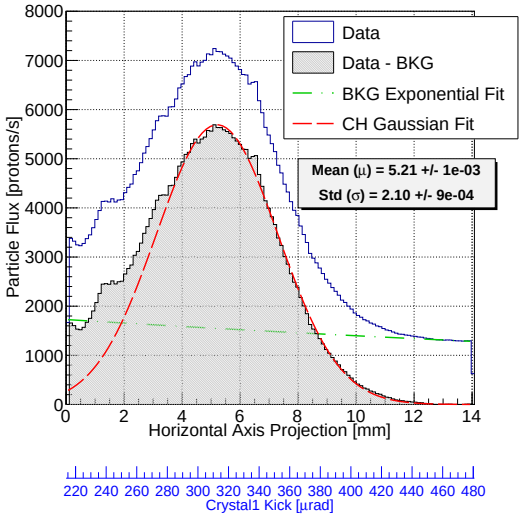

(b) The horizontal projection of the Timepix image. An Exponential function (green dot-dashed line) has been used for the background fit, while a Gaussian function (red dashed line) for the channeled peak fit.

Figure 7.28: Timepix image of the channeled beam at the SPS, where Crystal1 is in CH orientation, while Crystal2 with attached W target is in AM.

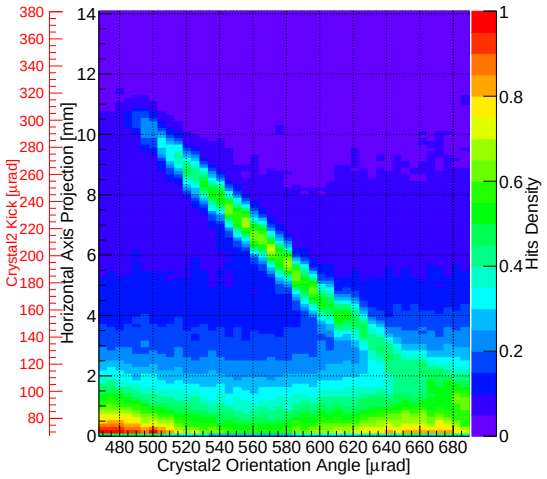

(a) Timepix image of the double-channeled beam spot projection on the horizontal axis as a function of the Crystal2 orientation angle. Bin size 0.11×5 μrad.

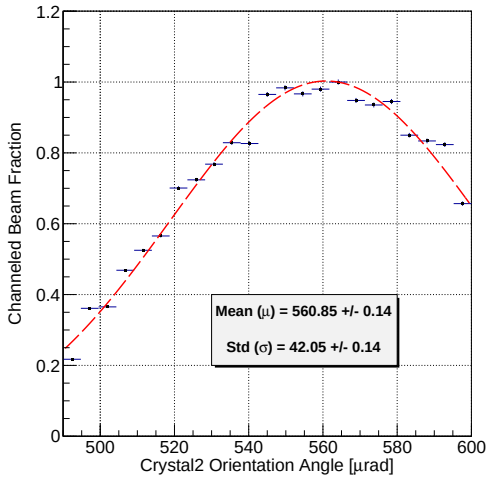

(b) Double-channeled beam fraction as a function of the crystal orientation angle. Red dashed line illustrates a Gaussian function fit of the distribution.

Figure 7.29: Single-pass particle deflection as a function of the crystal orientation.

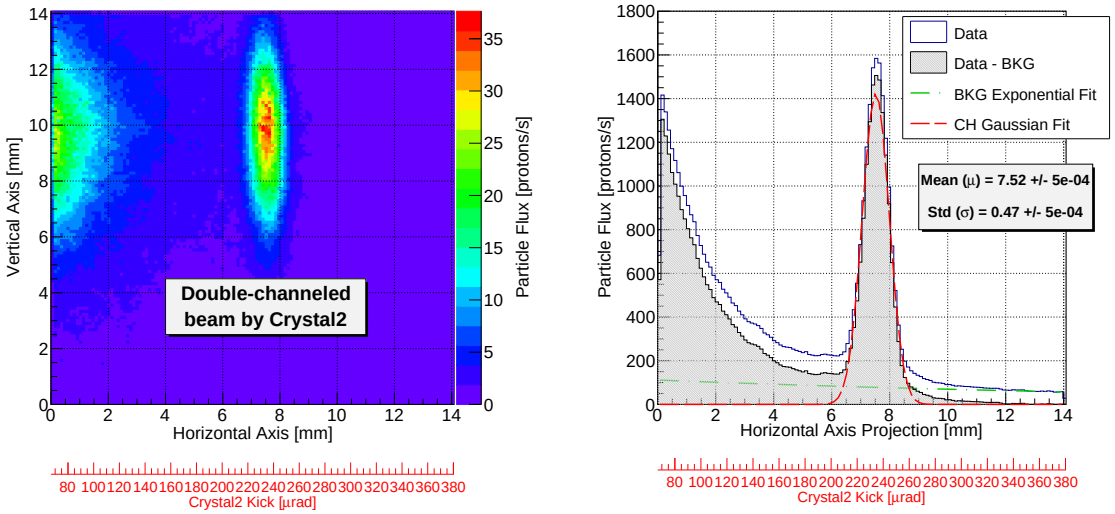

(a) Integrated Timepix image of the double-channeled. Medipix mode, 0.1 s of the acquisition time window with 48 MHz clock, integration over 396 frames. Bin size 0.11×5 μrad.

(b) The horizontal projection of the Timepix image. An Exponential function (green dot-dashed line) has been used for the background fit, while a Gaussian function (red dashed line) for the channeled peak fit.

Figure 7.30: Timepix image of the channeled beam at the SPS, where Crystal1 and Crystal2 are in CH orientation.

Figure 7.31 illustrates a linear scan by means of the CpFM detector crossing double- and single-channeled beams. It can be seen a big variation of the data value due to the low collected statistics. However, the profile of the beam has been reconstructed. The value of a single-channeled beam plateau is about $4 \cdot 10^5$ protons/s, which is close to the measured particle flux by means of the Timepix detector.

Considering the above results, the double-crystal setup has been performed with and without target in front of the downstream crystal at the SPS. Measured deflected beam parameters by means of the different detector types are in a good agreement. The two configurations can be compared through the summary Table 7.8,7.9. The methodology of crystals alignment has been developed. It has been possible to achieve a double-channeling efficiency of about 8.5%, which is a convolution of multiturn and single-pass deflection efficiencies. By means of pixel and Cherenkov detector the angular and spatial distributions of the channeled beam have been studied as well.

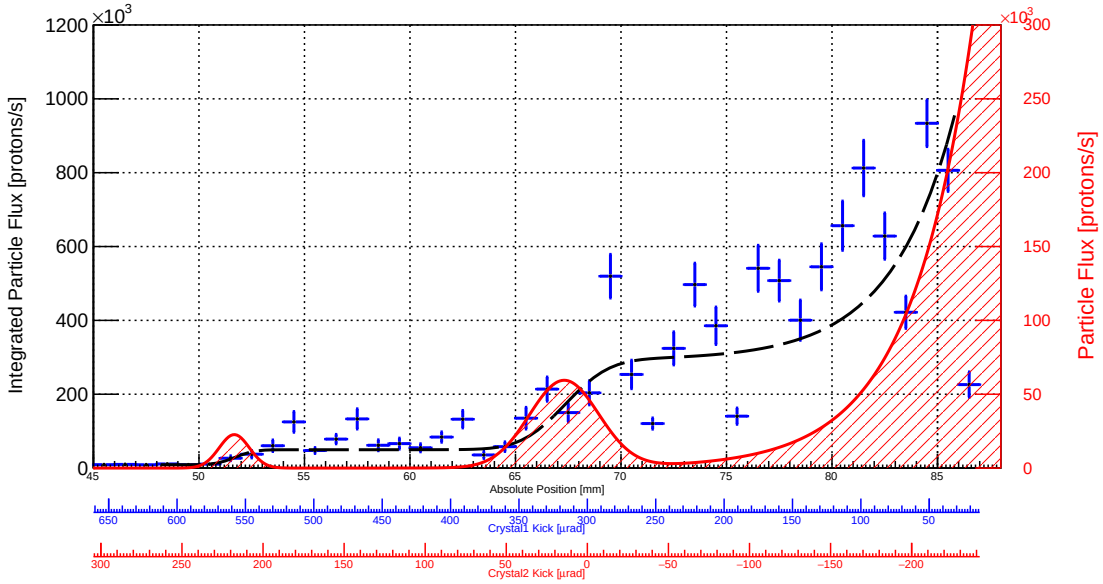

Figure 7.31: CpFM linear scan. Integrated particle flux as a function of the detector position. Black dashed line illustrates a Double-Error function fit of the distribution with an Exponential tail near the main beam edge. Red solid line is a differential of the fit function, represents the profile of the beam. Bin size is 1 mm.

Detector	$w_x^{coll.}$ [mm]	θ_{kick} [μrad]	
		μ [μrad]	σ [μrad]
Deflected beam by the Crystal1			
Timepix	4.68±0.01	312.60±0.02	39.81±0.03
CpFM	2.45±0.33	297.31±2.16	23.76±6.08
Deflected beam by the Crystal2			
Timepix	1.05±0.01	234.32±0.01	10.47±0.01
CpFM	0.80±0.10	205.81±1.04	6.51±1.69

Table 7.9: Parameters of the single- (by Crystal1) and double-channeled (by Crystal2) particle beams with a tungsten target. $w_x^{coll.}$ is a width of the beam at the collimator longitudinal position, measured by different detectors taking into account beta function values; θ_{kick} is a measured deflection angle of the crystal, where μ is a mean value, and σ is a standard deviation.

7.4.2 Beamline measurement

To verify the reduction of the single-pass channeling efficiency for the Crystal2 with attached tungsten target, measurements on the H8 beamline have been performed. A 180 GeV/c pion beam with a divergence of 29.68 μrad was directed onto the target with a crystal in CH. The crystal (6 mm long, 4 mm wide, bending radius of 29 m) had the same parameters as the SPS Crystal2. The target itself was positioned in such a way to cover only a half of the crystal surface (Fig. 7.32a). This configuration gave a possibility to compare results of the same particle beam interaction with and without target simultaneously.

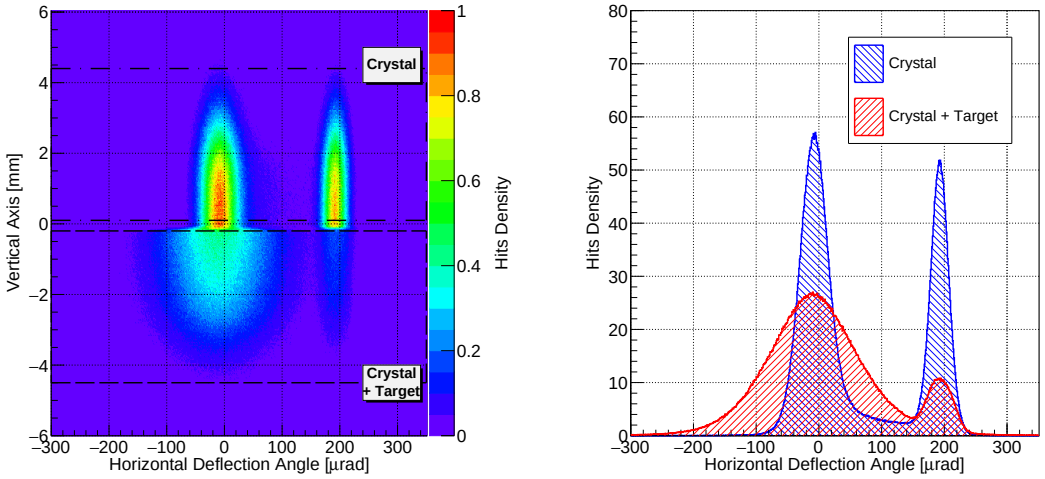

(a) Horizontal deflection angle of the primary particles as a function of the vertical incident position.

(b) Horizontal deflection angle.

Figure 7.32: H8 measurements with crystal and target for a 180 GeV/c pion beam. Diffusion of the particle beam for the crystal region with target is due to the multiple Coulomb scatterings inside 3 mm of tungsten.

Figure 7.32b illustrates deflection angle distributions for two cases. incident primary particles have been selected within the following range: $\pm 3\sigma = \pm 25.32$ μrad, where σ is a standard deviation of a single-channeled beam at the SPS (Tab. 7.6).

It can be seen that due to the multiple Coulomb scattering of the incident particles inside the target, the standard deviation ratio between with and without target cases for the AM peak is about 3, which is the same for SPS measurements by means of the Timepix detector. For the CH peak the ratio value of 1.4 has been computed from the beamline and circular accelerator as well. The measured deflection efficiencies at H8 are $0.35 \pm 0.01\%$ and $0.10 \pm 0.01\%$ for the crystal and crystal+target

Peak	μ [μrad]	σ [μrad]
Crystal		
AM	-7.21±0.04	23.45±0.03
CH	192.65±0.02	14.83±0.02
Crystal + W target		
AM	-5.83±0.27	71.30±0.19
CH	191.84±0.08	21.48±0.06

Table 7.10: Parameters of the particle beam with and without a tungsten target on the H8 beamline with 180 GeV/c pions. μ is a mean value of the measured particle deflection angle, while σ is a standard deviation.

cases respectively. It leads to the reduction factor of about 3.5, while for the SPS measurements it is $\sim$2.7.

Concerning BLM counts during Crystal2 linear and angular scans, any signal, caused by the target insertion into a single-channeled beam, was not observed. Low sensitivity of the losses monitors and particle flux ($10^{10} - 10^{11}$ protons/bunch) circulating inside the machine explain such behavior.

Chapter 8

Measurements of short-living baryons properties at the SPS and LHC

In this Chapter, an idea of the magnetic dipole moment (MDM) measurements for short-living baryons is described. In particular, we will focus on charm baryon Λ_c^+. Using a strong effective magnetic field between atomic planes of a bent crystal, we will investigate the spin precession of the particle. Feasibility of the MDM measurements and possible experimental layout at the SPS and LHC will be discussed as well.

8.1 Motivation

The main idea of the present study is to investigate the magnetic dipole moment, which is a fundamental characteristics of of a particle. It defines the interaction between the particle inside an external magnetic field. For a plenty of particles the MDM is well known [124]. However, for hadrons, there is a strong interest in the MDM measurement to prove the quark model predictions about hadrons composition.

The magnetic moment of a charged, spin-1/2 particle is given by:

$$\overrightarrow{\mu} = \frac{2\mu}{\hbar} \cdot \overrightarrow{S}, \qquad \mu = g \cdot \frac{q}{2mc} \cdot \frac{\hbar}{2}, \tag{8.1}$$

where $\overrightarrow{S} = \overrightarrow{\sigma} \cdot \hbar/2$, m and q are the particle spin, mass and charge respectively. g is a gyromagnetic factor as a result of relativistic quantum mechanics (the Dirac equation) [132]. The magnetic interaction is associated with a rotation of the spin of

the particle. In case of $g = 2$ the particle is a Dirac particle, while $g \neq 2$ (magnetic moment anomaly) signals about a composite structure of the particle.

In the quark model, the MDM of the baryons is defined by the MDMs of its constituent quarks. For instance, the magnetic moment for a proton ground state (uud):

$$\overrightarrow{\mu_p} = \overrightarrow{\mu_u} + \overrightarrow{\mu_u} + \overrightarrow{\mu_d}, \tag{8.2}$$

which leads to the following proton MDM equation:

$$\mu_p = \frac{4}{3}\mu_u - \frac{1}{3}\mu_d \simeq 2.793\mu_N, \tag{8.3}$$

where $\mu_N = e\hbar/(2m_pc)$ is a nuclear magneton, and $\mu_{u,d} = q_{u,d}e\hbar/(2m_{u,d})$ are the quark magnetons. Analogy for the neutron (udd):

$$\mu_n = \frac{4}{3}\mu_d - \frac{1}{3}\mu_u \simeq -1.913\mu_N. \tag{8.4}$$

A slightly different situation for the $\Lambda_c^+(udc)$, which is an object of our study. This baryon contains $u-$ and $d-$quarks whose spins are coupled to 0 and so contribute neither to the spin nor to the magnetic moment of the baryon [132]. Therefore, the spin and MDM of the Λ_c^+ are determined by the $c-$quark:

$$\mu_{\Lambda_c^+} = \mu_c. \tag{8.5}$$

According to ψ-meson spectroscopy [133] an "effective" mass of the charm quark is equal to $m_c \simeq 1.6$ GeV. Therefore, the Λ_c^+ MDM and g-factor can be expressed in terms of the c-quark g-factor:

$$\mu_{\Lambda_c^2} = 0.39\frac{g_c}{2}\mu_N, \qquad g_{\Lambda_c^+} = 1.91\frac{g_c}{2}. \tag{8.6}$$

There is a variety of the MDM calculations for the charm baryons based on different models. As for the Λ_c^+, the predicted g-factor is in the ranges:

$$\mu_{\Lambda_c^+} = (0.37 \div 0.42)\mu_N, \qquad g_{\Lambda_c^+} = 1.80 \div 2.05. \tag{8.7}$$

The measurement of the charm baryon MDM is a very important and useful to distinguish between different theoretical approaches. At the same time, studies of the charm quark MDM will tell us about the quark structure: $g_c = 2$ – a point-like Dirac particle, $g_c \neq 2$ – a composite particle (beyond the Standard Model).

8.2 Measurements approach

Due to the fact that baryons produced in nucleon-nucleon reactions are polarised, we are able to measure their MDMs. The method consists of measuring the initial

particle polarization vector and the precession angle after passing of an intense magnetic field. The polarization of the particle is reconstructed by measuring the angular distribution of its decay products. A short lifetime ($c\tau \sim 100$ μm) of baryons, with heavy flavored quarks, and required strong magnetic field (10-100 T), for the measurable precession angle, make impossible the use of conventional magnets ($\sim$10 m for 8-10 T [134]) for the MDM measurements. Therefore, it was proposed first by Baryshevsky [135] and Lyuboshitz [136] in 1979 to use an effective magnetic field between atomic planes of a bent crystal ($\sim$1 cm for up to 1000 T). The theoretical formalism of the spin precession in external electric and magnetic fields for a curved crystal case has been described in [8, 135–138]. The possibility to measure the magnetic and electric moments of short-lived particles at the LHC using of the spin rotation in bent crystals have been discussed in [139, 140] with preliminary estimations. In [1] authors revisited the idea, discussing the feasibility of the measurements at the LHC in the next years.

The first experimental realisation of the hyperon spin precession measurements using a bent crystal was conducted in 1992 at Fermilab [141]. A 800 GeV/c proton beam was directed onto a Cu target producing Σ^+ (uus) baryons ($c\tau \simeq 2.4$ cm) with an average momentum of 375 GeV/c and absolute polarization of (12$\pm$1)%. The precession angle of the polarization after channeling inside a 4.5 cm bent crystal ($\theta_{def} \simeq 1.6$ mrad) was measured of about 60°. Therefore, the received MDM value $\mu_{\Sigma^+} = (2.40 \pm 0.46_{stat} \pm 0.40_{syst})\mu_N$ is in agreement with the world-average value [124].

The MDM measurements of charm or beauty baryons at the LHC is complicated by three orders of magnitude shorter lifetime compare to the Σ^+. Therefore, to measure the magnetic moment of the Λ_c^+ at the LHC energies, a study of the bent crystal optimization, target-converter and possible layout have to be done. From now on in the text we will discuss only the most important (master) formulas and principles of the measurements at the LHC. A detailed information about precise calculations can be found in [1].

8.2.1 Precession of the polarization vector

Figure 8.1 illustrates a schematic layout of the experiment, where an incident proton beam hits a target-converter and produces polarized Λ_c^+ baryons, which are isotropically distributed over the azimuthal angle. The polar angle θ in the laboratory frame has a value of the order of γ^{-1} ($\theta \approx 10^{-3}$ rad for LHC energies), where γ is a Lorentz factor of the baryon. Due to the angular acceptance of the crystal, follows the target, only a small fraction of the Λ_c^+ will be channeled within

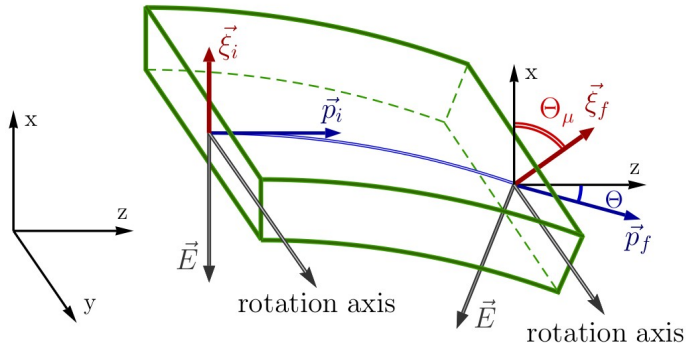

Figure 8.1: Schematic layout of the experiment. Effective electric field $\overrightarrow{E}$ is orthogonal to the momentum $\overrightarrow{p}$. The figure shows the case for $g > 2$. From [1].

a critical angle range.

Lets consider the case, where the baryon enters the crystal parallel to the Z-axis (Fig. 8.1), while the crystal is bent around Y-axis. In such a frame, we can write the initial $\overrightarrow{\xi_i}$ and final $\overrightarrow{\xi_f}$ polarization vectors as the follows:

$$\overrightarrow{q} = (0, q_y, q_z), \tag{8.8a}$$

$$\overrightarrow{p_i} = p(0,0,1), \qquad \overrightarrow{p_f} = p(-sin\Theta, 0, cos\Theta), \tag{8.8b}$$

$$\overrightarrow{E_i} = E(-1,0,0), \qquad \overrightarrow{E_f} = E(-cos\Theta, 0, sin\Theta), \tag{8.8c}$$

$$\overrightarrow{E} \times \overrightarrow{p} = Ep(0,1,0) \tag{8.8d}$$

$$\overrightarrow{\xi_i} = \xi(1,0,0), \qquad \overrightarrow{\xi_f} = \xi(cos\Theta_\mu, 0, sin\Theta_\mu), \tag{8.8e}$$

where $\overrightarrow{q}$ is the incident proton momentum, $\overrightarrow{p_i}$ and $\overrightarrow{p_f}$ are the baryon initial and final momentums respectively, $\overrightarrow{E_i}$ and $\overrightarrow{E_f}$ are effective electric fields in the crystal, $\overrightarrow{E} \times \overrightarrow{p}$ defines a rotation axis. The process of the Λ_c^+ production conserves the absolute value of the polarization:

$$p + A \to \Lambda_c^+ + X \qquad \Rightarrow \qquad \xi = |\overrightarrow{\xi}| = Const, \tag{8.9}$$

where the initial polarization vector is orthogonal to the production plane spanned by the incident proton and baryon momentums, due to the space-inversion symmetry of the strong interaction [1]. The angle of the polarization vector rotation Θ_μ after the passing of the crystal with a bending angle of Θ is defined as the follows [136, 137]:

$$\Theta_\mu = \gamma\left(\frac{g}{2} - 1 - \frac{g}{2\gamma^2} + \frac{1}{\gamma}\right)\Theta \approx \gamma\left(\frac{g-2}{2}\right)\Theta, \tag{8.10}$$

where the Lorentz factor $\gamma \sim 10^3$ for the LHC conditions.

8.2.2 Angular analysis and sensitivity studies

According to [1], we can measure the direction of the final baryon polarization vector after the crystal from the angular distribution of its decay products. Considering a weak decay of the spin-$\frac{1}{2}$ baryon into a final states of two particles (baryon and meson), the following relation holds in the rest frame of the baryon [1]:

$$\frac{1}{N} \cdot \frac{dN}{dcos\theta} = \frac{1}{2}(1 + \alpha\xi cos\theta), \tag{8.11}$$

where N is a number of events, θ is an angle between the final baryon and the polarization angle ξ_f, α is a week-decay parameter (a decay-channel-dependent quantity) [124], which characterizes parity violation in the decay.

The absolute statistical error of the g-factor measurements can be obtained from the angular analysis as the follows:

$$\Delta g = \frac{1}{\alpha|\xi|\gamma\Theta}\sqrt{\frac{12}{N_{\Lambda_c^+}}}, \tag{8.12}$$

where $N_{\Lambda_c^+}$ is a number of Λ_c^+ reconstructed and deflected by the crystal. This number can be expressed as the follows:

$$N_{\Lambda_c^+} = \Phi t \eta_{det} \frac{\Gamma_j}{\Gamma} N_{tar+crys}, \tag{8.13}$$

where $N_{tar+crys}$ is a number of the deflected baryons per incident proton:

$$N_{tar+crys} = \int \frac{\partial N_{tar}}{\partial \varepsilon} \eta_{def} e^{-\frac{L_{crys}}{c\tau\gamma}} d\varepsilon. \tag{8.14}$$

Here $\frac{\partial N_{tar}}{\partial \varepsilon}$ is the Λ_c^+ energy distribution after the target:

$$\frac{\partial N_{tar}}{\partial \varepsilon} = \rho N_A \sigma_{\Lambda_c^+} \frac{A_{tar}}{M_{tar}} \frac{\partial N}{\partial \varepsilon} \int_0^{L_{tar}} e^{-\frac{L}{c\tau\gamma}} dL, \tag{8.15}$$

Therefore, the final expression (master formula) for the statistical error of the measured g-factor can be written as the follows:

$$\Delta g = \frac{1}{\alpha|\xi|\Theta}\sqrt{\frac{12}{\Phi t \eta_{det} \frac{\Gamma_j}{\Gamma} \int \frac{\partial N_{tar+crys}}{\partial \varepsilon} \gamma^2 d\varepsilon}}. \tag{8.16}$$

Table 8.1 lists the definitions and values of different terms in Eqs. 8.13-8.16. The LHCb has been used as a reference detector for preliminary estimation of the detection efficiency.

The use of the non-channeled baryons determines the initial value of the Λ_c^+ polarization vector. Figure 8.2 shows measured and predicted Λ_c^+ polarization for different transverse momentum of the baryon. To calculate the mean value of the Λ_c^+

Terms	Values	Units
Proton flux, Φ	5×10^8	s^{-1}
Time of data taking, t	$\sim 10^6$	s
Detection efficiency (e.g. LHCb), η_{det}	0.002-0.03	–
Deflection efficiency, η_{def}	$10^{-4} - 10^{-2}$	–
Crystal length, L_{crys}	4-12	cm
Λ_c^+ decay length, $c\tau$	60	μm
Lorentz factor of Λ_c^+, γ	500-2000	–
Normalized production spectra, $\frac{\partial N}{\partial \varepsilon}$	Fig. 8.2	TeV^{-1}
Cross-section ($p + p \to \Lambda_c^+ + X$), $\sigma_{\Lambda_c^+}$	13.6±2.9	μb
Target density, ρ	19.25	g/cm^3
Avogadro number, N_A	6.022×10^{23}	mol^{-1}
Nucleon number of target, A_{tar}	183.84	–
Molar mass of target, M_{tar}	183.84	g/mol
Target thickness, L_{tar}	0.5-2	cm

Table 8.1: List of notations in Eqs. 8.13-8.16 [1].

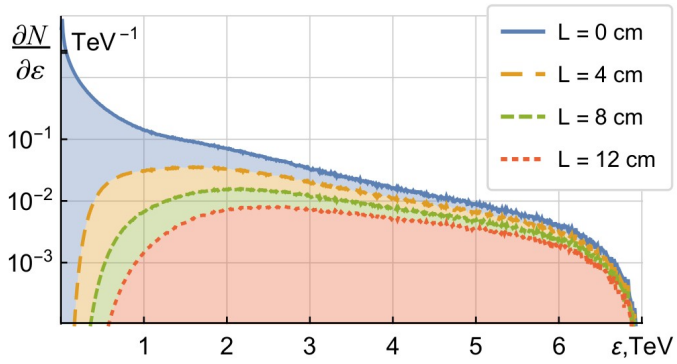

Figure 8.2: Energy distribution of Λ_c^+ baryons produced by 7 TeV protons in pp collision in a fixed target normalized to one produced Λ_c^+ baryon. Solid blue curve is for the initial distribution ($L = 0$), dashed curves are for different distances from the production point (listed on the right). From [1].

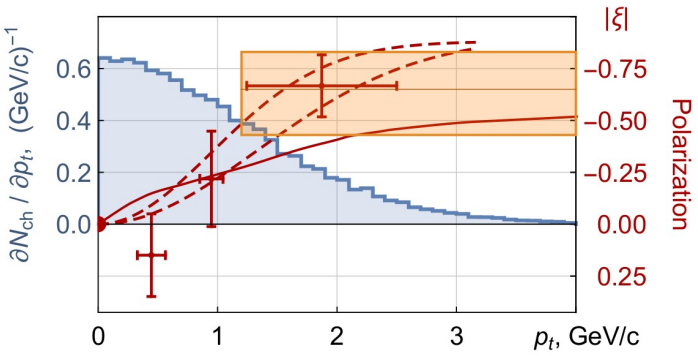

Figure 8.3: Polarization of Λ_c^+ as a function of its transverse momentum p_t. Experimental data: red crosses [142], orange rectangular area [143]; dashed red curves – experimental data fit by the normal distribution; solid red curve – theoretical prediction by the so-called hybrid model [144] for the process $\pi^- p \to \Lambda_c^+ + X$. Channeled baryons distribution over transverse momentum: blue histogram (simulation results obtained using PYTHIA8 version 8.1 [145]). From [1].

polarization we have used a convolution of the transverse momentum distribution and polarization curve as a function of the transverse momentum. The obtained values are about -0.37 and -0.40±0.05 for the theoretical prediction and experimental data, respectively.

The obtained results show that a precision of ±0.1 on the g-factor could be reached for up to a month of the continues data taking.

8.3 Possible experimental setup

A scenario of using a bent crystal to direct halo particles onto a target-converted followed by the second crystal in front of the existing detector has been proposed in a frame of the Physics Beyond Colliders at CERN. A possible optical layout including an existing installation at the LHC IR8 LSS was presented in [127], where the LHCb detector has been suggested to use for particle identifications and MDM measurements. Before to perform such an experiment at the LHC, in June 2016 it was proposed [129] to use an existing UA9 Collaboration setup at LSS5 zone of the SPS to proof of concept and measurement technique development (e.g. double-crystal setup, see Chapter 7).

Considering the obtained results from the H8 SPS extraction beamline measurements and double-crystal setup at the circular accelerator, the study of the possibility to measure baryons MDM includes investigations of the optimal (1) crystal

parameters (i.e. length, bending radius) and (2) detectors layout (i.e. type and size of the detector, configuration, position along the beam, etc.) for the measurements.

8.3.1 Crystal optimization for the SPS

For the fixed-target experiment at the SPS 270 GeV proton beam on COAST the centre of mass energy is $\sqrt{s} = 23$ GeV. There are no measurements at the given energy of the Λ_c^+ cross-section production. Therefore, we have estimated this value by means of the PYTHIA8 version 8.185 [145] as follows:

$$\sigma_{\Lambda_c^+}(p + p \to \Lambda_c^+ + X) = \{\sigma(g\overline{g} \to c\overline{c}) + \sigma(q\overline{q} \to c\overline{c})\} \cdot f(c \to \Lambda_c^+), \tag{8.17}$$

where $\sigma(g\overline{g} \to c\overline{c})$ and $\sigma(q\overline{q} \to c\overline{c})$ are charm cross-sections of the Hard QCD process, while $f(c \to \Lambda_c^+)$ is a fragmentation function of the baryon. These values are shown in Table 8.2. Therefore, the total computed cross-section of the Λ_c^+ production at $\sqrt{s} = 23$ GeV is $\sigma_{\Lambda_c^+}(p + p \to \Lambda_c^+ + X) = 2.558 \pm 0.001$ μb.

Terms	Values	Units
$\sigma(g\overline{g} \to c\overline{c})$	9.007	μb
$\sigma(q\overline{q} \to c\overline{c})$	2.808	μb
$f(c \to \Lambda_c^+)$	21.65±0.01	%

Table 8.2: Λ_c^+ production parameters from PYTHIA8.

A 3 mm long tungsten target was chosen as a converter for Λ_c^+ baryons production in the fixed-target experiment at the SPS. Figure 8.4 shows simulation results from the PYTHIA8 framework.

Varying Si crystal parameters (i.e. lengths, bending radius) an optimal configuration can be found by calculating an absolute g-factor relative error as the follows:

$$\left(\frac{1}{\Delta g}\right)_{norm} = \frac{\Delta g_{max}}{\Delta g} = \frac{\Theta}{\Theta_{max}} \sqrt{\frac{\int \frac{\partial N_{tar+crys}}{\partial \epsilon} \gamma^2 |\xi|^2 d\epsilon}{\int \frac{\partial N^{max}_{tar+crys}}{\partial \epsilon} \gamma^2 |\xi|^2 d\epsilon}}, \tag{8.18}$$

where index max corresponds to the maximum value of the Δg distribution in (L, R) phase-space. To reduce a computational time an optimization algorithm is based on a crystal parametrization routine [1].

Figure 8.5 shows the behaviour of the Δg^{-1}_{norm} value as a function of the crystal length and bending radius. It can be seen that the optimal crystal parameters as follows: R_{crys} = 0.5-2.0 m, L_{crys} = 5-15 mm. Fixing the radius at 1 m, the influence of the crystal length has been investigated. The most important criterion

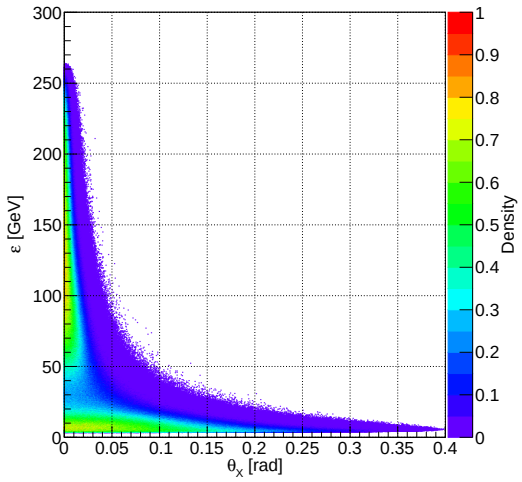

(a) Baryon energy as a function of the horizontal angle (i.e. in the deflection plane).

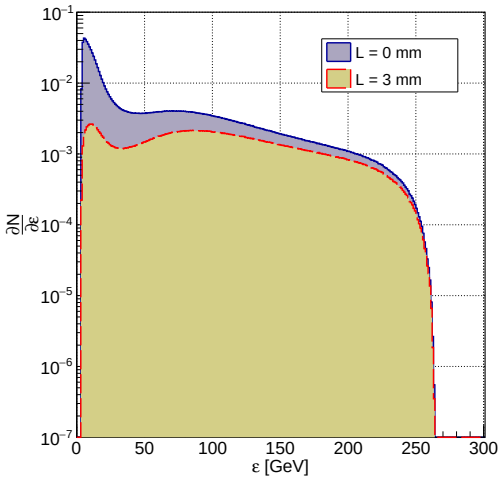

(b) Energy distribution of the Λ_c^+ at the production position ($L = 0$ mm, blue solid line), and after a certain distance from the production point ($L = 3$ mm, red dashed line). The distribution is normalized to one baryon.

Figure 8.4: PYTHIA8 simulation results of the Λ_c^+ spectrum produced in a pp-collision at $\sqrt{s} = 23$ GeV.

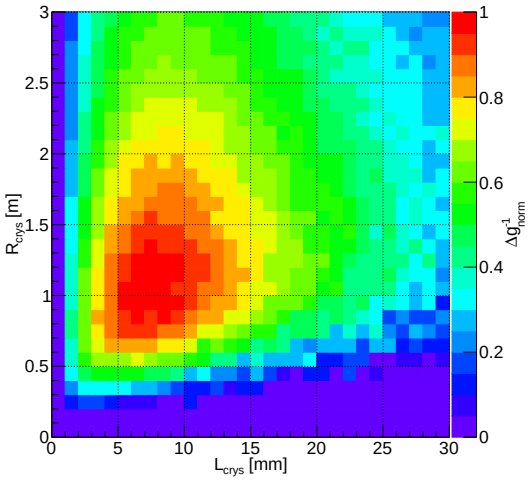

Figure 8.5: Normalized relative error of the g-factor as a function of the crystal length and bending radius. Due to the critical radius issue and dechanneling process, the regions at low bending radius and crystal length are less populated.

is a separation between (1) Signal: completely deflected baryons, which did not decay along the target+crystal, and (2) Background: not deflected baryons, which had the same angle as the channeled particles after passing the crystal, and did not decay along the target+crystal.

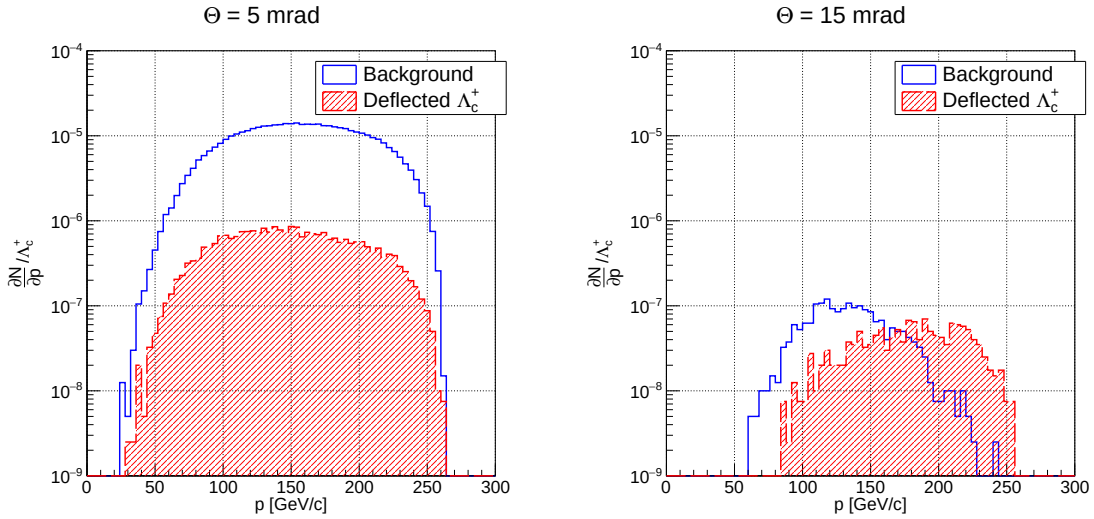

(a) R_{crys} = 1 m, L_{crys} = 5 mm. (b) R_{crys} = 1 m, L_{crys} = 15 mm.

Figure 8.6: Distribution of the Λ_c^+ baryons decayed after the target+crystal per one Λ_c^+ produced in a pp-collision at $\sqrt{s}$ = 23 GeV. Three times increasing of the bending angle degrees signal and background by 1 and 2 orders of magnitude respectively.

Due to a wide angular divergence of the produced baryons in a target, a large bending angle of the crystal is needed to separate Signal from Background (Fig. 8.6). Therefore, a silicon crystal with $\Theta = 15$ mrad was selected for further studies.

8.3.2 Baryons decay simulation

The parameter α has been well measured for the Λ_c^+ decay channels, which contain Λ baryon in the final states [124]. A large branching fraction has a decay channel $\Lambda_c^+ \to pK^-\pi^+$ ($\Gamma_j/\Gamma = 6.23 \pm 0.33$ % [124]). However, the most suitable decay channel for the present investigation was selected the following: $\Lambda_c^+ \to \Lambda\pi^+$ ($\Gamma_j/\Gamma = 1.29 \pm 0.07$ % [124]), while $\Lambda \to p\pi^-$ ($\Gamma_j/\Gamma = 63.9 \pm 0.5$ % [124]), with $\alpha = -0.91 \pm 0.15$ [124].

To increase statistics and optimize computing time a two-body decay simulation (2bDsim) routine has been developed for baryons decay processes. Figure 8.7 shows a comparison between Pythia8 and 2bDsim routine results for Λ baryon decay production. It can be noticed a good agreement with a discrepancy of less than 1%.

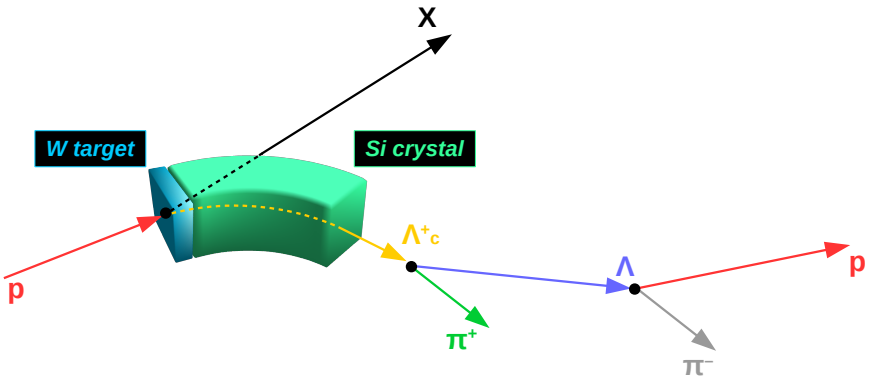

Figure 8.7: Baryons production and decay scheme: $p+N \to \Lambda_c^+ + X$, $\Lambda_c^+ \to \Lambda + \pi^+$, $\Lambda \to p + \pi^-$.

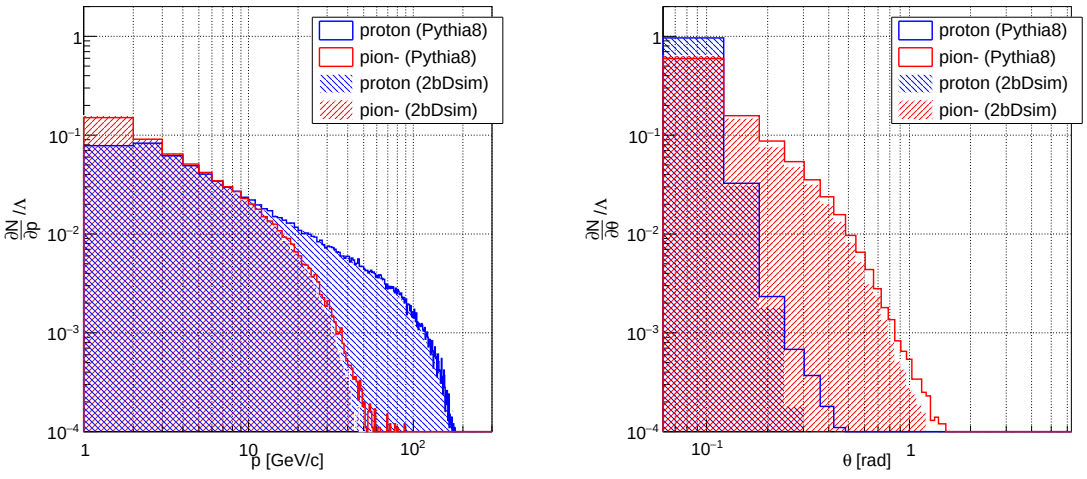

(a) Momentum distribution.

(b) Polar angle distribution.

Figure 8.8: Pythia8 and 2bDsim comparison between Λ baryon decay products ($\Lambda \to p + \pi^-$) distributions in a pp-collision at $\sqrt{s} = 23$ GeV. Normalized to one baryon.

8.3.3 Detectors configuration

The MDM measurements at the SPS have been proposed to conduct with minimum changes of the machine and existed detectors configurations. Furthermore, to measure the momentum of the charged particles an external magnetic field is required. Therefore, considering the present layout of the UA9 experiment (Fig. 4.7b) and future installation of the SPS dump in LSS5 after the Long Shutdown 2 (LS2) [146], there are two possibilities for the experimental configuration:

1. Use of a quadrupole magnet installed right after the target+crystal (Fig. 8.9a).
2. Extraction particle onto a septum-like electromagnetic deflector outside the beam pipe (Fig. 8.9b).

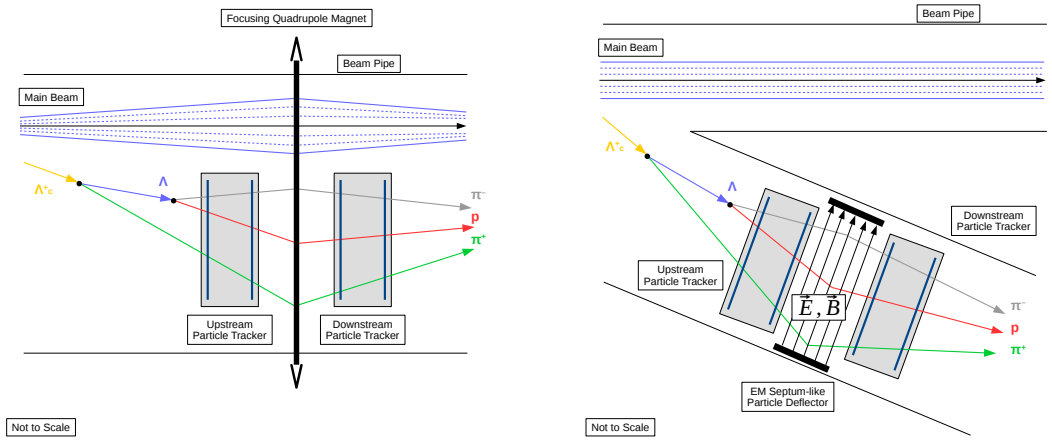

(a) An existing focusing quadrupole magnet.

(b) An extraction line equipped with an EM septum-like particle deflector.

Figure 8.9: Possible experimental configuration for MDM measurements at the SPS with different particle spectrometers.

A particle telescope based on Quadpix (28×28 mm^2) detectors (Subsec. 6.2.3.3), which has been tested at the H8 beamline [79], was proposed as a reference tracker for the measurements at the SPS.

8.3.3.1 Quadrupole magnetic spectrometer

An detailed drawing of the SPS LSS5 components can be found in [147]. Herein we will focused on region (Half Period 51810-51910), which is right after the target+crystal, and equipped with quadrupole magnet (QFA51810). This magnet (field

gradient of 10.4 T/m for the beam in COAST, length of 3.1 m for the core, and 3.3 m overall) focuses in a horizontal plane and defocusing in vertical one for positively charged particles, and vice verse for negatively charged.

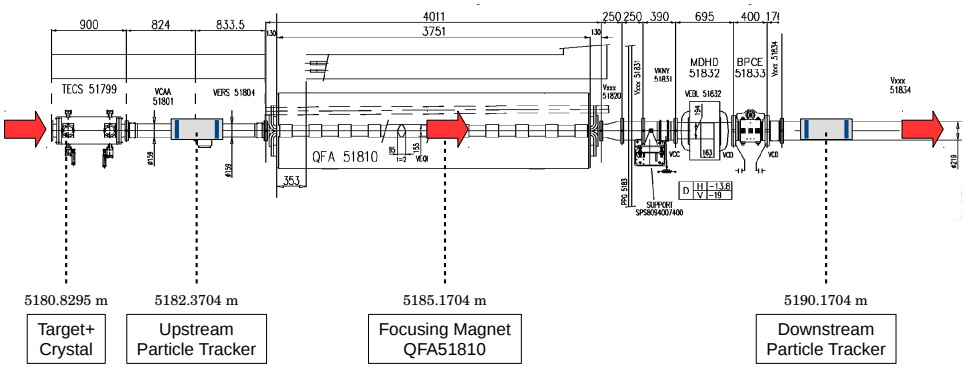

Figure 8.10: Possible experimental setup for MDM measurements at the SPS LSS5 with a quadrupole magnet.

Figure 8.10 shows an experimental layout for the measurements around the quadrupole magnet at the SPS LSS5. Λ_c^+ baryons produced in a target decay right after the channeling inside a bent crystal. Decay products π^- from the charm-baryon, π^+ and p from the Λ go through the upstream tracker. Figure 8.11 illustrates distributions of the products, where:

- Λ is required to be decayed before the upstream tracker;
- all products must be within an aperture acceptance of the quadrupole (ellipse with vertical half-axis of 0.01915 m, and horizontal – 0.076 m).

The orientation of the crystal was chosen to deflect particles towards the main beam in order to keep all decay products inside the beam pipe and aperture of the quadrupole.

Figure 8.12 shows spatial distributions of the baryons decay products at two positions of the particle tracker. An Upstream telescope consists of two identical set of planes from Internal and External sides of the machine ring to detect all needed particles. A Downstream telescope has only a tracker from the External side. The minimum distance between the detector edge and main beam (0;0) is about 3 mm, which is equal to 4σ of the horizontal beam size. A possible position of the sensor has been illustrated using a black solid rectangle. It can be seen that sensors cannot cover the entire distribution. Therefore, an estimated detection

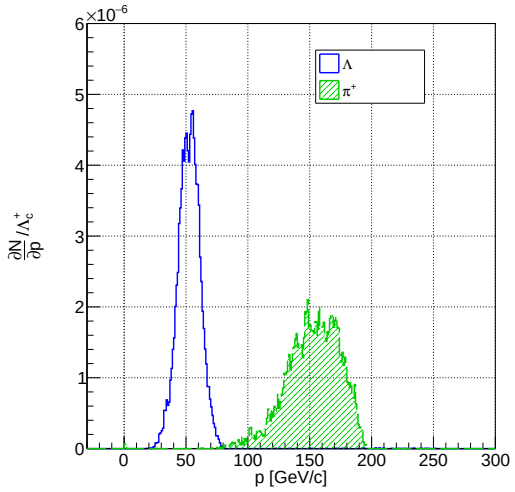

(a) Momentum distribution of the Λ_c^+ decay products.

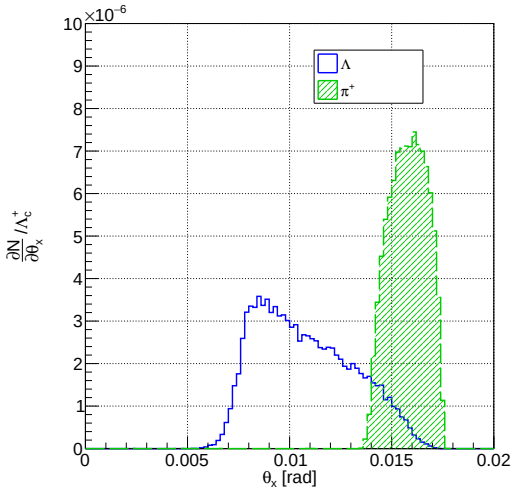

(b) Angular distribution in a horizontal plane of the Λ_c^+ decay products.

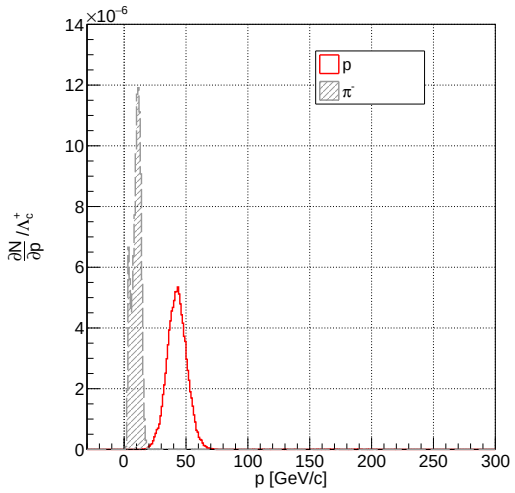

(c) Momentum distribution of the Λ decay products.

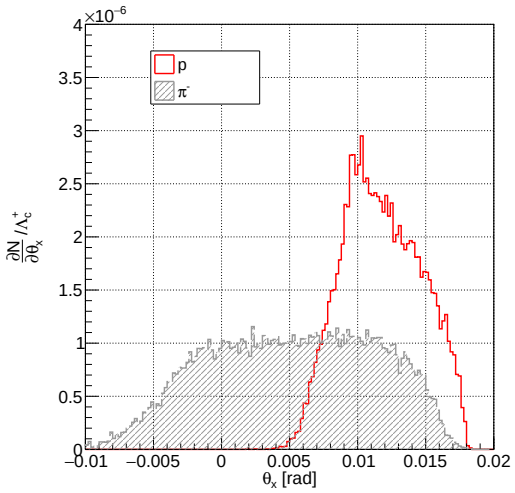

(d) Angular distribution in a horizontal plane of the Λ decay products.

Figure 8.11: Particle distributions of the baryons decay products in a laboratory reference frame. Normalized to one channeled Λ_c^+.

efficiency (simulations registration of all Λ_c^+ decay products) in a such configuration is about 10^{-8}.

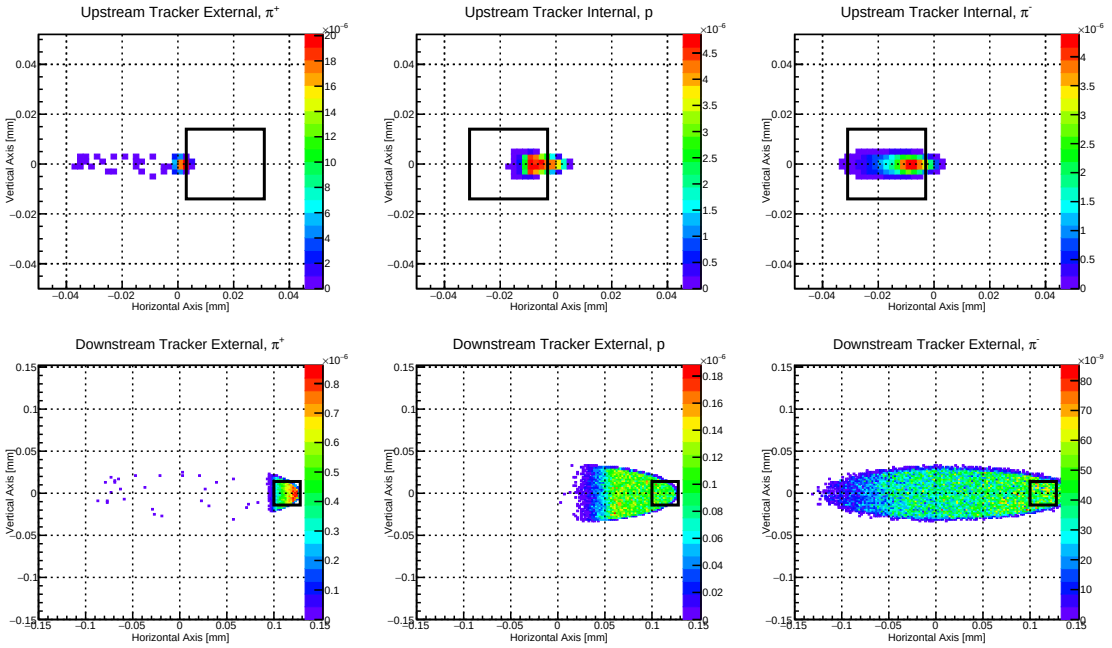

Figure 8.12: Spatial distribution of the baryons decay products at Upstream and Downstream trackers position. Black solid line illustrates a Quadpix detector sensitive area (28×28 mm^2). Normalized to a channeled Λ_c^+ baryon.

8.3.3.2 Septum-like spectrometer

Considering an EM septum-like deflector the downstream crystal with an attached target can be moved after the quadrupole QFA51810 (Fig. 8.13). An upstream particle tracker is placed about 1.5 m downstream the target+crystal. The crystal with a 15 mrad of bending angle deflects particles away from the main beam. Such a configuration in 3.5 m downstream the crystal produces about 5 cm of the separation between the main and deflected beams. It gives a possibility to insert a 4-5 m long section with particle telescopes before and after the EM deflector. Magnetic septum (Direct Drive Pulsed Magnetic Septum, Direct Drive DC Magnetic Septum, Eddy Current Septum, Lambertson Septum) [148] was chosen as the most promising device for particle spectrometry due to its short field length (0.3–1.2 m), and a wide range of the magnetic field (0.1–1.6 T).

According to Figure 8.11, momentums of the baryons decay products are varying from 1 GeV/c up to 200 GeV/c. Due to the active are of the Quadpix sensor of 28×28 mm^2, the maximum kick angle given by the deflector can be about $\theta_{kick}^{max} \approx 28$ mm/2 m $= 14$ mrad, where 2 m is a distance between the deflector and

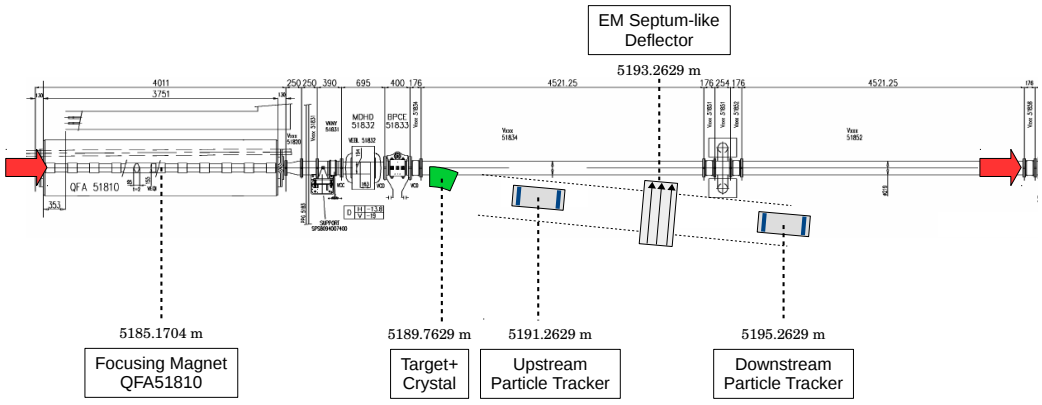

Figure 8.13: Possible experimental setup for MDM measurements at the SPS LSS5 with a EM septum-like deflector magnet.

downstream tracker (Fig. 8.13).

According to the Lorentz force equation $F = q[E + (v \times B)]$, the horizontal kick angle of the charged particle in a magnetic field can be written as follows [149]:

$$\theta_{kick,x} = \left[\frac{0.2998}{p}\right] \cdot \int B_y dl = \left[\frac{0.2998 \cdot l_{eff}}{p}\right] \cdot |B_y|, \tag{8.19}$$

B_y is the magnetic field in the y-direction (T), p is the beam momentum (GeV/c), l_{eff} is the effective (field) length of the magnet (m). Therefore, the maximum magnetic field for 1 GeV/c particle to produce 14 mrad deflection is about 50 mT for $l_{eff} = 1$ m. The minimum kick angle $\theta_{kick}^{min} = 70$ μrad is defined by the angular resolution of the tracker. Thus, for 200 GeV/c charge the field has to be not lower than 60 mT. In such a way the optimal amplitude of the magnetic field is about ~ 55 mT (~ 100 A of the coil current).

Figure 8.14 shows a typical magnetic septum with a rectangular aperture of 40 mm and 20 mm in horizontal and vertical planes respectively [150]. Figure 8.15 illustrates the spatial distribution of the baryons decay products. The estimated detection efficiency in a such configuration is about 10^{-4}.

8.3.4 Estimation results

According to the results discussed above and Eqs. 8.12-8.16, the final master formula can be written as the follows:

$$\Delta g = \frac{1}{\sqrt{\Phi \cdot t \cdot \eta_{det} \cdot \eta_{prod}}}, \tag{8.20}$$

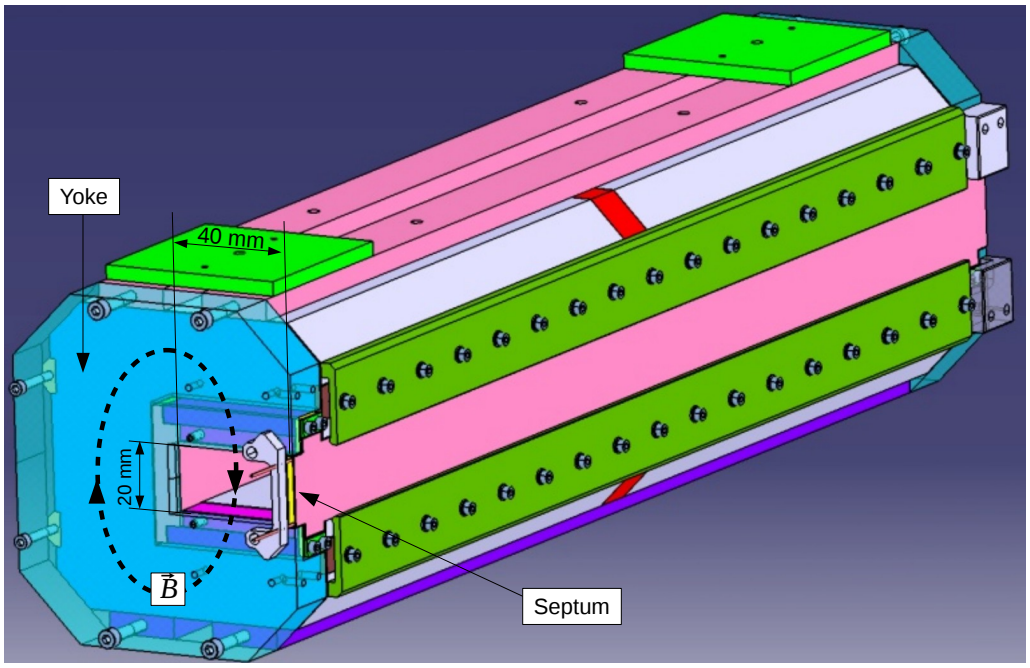

Figure 8.14: 3D drawing of the typical magnetic septum. From [148].

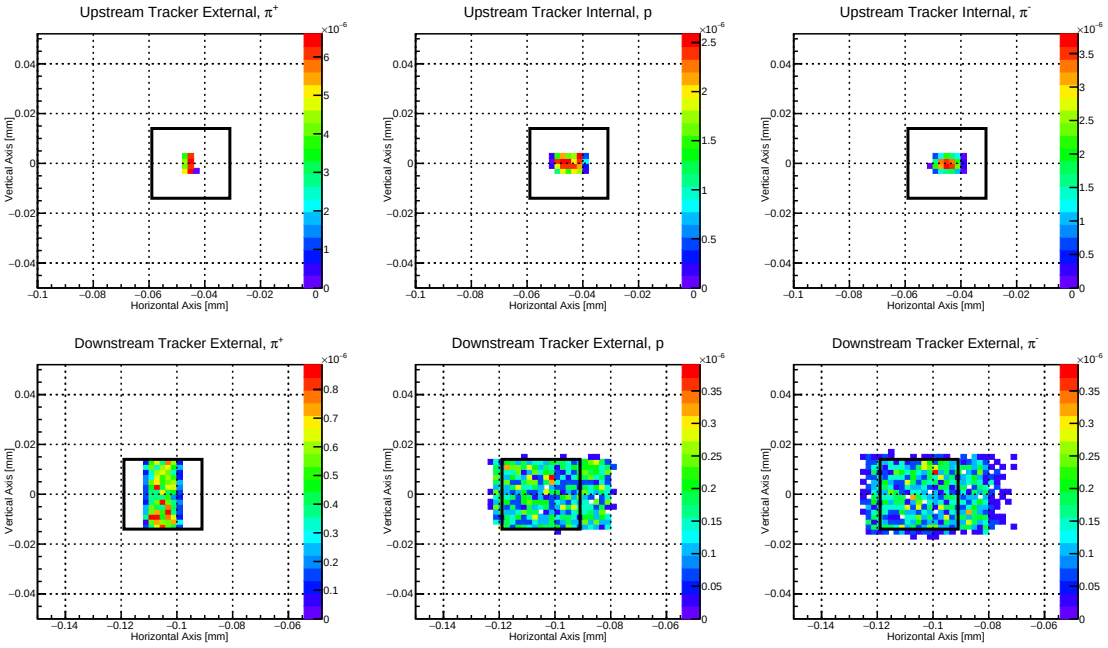

Figure 8.15: Spatial distribution of the baryons decay products at Upstream and Downstream trackers position. Black solid line illustrates a Quadpix detector sensitive area (28×28 mm^2). Normalized to a channeled Λ_c^+ baryon.

where η_{prod} is the baryon production efficiency, which is about $3.4 \cdot 10^{-16}$ Λ_c^+/proton. Figure 8.16 shows an absolute error of the g-factor as a function of the incident particles on a target ($\Phi \cdot t$).

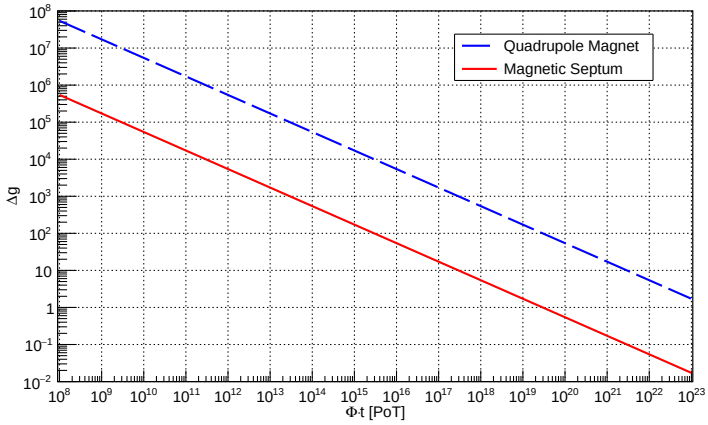

Figure 8.16: Estimated value of the absolute error of the g-factor as a function of the particles on a target (PoT) at the SPS.

It can be seen that to reach $\Delta g \sim 0.1$ within 1 month of the continuous machine operation, an incident particle flux of $\Phi \sim 10^{14}$ p/s is needed. Therefore, at the SPS accelerator these measurements are very challenging (or even impossible) to perform. However, to verify the experimental technique, a particle (kaon, pion, etc.) tagging can be done. For instance, a $\Sigma^+(uus)$ hyperon with a given decay channel provides $\eta_{prod}(\Sigma^+ \to p\pi^0) \sim 10^{-8}$ Σ^+/proton using a 2 cm long Si crystal with 2 m of the bending radius, by measuring momentums and angles of the hyperon and proton. It leads to $\Phi \sim 10^6 - 10^8$ p/s for one month of the operation to reach $\Delta g \sim 0.1$, which is more feasible at the present configuration.

Chapter 9

Conclusions

The measuring of the MDM of charm baryons is a fundamental study and validation of the Standard Model. Therefore, the ability to study this characteristic of the particle which contains heavy quarks is of great value in high-energy physics. By measuring the spin precession angle of the baryon in the effective magnetic field of a bent crystal gives a possibility to determine the gyromagnetic (g) factor of the charm quark. In this work, the absolute error of the measured g-factor were evaluated for two proposed experimental layouts at the SPS machine. Due to a small cross-section of the $p - N$ reaction ($\sigma \approx 2.6$ μb) with the production of the Λ_c^+ baryon, the necessary particle flux deflected by the crystal exceeds the capabilities of the SPS accelerator ($\sim 10^{11}$). However, to verify the measurement methods, it was proposed to carry out the tagging of particles with a higher production cross-section (e.g. Σ^+). Such a kind of measurements on the circular accelerator create certain requirements for the monitoring of the incident particles to the target and deflected beam by a bent crystal. Therefore, the main part of this thesis is focused on the development, calibration, and test of the devices for the absolute counting of the particles inside the beam pipe.

The improved geometry of the Cherenkov radiator for the CpFM detector makes it possible to count particles with a high resolution ($\sim$20%) per particle. A wide voltage range of the PMT gives a possibility to monitor the deflected beam from 1 to 1000 protons per bunch ($\sim$3 ns). Using a thinner radiator ($\sim$5 mm) a beam contamination study inside the circular accelerator can be performed. An important result of the research is the full matching between the expected particle flux and measured by the two independent and different types of detector: CpFM and Timepix. These devices were well-calibrated on the beamline and circular accelerator. Different operational modes of the pixel detector (Medipix, ToA, ToT) provide a quantitative characterization of the incident beam bunch per bunch, with possibilities of the

beam time structure investigation and integral particles counting. Using a sequence of such detectors, the tracking of particles on the extraction line was carried out and an angular resolution of 70 μrad was reached, which served as a reference to find the optimal experimental configuration for the MDM measurements at the SPS.

According to the obtained results, we are able to perform measurements of the various Z particle flux inside a circular accelerator by selecting: (A) a certain configuration of the Cherenkov radiator (pyramid or straight bar shape), (B) the supply voltage of the PMT, and (C) the operational modes of the Timepix. Development of faster electronics for the CpFM will make it possible to track changes in the intensity of the beam bunch per bunch (up to 43 kHz). For the pixel detector usage as a position sensitive device it is better to switch from the Timepix+FITPix to Timepix3+Katherine electronics [151, 152], which is faster (1.56 ns Clock, DAQ rate is up to 15 MHits/s), and works in ToA and ToT modes simultaneously.

This manuscript summarizes the work of the UA9 experiment from the point of view of detector physics and determines the vectors of further studies for the baryon MDM measurements using a double-crystal setup at the CERN SPS and LHC.

Acknowledgements

I want to send my warmest words of gratitude to my parents and sister Alyona. Thank them very much for their support and understanding. In the most difficult moments of my life, these people always helped me. Words of gratitude and love I send to my wife Tamara and little daughter Amélie. They became the greatest happiness and achievement during my PhD period and the whole of my life. Thank them for their care and support.

I want to express my deep gratitude and respect to my supervisor Achille Stocchi and co-supervisor Oleg Bezshyyko. Thanks to their advice, knowledge and experience, I have made this huge step towards becoming an independent highly qualified scientist. With the deepest respect, I will share all the knowledge that they have given me with the next generations. It is necessary to gratitude mention my mentor at CERN Walter Scandale. His invaluable experience and wisdom allowed me to understand more deeply the significance of those things with which I had to work. It is always pleasant to discuss with him not only working issues but also to share some life experiences. Thank him for his attention and help.

My technical curators deserve special attention. Veronique Puill and Fabrizio Murtas, thank them for all the time they gave me. I am very grateful to them for their work. Without them, I could not have gained such an invaluable experience in the instrumentation physics of Cherenkov and pixel detectors. Veronique always took care of me like my second mother. Fabrizio plunged me into the world of Italian atmosphere and friendliness. I will never forget the *spaghetti con la bottarga*. Merci beaucoup and grazie mille.

Leonid Burmistrov and Yury Gavrikov. These two people have invested not only strength but also their soul in my development as a physicist. Thank them for their support and always "on time" advice. I will never forget our snowboarding lessons, nightly experimental work on the beamline, with various types of detectors, motorized linear stages, etc. They have become more than just best friends for me. Thank them for everything!

Of course, I have to mention all those who surrounded me all this time: Marco

Garattini, Roberto Rossi, Francesca Addesa, Sebastien Dubos, Alex Fomin, Daniele Mirarchi, Chaumat Vincent, Sergey Barsuk, Stefano Petrucci, Francesca Galluccio, Francesco Iacoangeli, Simone Montesano, Luigi Esposito, and all those collegues from the UA9, EN/STI CERN, PNPI, IHEP, LAL, V.Karazin KhNU and T.Shevchenko KNU, which I did not mention because of my forgetfulness. Thank them very much for all their advices and support. I am very grateful to them for the friendly atmosphere.

Many thanks to my friends and students with whom I was lucky to work together. Without them, this period of my life was not full and colourful. Thank them for having fun evenings and travels, for dancing and songs.

I want to thank the workshop mechanicians group at LAL and EN/STI CERN for their efficiency in the production of all necessary components and tools for my research. Thanks also to Oleksandr Hryhorenko and his supervisor from IPNO for their professional assistance in the fused silica surface quality characterization by means of a confocal microscope.

Also many thanks to the reviewers and editors of this thesis. Without them, it would not have been possible to bring this manuscript into an academically qualitative shape.

I would like to complete by the following words of Albert Einstein: "Look deep into nature, and then you will understand everything better".

Andrii

Bibliography

[1] A.S. Fomin et al. Feasibility of measuring the magnetic dipole moments of the charm baryons at the LHC using bent crystals. *Journal of High Energy Physics*, 08:120, 2017.

[2] E. Bagli et al. Electromagnetic dipole moment of charged baryons with bent crystals at the LHC. *The European Physical Journal C*, 77:828, 2017.

[3] J. Stark. Bemerkung über Zerstreuung und Absorption von β-Strahlen und RöntgenStrahlen in Kristallen. *Physikalische Zeitschrift*, 13:973 – 977, 1912.

[4] V. Biryukov, Y. Chesnokov, and V. Kotov. *Crystal channeling and its application at high energy accelerators*. Springer, 1996.

[5] J. Lindhard. Influence of crystal lattice on motion of energetic charged particles. *Matematisk-fysiske Meddelelser udgivet af Det Kongelige Danske Videnskabernes Selskab*, 34:1 – 64, 1965.

[6] A. Taratin. Particle channeling in a bent crystal. *Physics of Particles and Nuclei*, 29:437 – 462, 1998.

[7] D. S. Gemmell. Channeling and related effects in the motion of charged particles through crystals. *Reviews of Modern Physics*, 46:129 – 227, 1974.

[8] V. M. Biryukov, V. I. Kotov and Yu. A. Chesnokov. Steering of high-energy charged-particle beams by bent single crystals. *Physics-Uspekhi*, 37:937 – 961, 1994.

[9] J. S. Forster et al. Deflection of GeV particle beams by channeling in bent crystal planes of constant curvature. *Nucler Physics B*, 318:301 – 318, 1989.

[10] E. N. Tsyganov. Some aspects of the mechanism of a charge particle penetration through a monocrystal. *Fermilab Report TM-682*, 1976.

[11] E. N. Tsyganov. Estimates of cooling and bending processes for charged particle penetration through a monocrystal. *Fermilab Report TM-684*, 1976.

[12] A. F. Elishev et al. Steering of charged particle trajectories by a bent crystal. *Physics Letters B*, 88:387 – 391, 1979.

[13] A. M. Taratin and S. A. Vorobiev. "Volume Reflection" of high-energy charged particles in quasi-channeling states in bent crystals. *Physics Letters A*, 119: 425 – 428, 1987.

[14] N.F. Shul'ga, V.I. Truten', V.V. Boyko, A.S. Esaulov. Scattering of high-energy particles by field of the bent crystal atomic planes. *Physics Letters A*, 376:2617 – 2621, 2012.

[15] Yu. M. Ivanov et al. Volume Reflection of a proton beam in a bent crystal. *Physics Review Letters*, 97:144801–1 – 144801–4, 2006.

[16] Yu. M. Ivanov et al. Volume Reflection of 1-GeV protons by a bent silicon crystal. *Journal of Experimental and Theoretical Physics Letters*, 84:372 – 376, 2006.

[17] W. Scandale et al. High-Efficiency Volume Reflection of an Ultrarelativistic Proton Beam with a Bent Silicon Crystal. *Physics Review Letters*, 98:154801–1 – 154801–4, 2007.

[18] W. Scandale et al. Volume Reflection Dependence of 400 GeV/c Protons on the Bent Crystal Curvature. *Physics Review Letters*, 101:234801–1 – 234801–4, 2008.

[19] W. Scandale et al. Multiple volume reflections of high-energy protons in a sequence of bent silicon crystals assisted by volume capture. *Physics Letters B*, 688:284 – 288, 2010.

[20] S. Baricordi, V. Guidi, A. Mazzolari, D. Vincenzi and M. Ferroni. Shaping of silicon crystals for channelling experiments through anisotropic chemical etching. *Journal of Physics D: Applied Physics*, 41:245501, 2008.

[21] J. H. Barett et al. Hyperchanneling. *Atomic Collisions in Solids*, pages 645 – 668, 1975.

[22] N. F. Shul'ga and A. A. Greenenko. Multiple scattering of ultrahigh-energy charged particles on atomic strings of a bent crystal. *Physics Letters B*, 353: 373 – 377, 1995.

[23] W. Scandale et al. High-Efficiency Deflection of High-Energy Protons through Axial Channeling in a Bent Crystal. *Physics Review Letters*, 101:164801, 2008.

[24] W. Scandale et al. High-efficiency deflection of high energy protons due to channeling along the $< 110 >$ axis of a bent silicon crystal. *Physics Letters B*, 760:826 – 831, 2016.

[25] V. Previtali. Performance evaluation of a crystal-enhanced collimation system for the LHC. *Ph.D. thesis, École Polytechnique Fédérale de Lausanne*, 2010.

[26] S. Timoshenko and J. N. Goodier. *Theory of elasticity*. Mc-GRAW-HILL BOOK COMPANY, Inc., 1951.

[27] V. M. Biryukov et al. Crystal deflector for highly efficient channeling extraction of a proton beam from accelerators. *Review of Scientific Instruments*, 73: 3170 – 3173, 2002.

[28] V. Guidi et al. Study of anticlastic deformation in a silicon crystal for channeling experiments. *Journal of Applied Physics*, 107:113534, 2010.

[29] Yu. M. Ivanov et al. Observation of the Elastic Quasi-Mosaicity Effect in Bent Silicon Single Crystals. *Journal of Experimental and Theoretical Physics Letters*, 81:99 – 101, 2005.

[30] Klaus Wille. *The Physics of Particle Accelerators*. Oxford University Press, 2000.

[31] J. Le Duff. Longitudinal beam dynamics in circular accelerators. *CERN European Organization for Nuclear Research-Reports-CERN*, 1994.

[32] The RD22 Collaboration. Status Report on RD22: Crystal Extraction at the SPS. *RD22 Status Report*, CERN/DRDC 92-51:1 – 11, 1992.

[33] The RD22 Collaboration. Second Status Report on RD22: Crystal Extraction at the SPS. *RD22 Status Report*, CERN/DRDC 94-11:1 – 16, 1994.

[34] G. Arduini et al. Deflection and Extraction of Pb Ions up to 33 TeV/c by a Bent Silicon Crystal. *Physical Review Letters*, 79:4182 – 4185, 1997.

[35] A. G. Afonin et al. The schemes of proton extraction from IHEP accelerator using bent crystals. *Nuclear Instruments and Methods in Physics Research B*, 234:14 – 22, 2005.

[36] R. P. Fliller III et al. Results of bent crystal channeling and collimation at the Relativistic Heavy Ion Collider. *Physical Review Special Topics - Accelerators and Beams*, 9:013501, 2006.

[37] C. T. Murphy et al. First results from bent crystal extraction at the Fermilab Tevatron . *Nuclear Instruments and Methods in Physics Research B*, 119:231 – 238, 1996.

[38] R. Assmann, S. Redaelli, W. Scandale. Optics study for a possible crystal-based collimation system for the LHC. *LHC Project Report*, 918:1 – 4, 2006.

[39] J. B. Jeanneret. Optics of a two-stage collimation system. *Physical Review Special Topics - Accelerators and Beams*, 1:081001, 1998.

[40] R. Assmann et al. Designing and building a collimation system for the high-intensity LHC beam. *LHC Project Report*, 640, 2003.

[41] G. Apollinari et al. High-Luminosity Large Hadron Collider (HL-LHC). Technical Design Report V. 0.1. *CERN Yellow Reports: Monographs. CERN-2017-007-M*, 4, 2017.

[42] D. Mirarchi. Crystal collimation for LHC. *Ph.D. thesis, Imperial College London*, 2015.

[43] R. Rossi. Experimental Assessment of Crystal Collimation at the Large Hadron Collider. *Ph.D. thesis, Sapienza Universitá di Roma*, 2017.

[44] R. Losito. UA9 Instrumentation and Detectors in the CERN-SPS. *CERN-ATS-2010-150*, 2010.

[45] W. Scandale et al. The UA9 experimental layout. *Journal of Instrumentation*, 6:T10002, 2011.

[46] M. Pesaresi et al. Design and performance of a high rate, high angular resolution beam telescope used for crystal channeling studies. *Journal of Instrumentation*, 6:P04006, 2011.

[47] M. Pentia et al. Multiple scattering error propagation in particle track reconstruction. *Romanian Journal of Physics*, 40:181 – 191, 1995.

[48] F. Iacoangeli et al. Nuclear Interaction Detector system for UA9 experiments based on ArduSiPM prototype. *Proceedings of the IEEE Nuclear Science Symposium and Medical Imaging Conference*, 2015.

[49] F. Iacoangeli, A. Natochii et al. A smart adjustable Inelastic Nuclear Interactions counter based on compact Arduino control system and readout. *Proceedings of the IEEE Nuclear Science Symposium and Medical Imaging Conference*, 2017.

[50] A. Natochii et al. Motorized linear stages for the UA9 experiment. *Preprint at the CERN Document Server*, CERN-EN-2019-001:1 – 15, 2019.

[51] W. Scandale et al. Probability of inelastic nuclear interactions of high-energy protons in a bent crystal. *Nuclear Instruments and Methods in Physics Research B*, 268:2655 – 2659, 2010.

[52] W. Scandale et al. Study of inelastic nuclear interactions of 400 GeV/c protons inbent silicon crystals for beam steering purposes. *The European Physical Journal C*, 78:505, 2018.

[53] R. Brun and F. Rademakersh. ROOT - An object oriented data analysis framework. *Nuclear Instruments and Methods in Physics Research A*, 389:81 – 86, 1997.

[54] S. Montesano and W. Scandale. Apparatus and experimental procedures to test crystal collimation. *Proceedings of the 3rd International Particle Accelerator Conference*, THEPPB011:3254 – 3256, 2012.

[55] E. Piselli et al. CERN-SPS wire scanner impedance and wire heating studies. *Proceedings of the 3rd International Beam Instrumentation Conference*, 2014.

[56] M. Gasior et al. Introduction to Beam Instrumentation and Diagnostics. *Proceedings of the CERN Accelerator School: Advanced Accelerator Physics Course*, 2013.

[57] Michael F. L'Annunziata. *Handbook of Radioactivity Analysis*. Elsevier, 2012.

[58] P. A. Cherenkov. Visible emission of clean liquids by action of γ-radiation. *Doklady Akademii Nauk SSSR*, 2:385 – 388, 1934.

[59] Il'ja Frank and Igor Tamm. Coherent Visible Radiation of Fast Electrons Passing Through Matter. *Doklady Akademii Nauk SSSR*, 14:109 – 114, 1937.

[60] S. P. Denisov. Radiation of faster than light particles (Cherenkov effect). *Sorosovsky Obrazovatelny Zhurnal*, 2:89 – 97, 1996.

[61] Wolfgang von Sellmeier. Zur Erklärung der abnormen Farbfolge im Spektrum einiger Substanzen. *Annalen Der Physik Und Chemie*, 219:272 – 282, 1871.

[62] I. H. Malitson. Interspecimen Comparison of the Refractive Index of Fused Silica. *Journal of the optical society of America*, 55:1205 – 1209, 1965.

[63] M. Badea and I. Lazanu. Role of phase and group velocities in Cherenkov radiation and applications in HEP experiments. *Romanian Reports in Physics*, 62:298 – 308, 2010.

[64] M. Gasior et al. Introduction to Beam Instrumentation and Diagnostics. *CERN Yellow Report CERN-2014-009*, pages 23 – 60, 2013.

[65] V. Puill, F. Addesa, L. Burmistrov, D. Breton, V. Chaumat, G. Cavoto, S. Conforti Di Lorenzo, S. Dubos, Yu.A. Gavrikov, F. Iacoangeli, J. Jeglot, J. Maalmi, A. Natochii, R. Rossi, S. Montesano, W. Scandale, A. Stocchi and J.-F. Vagnucci. The CpFM, an in-vacuum Cherenkov beam monitor for UA9 at SPS. *Journal of Instrumentation*, 12:P04029, 2017.

[66] W. Scandale et al. First results on the SPS beam collimation with bent crystals. *Physics Letters B*, 692:78 – 82, 2010.

[67] P. Strubin. Large high-vacuum systems for CERN accelerators. *Journal of Physics: Conference Series*, 114:012001, 2008.

[68] D. Breton, E. Delagnes, J. Maalmi and P. Rusquart. The WaveCatcher Family of SCA-based 12-bit 3.2-GS/s Fast Digitizers. *2014 19th IEEE-NPSS Real Time Conference*, 2014.

[69] Gerhard Lutz. *Semiconductor Radiation Detectors. Device Physics*. Springer, 2007.

[70] Leonardo Rossi, Peter Fischer, Tilman Rohe, and Norbert Wermes. *Pixel Detectors. From Fundamentals to Applications*. Springer, 2006.

[71] J. Jakubek. Semiconductor Pixel detectors and their applications in life sciences. *Journal of Instrumentation*, 4:P03013, 2009.

[72] Salim Reza. *Semiconductor Radiation Detectors. Technology and Applications*. CRC Press, 2017.

[73] Z. He. Review of the Shockley–Ramo theorem and its application in semiconductor gamma-ray detectors. *Nuclear Instruments and Methods in Physics Research A*, 463:250 – 267, 2001.

[74] M. C. Vignali. Silicon Sensors for the Upgrades of the CMS Pixel Detector. *Ph.D. thesis, Universität Hamburg*, 2015.

[75] H. Spieler. Semiconductor Detector Systems. *CLARENDON PRESS. OXFORD*, 2005.

[76] X. Llopart et al. Timepix, a 65k programmable pixel readout chip for arrival time, energy and/or photon counting measurements. *Nuclear Instruments and Methods in Physics Research A*, 581:485 – 494, 2007.

[77] L. Pinsky. An Update on Medipix in Space and Future Plans (Medipix2, 3 & 4). *6th International Workshop on Analogue and Mixed-Signal Integrated Circuits for Space Applications*, 2016.

[78] C. Granja et al. The SATRAM Timepix spacecraft payload in open space on board the Proba-V satellite for wide range radiation monitoring in LEO orbit. *Planetary and Space Science*, 125:114 – 129, 2015.

[79] A. Natochii et al. Use of a hybrid semiconductor pixel detector as a precision beam monitor at CERN accelerator facilities. *Journal of Instrumentation*, 14: P03018, 2019.

[80] R. Ballabriga, M. Campbell, X. Llopart. Charge Collection Characterization with Semiconductor Pixel Detector Timepix. *2008 IEEE Nuclear Science Symposium Conference Record*, pages 259 – 262, 2008.

[81] D. H. Wilkinson. The Geiger Discharge. *Physical Review*, 74:1417 – 1429, 1948.

[82] R. Ballabriga, M. Campbell, X. Llopart. Asic developments for radiation imaging applications: The medipix and timepix family. *Nuclear Instruments and Methods in Physics Research A*, 878:10 – 23, 2018.

[83] V. Kraus et al. FITPix - fast interface for Timepix pixel detectors. *Journal of Instrumentation*, 6:C01079, 2011.

[84] D. Turecek et al. Pixelman: a multi-platform data acquisition and processing software package for Medipix2, Timepix and Medipix3 detectors. *Journal of Instrumentation*, 6:C01046, 2011.

[85] E. J. Schioppa. The color of X-rays. Spectral X-ray computed tomography using energy sensitive pixel detectors. *Ph.D. thesis, Universiteit van Amsterdam*, 2014.

[86] M. Oriunno et al. The Roman Pot for the LHC. *Proceedings of the 10th European Particle Accelerator Conference*, pages 562 – 564, 2006.

[87] M. Deile et al. Beam coupling impedance measurement and mitigation for a TOTEM Roman Pot. *Proceedings of the 11th European Particle Accelerator Conference*, pages 1598 – 1600, 2008.

[88] The RD22 Collaboration. Second Status Report on RD22: Crystal Extraction at the SPS. *CERN/DRDC 94-11*, 1994.

[89] A. G. Afonin et al. High-Efficiency Beam Extraction and Collimation Using Channeling in Very Short Bent Crystals. *Physical Review Letters*, 87:094802, 2001.

[90] R. A. Carrigan et al. Beam extraction studies at 900 GeV using a channeling crystal. *Physical Review Special Topics – Accelerators and Beams*, 5:043501, 2002.

[91] S. Agostinelli et al. Geant4 – a simulation toolkit. *Nuclear Instruments and Methods in Physics Research A*, 506:250 – 303, 2003.

[92] T. T. Böhlen et al. The FLUKA Code: Developments and Challenges for High Energy and Medical Applications. *Nuclear Data Sheets*, 120:211 – 214, 2014.

[93] W. Scandale, F. Cerutti, L. S. Esposito, M. Garattini, S. Gilardoni, S. Montesano, R. Rossi, A. Natochii, V. Zhovkovska et al. Observation of probability asymmetry for nuclear interactions of high energy particles in short bent crystals. *Submitted to The European Physical Journal C*, 2019.

[94] A.I. Akhiezer, I.A. Akhiezer, N.F. Shul'ga . Theory of bremsstrahlung of relativistic electrons and positrons in crystals. *Journal of Experimental and Theoretical Physics*, 49:631 – 635, 1979.

[95] Yu. A. Chesnokov et al. About the probability of close collisions during stochastic deflection of positively charged particles by a bent crystal. *Physics Letters B*, 731:118 – 121, 2014.

[96] L. Burmistrov et al. Test of full size Cherenkov detector for proton Flux Measurements. *Nuclear Instruments and Methods in Physics Research A*, 787: 173 – 175, 2015.

[97] P. Russo et al. ^{18}F-FDG positron autoradiography with a particle counting silicon pixel detector. *Physics in Medicine and Biology*, 53:6227 – 6243, 2008.

[98] C. Scharf and R. Klanner. Precision measurement of the carrier drift velocities in $< 100 >$ silicon. *Journal of Instrumentation*, 10:C11008, 2015.

[99] M. M. Devi et al. Hadron energy response of the Iron Calorimeter detector at the India-based Neutrino Observatory. *Journal of Instrumentation*, 8:P11003, 2013.

[100] K. Akiba et al. The Timepix Telescope for High Performance Particle Tracking. *Nuclear Instruments and Methods in Physics Research A*, 723:47 – 54, 2013.

[101] S. P. George et al. Particle tracking with a Timepix based triple GEM detector. *Journal of Instrumentation*, 10:P11003, 2015.

[102] M. Pentia et al. Multiple scattering error propagation in particle track reconstruction. *Romanian Journal of Physics*, 40:181 – 191, 1995.

[103] M. Pentia, G. Iorgovan and A. Mihul. Multiple scattering error propagation in particle track reconstruction. *Romanian Journal of Physics*, 40:181 – 191, 1995.

[104] M. J. Barnes et al. Injection and extraction magnets: septa. *CERN Accelerator School: Specialised course on Magnets*, CERN-2010-004:167 – 184, 2011.

[105] B. Goddard. Injection and extraction. *The Introduction to Accelerator Physics Course*, 2008.

[106] The RD22 Collaboration. Second Status Report on RD22: Crystal Extraction at the SPS. *CERN/DRDC 94-11*, 1994.

[107] R. A. Carrigan et al. Beam extraction studies at 900 GeV using a channeling crystal. *Physical Review Special Topics - Accelerators and Beams*, 5:043501, 2002.

[108] Yu. M. Ivanov et al. High-Efficiency Beam Extraction and Collimation Using Channeling in Very Short Bent Crystals. *Physical Review Letters*, 87:094802, 2001.

[109] W. Scandale, A. D. Kovalenko and A. M. Taratin. Possibility of high efficient beam extraction from the CERN SPS with a bent crystal. Simulation results. *Nuclear Instruments and Methods in Physics Research A*, 848:166 – 169, 2017.

[110] W. Scandale et al. Strong reduction of the off-momentum halo in crystal assisted collimation of the SPS beam. *Physics Letters B*, 714:231 – 236, 2012.

[111] A. M. Taratin and W. Scandale. Simulation of crystal assisted collimation experiment. *Nuclear Instruments and Methods in Physics Research B*, 313:26 – 32, 2013.

[112] F. M. Velotti et al. Reduction of resonant slow extraction losses with shadowind of septum wires by a bent crystal. *Proceedings of the 8th International Particle Accelerator Conference*, 2017.

[113] Y. Papaphilippou et al. Operational performance of the LHC proton beams with the SPS low transition energy optics. *Proceedings of the 4th International Particle Accelerator Conference*, 2013.

[114] H. Bartosik, G. Arduini and Y. Papaphilippou. Optics considerations for lowering transition energy in the SPS. *Proceedings of the 2nd International Particle Accelerator Conference*, 2011.

[115] F. Antoniou et al. Performance of the SPS transition energy optics for LHC ion beams. *Proceedings of the 4th International Particle Accelerator Conference*, 2013.

[116] M. A. Fraser et al. Experimental results of crystal-assisted slow extraction at the SPS. *Proceedings of the 8th International Particle Accelerator Conference*, 2017.

[117] F. M. Addesa et al. The SE-CpFM detector for the crystal-assisted extraction at CERN-SPS. *Proceedings of the 6th International Beam Instrumentation Conference*, 2017.

[118] E. Laface et al. Crystal collimation efficiency measured with the Medipix detector in SPS UA9 experiment. *Proceedings of the 1st International Particle Accelerator Conference*, 2010.

[119] L. Burmistrov. A detector for charged particle identification in the forward region of SuperB. *Ph.D. thesis, Université Paris-Sud 11*, 2011.

[120] H. Grote and F. Schmidt. MAD-X – An Upgrade from MAD8. *Proceedings of the Particle Accelerator Conference*, CERN-AB-2003-024-ABP:C030512, 2003.

[121] A. Natochii et al. Characterisation of the fused silica surface quality with a β-source. *Nuclear Instruments and Methods in Physics Research A*, 910:15 – 21, 2018.

[122] S. Agostinelli et al. Geant4 - a simulation toolkit. *Nuclear Instruments and Methods in Physics Research Section A*, 506:250 – 303, 2003.

[123] R. Jain, R. Kasturi, and B. G. Schunck. *Machine Vision*. McGraw-Hill, Inc., 1995.

[124] M. Tanabashi et al. Particle Data Group. *Physical Review D*, 98:030001, 2018.

[125] B. Hartmann et al. A Novel Method for Fragmentation Studies in Particle Therapy: Principles of Ion Identification. *International Journal of Particle Therapy*, 3:439 – 449, 2017.

[126] B. Hartmann. A Novel Approach to Ion Spectroscopy of Therapeutic Ion Beams Using a Pixelated Semiconductor Detector. *Ph.D. thesis, Ruperto-Carola University*, 2013.

[127] Kickoff meeting for the Physics Beyond Collider study. *Physics Beyond Colliders Kickoff Workshop*, 2016.

[128] M. Ferro-Luzzi, S. Redaelli, C. Hadjidakis. Studies for future fixed-target experiments at the LHC in the framework of the CERN Physics Beyond Collider study. *Proceedings of the 9th International Particle Accelerator Conference*, 2018.

[129] L. Burmistrov et al. Measurement of Short Living Baryon Magnetic Moment using Bent Crystals at SPS and LHC. *CERN-SPSC-2016-030/SPSC-EOI-012*, 2016.

[130] S. Montesano. Testing the double-crystal setup for Physics Beyond Colliders experiments in the UA9 experiment. *Proceedings of the 9th International Particle Accelerator Conference*, 2018.

[131] R.J. Steinhagen, et al. On the continuous measurement of the LHC beta-function - prototype studies at the SPS. *Proceedings of the 23rd Particle Accelerator Conference*, 2009.

[132] B. Povh, K. Rith, C. Scholz, and F. Zetsche. *Particles and Nuclei. An Introduction to the Physical Concepts*. Springer, 2008.

[133] J. Franklin et al. Wave-function mixing of flavor-degenerate baryons. *Physical Review D*, 24:2910, 1981.

[134] R. Perin. The Superconducting Magnet System for the LHC. *IEEE Transactions on Magnetics*, 27:1735 – 1742, 1991.

[135] V.G. Baryshevsky. Spin rotation of ultrarelativistic particles passing through a crystal. *Pis'ma v Zhurnal Tekhnicheskoi Fiziki (Soviet Technical Physics Letters)*, 5:182 – 184, 1979.

[136] V.L. Lyuboshitz. The Spin Rotation at Deflection of Relativistic Charged Particle in Electric Field. *Preprint of the Joint Institute for Nuclear Research*, P2:12559, 1979.

[137] I.J. Kim. Magnetic moment measurement of baryons with heavy-flavored quarks by planar channeling through a bent crystal. *Nuclear Physics B*, 229: 251 – 268, 1983.

[138] A.I. Akhiezer, N.F. Shul'ga, V.I. Truten', A.A. Grinenko, V.V. Syshchenko. Dynamics of high-energy charged particles in straight and bent crystals. *Physics-Uspekhi*, 38:1119 – 1145, 1995.

[139] V.G. Baryshevsky. The possibility to measure the magnetic moments of short-lived particles (charm and beauty baryons) at LHC and FCC energies using the phenomenon of spin rotation in crystals. *Physics Letters B*, 757:426 – 429, 2016.

[140] F.J. Botella et al. On the search for the electric dipole moment of strange and charm baryons at LHC. *The European Physical Journal C*, 77:181, 2017.

[141] D. Chen et al. First Observation of Magnetic Moment Precession of Channeled Particles in Bent Crystals. *Physical Review Letters*, 69:3286 – 3290, 1992.

[142] E.M. Aitala et al. Multidimensional resonance analysis of $\Lambda_c^+ \to pK^-\pi^+$. *Physics Letters B*, 471:449 – 459, 2000.

[143] J.G. Korner, G. Kramer, J. Willrodt. Weak Decays of Charmed Baryons. *Zeitschrift fur Physik C, Particles and Fields*, 2:117 – 135, 1979.

[144] G.R. Goldstein. Polarization of Inclusive Λ_c's in a Hybrid Model. *Proceedings of the Hyperon Physics Symposium*, C99-09-27.4:132 – 136, 1999.

[145] T. Sjostrand, S. Mrenna, P. Skands. A brief introduction to PYTHIA 8.1. *Computer Physics Communications*, 178:852 – 867, 2008.

[146] F.M. Velotti et al. Feasibility study of a new SPS beam dump system. *Proceedings of the 6th International Particle Accelerator Conference*, THPF097: 3930 – 3933, 2015.

[147] SPS-LSS5: LS2 Beamline Modifications. *The CERN Engineering and Equipment Data Management Service*, `https://edms.cern.ch/ui/file/1905117/0/spslnins0143-v0_plt_cpdf.pdf`, 2018.

[148] M.J. Barnes et al. Injection and Extraction Magnets: Septa. *Proceedings of the CAS-CERN Accelerator School: Magnets, Bruges, Belgium*, CERN-2010-004: 167 – 184, 2009.

[149] C. Bovet et al. A selection of formulae and data useful for the design of A.G. synchrotrons. CERN/MPSSI/Int. DL/70/4, 1970.

[150] S.H. Kim. Direct-Drive and Eddy-Current Septum Magnets. *Proceedings of the 2001 Particle Accelerator Conference*, LS-292:3233 – 3235, 2001.

[151] T. Poikela et al. Timepix3: a 65K channel hybrid pixel readout chip with simultaneous ToA/ToT and sparse readout. *Journal of Instrumentation*, 9: C05013, 2014.

[152] P. Burian et al. Katherine: Ethernet Embedded Readout Interface for Timepix3. *Journal of Instrumentation*, 12:C11001, 2017.

université PARIS-SACLAY | ÉCOLE DOCTORALE PHENIICS

Titre: Développement de détecteurs pour l'expérience UA9 au CERN SPS

Mots clés: Détecteur, Cherenkov, Cristal, Moment Dipolaire Magnétique, Timepix, LHC/SPS

Résumé: Les travaux de recherche documentés dans cette thèse s'inscrivent dans le cadre de la Collaboration UA9 au CERN. L'objectif principal de la collaboration est l'étude de la collimation et de l'extraction de faisceaux de particules de haute énergie. La thèse est principalement consacrée au développement des détecteurs et aux installations expérimentales correspondantes qui ont été mises en œuvre au SPS et au LHC au CERN.
En ce qui concerne la nature de l'interaction des particules chargées avec une structure monocristalline, un cristal courbé peut être utilisé pour orienter le faisceau de particules de haute énergie au moyen de la canalisation de particules entre les plans atomiques du cristal. Un tel phénomène est étudié de manière approfondie par la Collaboration UA9. Un des principaux objectifs de la recherche présentée dans cette thèse est de développer des dispositifs sensibles pour mesurer le flux et les caractéristiques de faisceau des particules déviées par le cristal au SPS et au LHC.
Pour cette thèse nous avons étudié les détecteurs Cherenkov (CpFM) et les détecteurs à pixel (Timepix). Depuis 2015, le CpFM (détecteur de Cherenkov pour la mesure du flux de protons) a été souvent modifié afin d'améliorer la précision pour le comptage des particules. La plage de fonctionnement du dispositif varie de 1 à 1000 particules par faisceau de particules ($\sim$3 ns) avec une résolution inférieure à 20% par proton. Fonctionnant dans le vide primaire de l'accélérateur et à des doses de rayonnement élevées, le détecteur a montré une grande stabilité et ayant la possibilité d'effectuer des études de contamination par faisceau. À son tour, le détecteur Timepix a été étalonné sur la ligne de faisceaux d'extraction de l'accélérateur SPS, fonctionnant dans le vide secondaire (Roman Pot). Une partie importante de la thèse est consacrée à la caractérisation et à l'étalonnage de ces détecteurs avec les développements des logiciels pour l'acquisition et l'analyse de données.
Dans cette thèse, nous proposons également la mesure du moment dipolaire magnétique (MDM) de baryons à courte durée de vie. Le MDM est une caractéristique importante de l'interaction des particules avec un champ magnétique externe. Pour cette thèse, nous nous concentrons sur la mesure le MDM du baryon Λ_c^+, qui pourrait fournir des informations sur le facteur gyromagnétique (g) du quark charme. Une valeur différente de g=2 indiquera une structure composite possible du c-quark et clairement la présence de physique au-delà du Modèle Standard (SM). Jusqu'ici, aucune mesure expérimentale du moment dipolaire magnétique des baryons avec des quarks lourds n'a été effectuée en raison d'une courte durée de désintégration de ces particules (environ 60 μm). La proposition faite dans cette thèse est de produire des baryons charmés par interaction forte entre les protons extrait (à l'aide d'un premier cristal courbé) et une cible. Après la cible, un deuxième cristal courbé à grand angle (de plusieurs mrad) est utilisé pour canaliser les baryons et induire une rotation du vecteur de polarisation des baryons charmés. Cette configuration s'appelle une configuration à double cristal et l'expérience est proposée au LHC.
Dans cette thèse, je me suis concentré principalement sur tous les tests et la validation nécessaires au SPS avant la mise en œuvre au LHC. Une configuration expérimentale possible pour les mesures MDM au niveau du SPS est également proposée avec une estimation de l'erreur absolue de la valeur mesurée du facteur g pour le baryon Λ_c^+.

Université Paris-Saclay
Espace Technologique / Immeuble Discovery
Route de l'Orme aux Merisiers RD 128 / 91190 Saint-Aubin, France

université PARIS-SACLAY | ÉCOLE DOCTORALE PHENIICS

Title: Detectors developments for the UA9 experiment at the CERN SPS

Keywords: Detector, Cherenkov, Crystal, Magnetic Dipole Moment, Timepix, LHC/SPS

Abstract: The research work documented in this thesis is done in a frame of the UA9 Collaboration at CERN. The main goal of the collaboration is the investigation of the high-energy particle beam collimation and extraction. The thesis is mainly devoted to the developments of detectors and the consequent experimental setups implemented at the SPS or LHC circulating machines at CERN.

Regarding the nature of the charged particle interaction with a monocrystalline structure, a curved crystal can be used for the steering of the high-energy particle beam by means of the particle channeling between atomic planes of the crystal. Such a phenomenon is intensively studied by the UA9 Collaboration. Therefore, one of the main goals of the presented research is to develop sensitive devices for measuring the flux and the beam characteristics of the particles deflected by the crystal at the circulating machines.

The detectors studied for this thesis are Cherenkov (CpFM) and pixel (Timepix). Since 2015, the CpFM (Cherenkov detector for proton Flux Measurement) has undergone various modifications to improve the particle counting characteristics. The range of the device operation varies from 1 to 1000 particles per bunch ($\sim$3 ns) with the particle resolution of less than 20% per single proton. Working in the primary vacuum of the accelerator and at high radiation doses, the detector showed high stability with the possibility to perform beam contamination studies. In turn, the Timepix detector has been calibrated at the extraction beamline and SPS accelerator, working in the secondary vacuum of the Roman Pot. A significant part of the thesis is devoted to the characterization and calibration of these detectors with the software developments for data acquisition and analysis.

In this thesis, we also make a proposal for the measurement of the magnetic dipole moment (MDM) of short-lived baryons. The MDM is an important characteristic of the particle interaction with an external magnetic field. For the thesis, we concentrate on the measurement of the Λ_c^+ MDM, which could provide information on the gyromagnetic (g) factor of the charm quark. Any discrepancy from g=2 will indicate a possible composite structure of the c-quark and clearly physics beyond the Standard Model (SM). So far, no experimental measurements of this value of baryons with heavy flavoured quarks have been carried out due to a short decay length of these particles (about 60 μm). The proposal made in this thesis is to produce charm baryons by a strong interaction of the extracted proton beam (using a first bent crystal) impinging onto a target followed by the second large angle bent crystal (of several mrad) to channel the baryons and to rotate their polarization vector. This configuration is called a double-crystal setup and the experiment is proposed to take place at the LHC.

In this thesis, I concentrate mainly on all the tests and validation needed at the SPS prior to the implementation at the LHC. A possible experimental configuration for the MDM measurements at the SPS is also proposed with an estimation of the absolute error of the measured g-factor value for the Λ_c^+ baryon.

Université Paris-Saclay
Espace Technologique / Immeuble Discovery
Route de l'Orme aux Merisiers RD 128 / 91190 Saint-Aubin, France